Data analysis for solar neutrinos: Final CNO measurement exploiting the directionality method with Borexino and JUNO's potential for solar neutrino measurement

Von der Fakultät für Mathematik, Informatik und Naturwissenschaften der RWTH Aachen University zur Erlangung des akademischen Grades einer Doktorin der Naturwissenschaften genehmigte Dissertation

vorgelegt von

Apeksha Singhal, M.Sc.

aus

Etawah, Indien

Berichter: Prof. Dr. Dr. Livia Ludhova

Prof. Dr. rer. nat. Christopher Wiebusch

Tag der mündlichen Prüfung: 03.12.2024

Abstract

This dissertation presents the recent solar neutrino measurements with the Borexino experiment and the expected sensitivity to solar neutrinos with the JUNO experiment. Solar neutrinos are created in the Sun through different fusion processes, that are classified as: the proton-proton (*pp*) chain and the Carbon-Nitrogen-Oxygen (CNO) cycle. The CNO cycle is a sub-dominant process in the Sun, while it is hypothesized to be the main source of energy in the heavier stars. Solar neutrinos are weakly interacting particles and thanks to their elusive nature, they are the only direct probes of the information about the solar interior. The Borexino experiment has already provided a comprehensive measurement of all *pp* chain neutrinos and the first detection of CNO solar neutrinos. It was a 280 t liquid scintillator (LS) detector located at the Laboratori Nazionali del Gran Sasso (LNGS) in Italy. It provided an improved measurement of CNO solar neutrinos and its implications for understanding the chemical composition of the Sun, using its latest and final data set collected in 2017-2021 period. My contributions towards the ^{210}Bi background constraint model, the production of fit inputs as well as performing the multivariate spectral fit to obtain CNO-ν rate, are presented in this thesis. These results have been published in Physical Review Letters. The first directional measurement of sub-MeV solar neutrinos in a liquid scintillator detector has also been accomplished by Borexino. A so-called Correlated and Integrated Directionality (CID) technique has been developed, which exploits the directional and sub-dominant Cherenkov information contained in the early hits of a solar neutrino event. The proof of concept of this method has been provided using ^{7}Be solar neutrinos and the results, including my contributions, are discussed in this thesis and have been published in a joint publication in Physical Review Letters and Physical Review D. The latest result from Borexino includes the directional measurement of CNO-ν solar neutrinos using CID and without the ^{210}Bi constraint for the first time. My contribution constitutes the optimisation of the fit inputs, calibration of group velocity of Cherenkov photons in the ^{7}Be-ν edge region, evaluation of the systematic uncertainties, and performing final CID fits to finally extract the CNO solar neutrinos. These results have been used to perform the combined CID and the multivariate spectral fit for the solar neutrino analysis, providing the most precise and Borexino's final CNO-ν rate, which has been published in Physical Review D. JUNO is a 20 kt LS experiment under construction in south China, with its primary goal of the determination of neutrino mass ordering. The potential of JUNO to perform ^{7}Be, *pep*, and CNO solar neutrino measurements with unprecedented precision is discussed in this thesis and my work includes executing the multivariate fits assuming various background contamination levels. These findings have been published in Journal of Cosmology and Astroparticle Physics. The first feasibility studies to perform the directional measurement of ^{7}Be and CNO solar neutrinos in JUNO using CID has also been explored in this thesis. I present my work regarding the CID analysis strategy and the preliminary results, which shows the improved JUNO's sensitivity to solar neutrinos.

Zusammenfassung

Diese Dissertation stellt die neuesten Messungen von Sonnenneutrinos mit dem Borexino-Experiment sowie die erwartete Sensitivität gegenüber Sonnenneutrinos mit dem JUNO-Experiment vor. Sonnenneutrinos entstehen in der Sonne durch verschiedene Fusionsprozesse, die als Proton-Proton-chain (*pp*-chain) und Carbon-Nitrogen-Oxygen-Zyklus (CNO-Zyklus) klassifiziert werden. Der CNO-Zyklus ist in der Sonne ein untergeordneter Prozess, während er in schwereren Sternen als Hauptenergiequelle vermutet wird. Sonnenneutrinos sind schwach wechselwirkende Teilchen und dank ihrer schwer fassbaren Natur sind sie die einzigen direkten Sonden für Informationen über das Sonneninnere. Das Borexino-Experiment hat bereits eine umfassende Messung aller *pp*-chain-Neutrinos und den ersten Nachweis von CNO-Sonnenneutrinos erbracht. Es handelte sich um einen 280 t flüssigen Szintillator-Detektor (LS), der sich in den Laboratori Nazionali del Gran Sasso (LNGS) in Italien befindet. Mit dem neuesten und letzten Datensatz, der im Zeitraum 2017-2021 gesammelt wurde, lieferte es eine verbesserte Messung der CNO-Sonnenneutrinos und deren Implikationen für das Verständnis der chemischen Zusammensetzung der Sonne. Meine Beiträge zum ^{210}Bi-Hintergrund-Beschränkungsmodell, zur Erstellung von Fit-Eingaben sowie zur Durchführung des multivariaten Spektral-Fits zur Bestimmung der CNO-ν-Rate werden in dieser Arbeit vorgestellt. Diese Ergebnisse wurden in den Physical Review Letters veröffentlicht. Der erste richtungsweisende Nachweis von sub-MeV- Sonnenneutrinos in einem Flüssigszintillator-Detektor wurde ebenfalls von Borexino erreicht. Eine sogenannte Correlated and Integrated Directionality (CID) Technik wurde entwickelt, die die richtungsweisende und untergeordnete Cherenkov-Information nutzt, die in den frühen Hits eines Sonnenneutrinoereignisses enthalten ist. Der Nachweis dieses Konzepts wurde mit ^{7}Be-Sonnenneutrinos erbracht und die Ergebnisse, einschließlich meiner Beiträge, werden in dieser Arbeit diskutiert und in einer gemeinsamen Veröffentlichung in den Physical Review Letters und Physical Review D veröffentlicht. Das neueste Ergebnis von Borexino umfasst die richtungsweisende Messung von CNO-ν-Sonnenneutrinos unter Verwendung von CID und erstmals ohne die ^{210}Bi-Einschränkung. Mein Beitrag umfasst die Optimierung der Fit-Eingaben, die Kalibrierung der Gruppenlaufzeit von Cherenkov-Photonen im ^{7}Be-ν-Randbereich, die Bewertung der systematischen Unsicherheiten und die Durchführung der finalen CID-Fits zur endgültigen Extraktion der CNO-Sonnenneutrinos. Diese Ergebnisse wurden verwendet, um die kombinierte CID- und multivariate Spektral-Analyse für die Sonnenneutrinoanalyse durchzuführen, was die präziseste und endgültige CNO-ν-Rate von Borexino liefert, die in Physical Review D veröffentlicht wurde. JUNO ist ein 20 kt LS-Experiment, das sich im Bau in Südchina befindet, mit dem Hauptziel, die Neutrinomassenhierarchie zu bestimmen. Das Potenzial von JUNO, ^{7}Be-, *pep*- und CNO-Sonnenneutrino-Messungen mit beispielloser Präzision durchzuführen, wird in dieser Arbeit diskutiert und meine Arbeit umfasst die Durchführung der multivariaten Fits unter Annahme verschiedener Hintergrundkontaminationsniveaus. Diese Erkenntnisse wurden im Journal of Cosmology and Astroparticle Physics veröffentlicht. Die ersten Machbarkeitsstudien zur Durchführung der richtungsweisenden Messung von ^{7}Be- und CNO-Sonnenneutrinos in JUNO unter Verwendung von CID wurden ebenfalls in dieser Arbeit untersucht. Ich präsentiere meine Arbeit zur CID-Analyse-Strategie und die vorläufigen Ergebnisse, die die verbesserte JUNO-Sensitivität gegenüber Sonnenneutrinos zeigen.

Contents

Introduction to the thesis

This thesis is organized in three parts. Part I starts with an overview of the neutrino physics in Chapter 1. It provides an introduction to neutrinos as a particle as well as about 100 year old history of neutrinos. The mathematical framework behind the phenomenon of neutrino oscillation in vacuum and matter is also provided. It also summarizes various sources of neutrinos including both natural and artificial sources. The current open questions in the field of neutrino physics and neutrino oscillations are also reviewed in this chapter. In this part, Chapter 2 is also included, that introduces the neutrinos from the Sun, called solar neutrinos, which are the main focus of this dissertation. Firstly, it describes the nuclear fusion processes for the hydrogen to helium conversion in the Sun, the dominant *proton-proton (pp)* chain and the subdominant Carbon-Nitrogen-Oxygen (CNO) cycle, in addition to the description of the types of neutrinos emitted in these reactions. The Standard Solar Model (SSM), which describes the state and evolution of the Sun and is used to predict the solar neutrino fluxes, is also summarized in this chapter. Here, the concept of the solar metallicity, a crucial input to the SSMs, is introduced. It is also discussed that the measurement of solar neutrinos provides an unique handle to test the SSM and plays a key role towards solving the so-called *solar metallicity problem*. This chapter also provides an overview of various solar neutrino experiments and also introduces their principle detection methods of solar neutrinos. These experiments include radiochemical, water Cherenkov, liquid scintillator, as well as the future hybrid detectors. As this dissertation focuses on the solar neutrino measurements with two liquid scintillator (LS) detectors, Borexino and JUNO, the typical backgrounds for the solar neutrino analysis in LS experiments are also summarized.

Part II is devoted to solar neutrino analysis with the Borexino experiment. Borexino, located in Laboratori Nazionali del Gran Sasso (LNGS) in Italy, was a 280 ton liquid scintillator detector. The technical information about Borexino constituting hardware and electronics, the important operations like calibration and thermal insulation, and various algorithms as well as the simulation framework used in the analysis, will be discussed in detail in Chapter 3. It took data from May 2007 to October 2021. Thanks to its unprecedented radiopurity, Borexino has provided the measurements of almost all *pp*-chain solar neutrinos [1], except *hep* neutrinos and the first experimental observation of CNO solar neutrinos [2]. It has also provided an improved measurement of CNO solar neutrinos and its implications on the solar metallicity problem by performing the analysis of most recent data collected in 2017-2021. This is discussed in Chapter 4. In these analyses, a spectral fit, exploiting energy and radial information of the events, is performed to disentangle the solar neutrino events from the background ones in data. One of the crucial background for the CNO solar neutrino analysis is the β-decay of ^{210}Bi due to its spectral degeneracy with the CNO neutrino events. An independent constraint on ^{210}Bi rate is obtained by performing a paraboloid fit on selected α decaying ^{210}Po (^{210}Bi daughter) data events in an so-called "low polonium field" region. The determination of ^{210}Bi constraint uses a model which describes the ^{210}Po spatial distribution, containing a parameter that represents the leakage of β-like events in the selected ^{210}Po data. I have worked on the determination of this parameter, necessary to take into account for the correct estimation of ^{210}Bi rate constraint, which is also presented in this chapter. The production of data and Monte Carlo inputs

for the spectral fit and the extracted result on CNO-ν rate using the fit, which I have performed, are also reported. The results have been published in [3].

In LS detectors, the event detection is done using the isotropic and dominant scintillation light. The directional Cherenkov light is also emitted which can be used to distinguish the neutrino signal from the backgrounds. However, the separation of Cherenkov light and the directional reconstruction of signal events using the Cherenkov light is typically not possible, due to its very low ($\lesssim$1%) contribution. A novel technique called Correlated and Integrated Directionality (CID) has been developed, which has been used to perform the first directional measurement of sub-MeV solar neutrinos in Borexino. In this method, the early individual photon hits of an event is correlated to the well-known position of the Sun and the integration over a large number of detected events is done to obtain an angular CID distribution. Since the directional Cherenkov light is emitted and arrives to PMTs, on average, earlier to the isotropic scintillation photons, the resulting angular CID distribution of solar neutrino events has a signature peak. The CID angular distribution of the background events is almost flat, as the charged particles from the decay are emitted in a direction, which is uncorrelated to the Sun position. This is utilised to extract the solar neutrino contribution in the data. This technique is described in detail in Chapter 5. After the introduction of the CID method, this chapter provides the studies regarding the proof-of-principle of CID, using first two hits of the events in the ^{7}Be-ν shoulder energy region in the so-called Phase-I period of the Borexino. My contributions for this analysis include the optimisation of the number of bins of CID angular distributions and the study of various systematic effects on the shape of background CID distributions using a toy MC method, which are also described in this chapter. These results were published in [4, 5]. Moreover, the CID method has also been utilized to perform the directional measurement of CNO solar neutrinos with about 5.3σ significance of detection, using all Borexino data and without using ^{210}Bi constraint for the first time. This is discussed in Chapter 5. For this analysis, an independent energy region has been chosen with respect to the ^{7}Be-ν CID analysis. I have contributed in this analysis by performing a sensitivity analysis for the optimisation of the number of bins as well as number of early hits, which are used for the CID analysis. I have also performed analysis for the calibration of Cherenkov photons using ^{7}Be solar neutrinos and the final fit to obtain the CNO-ν measurement using CID. My other contributions include the evaluation of expected counts of different neutrinos and backgrounds in the region of interests as well as the study of the systematic effects associated to the CID analysis. A combined spectral fit using CID results on the solar neutrinos in CNO-ν analysis energy region as a constraint has also been performed, which has disfavored no-CNO hypothesis with about 8σ significance. These results have been published in [6] and was co-written by me.

Part III is dedicated to the JUNO experiment and its sensitivity to sub-MeV solar neutrinos. Chapter 6 introduces the JUNO experiment, a 20 kt LS detector which is currently under construction in Guangdong province in south China. In this chapter, various physics programs of JUNO, including the determination of neutrino mass ordering which is its primary goal, are also summarized. This chapter also provides a summary of the simulation framework, which is crucial for all the analyses in JUNO. Thanks to its enormous target size, it can accumulate a large number of solar neutrino events and measure their rates with unprecedented uncertainties. In Chapter 7, the precision of ^{7}Be, *pep*, and CNO neutrino rates that JUNO can achieve, is estimated by performing the spectral analysis. The achievable accuracy of the solar neutrino measurements is highly dependent upon the radioactive background levels in JUNO. These results were published in [7]. I contributed to this analysis by performing spectral fits using

a MC based sensitivity analysis, under the assumption of different background levels and the exposures JUNO will acquire. I also co-wrote the publication. Finally in Chapter 8, JUNO's sensitivity to ^{7}Be and CNO solar neutrinos is explored using the CID method. Here, I present the complete analysis strategy, that has been developed to carry out directional analysis of solar neutrinos. This includes the investigation of properties of Cherenkov photons in JUNO MC, which I performed. The extracted properties have been used to produce CID probability density functions (PDFs) of both signal and background using a toy MC method, that has been developed by me. This method simulates the realistic properties of JUNO, that are necessary for the CID analysis by taking advantage of the experience from Borexino. These PDFs have been used to estimate the first JUNO's sensitivity towards the solar neutrino measurement using directional Cherenkov light, which is also summarized in this chapter. Moreover, the possible systematic effects for the CID analysis have also been investigated by me. This chapter concludes with a discussion on JUNO's enhanced sensitivity towards solar neutrino measurements using the combined spectral and CID analysis.

Part I

Neutrinos

Chapter 1

Introduction to neutrinos

This chapter provides a brief introduction to neutrino physics. It starts with an overview of the important milestones in the history of neutrinos in general, in Sec. 1.1. Neutrinos as a particle in the Standard Model are introduced in Sec. 1.2. Section 1.3 explains the neutrino oscillation theory including both the vacuum and matter effects. The different sources of neutrinos are elaborated in Sec. 1.4. The current open questions in the field of neutrino physics are discussed in Sec. 1.5.

1.1 History

The history of neutrino dates back to the time of study of the nuclear β-decay. In 1914, J. Chadwick discovered that the energy spectrum of electrons, emitted in the β-decay, has a continuous energy spectrum [8], with a maximum energy at Q-value of the reaction. This observation was in contrast to the unique energy of the electron with a peak at Q-value of the reaction, which is expected for a two body decay. This led to the two interpretations supporting this observation: firstly, the primary electrons have a continuous energy spectrum and secondly, there exists secondary processes, that broaden the original discrete electron energy. To test these interpretations, a calorimetric measurement was performed. If the first interpretation is correct, the calorimetric measurements should result in an average electron energy, which should be lesser than the Q-value. If the latter is true, the measured energy of the electrons would be the maximal energy. This calorimetric experiment was done by Ellis and Wooster in 1927 [9] using RaE (^{210}Bi), that undergoes a β-decay. It was observed that the measured average energy of the electrons is less than the Q-value of the reaction, which supports the first interpretation. This experiment was repeated by L. Meitner in 1930 [10]. This confirmed the continuous energy spectrum of primary electrons and no secondary processes are responsible for the continuous β spectrum. To remedy the problem of non-conservation of the energy as well as the spin, observed in the β-decay, Pauli proposed the existence of a neutral and weakly interacting particle with half spin, which is emitted in the decay, in an open letter to a physics conference dated 4 December 1930 [11].

In 1932, J. Chadwick discovered neutron [12] that we know today and in 1934, Fermi formulated a theory of β-decay [13], incorporating the Pauli's particle and named it as *neutrino*, meaning the "little neutral one" in Italian. In 1934, Bethe and Peierls estimated the cross section of neutrino interaction with a nucleus and found it to be very small ($\sigma < 10^{-44}\,\mathrm{cm}^{-2}$) [14]. Later, B. Pontecorvo proposed the first method of neutrino detection in 1946 [15], suggesting the radiochemical method (see Sec. 2.4) of neutrino detection and pointed out the Sun, nuclear reactors, and radioactive sources as the intensive sources of neutrinos. After the discovery of muon in 1937 [16, 17], Pontecorvo proposed the universality of the Fermi interactions of electrons and muons in 1947 [18].

In 1952, the first and indirect experimental evidence of neutrinos was found using the electron capture decay of ^{37}Ar:

$$^{37}\mathrm{Ar} + e^- \rightarrow {}^{37}\mathrm{Cl} + \nu_e, \tag{1.1}$$

with a Q-value of 0.816 MeV. As this reaction consists of only two particles in the final state, the recoil energy of the nucleus is estimated to be 9.67 eV using the energy and momentum conservation. This corresponded to an expected recoiled velocity of 0.71 cm μs^{-1}. The recoiled velocity was then measured using a time-of-flight measurement, based on the Auger electron emission time and the detection of recoiled nucleus in a spectrometer [19, 20]. The measurements were in good agreement with the theoretical predictions of the recoil energy and velocity. The discovery of (anti)neutrinos finally took place by measuring the inverse β-decay (IBD):

$$\bar{\nu}_e + p \rightarrow e^+ + n. \tag{1.2}$$

The first idea was to detect (anti)neutrinos from the nuclear explosions, using a proposed detector "El monstro" [21]. It was never constructed and instead, it was decided to use a large flux of antineutrinos from a nuclear reactor. Cowan and Reines used a tank filled with water with dissolved $CdCl_2$ for the detection of antineutrinos. It was surrounded by two liquid scintillators to detect photons from the positron annihilation (prompt) and a delayed photon signal from the neutron capture on the cadmium nuclei, which will be discussed in Sec. 1.4. In 1953, the Hanford neutrino detector [22] with 300 l of scintillator was built. The signal was observed with an insufficient evidence due to the poor shielding against the cosmic ray background. The successful evidence was found using the Savannah river experiment with an improved shielding, which consisted of two target tanks filled with 200 l of water with $CdCl_2$. These tanks were sandwiched between the three tanks of 4200 l of liquid scintillator in total and each with 110 photomultiplier tubes. By looking for prompt and delayed signals from all the liquid scintillator detectors and acquiring data in both reactor-on and off times, the existence of (anti)neutrinos was confirmed in 1956 and the observed cross section of the reaction was in well agreement with the expected one [23].

In 1953, Konopinski and Mahmoud introduced the concept of lepton number, L [24]. They assigned L=+1 to the electron, muon, and the neutrino, and L = -1 to positron, positive muon (μ^+), and the antineutrinos, suggesting the law of conservation of lepton number. Later in 1950s, Davis [25] tested this experimentally by looking for the reaction: $\bar{\nu}_e$ + ^{37}Cl $\rightarrow$ ^{37}Ar + e^-. As this reaction violates the lepton number, he could only set limits on the cross section for the process and concluded that the neutrinos and antineutrinos are distinct particles. The neutrinos and antineutrinos also differ in their helicity: neutrinos are left-handed, whereas the antineutrinos are right-handed, in the V-A theory of weak interactions formulated in 1958 [26, 27]. This was experimentally determined by Goldhaber et. al. [28] through the measurement of polarization of neutrino, using the electron capture decay of ^{152}Eu: e^- + ^{152}Eu $\rightarrow$ ^{152}Sm* + ν_e and ^{152}Sm* $\rightarrow$ ^{152}Sm + γ.

In 1962, a direct experimental proof of the muon neutrino was obtained at the Brookhaven AGS experiment [29] using a 15 GeV proton beam, bombarding the beryllium target. This produced an almost pure ν_μ beam through decay of the secondary pions and kaons. The idea of the experiment was proposed by Pontocorvo in 1959 [30]. The goal was to test whether ν_μ and ν_e are the same particles. The ν_μ beam produce μ^- through the reaction: ν_μ + N $\rightarrow$ μ^- + X. If ν_μ and ν_e are the same particles, the reaction: ν_μ + N $\rightarrow$ e^- + X, would also be observed and there will be equal number of muons and electrons. However, 29 muon-like events and six electron-like events were observed, proving that ν_μ and ν_e are different particles. It was further confirmed by

CERN in 1963 [31]. It was proven that two different "families" of leptons exist: (ν_e, e) and (ν_μ, μ).

After the τ-lepton was discovered in 1975-1977 at e^+e^- collider at Stanford [32], it was expected that there could exist a third family of lepton and therefore, a tau neutrino would also exist [33]. In 2000, the third type of neutrino was observed by the DONUT collaboration at Fermilab [34]. The question of how many families of leptons exist in nature, quickly came up. The answer to this question was obtained at LEP experiments [35]. It was established that the number of light ($m_\nu < m_Z/2$) neutrinos is 2.984 ± 0.008 by measuring the total width of decay: $Z^0 \rightarrow \nu_l + \bar{\nu}_l$, including different decay modes coupling to Z-boson. Thus, there exist three active light neutrinos in nature [36].

As discussed, the neutrino physics theory expanded with exciting experimental results over the years. A key result in the history of neutrino physics includes the discovery of neutrino oscillations, by SuperKamiokande [37] in 1998 and SNO experiment [38] in 2001 in the atmospheric and solar neutrinos, respectively. It solved the solar neutrino problem that was observed by several experiments, which will be discussed in Sec. 2.4. The existence of neutrino oscillations shows that the neutrinos have mass, providing evidence for the new physics beyond the Standard Model and the mixing of lepton flavours exists. The first idea of neutrino oscillation ($\nu \rightleftarrows \bar{\nu}$) was suggested by Pontecorvo in 1957, which was motivated by $K^0 \rightleftarrows \bar{K}^0$ mixing [39]. In 1962, Z. Maki, M. Nakagawa, and S. Sakata introduced the concept of mixing of flavour and mass eigenstates [40]. The theory of neutrino oscillation was further developed by several people, for which the historical details can be found in Ref. [33].

1.2 Neutrinos in the Standard Model

The Standard Model (SM) of particle physics [41] incorporates the fundamental forces of strong, weak, and electromagnetic interactions. In the SM, eight gluons, three weak bosons ($W^\pm$, Z), and photon mediate the strong, weak, and electromagnetic forces, respectively. The SM also includes Higgs boson, responsible for the mass generation. The other particles, which includes six quarks, three charged leptons, and three neutrinos, in SM are fermions with half-spin. All charged particles interact through the electroweak force and the quarks also participate in the strong interactions.

In the SM, neutrinos are chargeless and their interactions is governed by the weak forces, implying they interact through the weak Charged Current (CC) via the exchange of the $W^\pm$ or through the weak Neutral Current (NC) via the exchange of the Z boson. Neutrinos are part of the lepton doublets, where there exists one neutrino for each charged lepton, $l = e, \mu, \tau$, which are referred to as neutrino flavors: electron neutrino ν_e, muon neutrino ν_μ, and tau neutrino ν_τ. There also exists a corresponding antineutrino for each neutrino, with half spin and no electric charge. Antineutrinos differ from neutrinos by having opposite sign of lepton number L, which is +1 for neutrinos and charged leptons, and -1 for antineutrinos and charged anti-leptons. In the SM, a Yukawa coupling of the Higgs field with the fermion right-handed and left-handed component generates the masses of the fermions. The right-handed neutrinos are not included in the SM as they have not been observed, while only left-handed neutrinos and right-handed antineutrinos exist in SM. Hence, no Yukawa interaction can be built for neutrinos and consequently, the neutrinos are massless in the SM. However, the discovery of neutrino oscillations shows that neutrinos have masses. There are different proposed models that can introduce the neutrino mass in the theory [36]. The absolute mass of neutrinos and the nature of mass (Dirac or Majorana) is also not known, which will be discussed be in Sec. 1.5. The SM contains no sterile neutrinos,

which are defined as having no SM interactions, which will also be discussed be in Sec. 1.5.

1.3 Neutrino oscillation

In a charged-current weak interaction, a neutrino of a certain flavor α ($= e, \mu, \tau$), is created from a charged lepton or with a charged anti-lepton of same flavor α. However, after travelling some distance, there exist a finite probability to detect the flavor of the neutrino, that differs from its initial flavor. This phenomenon is referred to as the neutrino oscillation. In the theory of neutrino oscillations [36, 39, 40, 42], the neutrino flavor eigenstate $|\nu_\alpha\rangle$ is a coherent superposition of mass eigenstates $|\nu_j\rangle$ ($j = 1, 2, 3$), with weights proportional to $U^*_{\alpha j}$:

$$|\nu_\alpha\rangle = \sum_j U^*_{\alpha j} |\nu_j\rangle, \tag{1.3}$$

where U is an unitary mixing matrix, which is referred to as the Pontecorvo-Maki-Nakagawa-Sakata (PMNS) matrix. Assuming that the massive neutrino states evolve in time as the plane waves in vaccum and considering the ultra-relativistic nature of neutrinos, the solution of the Schrödinger equation for the neutrino mass state can be written as:

$$|\nu_j(t)\rangle = e^{-i(Et - p_j L)} |\nu_j(t=0)\rangle \approx e^{-i\left(\frac{m_j^2}{2E}\right)L} |\nu_j\rangle, \tag{1.4}$$

where t is time, L is the distance travelled, m denotes mass, and E is energy of neutrino. Therefore, the time evolution of neutrino flavor eigenstate is:

$$|\nu_\alpha(L)\rangle = \sum_j U^*_{\alpha j} e^{-i\left(\frac{m_j^2}{2E}\right)L} |\nu_j\rangle. \tag{1.5}$$

Here, the natural units, $c = \hbar = 1$, are used. Now, the probability to detect flavor β after a distance L, is calculated as [36]:

$$\begin{aligned} P_{\alpha\beta}(L) &= |\langle \nu_\beta | \nu_\alpha(L) \rangle|^2, \\ &= \sum_{j,k} U_{\alpha k} U^*_{\beta k} U^*_{\alpha j} U_{\beta j} e^{-i\left(\frac{\Delta m_{jk}^2}{2E}\right)L}, \end{aligned} \tag{1.6}$$

where $\Delta m^2_{jk} = m^2_j - m^2_k$, is called mass-splitting. It can be seen that neutrino oscillations occur only if neutrinos are massive as well as the mass states have different masses, so that the neutrino mass-splitting is non-zero. If $\alpha = \beta$, $P_{\alpha\beta}$ is called the survival probability, otherwise it is referred to as the appearance probability. For a simple two flavor model, which is reasonable approximation due to the large difference in the mass splittings, the PMNS matrix is given by:

$$U = \begin{bmatrix} \cos\theta & \sin\theta \\ -\sin\theta & \cos\theta \end{bmatrix},$$

where θ is the mixing angle. In this case, the probabilities are given as:

$$P_{\alpha\beta,\,\alpha\neq\beta} = \sin^2(2\theta) \sin^2\left(\frac{\Delta m^2 L}{4E}\right), \tag{1.7}$$

	Normal Ordering	Inverted Ordering
θ_{12} [°]	$33.67\ ^{+0.73}_{-0.71}$	$33.67\ ^{+0.73}_{-0.71}$
θ_{23} [°]	$42.3\ ^{+1.1}_{-0.9}$	$48.9\ ^{+0.9}_{-1.2}$
θ_{13} [°]	$8.58\ ^{+0.11}_{-0.11}$	$8.57\ ^{+0.13}_{-0.11}$
Δm^2_{21} [10^{-5} eV^2]	$7.41\ ^{+0.21}_{-0.20}$	$7.41\ ^{+0.21}_{-0.20}$
Δm^2_{3l} [10^{-3} eV^2]	$+2.505\ ^{+0.024}_{-0.026}$	$-2.487\ ^{+0.027}_{-0.024}$
δ_{CP} [°]	$232\ ^{+39}_{-25}$	$273\ ^{+24}_{-26}$

Table 1.1: Oscillation parameters in the three neutrino flavor framework from global data fit (March 2024). The number in the 1^{st} and 2^{nd} column are obtained assuming Normal Ordering (NO) and Inverted Ordering (IO) of neutrino mass eigenstates, respectively (see Sec. 1.5). Here, $\Delta m^2_{3l} = \Delta m^2_{31} > 0$ for NO and $\Delta m^2_{3l} = \Delta m^2_{32} < 0$ for IO. Taken from [43].

$$P_{\alpha\alpha} = 1 - \sin^2(2\theta)\sin^2\left(\frac{\Delta m^2 L}{4E}\right). \tag{1.8}$$

Generally, the probability $P_{\alpha\beta}$ is given as:

$$P_{\alpha\beta} = \delta_{\alpha\beta} - 4\sum_{j>k}\Re\left(U_{\alpha k}U^*_{\beta k}U^*_{\alpha j}U_{\beta j}\right)\sin^2\left(\frac{\Delta m^2_{jk}L}{4E}\right) + 2\sum_{j>k}\Im\left(U_{\alpha k}U^*_{\beta k}U^*_{\alpha j}U_{\beta j}\right)\sin\left(\frac{\Delta m^2_{jk}L}{2E}\right). \tag{1.9}$$

Given the 3 known neutrino flavor eigenstates, the 3×3 PMNS matrix is written as the following parametrization:

$$U = \begin{bmatrix} 1 & 0 & 0 \\ 0 & c_{23} & s_{23} \\ 0 & -s_{23} & c_{23} \end{bmatrix} \begin{bmatrix} c_{13} & 0 & s_{13}e^{-i\delta_{CP}} \\ 0 & 1 & 0 \\ -s_{13}e^{i\delta_{CP}} & 0 & c_{13} \end{bmatrix} \begin{bmatrix} c_{12} & s_{12} & 0 \\ -s_{12} & c_{12} & 0 \\ 0 & 0 & 1 \end{bmatrix} \begin{bmatrix} e^{i\alpha_1/2} & 0 & 0 \\ 0 & e^{i\alpha_2/2} & 0 \\ 0 & 0 & 1 \end{bmatrix},$$

where $s_{ij} = \sin\theta_{ij}$, $c_{ij} = \cos\theta_{ij}$ and θ_{ij} (for ij = 12, 13, 23) are the mixing angles. Here, θ_{23} is the *atmospheric mixing angle* and θ_{12} is the *solar mixing angle*, as they are used, at an leading order, to describe the oscillations of atmospheric muon neutrinos and solar electron neutrinos, respectively. The mixing angle θ_{13} couples the atmospheric and solar neutrino oscillations and have been measured by reactor experiments (see Sec. 1.4). Similarly, Δm^2_{32} and Δm^2_{21}, in eq. 1.9, are the atmospheric and solar mass-splitting parameters, respectively. The Dirac CP violating phase, δ_{CP} and Majorana phases, α_1, α_2 are also included in the matrix. The phases δ_{CP}, α_1, and $\alpha_2 \in [0, 2\pi]$. More discussion on the δ_{CP} parameter can be found in Sec. 1.5. The diagonal Majorana phase matrix does not have an effect on the neutrino oscillations and exists only if the neutrinos are Majorana, that is, if neutrinos are their own anti-particle. The current best estimates on the three neutrino oscillation parameters are reported in Table 1.1, which are obtained from global analysis of data [43] from different sources (Sec. 1.4).

Neutrino oscillation in matter

When neutrinos pass through the matter, its probability of flavor transformation is impacted due to the coherent forward scattering off electrons in matter. This is known as the "Mikheyev–Smirnov-Wolfenstein" (MSW) effect [44,45]. This is particularly relevant for the solar neutrinos, discussed in Chapter 2, as they are produced in the electron flavor and propagates through the dense solar medium. This is due to the fact that only electrons exist in the standard matter but not the muons or tau leptons. Therefore, the electron neutrinos travelling in matter experience the charged current (CC) interactions, through which other flavors of neutrinos do not interact in matter. This give rise to an extra interaction potential V, for electron neutrinos travelling in the matter:

$$V = \sqrt{2} G_F N_e, \tag{1.10}$$

where G_F is the Fermi coupling constant and N_e is the matter electron density. This interaction potential is added to the vacuum Hamiltonian in the Schrödinger equation to take into account the matter effect [36,46]. In this case, the mixing angle in matter is:

$$\cos 2\theta_{12}^M = \frac{\cos 2\theta_{12} - A}{\sqrt{\sin^2 2\theta_{12} + (\cos 2\theta_{12} - A)^2}}, \tag{1.11}$$

where A is given as:

$$A = \frac{2\sqrt{2} G_F \cos^2 \theta_{13} N_e E}{\Delta m^2}. \tag{1.12}$$

When there is a combination of E as well as N_e such that A = $\cos 2\theta_{12}$, the maximal mixing occurs. This is called the MSW resonance condition.

In the solar neutrino sector, the values of mixing paramters ($\Delta m^2_{12} \sim 7.5 \times 10^{-5}\,\text{eV}^2$ and $\sin^2\theta_{12} \sim 0.3$) corresponds to the so-called large mixing angle (LMA) solution, favored by global analysis of solar neutrino experiments data. Using the MSW effect on neutrino flavor conversion in the solar neutrino experiments, the positive sign of Δm^2_{21} has also been established [47]. For the MSW-LMA solution, the survival probability of solar neutrino is approximated to [1,48]:

$$P_{ee}^{MSW-LMA} = \cos^4\theta_{13}(\frac{1}{2} + \frac{1}{2}\cos 2\theta_{12}^M \cos 2\theta_{12}). \tag{1.13}$$

The MSW survival probability corresponds to the vacuum survival probability at low energies typical for *pp* neutrinos, while the matter dominated oscillations occur for high energy ^{8}B neutrinos (see Sec. 1.4 and Chapter 2). There also exists a transition region between the two regions, which exhibits a strong energy dependence. The energy dependent survival probability of solar neutrinos is shown in Fig. 4.1a in Chapter 4, obtained by the Borexino experiment.

1.4 Sources of neutrinos

Reactor neutrinos: The nuclear reactors are the strongest manmade source of neutrinos. As discussed in Sec. 1.1, the first discovery of neutrinos was made in 1956 using the nuclear reactor. The commercial nuclear reactors generate power via the fission of uranium and plutonium isotopes, mainly ^{238}U, ^{241}Pu, ^{235}U, and ^{239}Pu. The electron antineutrinos are released by the β-decay of the fission products. On average, each fission releases about 200 MeV of energy with about six $\bar{\nu}_e$'s. A 1 GW_{th} of thermal power of reactor produces about 2×10^{20} $\bar{\nu}_e$'s per second [36]. The reactor neutrino flux

is calculated as:

$$\Phi(E_\nu) = \frac{P_{th}}{\sum_i^{isotopes} f_i \times E_i} \sum_i^{isotopes} f_i \times \Phi_i(E_\nu), \tag{1.14}$$

where P_{th}, f_i, E_i, and $\Phi_i(E_\nu)$ are the thermal power of reactor, fission fraction of each isotope, energy released per fission, and neutrino spectrum of each fission isotope [49], respectively. The energy spectrum of reactor antineutrinos extends to about 10 MeV. If the reactor antineutrinos changes their flavor, the charged current interaction can not happen for the muon and tau flavored antineutrinos, as the energy would not be sufficient to produce heavier charged leptons. Therefore, the reactor experiments look for $\bar{\nu}_e$ disappearance and the survival probability is given by [50]:

$$P_{\bar{\nu}_e \to \bar{\nu}_e} = 1 - \sin^2 2\theta_{13} \left[\cos^2 \theta_{12} \sin^2 \left(\frac{\Delta m^2_{31} L}{4E} \right) + \sin^2 \theta_{12} \sin^2 \left(\frac{\Delta m^2_{32} L}{4E} \right) \right] - \cos^4 \theta_{13} \sin^2 2\theta_{12} \sin^2 \left(\frac{\Delta m^2_{21} L}{4E} \right). \tag{1.15}$$

The reactor antineutrinos are usually detected through the IBD interaction in liquid scintillator detectors. It is a CC process between electron antineutrinos and proton, as given in eq. 1.2. The antineutrinos, only with an energy greater than 1.8 MeV, can participate in the IBD interaction. An IBD event is detected through the positron and neutron, produced in the IBD reaction. In this reaction, the positron carries almost all energy of the neutrino. The positron deposits its kinetic energy and annihilates into two 0.511 MeV γ-rays. This gives a prompt signal with a visible energy E_p, which is correlated with incident antineutrino energy $E_{\bar{\nu}_e}$:

$$E_p = E_{\bar{\nu}_e} - 0.784\text{MeV}. \tag{1.16}$$

The neutron scatters in the detector and then, is captured by a proton within $\sim$200 μs, which mainly releases a 2.2 MeV γ-ray. The interaction of γ-ray in the medium results in a delayed signal. The time and space coincidence of the prompt and delayed signal helps to distinguish the backgrounds from antineutrino events. At the order of few MeV, the cross section of IBD interaction is about 100 times more than the cross section of the elastic scattering channel.

The reactor antineutrinos have been used to determine some of the oscillation parameters. In 2002, the KamLAND experiment in Japan observed the first neutrino oscillation pattern [51]. The flux-weighted average baseline of KamLAND experiment corresponds to about 180 km, taking into account >50 reactors. The measurements from KamLAND confirmed the large value of mixing angle of LMA solution and as well as Δm^2_{21} was determined with high precision [52]. In 2012, the first discovery of non-zero value of the smallest neutrino mixing angle, θ_{13} was made using the reactor neutrino experiments, Daya Bay in China [53] and RENO in Korea [54], with first indications from Double Chooz [55]. All these reactor neutrino experiments, measuring θ_{13}, had a baseline of $\sim$1 km. These experiments also employed near detectors at distance of few hundred metres from the reactor to allow measurement of relative antineutrino rate and reduce the reactor and detector systematic uncertainties from neutrino flux, target mass, and detection efficiencies. The JUNO detector, an upcoming reactor neutrino experiment, will also contribute to the studies of neutrino oscillations by improving the precision of known oscillation parameters and by determining the neutrino mass ordering, which is its main goal. The details of the experiment will be discussed in Chapter 6.

The reactor experiments have also been used for the detailed measurements of the antineutrino flux and shape of reactor antineutrino energy spectra. As a result of re-evaluation of the reactor antineutrino flux calculations in 2011 [56], a 6% deficit was observed in the measured reactor antineutrino flux in the very short baseline reactor experiments (L<100 m) compared to the predicted flux [57]. This is called the *reactor antineutrino anomaly* (RAA), which has been confirmed by the θ_{13} measuring reactor antineutrino experiments [58–60]. One popular hypothesis to explain RAA has been the neutrino oscillations from active to sterile neutrinos [57], which has not been confirmed so far. Several experiments [59, 61, 62] indicated the possibility of correlation of RAA with the predicted ^{235}U fission yield. The discrepancy between the shape of reactor antineutrino energy spectra from the predicted ones, is called the "5 MeV bump". This refers to an excess of $\bar{\nu}_e$ events over the expected energy spectrum around 5 MeV. It was first reported by RENO experiment [63] in 2014 and then, it was soon confirmed by several experiments with baselines ranging from order of 10 m to 1 km. The origin of this excess is still under debate. The details can be found in Ref. [64]. DayaBay provided the improved measurement of the reactor antineutrino flux and spectrum with very large statistics of about 3.5 million IBD events [65]. The JUNO-TAO experiment [66], which is also discussed in Chapter 6, will address these anomalies by measuring the reactor neutrino spectrum more precisely.

Atmospheric neutrinos: Atmospheric neutrinos are produced in the atmosphere of the Earth, due to the interactions of cosmic ray protons and heavy nuclei as well as the subsequent decays of kaons and pions. This leads to secondary weak decays of pions and muons:

$$\pi^{\pm} \rightarrow \mu^{\pm} + \nu_{\mu}(\bar{\nu}_{\mu}), \tag{1.17}$$

$$\mu^{\pm} \rightarrow e^{\pm} + \nu_e(\bar{\nu}_e) + \bar{\nu}_{\mu}(\nu_{\mu}). \tag{1.18}$$

The energy spectrum of atmospheric neutrinos, typically ranges from a fraction of GeV up to ∼100 TeV. At low energies, typically below 1 GeV, the probability of the parent particles in the decay chain is almost equal and the ratio of the number of muon to electron neutrinos is about 2. At higher energies, the ratio is higher as muons are less probable to decay before reaching ground. The atmospheric neutrino experiments began in 1960s. The atmospheric neutrinos were first observed by the Kolar Gold Field experiment in India [67] and East Rand Proprietary Mine in South Africa [68]. In 1998, SuperKamiokande experiment reported the evidence for the neutrino oscillations using atmospheric neutrinos for the first time [37]. Here, the signal manifests as the disappearance of the muon neutrinos. The measurements of atmospheric neutrino oscillations constrains the parameters θ_{23} and Δm^2_{32}. While the identification of ν_{τ} is experimentally challenging, which could provide an experimental proof of $\nu_{\mu} - \nu_{\tau}$ oscillation, the SuperKamiokande experiment provided evidence of tau neutrino appearance using atmospheric neutrino data with 4.6σ significance [69]. IceCube also reported the measurement of atmospheric tau neutrino oscillations [70]. Other experiments measuring atmospheric neutrino include ANTARES [71] and IceCube-DeepCore [72] that provided atmospheric neutrino oscillation measurements through ν_{μ} disappearance. Since the atmospheric neutrinos experience matter effects while travelling through the Earth, the neutrino mass ordering determination is also possible with atmospheric neutrinos. The atmospheric neutrinos will also be exploited in JUNO for the neutrino mass ordering determination, complementary to the reactor antineutrinos.

Accelerator neutrinos: The neutrinos from accelerator based sources are produced by colliding a beam of protons with a fixed target. This produces pions and kaons, which are focused using magnetic horns to create a collimated sign-selected beam.

Then, this enters a decay region, where they decay to neutrinos and leptons species. The undecayed mesons and muons are stopped in the beam absorber. As pions are the dominating product in the high energy collisions, a conventional neutrino beam contains a high portion of muon-type of neutrinos or antineutrinos. Kaon and muon decays also produce a small contamination of electron neutrinos. Most accelerator based neutrino beams operate using this same basic design. The accelerator neutrinos typically have energy in the order of GeVs. The first accelerator experiment dates back in 1960s, which was used to test that ν_μ and ν_e are distinct particles [29]. In accelerator neutrino experiments, the disappearance channel of muon neutrinos into other flavors are used for the measurement of atmospheric oscillation parameters. The ν_e appearance channel is typically used for measuring δ_{CP} and studying the neutrino mass ordering by comparing the neutrino and antineutrino oscillation probabilities (see Sec. 1.5). The long baseline experiments has a baseline of few hundreds to a thousand km. The current generation long baseline accelerator neutrino experiments include T2K in Japan [73] and NOvA in USA [74]. The T2K and NOvA experiments correspond to the baselines of 295 km and 810 km, respectively. Both experiments use the off-axis beam at an angle of 2.5° and 0.84°, respectively, in order to produce a peak in neutrino energy spectrum at an energy corresponding to first oscillation maximum. Each experiment also has two detectors: near and far, where near detector is placed close to the source to measure the neutrino flux before oscillations. This is required to measure the neutrino energy spectrum and constrain flavor composition of the produced muon neutrino beam as it may contain a small contamination of other neutrino flavors. In addition, the near detectors, along with far detectors, are used to reduce the systematic uncertainties from neutrino flux and neutrino interaction cross section. The most precise estimates of δ_{CP}, θ_{23}, and $|\Delta m^2_{32}|$ are obtained from the data of long baseline accelerator neutrino experiments, such as T2K, NOvA, and MINOS [75]. The future long baseline experiments are DUNE in USA [76] and HyperKamiokande [77] in Japan.

Geoneutrinos: Geoneutrinos are the antineutrinos produced by the natural radioactive isotopes, present inside the Earth. These elements are mainly ^{235}U, ^{238}U, ^{232}Th, and ^{40}K, as the decay half-life of ^{235}U, ^{238}U, and ^{40}K is comparable to and the half-life time of ^{232}Th exceeds the Earth's age [78]. Due to the lithophilic nature of these isotopes, it is expected that the geoneutrino fluxes originate from only crust and mantle of the Earth, where a larger contribution is typically from the crust. The measurement of geoneutrino flux provides a crucial, direct information about the composition of the Earth's interior, which is otherwise nearly impossible to obtain using traditional methods like seismology. The direct connection between geoneutrinos and the radiogenic heating of the Earth helps to gain insights about the formation and evolution of Earth, which is the one of fundamental questions in Geoscience [78]. The geoneutrinos are typically measured using IBD interactions in the liquid scintillator detector. Due to the IBD threshold, the geoneutrinos from only ^{238}U and ^{232}Th are detected as their energy spectrum extends upto 3.27 MeV and 2.25 MeV, respectively. The measurement of geoneutrino fluxes from Th and U have been provided by KamLAND [79] and Borexino [78] experiments. KamLAND measured 183 events with ∼15% precision in about 14.3 years, where a period of low reactor background is included. Borexino measured about 53 events with ∼17% precision in about 8.9 years. Borexino also provided evidence of geoneutrino signal contribution from the Earth's mantle. The future experiments, such as JUNO (see Chapter 6), SNO+ [80], and Jinping [81], aim to provide high statistics geoneutrino measurements, including separating contributions from U and Th as well as from the Earth's crust and mantle.

Supernova neutrinos: A core-collapse supernova (SN) is one of the most powerful cosmic sources of neutrinos. It originates from the death of stars with a mass greater than about 8 to 10 times the solar mass. At the end of the stellar evolution of these stars, their core, consisting primarily of iron, grows by silicon burning in the outer layers. Once the Chandrasekhar mass limit has reached for the star's core, this core collapses under gravity. When it reaches nuclear density, the collapse stops and the incompressible core bounce back and results in an explosion. This emits 99% of the gravitational binding energy in the form of neutrino and antineutrinos of all flavors. About 10^{58} neutrinos are released in the burst in about 10 seconds with energies in the order of MeV [82], along with the ejection of stellar debris. The detection of supernova neutrinos will be crucial to test and compare supernova models, leading to the understanding of explosion mechanisms. They can also be used to probe the neutrino flavor mixing and neutrino-neutrino interactions under high density conditions which are present in the dense supernova matter [83]. The burst of neutrinos have been detected from SN 1987A in the Large Magellanic Cloud by Kamiokande-II [84], Irvine-Michigan-Brookhaven (IMB) [85], and Baksan experiments [86], primarily through the IBD reaction. Even though the recorded statistics of supernova events were low, they confirmed the general mechanism of the core collapse as well as allowed to put limits on exotic physics [87]. At the same time, the determination of supernova and neutrino parameters was not possible. Future detectors such as JUNO [82], Hyper-Kamiokande [77], and DUNE [76] will be able to gather a large statistics of supernova neutrinos, provided the core-collapse occurs, as only one to three galactic core collapse supernovas per century are expected. Moreover, the detection of the so-called pre-SN neutrinos, which are emitted before core collapse via the thermal and nuclear weak processes, is also possible in future detectors like JUNO [82]. As the supernova neutrino burst is emitted promptly after the core collapse, a world-wide network of neutrino detectors, the so-called Supernova Early Warning System (SNEWS) has been established [88]. This will provide fast warning to astronomers about the SN burst, as it is expected that the first photons from shock breakout will arrive Earth at a delay of several hours after the neutrino wavefront reaching Earth. Even though the galactic SN events are rare, the SN explosions occur frequently in the visible universe. The so-called Diffuse Supernova Neutrino Background (DSNB) is integrated neutrino flux from all the past core-collapse supernovae. Their detection can be useful to probe the processes which occur on cosmological scales in time or space including the cosmic star formation rate and the fraction of failed black hole forming supernovae. SuperKamiokande [89], KamLAND [90], and Borexino [91] has provided constraints on the flux of DSNB. The upcoming detectors that will search for DSNB are Gadolinium-doped SuperKamiokande [92] as well as JUNO [93].

Solar neutrinos: Electron neutrinos are produced in the nuclear fusion reactions, generating energy in the core of the Sun. These reactions occur via two main mechanisms: the *pp* chain and the CNO cycle. Considering that it takes about 100,000 years for photons to propagate from the energy producing region to the Sun's surface, it takes only 8 min for solar neutrinos to travel from their production region to the Earth [1]. This is attributed to the weakly interacting nature of neutrinos that they can travel without being deflected or absorbed. Therefore, solar neutrinos are the excellent direct probes of the Sun's core and the solar energy generation. The development of Standard Solar Models [94] is also benefited by the implications of solar neutrino measurements on the determination of metal abundances in the Sun's core, which will be discussed in Chapter 2. Solar neutrino measurements are also used as probes to the neutrino properties and its interaction in matter. In fact in the past, the solar neutrino measurement

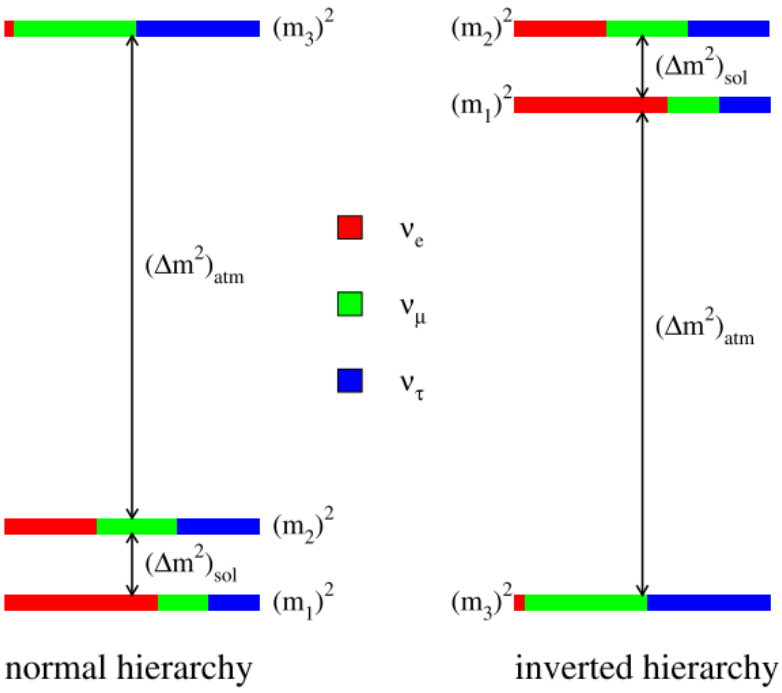

Figure 1.1: Illustration of the two neutrino mass orderings: normal hierarchy (left) and inverted hierarchy (right). Here, $(\Delta m^2)_{atm}$ is Δm^2_{31} for normal hierarchy and Δm^2_{32} for inverted hierarchy. The parameter $(\Delta m^2)_{sol}$ corresponds to Δm^2_{21}. The color shading represents the fraction $|U_{\alpha i}|^2$ of each neutrino flavor, $\alpha = e, \nu, \tau$ contained in each mass eigenstates. From [96].

has contributed to the evidence of neutrino flavor transformation [38]. A global analysis of all solar neutrino measurements provided the most precise determination of θ_{12} angle [36, 48]. The electron neutrino survival probability can be measured for different solar neutrino species and energy range from sub-MeV to about 15 MeV. Borexino has simultaneously tested the neutrino flavor conversion in the vacuum and matter dominated regime [1]. If matter effects were not present, the survival probability corresponds to the averaged vacuum oscillations:

$$P_{ee}^{vacuum} = \cos^4\theta_{13}(1 - \frac{1}{2}\sin^2 2\theta_{12}) + \sin^4\theta_{13}, \tag{1.19}$$

which does not depend on the energy of neutrino. However, the survival probability is dominated by vacuum oscillations below 1 MeV ($P_{ee} \approx 0.54$) and for energies higher than about 8 MeV, it is matter dominated ($P_{ee} \approx 0.32$) (see Sec. 1.3). For intermediate energies, a smooth transition occurs and the exact shape of this transition region is possibly sensitive to different models of non-standard interactions. Thus, solar neutrino measurements may also reveal the effects of physics beyond the Standard Model [95]. Chapter 2 provides a comprehensive overview of solar neutrino production reactions as well as the Standard Solar Model and open questions. All solar neutrino experiments are also summarized in the next chapter.

1.5 Open questions in neutrino physics

Neutrino mass ordering (NMO): In the standard three neutrino flavor framework, there exists six independent parameters, which drive the neutrino oscillations: neutrino mass-squared differences Δm^2_{21} and Δm^2_{31} (or Δm^2_{32}), the mixing angles θ_{12}, θ_{13}, and θ_{23}, and the CP-violating phase δ. The parameters Δm^2_{21}, $|\Delta m^2_{31}|$ ($\cong |\Delta m^2_{32}|$), θ_{12}

and θ_{13} are better-known parameters from a number of atmospheric, solar, accelerator, and reactor neutrino experiments [36]. One of the open questions for the neutrino oscillation is the sign of Δm^2_{31} (or Δm^2_{32}), which relates to the problem of NMO. It has been established from the MSW effect on neutrino flavor conversion in the solar neutrino experiments that the sign of Δm^2_{21} is positive, that is $m_2 > m_1$ [47]. However, it is not known which ordering of neutrino mass is true: the normal neutrino mass ordering $m_1 < m_2 < m_3$ (NO) or the inverted neutrino mass ordering $m_3 < m_1 < m_2$ (IO). Here, the neutrino states ν_1, ν_2, ν_3, whose masses correspond to m_1, m_2, m_3, are defined according to the decreasing order of electron flavor content. This is schematically shown in Fig. 1.1. Thus, it is in debate whether $\Delta m^2_{31} > 0$, which is true for NO or $\Delta m^2_{31} < 0$, true for IO. The determination of neutrino mass ordering is of fundamental importance in the field of particle physics, astrophysics, and cosmology including understanding of the origin of neutrino masses and flavor mixing, neutrinoless double beta decay search, supernova neutrino oscillations, and cosmological probes of absolute neutrino mass scale [50]. The long-baseline accelerator as well as atmospheric neutrino experiments are sensitive to the NMO measurement through MSW effects. In the long baseline accelerator experiments such as NOvA [74] and DUNE [76], the appearance of electron (anti)neutrinos from initial muon (anti)neutrinos is sensitive to mass ordering. Moreover, there exists a degeneracy between the determination of NMO and δ_{CP} in the long baseline accelerator neutrino experiments. Similar approach based on matter effects will be used via atmospheric neutrino by many future experiments, such as INO [97], PINGU [98], ORCA [99], and HyperKamiokande [77], for the NMO determination. Complementary to the NMO measurement via MSW effect, it is possible to determine NMO from vacuum antineutrino disappearance probability in the reactor neutrino experiments such as JUNO. At a baseline of 52.5 km, where JUNO is located, the reactor neutrino oscillation pattern is driven by both small (Δm^2_{21}) and large (Δm^2_{31} and Δm^2_{32}) mass splitting, which will be described in Chapter 6. The fast small oscillation peaks in the oscillated neutrino spectrum due to Δm^2_{31} and Δm^2_{32} are sensitive to the mass hierarchy, which will be utilized by JUNO for NMO determination [100]. While the normal ordering is preferred by some current experiments [73, 74], the future experiments are expected to answer this question.

Absolute neutrino mass and its nature: The discovery of neutrino oscillations have proven the existence of non-zero neutrino masses, an evidence of physics beyond the Standard Model. While all the neutrino oscillation experiments provide rather precise measurements of the neutrino mass splitting, they cannot measure the individual masses of the neutrino. The results from oscillation experiments, however, implies that at least two of the three neutrinos are massive and the heaviest neutrino mass is at least 0.05 eV [96]. The information about the mass scale of the neutrino can be probed in three experimental ways: through the kinematic weak decays, the neutrino-less double beta decays, and the cosmological observations.

The information on the neutrino mass scale can be obtained using the direct kinematic measurements of the β decay or electron capture spectrum. This method is independent of the mass nature of the neutrino or the cosmological model. Through the measurement of the distortion in the kinematic end point region in the energy spectrum, induced by the non-zero neutrino mass, the incoherent weighted sum of the neutrino masses can be probed:

$$m_\beta = \sqrt{\sum_{i=1}^{3} |U_{ei}|^2 m_i^2}. \tag{1.20}$$

Due to their low Q-value, short-half-lives, (super)allowed transition, and availability, tritium (^{3}H), that undergoes β decay and holmium-163 (^{163}Ho) undergoing electron capture, have been adopted as the two beta sources for probing the neutrino mass scale. They also allow to address $m_\beta(\bar{\nu}_e)$ and $m_\beta(\nu_e)$ independently. The Mainz neutrino mass experiment [101] and the Troitsk neutrino mass experiment [102] used the endpoint region of tritium β decay spectrum, and have reported upper limits on the effective electron (anti)neutrino mass < 2.3 eV and < 2.05 eV, respectively, at 95% CL. The latest result on the kinematic search for the neutrino mass in tritium decay has been given by the KATRIN experiment. It has not found any indication of $m_\beta(\bar{\nu}_e) \neq 0$ and set an upper limit of $m_\beta(\bar{\nu}_e) < 0.8$ eV at 90% CL [103]. It is currently running with an estimated sensitivity limit of 0.2 eV at 90% CL. The Project8 experiment [104] is a tritium based neutrino mass experiment, that is exploring a new technique for β-spectrometry based on cyclotron radiation. It has a potential to reach sensitivity down to $m_\beta(\bar{\nu}_e) <$ 40 meV. The electron capture decay of ^{163}Ho will be used to probe the neutrino mass by ECHo [105] and HOLMES [106] . These experiments use calorimetric techniques of measuring energy spectrum to search for the signature of neutrino rest mass and are expected to provide stringent limits on $m_\beta(\nu_e)$ in the future.

In addition to the neutrino mass, the nature of neutrino (Majorana or Dirac), can be probed via a search for neutrinoless double decay ($0\nu\beta\beta$) [107]. If this decay is observed, the neutrinos are Majorana in nature, that is, the neutrinos are their own antiparticle and the lepton number conservation does not hold. In the Standard Model (SM) forbidden $0\nu\beta\beta$ decay mode, no neutrinos are emitted and the decay reaction is given by: $(A, Z) \rightarrow (A, Z+2) + 2e^-$. This type of decay can occur only in the isotopes that also undergo SM allowed $2\nu\beta\beta$ decay and the single-β decay is forbidden or suppressed. In $0\nu\beta\beta$ searches, the signature is a monoenergetic peak in the energy spectrum at end point of the double beta decay. The half-life of the decay is the observable, determined by the experiments searching for $0\nu\beta\beta$ decay. Assuming that the light-Majorana neutrino exchange is dominant for the $0\nu\beta\beta$ channel, the decay half-life is [36]:

$$(T^{0\nu}_{1/2})^{-1} = G^{0\nu}|M^{0\nu}|^2 \left(\frac{m_{ee}}{m_e}\right), \tag{1.21}$$

where $G^{0\nu}$ is the phase space factor, $M^{0\nu}$ is the nuclear matrix element of transition, and m_{ee} is the effective Majorana mass of ν_e, which is given by:

$$m_{ee} = |\sum_{i=1}^{3} U^2_{ei} m_i|, \tag{1.22}$$

and can be used to probe neutrino mass scale. The term $\sum_{i=1}^{3} U^2_{ei} m_i$ is in general complex and depends on the Majorana phases. Depending upon the value of Majorana phases, m_{ee} can be smaller than m_i. The list of commonly used double beta decay isotopes can be found in Table 1 in Ref. [107]. So far, the $0\nu\beta\beta$ decay has not been observed. Therefore, the current most stringent limits derived from different isotopes are: 1) $m_{ee} <$ 79-180 meV and $T^{0\nu}_{1/2} > 1.8\times10^{26}$ years at 90% CL using ^{76}Ge by GERDA [108] and 2) $m_{ee} <$ 36-156 meV and $T^{0\nu}_{1/2} > 2.3\times10^{26}$ years at 90% CL using ^{136}Xe by KamLAND-Zen [109]. The CUORE experiment provided $m_{ee} <$ 90-305 meV and $T^{0\nu}_{1/2} > 2.2\times10^{25}$ years at 90% CL using ^{130}Te [110]. The spread in m_{ee} originates from the uncertainties in the model dependent nuclear matrix element calculation. These limits are valid only if neutrinos are Majorana fermions. The next generation experiments [36] of $0\nu\beta\beta$ searches offers the potential of a discovery at $T^{0\nu}_{1/2}$ of more than 10^{28} years [107], which would translate to $m_{ee} \approx$ 5-20 meV, depending on the isotope and nuclear matrix element calculation.

Cosmology is also a promising avenue for probing the absolute neutrino mass scale. Massive neutrinos leave unique imprints on the cosmological observables throughout the history of the Universe. The cosmological observables allow to constrain the sum of the neutrino masses [36]:

$$m_{tot} = \sum_{i}^{3} m_i. \tag{1.23}$$

To date, cosmology provides the strongest mass limits on the sum of neutrino masses. But they are model-dependent and also depend on the datasets, that need to be combined to break the degeneracy of many cosmological parameters. In the context of Lambda Cold Dark Matter (ΛCDM) model, the constraint from Planck 2018 satellite data alone is $m_{tot} < 0.26\,\text{eV}$ (95%) C.L [111]. When combining these Cosmic Microwave Background (CMB) observations from Planck with CMB lensing data, Supernova Ia luminosity distances and galaxy cluster data, the most constraining limit of $m_{tot} < 0.09\,\text{eV}$ (95%) C.L, is obtained [112]. Future cosmological measurements are crucial for probing neutrino mass scale, for example, DESI [113] have the sensitivity the measure the sum of neutrino masses to 0.02 eV.

CP violation: As discussed in the previous sections, the CP violation factor δ_{CP} in the PMNS matrix, can be measured in the long baseline accelerator experiments. The value of δ_{CP}, if different from 0 or π, indicates the violation of charge parity symmetry and its evidence could provide explanations of matter-antimatter asymmetry in leptons through leptogenesis [114]. The measurement of δ_{CP} relies on a comparison of ν_e and $\bar{\nu}_e$ appearance from ν_μ and $\bar{\nu}_\mu$, respectively. The NOvA measurements do not show large asymmetry in the rates of ν_e vs $\bar{\nu}_e$ appearance and exclude $\delta_{CP} = \pi/2$ (for IO) and $\delta_{CP} = 3\pi/2$ (for NO) with $>3\sigma$ and $>2\sigma$ significance, respectively [74]. Recently, T2K has reported a hint of CP violation at the 2σ level by performing a combined analysis of neutrino and antineutrino data [73]. The value of δ_{CP}, equal to 0 or π, is excluded at 90% C.L. Comparing the results from the two experiments, it has been found that the experiments consistently favor $\pi < \delta_{CP} < 2\pi$ in IO, while in NO, there is some tension. However, the current results are statistically limited and the joint analysis is foreseen. Moreover, the upgrade of these experiments will also address δ_{CP} [115]. The future experiments, DUNE and HyperKamiokande, will have excellent sensitivity to δ_{CP}. In DUNE, the CP violation can be observed with 3σ and 5σ significance after about 5 years and 10 years, respectively, for 50% of all the values of δ_{CP} [116]. HyperKamiokande will have 5σ sensitivity to CP violation for about 60% values of δ_{CP}, after 10 years of operation [117].

θ_{23} octant: The fit on the global data [43] indicates that the θ_{23} deviates from a value of 45°, which corresponds to maximal mixing angle in the atmospheric sector. However, it is not known whether $\theta_{23} < 45^\circ$ or $\theta_{23} > 45^\circ$, which is referred to as the octant degeneracy of θ_{23}. As discussed in Sec. 1.4, the atmospheric mixing angle can be measured by the atmospheric neutrino experiments as well as the accelerator neutrino experiments. The recent oscillation results from SuperKamiokande's atmospheric data favor $\theta_{23} < 45^\circ$ [118]. However, the long baseline accelerator experiments, T2K and NOvA favor $\theta_{23} > 45^\circ$ values [73,74]. These results corresponds to only mild preferences and the conclusive solutions are still not known. The next generation experiments are expected to the resolve the θ_{23} octant by providing a precise value of θ_{23} [119].

Sterile neutrinos: From the measurement of the width of Z-boson at LEP [35], the number of active neutrino flavors are established to be 3. However, one of the fundamental questions in neutrino physics is if there exists sterile neutrinos with no standard-model coupling, which are undetectable unless they can mix with active neutrinos. The motivation for the existence of sterile neutrinos originate from several neutrino oscillation anomalies at different experiments that could not be explained in the standard three neutrino flavor framework. The LSND experiment, which is an accelerator neutrino experiment with a baseline of 30 m, found 3.8 σ excess of $\bar{\nu}_e$ events over background in the $\bar{\nu}_\mu \rightarrow \bar{\nu}_e$ appearance search [120]. This was confirmed by MiniBooNE experiment with a baseline of 541 m, reporting excess in both $\bar{\nu}_e$ and ν_e events, corresponding to 4.8σ significance [121]. The calibration radioactive sources at the Gallium solar neutrino experiments (see Sec. 2.4) obtained lower event rate than the expected rate, at about 2.5σ significance. This anomaly is called "Gallium anomaly" [122]. This result was recently confirmed by BEST experiment [123]. In addition to the reactor antineutrino anomaly (RAA), discussed in Sec. 1.4, these anomalies have been interpreted as the hints for the existence of eV-scale fourth neutrino state, which must be sterile in nature. A so-called (3+1) scheme is used as a possibility to accommodate for the sterile mass eigenstate in addition to the three active mass eigenstate, to explain the anomalies. However, the ν_μ disappearance signature has not been observed at such short distances [119, 124], which is expected as the muon neutrinos oscillate to electron neutrinos through a sterile neutrino state if $\bar{\nu}_\mu \rightarrow \bar{\nu}_e$ appearance exists. Under the assumption of this model, the global fits of ν_e disappearance and appearance results are in tension with the ν_μ disappearance results [36]. These anomalies have been also scrutinized by recent experiments. The KARMEN [125] and MicroBooNE [126] experiments, located at about 18 m and 470 m from their targets, respectively, observed no excess of electron neutrino events and hence, no evidence of sterile neutrino oscillations is provided. Current and the next generation experiments, such as SBND, ICARUS, and JSNS^2, will further investigate the reported excess from LSND and MiniBooNE experiments [36]. Neutrino-4, a reactor neutrino experiment claimed observation of sterile neutrinos with about 2.7σ [127]. The reactor neutrino experiments, such as DANSS, NEOS, PROSPECT, and STEREO rejected RAA with a high significance and found no evidence for oscillation to sterile neutrinos [128]. Therefore, there have been no conclusive proof of sterile neutrino yet and the next generation experiments will further test the hypothesis of sterile neutrinos.

Chapter 2

Introduction to solar neutrinos

This chapter is dedicated to the description of neutrinos emitted in the fusion reactions occurring in the core of the Sun, the *solar neutrinos*. The sets of these nuclear reactions are discussed in Sec. 2.1. The fluxes of solar neutrinos are predicted by Standard Solar Model (SSM), which is described in Sec. 2.2. It is also discussed that the solar neutrinos can be powerful probes to understand the metallicity of the Sun's core, a fundamental input to SSMs. The solar neutrino interactions, focusing on the elastic scattering channel which is relevant for this dissertation is discussed in Sec. 2.3. Section 2.4 discusses various solar neutrino experiments, which are categorised as radiochemical, water Cherenkov, scintillator, and hybrid experiments. For each category, the past, current as well as future solar neutrino projects are also summarized. The backgrounds relevant for the solar neutrino analysis in the liquid scintillator experiments, within the context of this thesis, are reported in Sec. 2.5.

2.1 Fusion processes producing solar neutrinos inside the Sun

The Sun shines through the nuclear fusion reactions, in which a ^{4}He nucleus is formed as a result of the fusion of four Hydrogen nuclei:

$$4^1\mathrm{H} \rightarrow {}^4\mathrm{He} + 2e^+ + 2\nu_e \quad Q = 26.73\,\mathrm{MeV}, \tag{2.1}$$

where two positrons and two (solar) neutrinos are emitted and an energy of 26.73 MeV is released. This is based on the measurement of masses of hydrogen and helium by F.W. Aston [129], who found out that four hydrogen nuclei are heavier than a helium nucleus and two positrons. The idea that the Sun could shine by hydrogen to helium conversion based on Aston's findings, was given by A. Eddington in 1920s [130]. The idea was further developed by Bethe and Critchfield [131]. The stellar nuclear fusion reactions occur in a narrow energy range, the so-called Gamow peak. The Gamow peak is the product of the Maxwell-Boltzmann distribution of fusion reactants' velocity distribution and the tunneling probability. The area under the Gamow peak determines the fusion rate.

The net fusion reaction in eq. 2.1 proceeds via two distinct sets of reactions: the proton-proton (*pp*) chain or the Carbon-Nitrogen-Oxygen (CNO) cycle, which are shown in Fig. 2.1. The CNO cycle, which is a closed loop chain of nuclear reactions catalysed by carbon, nitrogen, and oxygen, was proposed by Bethe and Weizsäcker [132, 133] in 1930s. In the Sun, the *pp*-chain, studied by Fowler and his colleagues [134] contributes to about 99% of the total energy production in the Sun. However, it is expected that the CNO cycle is the primary energy producing process in the hotter and heavier stars, with a mass greater than about 1.3 times the solar mass. The fusion reactions take place in the solar core, however, the different types of solar neutrinos emitted in the *pp*-chain and CNO cycle have different radial profiles in which the specific reaction type occur, depending upon the solar chemical composition and the temperature profile [135]. Figure 2.2 shows the different solar neutrino production from the *pp*-chain as a function

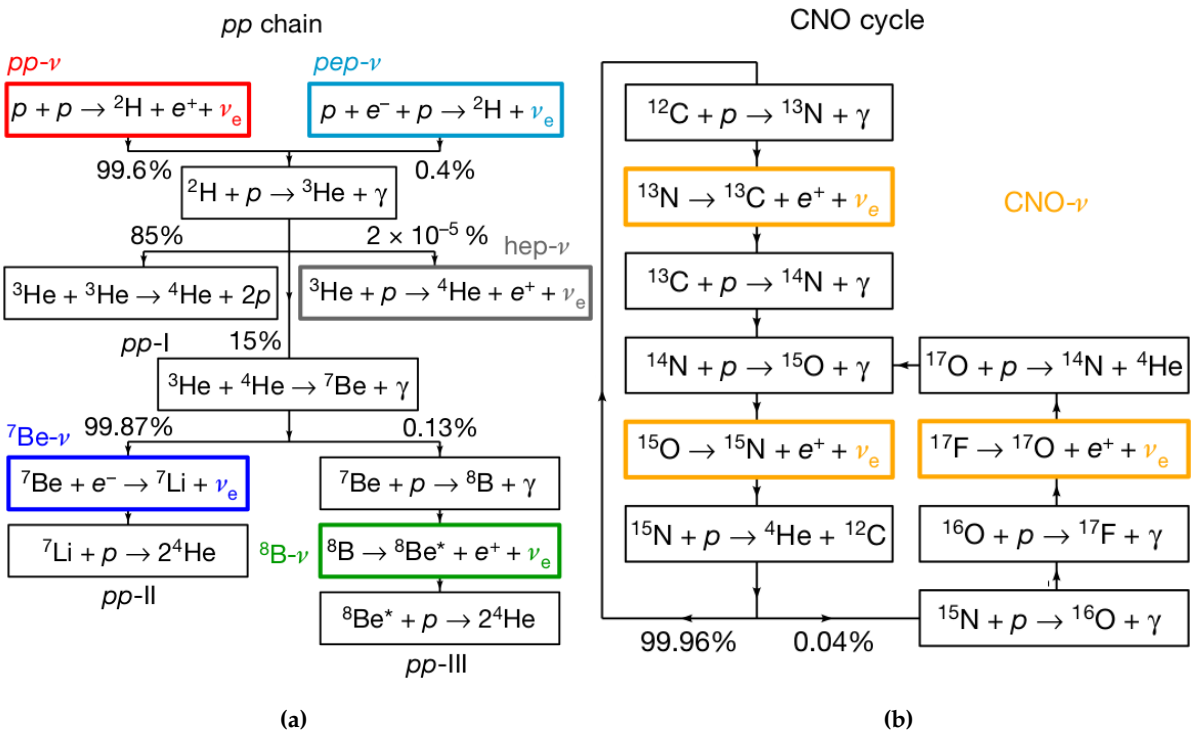

Figure 2.1: The schematic representation of all nuclear reactions in the (a) *pp*-chain and (b) CNO cycle. The solar neutrinos emitted in several reactions are also highlighted. From [1].

of the radius in the Sun. The solar neutrinos emitted in both the *pp*-chain and the CNO cycle have their own characteristic energy spectra, which is shown in Fig. 2.3.

The pp-chain

The first reaction in the *pp*-chain is the fusion of two protons with a branching ratio of ∼99.6%, emitting the so-called *pp* neutrinos:

$$p + p \rightarrow {}^{2}\mathrm{H} + e^{+} + \nu_e \quad E_\nu \leq 0.42\,\mathrm{MeV}. \tag{2.2}$$

The *pp* neutrinos have a continuous energy spectrum with the end point at 0.42 MeV. The total solar neutrino flux is dominated by *pp* neutrinos, whose flux corresponds to $\approx 6 \times 10^{10}\,\mathrm{cm}^{-2}\,\mathrm{s}^{-1}$. The alternative three body *pep* reaction, which also involves e^-, accounts for the remaining ∼0.4% branching ratio. This produces mono-energetic *pep* neutrinos with an energy of 1.44 MeV:

$$p + e^{-} + p \rightarrow {}^{2}\mathrm{H} + \nu_e \quad E_\nu = 1.44\,\mathrm{MeV}. \tag{2.3}$$

The flux of *pep* neutrinos is $\approx 1.4\times 10^{8}\,\mathrm{cm}^{-2}\mathrm{s}^{-1}$. The deuterium ^{2}H, produced in the above reaction, is then converted to ^{3}He without producing any neutrino. Afterwards, the chain is divided into branches, the so-called *pp*-I, *pp*-II, and *pp*-III. In *pp*-I branch, two ^{3}He fuse together to form ^{4}He and two protons are emitted. The *pp*-II and *pp*-III starts with the production of ^{7}Be by the fusion of ^{3}He and ^{4}He. The *pp*-II proceeds with a probability of 99.87%, where ^{7}Li is produced, in addition to the ^{7}Be neutrinos via the electron capture by ^{7}Be:

$${}^{7}\mathrm{Be} + e^{-} \rightarrow {}^{7}\mathrm{Li} + \nu_e \quad E_\nu = 0.862\,\mathrm{MeV} \text{ or } 0.384\,\mathrm{MeV}. \tag{2.4}$$

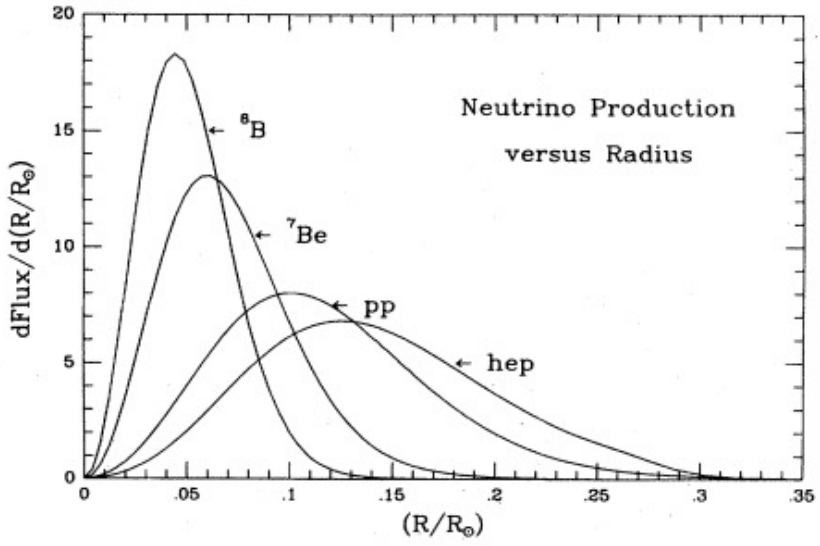

Figure 2.2: The radial profile of solar neutrinos from the *pp*-chain in the Sun. From [135].

With a probability of about 90%, this reaction produces ^{7}Li in the ground state and a mono-energetic ^{7}Be neutrino with an energy of 0.862 MeV is emitted. For the remaining 10% probability, it produces the excited state ^{7}Li with the emission of ^{7}Be neutrino of energy 0.382 MeV. The overall flux of ^{7}Be neutrinos is $\approx 5 \times 10^9\,\mathrm{cm}^{-2}\mathrm{s}^{-1}$. The *pp*-II terminates through the production of two ^{4}He nuclei by ^{7}Li and a proton. In *pp*-III, ^{7}Be captures a proton and produces ^{8}B nuclei, which decays via emitting e^+ and the so-called ^{8}B neutrinos:

$$^8\mathrm{B} \rightarrow {}^8\mathrm{Be}^* + e^+ + \nu_e \quad E_\nu \leq 15\,\mathrm{MeV}. \tag{2.5}$$

The ^{8}B neutrinos has low flux of $\approx 5 \times 10^6\,\mathrm{cm}^{-2}\mathrm{s}^{-1}$ and its energy spectrum extends to about 15 MeV. The *pp*-III terminates through the dissociation of ^{8}Be*, produced in the above reaction, into two ^{4}He nuclei. With a probability of about 2×10^{-5}%, ^{4}He, can also be created by:

$$^3\mathrm{He} + p \rightarrow {}^4\mathrm{He} + e^+ + \nu_e \quad E_\nu \leq 18.77\,\mathrm{MeV}, \tag{2.6}$$

via emitting the *hep* neutrinos, with a continuous energy spectrum having an endpoint energy of 18.77 MeV. The *hep* neutrinos have an extremely low flux that they have not been yet experimentally confirmed. The complete spectroscopy of almost all neutrinos from the *pp*-chain has been performed by the Borexino experiment, which will be summarized in Chapter 4. The most precise ^{8}B solar neutrino measurement is given by water Cherenkov experiments, which will be reviewed in Sec. 2.4. The principal reactions of the *pp*-chain with corresponding probabilities, and the associated neutrinos produced in the reactions are shown in Fig. 2.1a.

The CNO cycle

The CNO cycle, also known as the Bethe-Weizsäcker cycle, is a catalytic process where C, N, and O act as the catalysts for the nuclear fusion reactions. The contribution of the CNO cycle is strongly dependent on the star's core temperature and its metallicity (see Sec. 2.2). The CNO cycle is sub-dominant in the Sun and it is estimated to contribute about 1% of the total solar energy production. It has two sub-cycles: CNO-I and CNO-II, where CNO-I is more dominant ($\sim$99.95% probability). The reactions in the CNO

cycle are shown in Fig. 2.1b. The reactions, responsible for the emission of neutrinos, are summarized as follows:

The subcycle CNO-I begins with proton capture by ^{12}C to form ^{13}N and proceeds as following:

$$^{12}\mathrm{C} + p \rightarrow {}^{13}\mathrm{N} + \gamma. \tag{2.7}$$

Now, the ^{13}N decays to ^{13}C, with an emission of the so-called ^{13}N neutrinos:

$$^{13}\mathrm{N} \rightarrow {}^{13}\mathrm{C} + e^{+} + \nu_e \quad E_\nu \leq 1.2\,\mathrm{MeV}. \tag{2.8}$$

The ^{13}N neutrinos have a continuous energy spectrum with an end point at 1.2 MeV. The flux of ^{13}N corresponds to $\approx 2 \times 10^8\,\mathrm{cm}^{-2}\mathrm{s}^{-1}$. The cycle proceeds as follows:

$$^{13}\mathrm{C} + p \rightarrow {}^{14}\mathrm{N} + \gamma, \tag{2.9}$$

$$^{14}\mathrm{N} + p \rightarrow {}^{15}\mathrm{O} + \gamma, \tag{2.10}$$

$$^{15}\mathrm{O} \rightarrow {}^{15}\mathrm{N} + e^{+} + \nu_e \quad E_\nu \leq 1.73\,\mathrm{MeV}. \tag{2.11}$$

In the above reaction, the so-called ^{15}O neutrinos are produced, with a continuous energy spectrum with an end point at 1.73 MeV. The flux of ^{15}O is $\approx 2 \times 10^8\,\mathrm{cm}^{-2}\mathrm{s}^{-1}$. At this stage, ^{15}N either forms back to ^{12}C as following:

$$^{15}\mathrm{N} + p \rightarrow {}^{12}\mathrm{C} + \alpha, \tag{2.12}$$

or is converted to ^{16}O and further proceeds as below to form subcycle CNO-II:

$$^{15}\mathrm{N} + p \rightarrow {}^{16}\mathrm{O} + \gamma, \tag{2.13}$$

$$^{16}\mathrm{O} + p \rightarrow {}^{17}\mathrm{F} + \gamma, \tag{2.14}$$

$$^{17}\mathrm{F} \rightarrow {}^{17}\mathrm{O} + e^{+} + \nu_e \quad E_\nu \leq 1.74\,\mathrm{MeV}. \tag{2.15}$$

Here, the so-called ^{17}F neutrinos are produced, with a continuous energy spectrum with an end point at 1.74 MeV, which is almost same as of ^{15}O neutrinos end point. Its energy spectrum is also degenerate with the ^{15}O neutrino energy spectrum. The flux of ^{17}F is very low, which is in the order of $10^6\,\mathrm{cm}^{-2}\mathrm{s}^{-1}$.

$$^{17}\mathrm{O} + p \rightarrow {}^{14}\mathrm{N} + \alpha. \tag{2.16}$$

Now, the reaction 2.10 is repeated and the cycle continues as before.

The neutrinos emitted in the CNO-cycle are collectively referred to as the CNO neutrinos. The first detection of the CNO solar neutrinos has been performed in 2020 by the Borexino experiment [2]. Further, Borexino provided an improved measurement of the CNO solar neutrino flux, which is described in Chapter 4. The individual detection of ^{13}N, ^{15}O, and ^{17}F neutrinos have not been performed experimentally yet. However, JUNO has the potential to detect them individually, which will be discussed in Chapter 7.

2.2 Standard Solar Model

The Standard Solar Model (SSM) [94, 137] is a framework that describes the structure of the Sun and trace the evolution of the Sun to match the present conditions. The SSM calculations are used to make the predictions on the speed profiles of sound waves in the Sun as well as the solar neutrino fluxes and are based on the following assumptions:

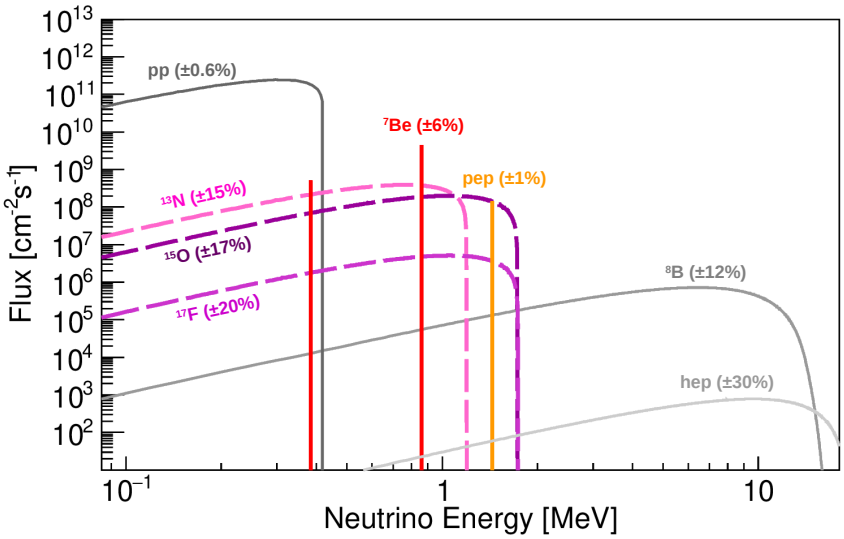

Figure 2.3: The energy spectra of solar neutrinos from the *pp* chain (solid lines) and CNO cycle (dashed lines). The spectral shapes are taken from http://www.sns.ias.edu/∼jnb/. The normalization is done according to flux predictions from the high-metallicity B16-GS98 SSM predictions given in [136,137]. The units of neutrino flux is $cm^{-2}s^{-1}MeV^{-1}$ for the continuum sources and $cm^{-2}s^{-1}$ for the monoenergetic sources. The values in parenthesis show the corresponding relative uncertainties of the high-metallicity B16-GS98 SSM predictions. Adapted from [1]. Used in [7].

- The Sun is in a state of hydrostatic equilibrium, where a local balance between the gravitation force and the pressure gradient is maintained.
- The Sun produces energy using eq. 2.1 via the *pp*-chain dominantly and with a small contribution from the CNO cycle. The nuclear cross sections of different processes are taken from the experiments or the theory.
- The energy transport takes place via radiation and convection mechanisms in the inner and outer regions, respectively, where the radiative transport is described by opacity.
- Boundary conditions include the modern Sun's mass, radius, age, and luminosity. The initial chemical composition and the mixing length parameter are used to calibrate the SSM. The initial solar (or pre-solar) composition are estimated to be equal to the present photospheric compositions, corrected for diffusion effects over the Sun's lifetime. The chemical composition of the core, which is assumed to be homogeneous initially, evolves as a function of time only according to the rates of the nuclear reactions.

Solar metallicity problem

The SSM predictions are tested by the helioseismology, which determines the solar interior properties through the study of propagation of seismic waves at the surface of the Sun, and the solar neutrino experiments, measuring the solar neutrino fluxes. The solar metallicity, an input to the SSM, is still poorly understood. The solar metallicity refers to the fraction of elements heavier than Helium, which is a crucial parameter for the SSM. It is denoted by Z/X, where Z is the abundance of elements heavier than Helium and X refers to the abundance of Hydrogen and Helium in the Sun. The metallicity is determined experimentally from the spectral analysis of the Sun's photosphere and sometimes, using the studies of meteorites. The measurements from GS98

(Grevesse and Sauval in 1998) [136] provides the metallicity ratio, Z/X = 0.0229. However, the updated techniques used to derive the abundances, the three-dimensional hydrodynamic model of the Sun's atmosphere, yields a lower Z/X ratio = 0.0178, as given by AGSS09met in 2009 [138]. The newest generation of SSMs, called B16 [137], using the two different metallicity inputs form B16-GS98 and B16-AGSS09met SSMs. The predictions from older and high-metallicity SSM B16-GS98 are in agreement with the helioseismological observations, while this agreement is spoiled with the newer low-metallicity SSM B16-AGSS09met predictions [137], that provides the best description of the solar atmosphere. The recent metallicity measurements from C11 [139] and AAG21 [140] also point to the low-metallicity compositions, however, the most recent determination from MB22 [141] provides a high-metallicity ratio. This unresolved problem is referred to as the solar metallicity puzzle. The metallicity input for the SSMs also has an influence on the solar neutrino fluxes predictions, as shown in Table 4.1 for the B16-GS98 and B16-AGSS09met SSMs. The metal content in the Sun core affects the solar opacity, determining the efficiency of radiative energy transfer and therefore, affects the solar temperature profile and impacts the nuclear reaction rate and neutrino emissions. It also affects the relative intensity of *pp*-chain and the CNO cycle. In fact, the solar neutrino flux predictions from B16-GS98 and B16-AGSS09met SSMs for 7Be and ^{8}B differ by about 9% and 18%, respectively. Additionally, the CNO neutrino flux has an additional direct dependence on the metallicity of the Sun's core, as the CNO cycle is affected by presence of "metals", namely carbon, nitrogen, and oxygen. The relative difference in the CNO neutrino predictions by the two models is about 28%. The CNO neutrinos are a unique probe of the initial chemical composition of the Sun at the time of its formation, since the metal abundance in the solar core is believed to be not influenced by the solar surface. Therefore, the precise measurement of the solar neutrino fluxes, especially the CNO-ν flux, can help to provide a solution to the solar metallicity puzzle. The recent measurements of the CNO solar neutrino flux by Borexino experiment has provided insights to the solar metallicity problem, which will be discussed in Chapter 4. However, more precise measurement of the solar neutrino fluxes from the future experiments, such as JUNO, is needed to have conclusive results on the solar metallicity problem.

2.3 Solar neutrino interactions

In the liquid scintillator experiments and water Cherenkov experiments, the solar neutrinos interact through elastic scattering (ES) process on electrons. It takes place by the neutrinos of all flavors:

$$\nu_x + e^- \rightarrow \nu_x + e^- \qquad x = e, \mu, \tau. \tag{2.17}$$

However, the cross section for scattering of ν_e is $\sim$6 times larger than that of ν_μ and ν_τ. This is because ν_e interacts through both CC and NC interactions, while the other flavours of neutrinos interact through NC interactions only. At MeV energies, only ν_e interact via CC because muons and tau leptons are too heavy to be created. In ES process, only a fraction of the neutrino energy E_ν is transferred to the recoiled electron. Using the energy and momentum conservation laws for the scattering process, the gained kinetic energy T_e is given by:

$$T_e = \frac{2m_e c^2 cos^2\theta}{(1 + \frac{m_e c^2}{E_\nu})^2 - cos^2\theta}, \tag{2.18}$$

where m_e is the electron rest mass and θ is scattering angle. The elastic scattering process has no intrinsic threshold. One can also deduce the maximum kinetic energy of recoiled electron ($T_e^{\max}$):

$$T_e^{\max} = \frac{E_\nu}{1 + \frac{m_e c^2}{2E_\nu}}, \tag{2.19}$$

which is achieved at cosθ = +1 [142]. This implies that when the maximum energy is transferred to an electron, the recoiled electron preserves the neutrino direction. Furthermore, a continuous electron recoil spectrum is obtained even in the case of a mono-energetic neutrino source, such as ^{7}Be and *pep* solar neutrinos. The expected rate of ν-e^- interaction in a given target R is calculated as the product of the incoming neutrino flux, the number of electrons in the target, and the cross section of ν-e^- elastic scattering, taking into account the survival probability of the electron neutrino:

$$R = N_e \int dE_\nu \frac{d\Phi}{dE_\nu} \int dT_e \left[\frac{d\sigma_e}{dT_e} P_{ee}(E_\nu) + \frac{d\sigma_{\mu,\tau}}{dT_e} \left(1 - P_{ee}(E_\nu)\right) \right], \tag{2.20}$$

where N_e is the electron density of the medium, Φ is the incoming neutrino flux, $\mathrm{d}\Phi/\mathrm{d}E_\nu$ is the differential energy spectrum of neutrinos, σ_e and $\sigma_{\mu,\tau}$ are the elastic scattering cross section of ν_e and $\nu_{\mu,\tau}$ [142], respectively. Here, P_{ee} is the survival probability of ν_e. All the interactions, discussed above, are used in the detection of solar neutrinos, which will be discussed in Sec. 2.4.

Solar neutrinos also interact through CC and NC interactions on the nuclei, such as deuterium in the SNO experiment (see Sec. 2.4) and ^{13}C in the JUNO experiment (see Sec. 6.3). The CC interaction is sensitive to electron neutrinos only, while the NC reaction is equally sensitive to all flavors of neutrinos. These reactions have been used to perform ^{8}B solar neutrinos measurement to solve solar neutrino puzzle, which will be discussed in Sec. 2.4.

2.4 Solar neutrino experiments

While the flux of solar neutrinos on the Earth is enormous ($\sim 7 \times 10^{10}\ \nu_e\,\mathrm{cm}^2\mathrm{s}^{-1}$), their detection is extremely challenging because they only interact very weakly. Therefore, the measurement of solar neutrinos requires the large detectors to gain a good statistics as well as the background contribution (see Sec. 2.5) should be kept sufficiently low. This section provides an overview of the solar neutrino experiments, beginning from the historical radiochemical methods to the current real-time water Cherenkov and liquid scintillator ones. The important solar neutrino results in each category are also summarized. It also briefly mentions the upcoming experiments in these categories, including the future detectors, whose physics program also covers the solar neutrino measurement:

Radiochemical detectors

The radiochemical experiments utilize the CC interaction of the electron-neutrinos on the nuclei of a selected target, which produces the radioactive daughter nuclei. The number of daughter nuclei is measured, after they are separated from the target nuclei using the chemical extraction techniques. The daughter nuclei are detected through their own decay signatures. Due to very low event rates in these detectors, a custom unit of the SNU (solar neutrino unit) = 10^{-36} captures per target nucleus per second, has been defined. In this detection method, the information of the time, direction, and the energy of an event are lost and the integrated reaction rate over a time period is measured.

The first radiochemical detection of solar neutrinos was performed by "the Chlorine experiment" in the Homestake gold mine in South Dakota, USA [143]. This experiment was built in the period 1965-1967. It consisted of a underground tank containing ∼615 t of C_2Cl_4, which exploited the CC interaction of solar neutrino on ^{37}Cl:

$$^{37}\mathrm{Cl} + \nu_e \rightarrow {}^{37}\mathrm{Ar} + e^-. \tag{2.21}$$

The energy threshold of this reaction is 0.814 MeV, which is above the end point of *pp*-neutrinos. The Chlorine experiment measured ^{7}Be, *pep*, CNO, and it covered a large portion of energy spectrum of ^{8}B solar neutrinos. The half-life of ^{37}Ar is about 35 days. The produced ^{37}Ar was extracted every two months. After extraction, ^{37}Ar decay via K-capture, which resulted in X-rays of 2.82 keV and the Auger electrons. The ^{37}Ar decays were detected in small and low-background proportional counters. The final result obtained on the average neutrino capture rate in the Homestake experiment was $2.56 \pm 0.16\,(\mathrm{stat.}) \pm 0.16\,(\mathrm{syst.})$ SNU. This result is almost one-third of the SSM predictions of that time: $7.6^{+1.3}_{-1.1}$ SNU [144]. This marked the beginning of the so-called solar neutrino problem, showing a discrepancy between the measured number of solar neutrinos and their theoretical prediction.

The Gallium based radiochemical experiments, the Soviet-American Gallium Experiment (SAGE) [145] at the Baksan Neutrino Observatory in Russia, and the Gallium Experiment (GALLEX)/ Gallium Neutrino Observatory (GNO) [146,147] in Gran Sasso Laboratory (LNGS) in Italy, followed the Homestake experiment. In these experiments, the ^{71}Ga served as the target nuclei:

$$^{71}\mathrm{Ga} + \nu_e \rightarrow {}^{71}\mathrm{Ge} + e^-, \tag{2.22}$$

where ^{71}Ge, with half-life of 11.4 days, was extracted and its decays were counted in proportional chambers. The energy threshold of this reaction is 0.233 MeV, which is lower than that of the Homestake experiment as well as the end point of *pp*-neutrino spectrum. Hence, they measured all solar neutrinos. The SAGE experiment used about 50 t of liquid metallic Gallium as target. The GALLEX/GNO experiment used 101 t of $GaCl_3$, containing 30.3 t of Gallium. The measured neutrino capture rate in all three Gallium experiments was 66.1 ± 3.1 SNU, by taking the weighted average of each experiment, which is ∼50% of the theoretical predictions [148]. The deficit observed by the gallium experiment is smaller than the one seen by the Chlorine experiment, which is now attributed to the matter enhanced oscillations in the Chlorine experiment and the vacuum oscillations of solar neutrinos in the Gallium experiment, as the Gallium experiment was sensitive to the dominant *pp* solar neutrinos.

Water Cherenkov detectors

The solar neutrino deficit was also observed by Kamiokande (Kamioka Nucleon Decay Experiment), a 3 kt water Cherenkov detector [149]. It was built in the Kamioka mine in Japan in 1980s and the main goal of this experiment was the proton decay search. In Kamiokande, the solar neutrinos interact via the elastic scattering off electrons, where electrons are recoiled in a direction, correlated with that of the incoming neutrino. The recoiled electrons produce Cherenkov light. The Cherenkov photons are emitted in a cone, when the speed of charged particle is greater than the speed of light in the medium. The emitted photons were detected by 948 photomultiplier tubes (PMTs). The cosine of angle of the Cherenkov cone (θ_{ch}) is given by [36]:

$$cos\theta_{ch} = \frac{c}{nv}, \tag{2.23}$$

where n is the refractive index in water, v is speed of the charged particle, and c is the speed of light. The analysis energy threshold was $\geq$7 MeV in Kamiokande and as a result, it was primarily sensitive to ^{8}B solar neutrinos, and the light yield was about 40 hits per event [149]. The event position and its energy were reconstructed based on the position and time of the hit PMTs. It provided the first observation in real time of the flux of ^{8}B solar neutrinos. The number of measured ^{8}B solar neutrino events in Kamiokande corresponded to about 49.6% of the SSM predictions [149]. In addition, it was the first experiment to perform event by event measurement of solar neutrinos and established their origin with the Sun by using the correlated angle of the event direction with respect to the solar neutrino direction [150].

The SuperKamiokande detector (SuperK) [151], the successor of the Kamiokande experiment, started data taking in 1996. It is a Cherenkov imaging detector with same detection principle as of Kamiokande experiment. It contained 50 kt of pure water and was instrumented with about 12,000 PMTs. Due to the high energy threshold of SuperK ($\geq$3.5 MeV for present [152]), it is sensitive to only ^{8}B solar neutrinos. Similar to the previous experiments, it also measured ^{8}B solar neutrino flux to be about 45% of the SSM predictions [153].

The solar neutrino puzzle was solved by the Sudbury Neutrino Observatory (SNO) in SNOLAB in Canada [154]. It was a Cherenkov detector containing 1 kt of heavy water (D_2O) as the target. It has permitted the detection of solar neutrinos through three different interaction channels including ES, CC, and NC. The CC interaction on the proton of the deutron:

$$\nu_e + d \rightarrow e^- + p + p, \tag{2.24}$$

is sensitive to only ν_e. As discussed before, ES reaction is sensitive to all flavours of neutrinos but unequally. The electrons in the ES and CC reactions are detected through Cherenkov light emission in heavy water, which are detected by about 9500 photomultipliers. By comparing the SuperK precision results on ^8B-ν flux [153], which was inferred from ES reaction, with the measured CC reaction rate in SNO, an evidence of an active non-ν_e component in solar neutrino flux was provided [155]. In SNO, the NC interaction on the deuterium is :

$$\nu_x + d \rightarrow \nu_x + p + n, \tag{2.25}$$

which is equally sensitive to all flavours of neutrinos (ν_x, where $x = e, \mu,$ andτ). The photons, emitted by the neutron capture on deuterium and chlorine from dissolved NaCl, were detected in the first and second phase of the experiment, respectively. In the third phase, ^{3}He based proportional counters were used for neutron detection. These photons produce a photomultiplier signal through Compton scattering on electrons of medium, providing the Cherenkov light for detection. By including the result of NC reaction in 2002, the SNO experiment established the presence of non-electron flavoured neutrino component in solar neutrino flux with 5.3σ of statistical significance. This result provided a strong evidence for the neutrino flavor transformation, which was consistent with neutrino oscillations. The total flux of active ^{8}B solar neutrinos, measured with NC reaction, is found to be consistent with the theoretical predictions [38].

Furthermore, the global analyses of all solar neutrino data, including SNO and SuperK, favored the LMA solution of the neutrino oscillations [47]. The matter effects on the solar neutrino oscillations result in the so-called day-night effect. The day-night effect is due to the fact that high energy ^{8}B neutrinos cross Earth at night, which can lead to the coherent regeneration of ν_e as a result of matter effects. Hence, the flux, measured at night, differ from the one measured at day-time. SuperK experiment has provided the first indication of day-night effect by measuring the asymmetry between the experimentally observed ^{8}B neutrino flux at day and at night, implying the matter

effects on the neutrino oscillations [156]. Moreover, the high precision measurement of ^{8}B solar neutrinos come from SNO [157] and SuperK [152] experiments. The SNO experiment has set most stringent upper limit on the *hep* solar neutrinos [158].

Recently in 2020, the new SuperK experiment (SK-Gd) [92] has started in its sixth phase with the addition of Gadolinium in the water to increase the neutron capture efficiency. The main goal is to perform the first detection of supernova relic neutrinos produced by the supernova explosions since the beginning of the Universe. The next generation of the water Cherenkov detector will be the HyperKamiokande, a Cherenkov detector that will be filled with 260 kt of extremely ultra pure water and its fiducial volume will about 10 times bigger than that of the SuperK. It will have a rich variety of physics program, ranging from the study of the solar, supernova, atmospheric, and accelerator neutrinos, proton decay search, etc. One of the major goals is to investigate the CP violation of neutrinos and resolve the neutrino mass hierarchy problem [77].

Liquid scintillator detectors

The liquid scintillator (LS) detectors also constitute the current generation of the solar neutrino experiments, which also includes the ones discussed in this thesis. In LS experiments, the solar neutrinos are detected through elastic scattering off electrons. The recoiled electron deposits its kinetic energy in LS by exciting the LS molecules, which results in the emission of isotropic scintillation photons, that are detected by the photomultiplier tubes. Typically, a small quantity of a wavelength shifter is added in LS, which emits the photons at longer wavelengths to allow the photons to propagate through the material, by reducing self-absorption and matching the quantum efficiency of the photomultiplier tubes. The LS experiments has typically a high light yield as compared to the water Cherenkov detectors, which allows the study of sub-MeV solar neutrinos. In LS detectors, the amount of detected light is not simply related to total energy deposited by the particle. Various effects, such as light quenching as well as the amount of Cherenkov photons, are also included. The quenching refers to the process in which the scintillator de-excites without emitting the scintillation light. It is represented by the so-called quenching factor Q, where $Q < 1$, introducing a non-linear relation between the deposited energy and the visible energy. It is given according to the Birk's quenching model [159] and depends on the particle type. The quenching effect of α particles with few MeV of energy is higher than that of the β particles and consequently, the amount of emitted light is reduced by a factor of $\sim$10 compared to an electron with the same energy. A non-negligible fraction of Cherenkov photons are emitted, which is dependent on the wavelength dependent refractive index of the medium. The spectrum of Cherenkov photons is given by the Frank-Tamm formula [36]. The wavelength spectrum of the Cherenkov photons are usually not detectable by photomutiplier tubes in LS experiments and hence, a large fraction of it are absorbed by the scintillator and are re-emitted as isotropic scintillation light. As a result, the non-directional scintillation photons are dominant in the LS experiments and are typically used for the solar neutrino analysis (see Chapter 4). However, a method exploiting the directional Cherenkov photons in the LS experiments has been developed, which will be discussed in Chapter 5. The LS experiments have additional good characteristics such as low energy threshold, good energy and position resolutions, and the pulse shape discrimination capabilities, but they usually suffer from the loss of directionality as the Cherenkov photons have very small contribution.

The Borexino [160] and JUNO [100] experiments are the liquid scintillator detectors, which are discussed in detail in Chapter 3 and Chapter 6, respectively. The Borexino detector, located in the LNGS in Italy, contained 280 t of LS and took data from 2007 to 2021. Due to its unprecedented radiopurity, it has provided exceptional results in the solar neutrino measurement, which will be discussed in Chapters 4 and 5. The

upcoming JUNO experiment, located in Southern China, will consist of 20 kt of LS. Its construction is expected to finish at the end of 2024. The main goal of JUNO is the determination of neutrino mass ordering, using reactor antineutrinos at a baseline of about 53 km. Its enriched physics program also includes the solar neutrino measurement, which will be discussed in Chapters 6, 7, and 8.

The Kamioka Liquid Scintillator Anti-Neutrino Detector (KamLAND) detected antineutrinos from more than 50 reactors, with an average baseline of about 180 km and consisted of 1 kt of LS. The primary goal of the KamLAND experiment was to search for the oscillation of reactor ν_e. In 2002-03, KamLAND provided first evidence of oscillation from reactor antineutrino disappearance as well as confirmed the LMA solution [51]. In addition, the solar mass splitting Δm^2_{12} was determined with high precision [52]. It has high background contamination levels to perform a complete solar neutrino spectroscopy, nevertheless, it has provided ^{7}Be solar neutrino measurement [161]. In 2011, KamLAND detector has been modified to KamLAND-Zen, containing 13 t of Xe-loaded LS. The main goal of KamLAND-Zen experiment is the search for neutrinoless double beta decay [162].

The SNO+ experiment [80], an upgraded version of the SNO experiment, is a liquid scintillator experiment. It started data taking in 2017, where in its first phase, it was filled with "light" water (H_2O) until 2019 and then, it was filled with 780 t of LS in its second phase. In this third phase, the detector will be loaded with 3.9 t of natural Tellurium. The main goal of the SNO+ experiment is to search for the neutrinoless double beta decay. It also offers the exploration of other physics programs that include the studies of geoneutrinos, solar neutrinos, supernova explosions, and the search of exotic physics. Recently, it has also provided first event by event directional reconstruction of ^{8}B solar neutrinos in its liquid scintillator commissioning phase [163].

Hybrid detectors

The development of hybrid detectors encompasses the goal to combine the advantages of both water Cherenkov as well as LS detectors. The Cherenkov light would provide the directional information, which can be used for the potential background rejection and the detector has low energy threshold, as well as a good energy and position reconstruction performances by benefiting from the scintillation light. Currently, there are ongoing activities that include development of new target materials [164–166], fast-photo sensors [167], and dichroic reflectors for spectral photon sorting [168].

Theia is one of such proposed hybrid detector [169]. The detector will have a mass of 25-100 kt and will contain water-based liquid scintillator (WbLS). In Theia, a small quantity of liquid scintillator will be dispersed in water, in order to reduce the absorption of Cherenkov photons as well as to produce the scintillation photons. It will be located at the Stanford Underground Research Facility in USA and will be equipped with a mix of conventional photomultiplier tubes and Large Area Picosecond Photo-Detectors (LAPPDs), to achieve better photon separation for better event reconstruction performances. It will have a broad program of physics, including precision measurement of *pp*, *pep*, and CNO solar neutrino fluxes as well as probing of transition region between the vacuum and matter dominated oscillations. The other physics goals include the detection of DSNB, measurement of geoneutrinos with unprecedented statistics, sterile neutrinos search, and long baseline neutrino oscillation measurements as well as search for CP violation. Theia is planned to be realized in three phases: in first phase, it will contain low yield WbLS and very fast photosensors and in the following phase, it will have an enhanced photon detection and high-yield or slow LS to enable solar neutrino studies. The third phase will include doping with a neutrinoless double beta decay isotope for the neutrinoless double beta decay search. More details can be found in Ref. [169].

The Jinping neutrino experiment [81], a future detector, will be located in China Jinping Underground Laboratory (CJPL) in Sichuan province in China. The laboratory is situated about 2400 meters under Jinping mountain. The main goal of this neutrino experiment is the measurement of solar neutrinos from *pp*-chain and CNO cycle, in addition to the geoneutrinos and supernova neutrinos. Two detectors are planned to be built: one with 2000 t fiducial mass for the solar neutrino studies and other one is proposed to have 3000 t fiducial mass for the geoneutrinos and supernova neutrinos measurements. It is under consideration to use a slow LS as the target material, for the separation of Cherenkov and scintillation light. The fast Cherenkov light can be used for the directional reconstruction of charged particles, while the scintillation light can be used for the event energy reconstruction.

2.5 Backgrounds for solar neutrinos in liquid scintillator detectors

In the liquid scintillator experiments such as Borexino and JUNO, the backgrounds for the solar neutrino analysis can be classified into three categories: internal, external, and cosmogenic backgrounds. In addition, the pileup events also constitute to the backgrounds. The internal backgrounds represent the intrinsic radioactive contaminants of the liquid scintillator. The external backgrounds constitute the radioactive impurities of the materials surrounding the liquid scintillator. The cosmogenic backgrounds are related to the isotopes produced by cosmic muons crossing the detector. In this section, the radioactive elements in each of these three categories are discussed, which are relevant for the solar neutrino analysis described in this thesis and focusing on the origin, decay type, lifetime, and the Q values [159]. The background levels in each of the Borexino and JUNO experiments is discussed in Chapter 3 and Chapter 6, respectively.

Internal Backgrounds

^{14}C : ^{14}C is the most abundant background for the solar neutrino analysis. It decays via emission of β^- and has a mean life of about 8270 years. It is produced by cosmogenic reactions in the atmosphere and thus, it is a part of all organic compounds. The organic liquid scintillators are derived from the petroleum from deep undergrounds and therefore, are expected have a reduced concentration compared with organic materials from the surface. Given its low end point at about 156 keV, it usually determines the low energy threshold for the solar neutrino analysis. ^{14}C is a crucial background for the *pp* solar neutrinos due to their overlapping energy spectra.

^{85}Kr : ^{85}Kr undergoes a β-decay with a mean life of about 15.4 years. It has an end point of 687 keV and has an energy spectral shape, which is very similar to the recoiled electron spectrum of ^{7}Be solar neutrinos. Thus, it is a crucial background for the ^{7}Be-ν analysis. ^{85}Kr also decays to ^{85m}Rb which is meta-stable nuclei and β particle with maximum kinetic energy of 173 keV. This decay has a small branching ratio of about 0.43%. The ^{85m}Rb decays ^{85}Rb at ground state emitting a 514 keV γ-ray with mean life of 2.06 μs. This $\beta - \gamma$ coincidence can also be used to measure ^{85}Kr concentration. The origin of ^{85}Kr is the nuclear explosions in the atmosphere and it can contaminate the scintillator even with very small air exposures.

^{40}K : ^{40}K isotope has a mean life of about 1.85×10^9 years. It decays dominantly via emitting β-decay with 89.3% branching ratio (BR) and has an end-point of 1310 keV. It also decays via electron capture with 10.7% probability, resulting in the emission of

mono-energetic 1460 keV γ-ray. It can enter into the scintillator through dust particulates and its contamination can be reduced with scintillator purification techniques.

^{232}Th : ^{232}Th is an isotope of natural thorium with 100% natural abundance. It decays into ^{228}Ra by emitting α and has a mean life of 2.03×10^{10} years. The ^{232}Th decay chain consist of six α and four β decays considering the main branches and it terminates with a stable ^{208}Pb creation. The ^{232}Th contamination can be inferred using the fast decay coincidence (τ = 433 ns) of ^{220}Rn daughters, ^{212}Bi-^{212}Po, where ^{212}Bi is a β emitter with Q value of 2.25 MeV and ^{212}Po undergoes α decay emitting 8.95 MeV energy to create ^{208}Pb.

^{238}U : Due to its natural abundance of $\sim$99%, ^{238}U is an prevalent isotope of uranium. It has a mean life of 6.45×10^9 years. ^{238}U isotope decays into ^{232}Th via the emission of α. Its decay chain consists of 8 α and 6 β decays, that ends with the production of stable ^{206}Pb. The concentration of ^{238}U decay chain can be measured by identifying fast decay coincidence (τ = 238 μs) of ^{222}Rn daughters, ^{214}Bi-^{214}Po, where ^{214}Bi is a β emitter with Q value of 3.27 MeV and ^{212}Po undergoes α decay emitting 7.69 MeV energy to create ^{210}Pb.

^{210}Pb : ^{210}Pb is a β emitting isotope in ^{238}U decay chain. It can also be present as out-of-equilibrium component with ^{222}Rn section, due to its long mean lifetime of 32.2 years and its tendency to absorb on the surfaces. Due to its very low end-point (Q = 63.5 keV), its energy spectrum lies below region of interest for solar neutrino analysis as well as the dominant ^{14}C end point. However its daughters, ^{210}Bi and ^{210}Po constitute major backgrounds.

^{210}Bi : ^{210}Bi, the daughter nuclei of ^{210}Pb, is a β emitter with a mean lifetime of about 7.23 days. It decays to form ^{210}Po and the Q-value of its decay is 1160 keV. This background is crucial for the CNO and *pep* neutrino analysis due to their overlapping and similar energy spectra, which will be discussed in Chapter 4.

^{210}Po : ^{210}Po is an α decaying isotope, with a mean lifetime of about 200 days. The Q-value of its decay is 5.3 MeV but due to quenching effects, its visible energy spectrum lies in the ^{7}Be solar neutrino energy region. ^{210}Po has been utilized to extract the constraint on ^{210}Bi rate in Borexino for CNO analysis, which will be discussed in Chapter 4. ^{210}Po can also be present as out-of-equilibrium component with ^{238}U-decay chain as well as the ^{210}Pb decay, which is critical for ^{7}Be neutrino analysis, which will be shown in JUNO in Chapter 7.

External Backgrounds

The external backgrounds originate from the materials, that contain and surround the scintillator. As the radioactive decays of external background isotopes occur outside the scintillator, only the γ rays reach the inner detector volume and deposit their energy. The contributing external γ emitting backgrounds for the sub-MeV solar neutrinos are ^{208}Tl (Q-value = 2614 keV, τ = 4.4 min), ^{40}K (Q-value = 1460 keV, $\tau = 1.85 \times 10^9$ years), and ^{214}Bi (Q-value < 1764 keV, τ = 28.4 min) [1,159]. Their contributions are usually suppressed by using a fiducial volume cut for the analysis. In addition, the radial distribution of the external γ events is exponential, which is different from the

Isotope	$\mathcal{Q}$ (MeV)	Mean lifetime	Decay mode
^{85}**Kr**	0.687	15.4 y	β^-
^{40}**K (BR=89.3%)**	1.31	1.85×10^9 y	β^-
^{40}**K (BR=10.7%)**	1.46	1.85×10^9 y	e^- capture + γ
^{232}**Th chain**	8.8	2.03×10^{10} y	α, γ, β^-
^{238}**U chain**	7.8	6.45×10^9 y	α, γ, β^-
^{210}**Pb**	0.063	32.2 y	γ, β^-
^{210}**Bi**	1.16	7.23 d	β^-
^{210}**Po**	5.3	200 d	α

Table 2.1: Summary of the internal backgrounds relevant for the sub-MeV solar neutrinos analysis. Note that for the ^{232}Th and ^{238}U chains, the lifetime of the parent isotope of the decay chain, and the highest $\mathcal{Q}$ value of the chain isotopes [7, 159], are reported.

uniform internal components. This is utilised in the solar neutrino analysis, which will be discussed in Chapter 4.

Cosmogenic Backgrounds

The liquid scintillator detectors are typically built in an underground laboratory to suppress the muon flux by serveral orders of magnitude. The cosmogenic backgrounds are created by the interaction of the residual muons on carbon atoms in the liquid scintillator. A number of cosmogenic isotopes are produced in this interaction. Many of them can be removed by using a veto in coincidence with the muons (see Chapter 3). The remaining isotopes are long-lived such as ^{11}C, ^{10}C, and ^{6}He, as well as their energy spectra lie in the solar neutrino energy region. So, they constitute backgrounds for the solar neutrino analysis.

The dominant cosmogenic background is ^{11}C isotope, which is crucial for the measurement of *pep* and CNO solar neutrinos. It is created through the following reaction:

$$\mu + {}^{12}\mathrm{C} \rightarrow \mu + {}^{11}\mathrm{C} + n. \tag{2.26}$$

With a mean lifetime of 29.4 min, ^{11}C decays via the positron emission:

$${}^{11}\mathrm{C} \rightarrow {}^{11}\mathrm{B} + e^+ + \nu_e. \tag{2.27}$$

The total energy released ranges from 1.02 MeV to 1.98 MeV, which overlaps with the energy spectra of *pep* and CNO solar neutrinos. The other cosmogenic backgrounds, ^{10}C (β^+, Q = 3.65 MeV) and ^{6}He (β^-, Q = 3.51 MeV), have a mean lifetime of 27.8 sec and 1.16 sec, respectively [159]. A so-called Three-Fold-Coincidence (TFC) algorithm has been developed by Borexino [170] and is utilized to identify the cosmogenic events for the solar neutrino analysis, which will be discussed in Sec. 3.2.3.

Pile-up

The pile-up events refer to the occurrences of two uncorrelated events close in time such that they are measured as a single event. The dominant pile-up contribution is due to the overlapping of two or more ^{14}C events as ^{14}C is the most abundant background. Other possible combinations, such as ^{14}C event with ^{210}Po or the external backgrounds, also constitute the pileup events as seen by Borexino [1]. It can also

affect the spectral analysis of solar neutrinos in JUNO, which will be mentioned in Chapter 6.

Part II

The Borexino Experiment

Chapter 3

Introduction to Borexino experiment

This chapter describes the complete Borexino experiment including its design, the radiopurity levels, its past scientific programs, reconstruction algorithms as well as the simulation software. The chapter starts with a description of the experiment in Sec. 3.1. The structure of Borexino detector is detailed in Sec. 3.1.1. Section 3.1.2 covers the description about data acquisition system in Borexino. The summary about the calibration campaign with the goal of understanding the detector response is provided in Sec. 3.1.3. Section 3.1.4 describes the radiopurity levels achieved in Borexino. Section 3.1.5 is dedicated to the thermal stability operation of Borexino detector, crucial for the CNO solar neutrino spectroscopy with Borexino.

Section 3.2 provides the description of all the analysis tools and software, developed and used in Borexino. The energy and position reconstruction of data events in Borexino is summarized in Sec. 3.2.1. The pulse shape discrimination methods and the ^{11}C identification technique in Borexino are discussed in Sec. 3.2.2 and 3.2.3, respectively. Section 3.2.4 is dedicated to the explanation of standard cuts applied to select neutrino candidates from the collected data in Borexino. The final section of the chapter, Sec. 3.2.5, describes the Monte Carlo (MC) simulation of Borexino.

3.1 The Borexino detector

Borexino detector started data taking in May 2007 and ended data taking in October 2021. The entire data taking period of Borexino is divided into three phases: Phase-I (May 2007 - May 2010), Phase-II (December 2011 - May 2016), and Phase-III (July 2016 - October 2021). Different important detector operations, namely calibration (Sec. 3.1.3), purification (Sec. 3.1.4), and thermal insulation (Sec. 3.1.5) were also carried out in this period. The timeline of all phases along with the detector operations is schematically shown in Fig. 3.1.

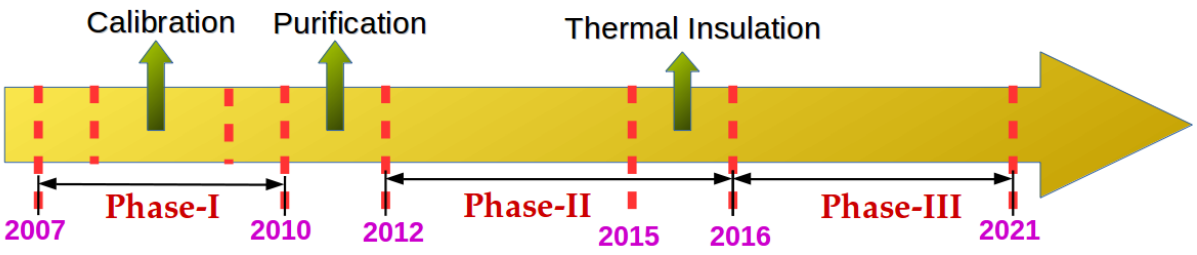

Figure 3.1: The timeline of Borexino.

3.1.1 Detector design

Borexino is a liquid scintillator (LS) detector [160], situated underground in the Hall C of the *Laboratori Nazionali del Gran Sasso* (LNGS) in Italy. The location of detector has

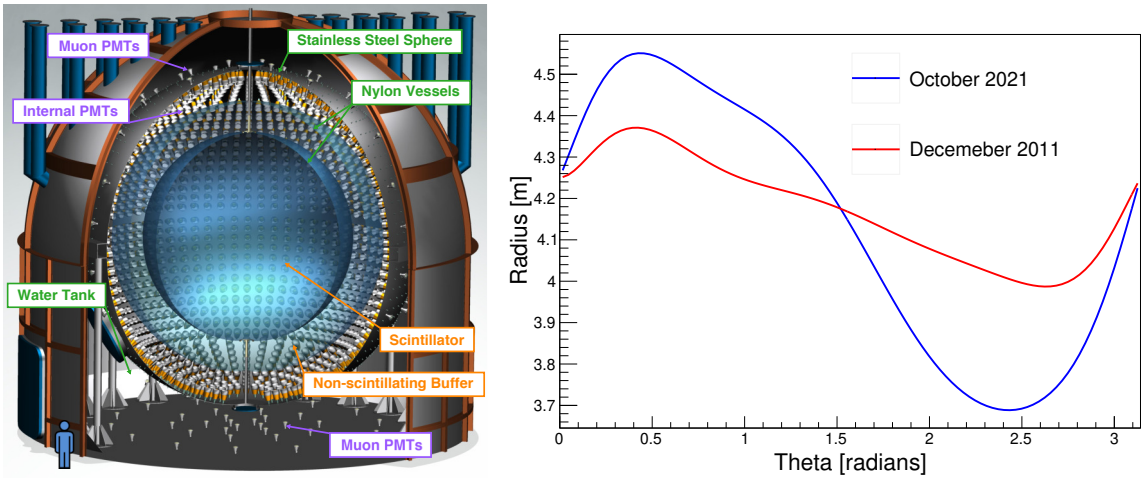

(a) **(b)**

Figure 3.2: (a) Scheme of the Borexino detector, taken from [5]. (b) Change in the inner vessel shape plotted in polar coordinates from December 2011 to October 2021 due to a small leak detected in 2008 [159].

3800 m water equivalent rock shielding above it, which corresponds to comic muon flux suppression by a factor of 10^6. The structure of the Borexino detector is depicted in Fig. 3.2a. Borexino can be divided into two sub-detectors: the Inner and Outer Detector. The inner detector (ID) and the outer detector (OD) is separated by a stainless steel sphere (SSS) of radius 6.85 m.

Inside SSS structure, there are two concentric spherical vessels made up of nylon : the Inner Vessel (IV) and the Outer Vessel (OV) of radii 4.25 m and 5.50 m, respectively. Each of the two vessels has a thickness of 125 μm. As a consequence of the two vessels, ID is divided into three layers. The innermost layer contains 278 ton of LS target. The scintillator is a solution of pseudocumene (PC, 1,2,4-trimethylbenzene) as a solvent and fluor PPO (2,5- diphenyloxazole) as a solute at concentration of 1.5g/l. PPO is added to improve the time response and shift the emission wavelength spectrum to higher wavelengths in order to match the PMT efficiency window. The density of the scintillator is $(0.878 \pm 0.004)\,\mathrm{g\,cm^{-3}}$, where the error includes the changes during the whole period due to the temperature variations [78]. The light yield of PC+PPO mixture is $\sim$10,000 photons/MeV. The other two layers outside the IV consist of a buffer solution containing dimethylphthalate (DMP) light quencher in PC to shield the core of detector against external backgrounds (see Chapter 1). Combining the effects of absorption of scintillator and buffer fluid, the overall light yield is $\sim$500 photons/MeV of deposited energy, which corresponds to energy resolution of 5% at 1 MeV. The reconstruction of time-dependent shape of IV is performed using the reconstructed position of radioactive isotopes present on IV surface on a weekly basis. Since there was a small leak detected in 2008, it is necessary to take the time dependent deformation of IV shape into account [159]. Figure 3.2b shows the the inner vessel shape change in polar coordinates in years 2011 and 2021. The OV, immersed in the buffer solution, provides the shielding against ^{222}Rn emanating from detector materials. There are 2212 photomultiplier tubes (PMTs), that are mounted on the inner surface of SSS to collect the scintillation light from the energy deposition by a charged particle interaction in LS.

The OD consists of a water tank (WT) of 9 m base radius and height of 16.9 m filled with 1 kt of ultra-pure water. It acts as a barrier against neutron and external γ backgrounds and also the detection and tracking of cosmogenic muons producing Cherenkov light during their passage in the water. The Cherenkov light emitted in the water is collected by 208 PMTs placed on the floor of water tank and on the outer

surface of SSS, which is contained inside water tank. The interior of WT and SSS is covered by Tyvek material to enhance the light collection efficiency. More details of the detector design can be found in [160].

3.1.2 Data Acquisition

As summarized in Sec. 3.1.1, ID consists of 2212 PMTs mounted on the inner surface of SSS that collect the scintillation light from LS, while OD has 208 PMTs to detect the Cherenkov light produced by the muons in water. As the scintillation photons are recorded by ID PMTs, the front end electronics performs the analog processing of the PMT signal. These PMT signals are further processed by the digital electronics system (so-called *Laben boards*) providing the arrival time and charge of each light pulse. The charge in photo-electrons (p.e) is obtained from the pulse integration within the time window of 80 ns. The digital boards do not resolve multiple photon hits on the same PMT when the time difference between two consecutive hits is less than 180 ns [159] and therefore, one recorded hit in electronics can also correspond to more photons. Then, the data is temporarily saved in an internal buffer and the system looks for a trigger. The Borexino trigger board (BTB) issues a trigger signal when at least one of ID or OD is triggered. The ID's trigger threshold is set to 20-25 PMTs that are hit within a selected time window (typically $\sim$100 ns). The information on PMT hits is acquired in a 16.5 μs data acquisition (DAQ) gate after the trigger of ID. This record is saved in a VME readable memory. For outer detector, the front end electronic board generates a signal and a Muon Trigger Board (MTB) sends signal to BTB when at least 6 PMTs are hit within the time window of 150 ns.

The main physics trigger type for ID events is the so called TT1 & BTB0 when OD did not see a signal. There also exists a special trigger, TT128, a 1.6 ms long trigger issued to detect the cosmogenic neutrons after a trigger from internal muon passing through both ID and OD (TT1 & BTB4). Special triggers such as TT2 for muons detected by OD only, TT64 for monitoring dark noise and ^{14}C dominated energy spectrum, electronic pulse trigger (TT32), and laser trigger (TT8) were also developed [160].

Each set of PMT hits, called trigger event, with their hit time and charge info is reconstructed using ROOT [171] based reconstruction software ECHIDNA, developed by the Borexino collaboration. This software processes the raw PMT hits by removing the non-physical PMT hits and the resulting hits are called decoded hits. Then, it groups the hits belonging to the same scintillation event known as clusters and this process is called clustering. Each cluster represents a physical event and the reconstruction of event's energy and position, particle discrimination are applied on clusters. The clustering algorithm recognizes two physical events as the two distinct clusters if their time separation is more than $\sim$230 ns. The raw hits are processed in batches corresponding to the data taking time of $\sim$6 hours. These batches are called as runs.

3.1.3 Calibration

In order to determine the neutrino interaction rates with high precision and understand the detector response, several calibration campaigns [172] were carried out between 2008 and 2011. Internal calibration sources were deployed in four calibration campaigns between 2008 and 2009: October 2008, January 2009, June 2009, and July 2009. The major goals were the determination of energy scale, study of the non-uniformity of detector response, testing of the position reconstruction algorithm (Sec. 3.2.1), validation of the Monte Carlo (MC) simulation (Sec. 3.2.5), study of the systematics of fiducial volume (Sec. 3.2.4), and the trigger efficiency (Sec. 4.4.3). The internal sources used were:

- The mono-energetic γ sources were used for energy calibration.
- The ^{222}Rn-^{14}C as a α/β source was used to probe uniformity of trigger efficiency, to test position reconstruction performance in the energy region of 0-3.2 MeV, and to evaluate the systematic error related to fiducial volume selection.
- ^{241}Am-^{9}Be was deployed as a neutron source to perform position studies at higher energies.
- A laser source of wavelength 394 nm to perform independent check of PMT time equalization.

The γ-sources are also used for the calibration of Cherenkov light in Borexino and an improved time calibration using ^{222}Rn-^{14}C is also performed for directional analysis described in Chapter 5. Additionally, the calibration sources are also used to determine the fiducial volume systematics in Chapter 5.

In addition, the Borexino detector was calibrated with the external calibration sources in the outer buffer region. The goal was to study the energy spectrum shape and radial dependence of external backgrounds (see Chapter 1). A custom made ^{228}Th source was used to serve this purpose in two external source calibration campaigns: July 2010 and November - December 2011 [172].

3.1.4 Radiopurity levels in Borexino

In order to measure the solar neutrinos, the radiopurity of the detector is a crucial requirement. The purity levels of Borexino are unprecedented, thanks to the careful selection of materials surrounding the scintillator and other components along with a special care taken during construction and installation of the detector components and many years of R&D efforts. In addition to this, the LS was purified in various steps in special plants installed near to the detector. The first purification was done in 2007 during the initial scintillator filling. An additional purification campaign was carried out between July 2010 and November 2011 through several cycles of ultra-pure water extraction. The main aim of the last extensive purification cycle was to reduce the levels of ^{210}Bi and ^{85}Kr. The levels of ^{210}Bi and ^{85}Kr contaminations were reduced by a factor $\sim$2.3 and $\sim$4.6, respectively [173]. The purification campaign also led to the significant reduction of ^{238}U ($< 9.4 \times 10^{-20}$ g/g at 95% C.L) and ^{232}Th ($< 5.7 \times 10^{-19}$ g/g at 95% C.L) levels [1]. This corresponds to the concentrations of $\sim$ 10 orders of magnitude lower than in any natural material on Earth. ^{14}C is the largest Borexino background, determining the low-energy threshold of the analysis, see Chapter 4. In Borexino, there is also contribution from the external backgrounds, namely ^{208}Tl, ^{214}Bi and ^{40}K, originating from the radioactivity present on the SSS, vessels' support structure, the PMTs and the light cones. Their contamination present on each component, is reported in [159]. They serve as one of the main backgrounds for CNO-ν analysis. A fiducial volume is defined to suppress their contribution. They are further dis-entangled by fitting the radial distributions (Sec. 4.4.4).

Radioactive isotopes belonging to ^{238}U decay chain such as ^{222}Rn, ^{210}Pb and ^{210}Po were also present in the detector through the independent contaminations, which are not in equilibrium with ^{238}U decay. A temporary contamination of ^{222}Rn was found in the detector, that was emanated during the water extraction period. Due to its lifetime in the order of few days, ^{222}Rn contribution is negligible. The contribution from ^{210}Pb was also out of secular equilibrium in the liquid scintillator due to its tendency to absorb on to surfaces and from the ^{222}Rn decay. Due to its low end point, ^{210}Pb is not a problem for the CNO analysis. In Borexino, there is also the ^{210}Po contamination, which is in equilibrium with the parent ^{210}Pb/^{210}Bi isotopes in the liquid scintillator

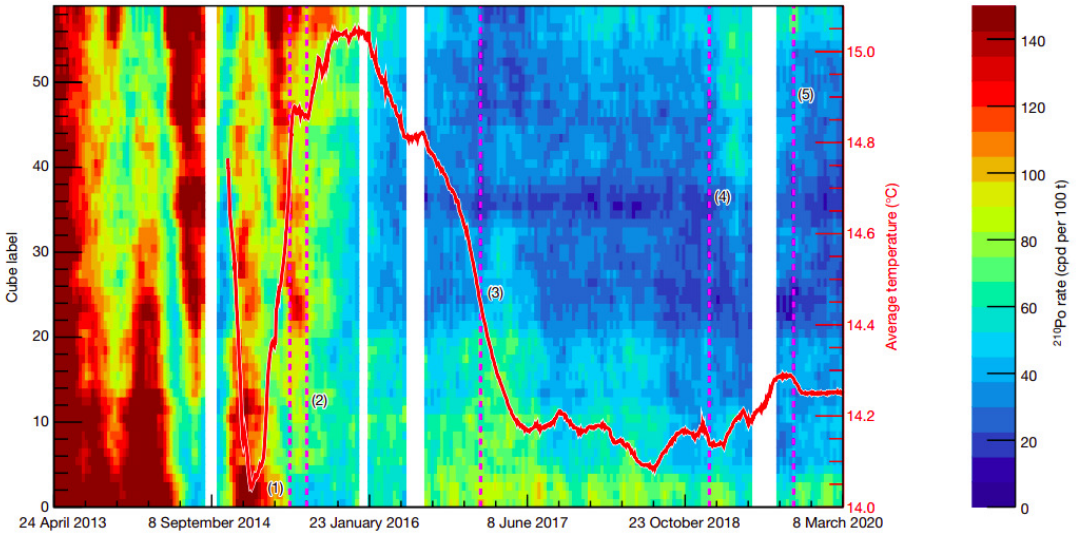

Figure 3.3: Evolution of the ^{210}Po rate in small cubes of 3 t numbered from 0 (bottom of detector) to 58 (detector top). Variations with high ^{210}Po rate can be seen until 2015. The red curve shows the average temperature in the innermost region. The dashed vertical lines show the different milestones of thermal stabilisation operation: 1. beginning of the campaign; 2. turning off of the water re-circulation system in the water tank; 3. first operation of the active temperature control system; 4. change of the active control set point; 5. installation and commissioning of the Hall C temperature control system. The white vertical bands show different DAQ interruptions due to technical issues, taken from [2].

and is referred to as *supported component*. By using pulse shape discrimination methods (Sec. 3.2.2) to tag supported ^{210}Po events, ^{210}Bi rate can be determined in the case of secular equilibrium. An additional contribution of ^{210}Po, produced from the ^{210}Pb decays on the inner surface of the nylon vessel, was brought to the inner region of the detector by convective motions in the liquid scintillator. This additional ^{210}Po is referred to as *convective component*. The convective component has posed an challenge in determining the constraint on ^{210}Bi rate (Sec. 4.4.2) as ^{210}Bi is the major background for CNO-ν analysis.

3.1.5 Thermal stabilisation of the detector

The thermal stability of Borexino detector [2] was necessary to avoid variations of the undesirable background especially ^{210}Po, caused by the convective currents that were induced by the temperature changes. The convective currents were associated to the seasonal temperature variations and the human activities affecting Hall C temperature. These convective currents brought the ^{210}Po from ^{210}Pb contamination of the vessel. To reduce the convective motions inside the detector, the establishment of vertical thermal gradient took place. The bottom of the detector is in contact with the heat sink provided by the rock with the temperature of 7.5°C, while the temperature of top part is 15.8°C. However, the instabilities of air temperature, was a hindrance in achieving the thermal gradient. The Borexino water tank was covered with 2 layers of mineral wool between May - December 2015. An active temperature control system was also installed in January 2016. In addition, a monitoring system of 66 probes with a resolution of 0.07°C was used to monitor the temperature of Borexino. As a result, the inner detector temperature was effectively stabilized. Figure 3.3 shows the ^{210}Po rate and average temperature in the innermost region of the detector as a function of time and at different locations inside the detector. It can be seen that the ^{210}Po rate was extremely high and had large fluctuations before 2016.

The thermal stabilisation of the detector led to the formation of a clean region of ^{210}Po inside the innermost part of the detector, referred to as Low Polonium Field (LPoF). However, a residual temperature variations of the order of 0.3°C over 6 months was also observed in the top part of the detector but its effect is small. An active system to control air temperature entering Hall C and around water tank was installed in 2019. It controlled the inlet air temperature within ∼0.05°C. In August 2020, the final thermal operations were performed when Hall C set point was increased above the Hall C's natural temperature in summer. These two final operations has led to extremely stable detector until the end of data taking [174]. These measures played a key role in the CNO solar neutrino spectroscopy, described in Chapter 4.

3.2 Analysis software and tools

3.2.1 Event reconstruction

Energy reconstruction

In Borexino, the PMTs mainly work in a single photoelectron regime. The energy of the event occurring in Borexino is given by the number of detected photoelectrons or just the number of hit PMTs. One MeV of deposited energy by an electron produces about 500 photoelectrons in Borexino detector, which results in the energy resolution of $5\%/\sqrt{\mathrm{E(MeV)}}$. In order to estimate the energy of an event, a number of energy estimators are provided by ECHIDNA based on each corresponding cluster of PMT hits. Energy estimators describe the visible energy of a physical event. The energy estimators typically used in the Borexino analyses [78, 159, 173] are:

- N_p - number of PMTs with at least one detected hit.
- N_h - number of PMT hits including the multiple hits on the same PMT.
- N_{pe} - number of photo-electrons (p.e) estimated as the sum of charges of all individual hits in N_h.
- N_p^{dt1} - number of PMT hits within the first 230 ns after the start time of the cluster.
- N_p^{dt2} - number of PMT hits within the first 400 ns after the start time of the cluster.

The number of working channels varies over time due to the permanently dying of PMTs. To account for this, the energy estimators are normalized to the fixed number of total PMTs (N_{tot} = 2000 PMTs) through the following equation:

$$N_x^{norm} = \frac{2000}{N_{live}} N_x^m, \tag{3.1}$$

where x = p,h, and pe. Here, N_x^m is the measured value of energy estimator and N_{live} is the time dependent number of working channels. Another energy estimator used for the analysis presented in this thesis is referred to as the geometrically normalised energy variable ($N_x^{geonorm}$). This takes into account the radial dependence of the energy estimators which means that if event deposits energy off-center, the close-by PMTs see more hits than the farther PMTs. Here, the energy variable is normalized by a value (N_{live}^{geo}) proportional to the solid angle of live PMTs with respect to the reconstructed event position. This variable considers both decreasing number of working channels and the radial dependence of events happening in the detector. Different energy estimators have been utilized in various studies. $N_{pe}^{geonorm}$ is used in obtaining the ^{210}Bi upper limit and N_h^{norm} is used in the spectral fit (see Chapter 4). $N_h^{geonorm}$ is utilized for the energy selection cut for the directional analysis in Chapter 5.

Position reconstruction

In Borexino, the position reconstruction of an event [172] is based on the maximisation of the likelihood $L_E((\vec{r}_0, t_0)|(\vec{r}^j, t_i^j))$ that the event occurs at time t_0 in the position $\vec{r}_0$, given the arrival hit time t_i^j of the PMT j placed at $\vec{r}^j$. The likelihood computation uses the reference hit time probability density function (PDF) of each hit which also depends on the total number of collected p.e in that hit. For each measured t_i^j, a position dependent time of flight (T_{flight}^j) from interaction point to PMT j is subtracted, using an effective refractive index (n_{eff}) values defining "effective" velocity of the optical photons. This parameter takes into account the fact that the photons with different wavelengths travel with different group velocities and they can be scattered or reflected from emission to detection points. The used value of n_{eff} (1.68 in data and 1.66 in MC [175]) is determined using calibration data to optimise the position reconstruction algorithm. The position resolution in Borexino is $\sim$10 cm at 1 MeV at the center of detector.

3.2.2 Pulse shape discrimination techniques

α/β discrimination

The time distribution of emitted photons after the particle's energy deposition depends on the particle type and its energy loss in the LS. This property is exploited to differentiate between α/β and e^+/e^- [173]. In Borexino, the α pulses are slower and their time distribution has longer tail with respect to the β pulses. A neural network algorithm known as Multi Layer Perceptron (MLP) technique [176, 177] was developed, which aided in the distinction of α-like and β-like events.

The MLP uses 13 input variables that are computed of each event from the pulse time distribution. These input variables include the mean and variance of hit time distribution, its skewness, the tail-to-total ratio etc [78]. The output is the so-called MLP parameter. The parameters of the algorithm have been tuned using ^{214}Bi(β^- emitter) - ^{214}Po(α emitter) coincidence sample, the daughters of ^{222}Rn which was present inside detector during water extraction phase of scintillator purification campaign. The MLP parameter value tends to be 0 for α-like event and 1 for β-like events, also shown in Fig. 3.4a. The MLP algorithm has been used various times in this work for extraction or elimination of ^{210}Po from data. The optimised cut on MLP parameter varies with the goal of different analyses such as to apply standard selection cut for the solar analysis (see Sec. 3.2.4) and to determine constraint on ^{210}Bi for spectral fit (see Sec. 4.4.2 in Chapter 4).

The performance of MLP tool is mainly given by α/β efficiency and β/α leakage. The $\alpha(\beta)$ efficiency represents the fraction of correctly identified $\alpha(\beta)$ events and is given by the ratio of residual number of events after the MLP cut application to the total number of events before MLP selection. The misidentification of $\beta(\alpha)$ events as $\alpha(\beta)$ events by MLP cut is referred to as $\beta(\alpha)$ leakage. In addition to the chosen MLP parameter for the selection, the performance of MLP selector also has a dependency on the radial distance, the energy region and the period of time in which MLP has been used [176]. My work has also been dedicated to the determination of these performance parameters for ^{210}Bi constraint analysis for the CNO-ν measurement (see Sec. 4.4.2 in Chapter 4).

β^+/β^- discrimination

In Borexino, it is also possible to distinguish β^+/β^- events based on the time distribution of detected scintillation light [173]. Their time distribution is different due to

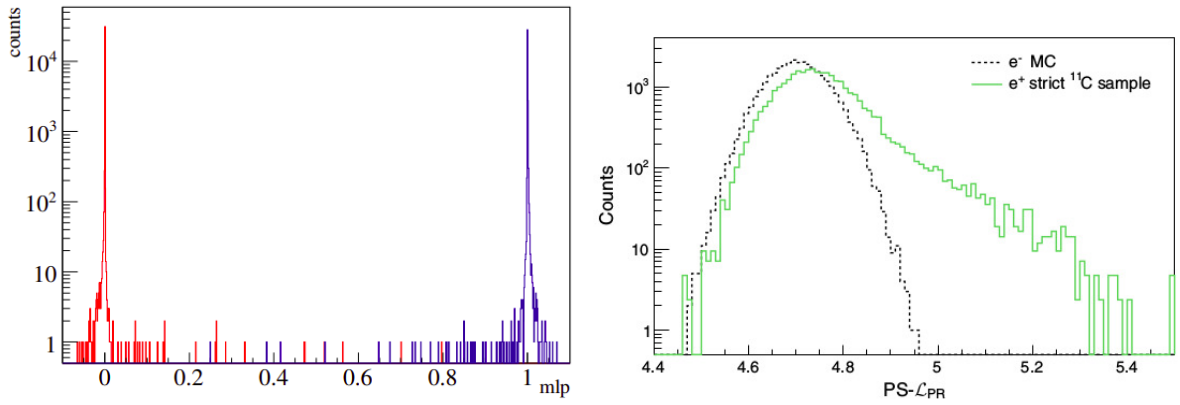

(a) (b)

Figure 3.4: (a) MLP parameter distribution for α (red) and β (blue) obtained using ^{214}Bi(β^-) - ^{214}Po(α) coincidence sample, taken from [177]. (b) The distribution of PS-$\mathcal{L}_{PR}$ estimator for Monte Carlo generated e^- events and for e^+ events selected from data using Three Fold Coincidence (TFC) technique with strict cuts. From [173].

the formation of ortho-positronium (mean life time of $\sim$ 3 ns) in β^+ events and the deposition of energy in multiple sites due to 511 KeV annihilation γs. A novel discrimination variable (PS-$\mathcal{L}_{PR}$), based on the likelihood used in the position reconstruction algorithm (Sec. 3.2.1), is introduced [173]. Since the position reconstruction algorithm uses the PDFs of β^- events, the particles having different photon time pattern can be distinguished. Figure 3.4b shows the distribution of PS-$\mathcal{L}_{PR}$ estimator for Monte Carlo generated e^- events and for e^+ events selected from data using Three Fold Coincidence (TFC) technique, described in the next section. However, the discrimination between β^+/β^- events is not performed on an event by event basis, unlike α/β discrimination, but the difference in their distributions have been used in the analysis [173].

3.2.3 Three Fold Coincidence (TFC) technique

As discussed in Chapter 1, the interaction of cosmic muon with ^{12}C in detector produces cosmogenic isotope ^{11}C, along with one or more neutrons. These daughter neutrons are thermalized and get captured by the hydrogen in scintillator with $\tau \sim$260μs with the emission of 2.2 MeV γ-rays. Due to the long mean lifetime (=29.4 min) of ^{11}C compared to the rate of muons crossing the detector ($\sim$3 min^{-1}), it is not possible to tag ^{11}C via coincidences with muons.

A so-called Three Fold Coincidence (TFC) technique [170] has been developed to identify ^{11}C candidates by using their space-time correlation with the parent muon and muon-induced neutrons. TFC is used to create two subsets of data: TFC-tagged data which is enriched in ^{11}C events containing $\sim$90% ^{11}C events and $\sim$40% of exposure and the other is TFC-subtracted, which is depleted in ^{11}C events with complementary exposure and ^{11}C events. The two subsets are shown in Fig. 3.5b. This algorithm has been thoroughly used in this work as ^{11}C is the main background for the analysis of the *pep* and CNO solar neutrinos.

There are two implementations of the TFC technique: the hard cut (HC) approach usually called TFC Milano (TFC MI) and the likelihood approach also referred to as TFC Mainz (TFC MZ). The HC approach makes a binary decision whether an event should be regarded as ^{11}C event or not. After finding the coincidences of muon and subsequent neutrons within a time window of 1.6 ms after the muon, this algorithm defines geometrical veto regions. These regions include a cylinder of radius 0.7 m

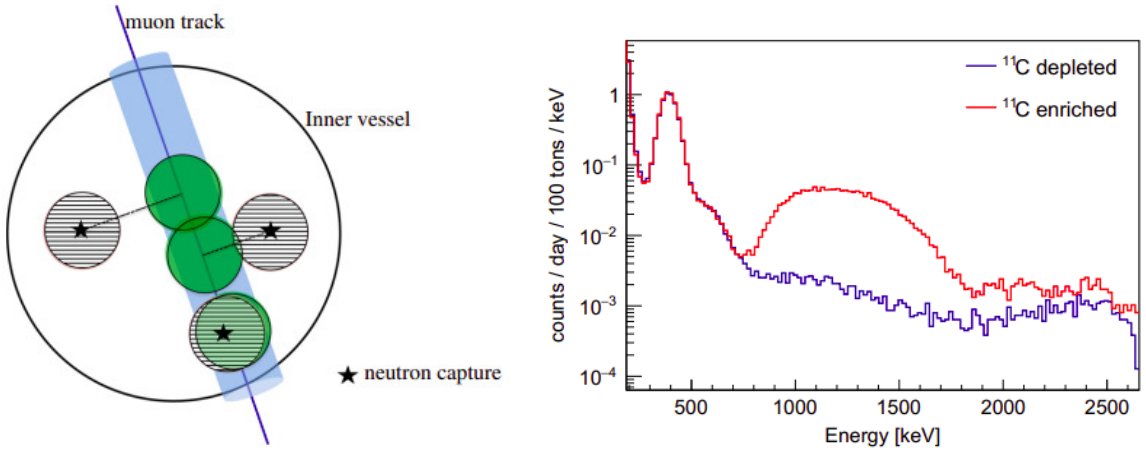

Figure 3.5: (a) The geometrical veto regions of TFC: cylindrical region around the muon track (blue), the spherical regions around neutron caption position (shaded), and the projected spheres on the muon track (green). (b) The energy spectra of Phase-II data splitted after TFC application: TFC-tagged (in red) and TFC-subtracted (in blue), where both spectra are normalized to the same exposure. From [170].

around the reconstructed muon track, a spherical region of radius 1.2 m around the reconstructed position of neutron capture and a spherical region of radius 1.2 m around the point on muon track, which is closest to the neutron capture position. This is illustrated in Fig. 3.5a.

Likelihood approach [170,173] assigns each event a non-binary likelihood to be a ^{11}C event. The likelihood calculation is based on several parameters such as the distance in space and time from the parent muon and neutrons (same as of HC approach), the neutron multiplicity and the differential energy loss dE/dx of parent muon. Another novel method to improve the identification of ^{11}C events is developed. The so called ^{11}C burst tagging technique [170] exploits the fact that most of the ^{11}C is also created by secondary processes occurring in the muon induced hadronic showers in addition to the primary muon spallation process. This technique can be combined with the TFC and improves the surviving exposure by $\sim$5%.

3.2.4 Standard selection cuts for solar neutrino analysis

The data selection cuts listed here are used for the standard solar neutrino analysis in Borexino [1, 159, 173] to filter out all the possible neutrino candidates. These so called *nusol cuts* are also applied for the work presented in this part of the thesis in Chapters 4 and 5. The cuts, listed below, are used to remove the muons and reduce the cosmogenic backgrounds as well as to suppress the radioactive backgrounds coincidences and the non-physical events:

- *Muon and muon daughter cut* - This cut removes the muon events and the products of muon spallation in LS. The muon rejection is achieved by combining Cherenkov veto in OD with the pulse shape analysis of scintillator signals [1]. The detector is vetoed for 300 ms, after a muon crossing ID is identified, as they saturate the electronics. This time veto also suppress cosmogenic neutrons and other spallation products, with an exception of ^{11}C. For the external muons, a veto of 2 ms deadtime is applied to eliminate the fast neutrons, that can penetrate through SSS from OD to ID.
- *Trigger cut* - Only main physics events (TT1 & BTB0) are selected.

- *Cluster cut* - The physical events with only one cluster in DAQ window of 16.5 μs or the first cluster of 2 cluster events are selected.
- ^{214}Bi - ^{214}Po *cut* - The coincidences of ^{214}Bi - ^{214}Po from ^{222}Rn, emanated during the water extraction period, are removed.
- *Fiducial volume cut* - The events, that are close to IV, are removed to suppress external backgrounds. The fiducial volume (FV) cut conditions varied with the analysis as will be described in later chapters.
- *Start time cut* - The events with cluster having a start time out of the DAQ gate or too late from gate start are removed.
- *Reconstructed charge cut* - Events with the mismatched reconstructed charge and the number of fired PMTs are removed.
- *Noise cuts* - The events with $N_h^{norm}/N_p^{norm} > 1.1$ are removed as the noise events.
- *MLP noise cut* - The events with $N_h^{norm} >= 350$ and MLP value < 0 [178] represent the nonphysical events and are removed for the analysis presented in this thesis.

Some selection conditions like energy region of interest and particle discrimination cuts vary depending on the analysis as will be mentioned later. The TFC cut can also be applied depending on the analysis, *e.g*. TFC-tagged events are vetoed for the directional analysis, presented in Chapter 5, while the events in data are not vetoed but splitted for the spectral fit described in Chapter 4.

3.2.5 Monte Carlo simulation

The Monte Carlo (MC) simulation package [175] of the Borexino detector is based on GEANT4 software. It not only simulates the geometrical design of the detector, but also the physics processes happening in the detector after the interaction of the particle in the detector. The code is technically structured into the following stages, chained together:

Event Generation and Light Tracking

A GEANT4 platform based simulation code called *g4bx2*, manages the feature of the event generation, energy deposition and tracking of optical photons until their detection by PMTs. It consists of an accurate description of all detector elements and of physical properties of the solid as well as liquid components and light sensors. A variety of generators were developed to simulate the solar neutrino and anti-neutrino interactions, the radioactive decays inside the scintillator and the radioactive sources used in the calibration campaign. The energy loss of the generated particle inside LS and detector components and the generation of the optical photons (both scintillation and Cherenkov light) are considered. In addition, the photon interaction in LS including absorption, re-emission, scattering and their tracking until they are detected by PMTs or absorbed are also taken into account by the simulation. The PMT response for photons absorbed by the PMT cathode is considered with their own effective quantum efficiencies.

Simulation of electronics response

The electronic simulation code *bxelec*, produces the simulation of electronics chain of Borexino including its trigger response using the PMT pulse time information and the

response of analog and digital electronics. It follows the real-time evolution of electronics on an event-by-event basis in the Borexino detector such as the intrinsic loss of PMTs or disabling of some data acquisition boards. The *bxelec* reproduces the time structure of collected real data and the real trigger system is also simulated. For each simulated event, not only the electronic response information of all hits is saved but also the information regarding true input parameters are stored in a data format, used also for real data.

Event reconstruction

At this stage of the MC simulation, the simulated data is processed using the same code ECHIDNA, that is also used to analyse the real data. The energy reconstruction into energy estimators is performed as explained in Sec. 3.2.1. The position of simulated events is also reconstructed in the same way summarized in Sec. 3.2.1.

The tuning of MC took place using a part of calibration data obtained during calibration campaign (see Sec. 3.1.3). The input parameters of MC simulation describing the scintillator properties and detector materials such as attenuation lengths, the reflectivity, re-emission probabilities and the refractive indices were determined. This is particularly important for the spectral analyses of solar neutrinos using the MC probability density functions (PDFs) (see next Chapter). The directional analysis (Chapter 4) also heavily relies on the MC simulation. The validation of MC tuning is performed using an independent set of calibration data or using the standard candles (^{210}Po or neutrons) from data taking. The precision level of disagreement in the data and MC contributes as systematic uncertainties. The procedure of MC PDFs production is specifically dependent on the type of analyses and will be explained in the respective chapters.

Chapter 4

Solar neutrino spectroscopy with Borexino

This chapter describes in detail the spectroscopic analysis of solar neutrinos with the Borexino experiment. The general strategy for this analysis is covered in Sec. 4.1. The two sections, Sec. 4.2 and Sec. 4.3 summarize the previous results from the two fusion mechanisms in the Sun: the comprehensive study of the *pp*-chain solar neutrinos [1] and the first evidence of solar neutrinos from the CNO cycle [2], respectively. The analysis reported in Sec. 4.2, exploits the Phase-II data to measure the interaction rate of *pp*, ^{7}Be, and *pep* solar neutrinos and to provide an upper limit on the CNO solar neutrinos. Furthermore, this analysis uses Phase-I+II data for the ^{8}B-ν studies. The discovery of CNO solar neutrinos was done using the Phase-III data, collected between July 2016 and February 2020, to which I contributed during my master thesis [179]. The data taking of the experiment continued at the same time.

Section 4.4 is devoted to the updated measurement of CNO solar neutrino flux in the Phase-III data collected from 2017 until the end of data taking of Borexino in 2021 [3]. The CNO-ν analysis uses the *pep*-ν constraint (Sec. 4.4.1) and an updated upper limit on ^{210}Bi interaction rate (Sec. 4.4.2), due to the CNO spectral degeneracy with *pep*-ν and ^{210}Bi. I have contributed to this recent analysis of CNO solar neutrinos and my contributions include: the parameters estimation in the model which is used to extract the ^{210}Bi constraint, the production of real and simulated data distributions (Sec. 4.4.3) as well as performing the spectral fit (Sec. 4.4.4) using these distributions as the inputs. The fit results and the systematic budget in this analysis is discussed in Sec. 4.4.5 and Sec. 4.4.6, respectively. Section 4.4.7 is dedicated to the methods and results of the implications on solar physics using the new updated measurement of CNO solar neutrino flux and provides insights to solar metallicity problem (Chapter 1). This chapter is then summarized in Sec. 4.5.

4.1 General strategy for solar neutrino spectroscopy

As discussed in previous Chapters, the solar neutrinos are detected via the elastic scattering of electrons in the Borexino experiment. Due to the presence of dominant scintillation light, the electrons scattered off by solar neutrinos can not be distinguished from the β or γ background components on an event-by-event basis. Therefore, the first step to perform the spectroscopic analysis of the solar neutrino is to apply selection cuts on the data to maximize the signal to background ratio in the selected period of Borexino's data taking. In addition to the standard cuts described in Sec 3.2.4, a fiducial volume (FV) with radius R< 2.8 m and -1.8 m < z < 2.2 m is generally applied to suppress the external background events. This FV will be referred to as *pepFV* and has a mass of 71.3 t.

For the analysis, the energy (TFC-tagged and TFC-subtracted) and radial distributions of data events are generally produced. The energy PDFs using the MC simulated events of each neutrino and background component are also obtained. For the radial part, the PDFs of uniform (β like events) and non-uniform components (external background events) are obtained in order to disentangle the external backgrounds from

data. Then, the distributions of data events are fitted with the MC PDFs. A multivariate likelihood based spectral fit technique, is performed using *bx-Goostats* machinery [180]. The constraints on the interaction rates of *pep*-ν and ^{210}Bi are used in the CNO-ν analysis, which are determined independently. More details of the fit is described in Sec. 4.4.4

The rate of each component as well as the log-likelihood profile of the species of interest with the statistical uncertainty is obtained from the fit. The possible sources of systematic uncertainties related to the fitting strategy and modelling of detector response and backgrounds, are also investigated. After folding likelihood profile with the systematic uncertainties, the final results on the solar-ν of interest are obtained. The final rates of the solar-ν are then converted to its total flux and its physics implications are investigated.

4.2 *pp*-chain measurement

This section summarizes the comprehensive study of *pp*-chain provided by Borexino experiment in 2019 [1]. Borexino measured simultaneously the interaction rates of *pp*, ^{7}Be, and *pep* solar neutrinos and provided an upper limit on the CNO solar neutrinos in a so-called low energy region (LER) corresponding to 0.19-2.93 MeV, using the Phase-II data extending between December 2011 and May 2016. The pepFV is chosen for the analysis in LER to maximally suppress external γ's backgrounds from ^{40}K, ^{214}Bi and ^{208}Tl. This results in a total exposure of 1,291.51 days $\times$ 71.3 t. After performing the standard selection cuts to reduce the rate of background events, the spectral fit is performed using MC PDFs. The fit is also performed using the so-called analytical PDFs that describe the detector's energy response using analytically derived functions [173]. The measurement of *pep* solar neutrino is complicated due to a strong correlation with CNO neutrinos. So, a constraint on the CNO-ν rate based on both SSM B16-AGSS09met and SSM B16-GS98 predictions [137], is used. Therefore, two different measurements on CNO solar neutrinos are obtained by repeating the analysis for SSM B16-AGSS09met and SSM B16-GS98 predictions on CNO rate. In addition, the presence of ^{11}C background also affects the measurement of *pep* neutrinos. Therefore, 2 energy spectra of the data, TFC-tagged and TFC-subtracted, are fitted with MC PDFs, as discussed in Chapter 3. To obtain upper limit on CNO solar neutrinos , an indirect constraint on *pep*-ν, exploiting the theoretically well known *pp* and *pep* flux ratio, is applied. Various possible sources of systematics effects such as the inaccuracies in the modelling of detector response, the choice of energy estimator, the fit range and binning, the pile-up modelling, the differences in the final results due to usage of analytical or MC PDFs, etc were also studied and included in the final results.

In the high energy region (HER) corresponding to 3.2-16 MeV, the ^{8}B solar neutrino interaction rate measurement was performed using the data collected between January 2008 and December 2016. This energy region is further divided into two subregions, 3.2-5.7 MeV (HER-I) and 5.7-16 MeV (HER-II). The HER-I analysis considers the fiducial volume with cut z<2.5 m and no radial cut. This cut aims to suppress the background events associated to leaking of LS into buffer region due to a small hole in the IV. The analysis in HER-II uses the entire scintillator volume. This results in the exposure of 2062.4 days $\times$ 227.8 (226.0) t for HER-I (HER-II) analysis. In addition to the fiducial volume cut, some of the data selection criteria that differs from LER but conceptually similar, are also applied in the HER. For instance, it involves the reduction of cosmogenic backgrounds with a larger time window following the internal muons. The details of residual backgrounds can be found in Ref. [1]. Here, the fit of radial distribution of events only is performed to extract the ^{8}B neutrinos. This is done to avoid any assumption on the survival probability shape in the transition region (see

Solar -ν	Rate (cpd/100 t)	Flux ($cm^{-2}s^{-1}$)	Flux-SSM predictions ($cm^{-2}s^{-1}$)
pp	$134 \pm 10^{+6}_{-10}$	$(6.1\pm 0.5^{+0.3}_{-0.5})\times10^{10}$	$5.98(1\pm0.006)\times10^{10}$ (HZ) $6.03(1\pm0.005)\times10^{10}$ (LZ)
^{7}Be	$48.3 \pm 1.1^{+0.4}_{-0.7}$	$(4.99\pm 0.11^{+0.06}_{-0.08})\times10^{9}$	$4.93(1\pm0.06)\times10^{9}$ (HZ) $4.50(1\pm0.06)\times10^{9}$ (LZ)
pep(HZ)	$2.43 \pm 0.36^{+0.15}_{-0.22}$	$(1.27\pm 0.19^{+0.08}_{-0.12})\times10^{8}$	$1.44(1\pm0.01)\times10^{8}$ (HZ) $1.46(1\pm0.009)\times10^{8}$ (LZ)
pep(LZ)	$2.65 \pm 0.36^{+0.15}_{-0.24}$	$(1.39\pm 0.19^{+0.08}_{-0.13})\times10^{8}$	$1.44(1\pm0.01)\times10^{8}$ (HZ) $1.46(1\pm0.009)\times10^{8}$ (LZ)
$^{8}B_{HER\text{-}I}$	$0.136^{+0.013+0.003}_{-0.013-0.003}$	$(5.77^{+0.56+0.15}_{-0.56-0.15})\times10^{6}$	$5.46(1\pm0.12)\times10^{6}$ (HZ) $4.50(1\pm0.12)\times10^{6}$ (LZ)
$^{8}B_{HER\text{-}II}$	$0.087^{+0.080+0.005}_{-0.013-0.005}$	$(5.56^{+0.52+0.33}_{-0.64-0.33})\times10^{6}$	$5.46(1\pm0.12)\times10^{6}$ (HZ) $4.50(1\pm0.12)\times10^{6}$ (LZ)
$^{8}B_{HER}$	$0.223^{+0.015+0.006}_{-0.016-0.006}$	$(5.68^{+0.39+0.03}_{-0.41-0.03})\times10^{6}$	$5.46(1\pm0.12)\times10^{6}$ (HZ) $4.50(1\pm0.12)\times10^{6}$ (LZ)
CNO	<8.1 (95% C.L.)	$<7.9\times10^{8}$ (95% C.L.)	$4.88(1\pm0.11)\times10^{8}$ (HZ) $3.51(1\pm0.10)\times10^{8}$ (LZ)
hep	<0.002 (90% C.L.)	$<2.2\times10^{5}$ (90% C.L.)	$7.98(1\pm0.30)\times10^{3}$ (HZ) $8.25(1\pm0.12)\times10^{3}$ (LZ)

Table 4.1: The results on measured rate of solar neutrinos using Phase-II (Phase-I and Phase-II) data in Low Energy Region, LER (High Energy Region, HER) as reported in [1,173]. The two measurements on *pep* solar neutrinos arises from using the constraint on CNO rate based on SSM B16-AGSS09met (LZ) and SSM B16-GS98 predictions (HZ). The last column reports the flux predictions from the SSM B16-GS98 as HZ and the SSM B16-AGSS09met as LZ [137].

Sec. 1.3) relevant for the energy shape of ^{8}B solar neutrinos. Moreover, a search for *hep* neutrinos was also performed in the energy region 11-20 MeV and an upper limit on its flux was obtained. The results on the interaction rates of solar neutrinos in both the LER and HER analysis are reported in Table 4.1.

These measurements were used to test the MSW-LMA paradigm assuming SSM predictions by inferring the electron neutrino survival probabilities, shown in Fig. 4.1a. The likelihood ratio tests of the neutrino flavour conversion both in the vacuum and

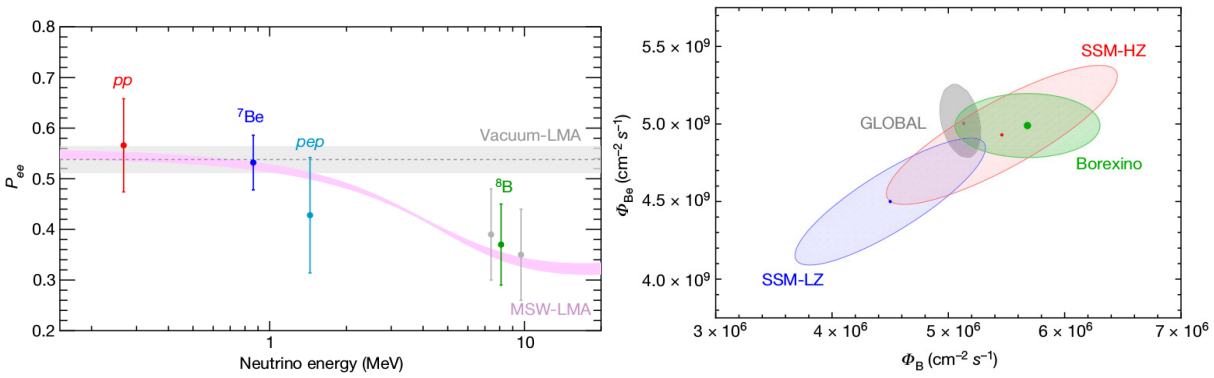

(a) (b)

Figure 4.1: (a) The electron neutrino survival probability (P_{ee}) as a function of neutrino energy. The pink and grey band show the 1σ predictions from the MSW-LMA and vaccum-LMA, respectively. (b) The allowed contours of ^{7}Be and ^{8}B fluxes for the SSM B16-GS98 predictions as SSM-HZ (red) and SSM B16-AGSS09met predictions as SSM-LZ (blue) [137], together with the Borexino results (green) and global analysis result from all solar and KamLAND data (grey) are shown. From [1].

in the matter-dominated regime were performed. These measurements were in excellent agreement with the MSW-LMA paradigm expectations and disfavour the vacuum-LMA hypothesis at 98.2% C.L. Moreover, the test of the SSM B16-AGSS09met and SSM B16-GS98 predictions were performed. The Borexino measurement on solar neutrinos fluxes provided a hint in the favour of the SSM B16-GS98 predictions as can be seen in Fig. 4.1b. A frequentist hypothesis test based on a likelihood-ratio test statistics (SSM B16-GS98 vs SSM B16-AGSS09met) was used and the data disfavour SSM B16-AGSS09met predictions at 96.6% C.L assuming SSM B16-GS98 predictions to be true. A Bayesian hypothesis test also resulted in the mild preference for SSM B16-GS98 predictions [1].

4.3 First evidence of CNO solar neutrinos

In 2020, Borexino reported the first direct observation of neutrinos from the CNO fusion cycle in the Sun [2]. The data collected between July 2016 and February 2020, corresponding to 1072 days of live time, was used. The energy region chosen for this analysis corresponds to 320 - 2640 keV (136 - 954 N_h^{norm}) and the pepFV cut is applied. The low energy region below 136 N_h^{norm} is excluded as it is strongly affected by decreased number of active channels in Phase-III (average value = 1238 channels), leading to the loss in energy and position resolutions at low energies. In this energy region, the contribution of *pp* solar neutrinos, ^{14}C and its pileup events are negligible. The standard selection cuts, listed in 3.2.4, are also applied on the data.

Its low counting rate (in the order of few cpd/100 t), the energy span of several residual backgrounds such as external backgrounds, cosmogenic ^{11}C, and ^{210}Bi overlapping with the energy region of CNO neutrinos, its featureless energy distribution of its recoiled electrons and its spectral shape degeneracy with the *pep* solar neutrinos and the ^{210}Bi background pose obstacles in disentangling the CNO signal from the data. Here, the multivariate fit is performed to extract the CNO rate, which is the same technique as discussed in the previous section of LER analysis for *pp* chain spectroscopy. The interaction rate of *pep* neutrinos is constrained with 1.4% precision (Sec. 4.4.1) to break the degeneracy between *pep* and CNO solar neutrinos. The *pep* neutrino rate constraint was applied using a symmetric Gaussian penalty term in the likelihood fit. In addition, a constraint on the ^{210}Bi rate [174] was also determined using an independent analysis on the daughter ^{210}Po distribution since their rates are

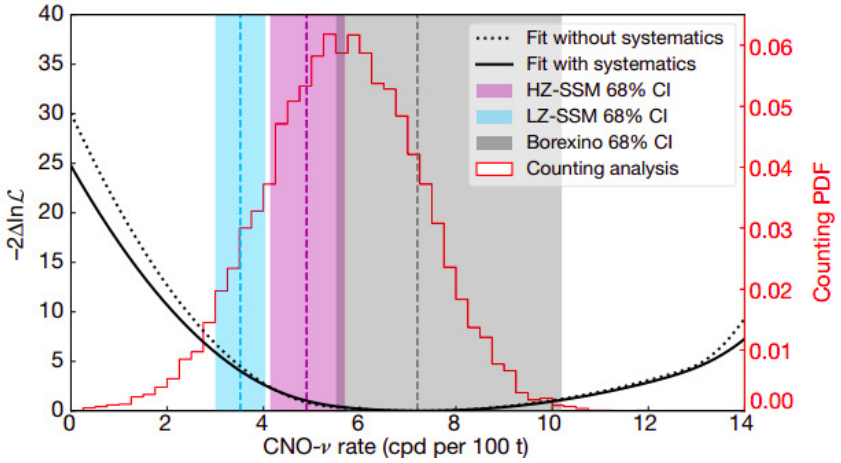

Figure 4.2: Negative log-likelihood profile of the CNO neutrino interaction rate from multivariate fit on the dataset collected between July 2016 and February 2020, is shown in black solid lines, after folding with the systematic uncertainties. The blue, violet, and grey band represents 68% C.L for the SSM B16-GS98 predictions as HZ-SSM, SSM B16-AGSS09met predictions as LZ-SSM [137] and the Borexino measurement on CNO rate, respectively. The red distribution is the probability density function obtained from a counting analysis. From [2].

equal in case of a secular equilibrium. The α decaying ^{210}Po events were selected by applying MLP discrimination technique and the minimum ^{210}Po rate in LPoF, which is almost free from the contribution of convective ^{210}Po (Sec. 3.1.4). Since it can not be guaranteed that the contribution of convective ^{210}Po is actually zero, an upper limit on ^{210}Bi rate ($\leq 11.5 \pm 1.0$ cpd/100 t) was imposed by using a half Gaussian term in the likelihood. More details on the determination of upper limit on ^{210}Bi rate will be discussed in Sec. 4.4.2.

Using the profile likelihood shown in Fig. 4.2, the final CNO interaction rate was obtained to be $7.2^{+3.0}_{-1.7}$ cpd/100 t and the corresponding CNO neutrino flux on Earth is $7.0^{+3.0}_{-2.0} \times 10^8$ cm^{-2}s^{-1}, including both statistical and systematic errors. Various systematic effects such as the binning values and the fitting range, the choice of theoretical ^{210}Bi shape, non-uniformity and non-linearity of detector response and the variation in absolute magnitude of light yield were included by performing several millions of Monte Carlo pseudo-experiments. By performing hypothesis test based on a profile likelihood test statistics, no-CNO signal hypothesis was rejected with a significance greater than 5.0σ at 99.0% C.L. Additionally, a counting analysis in a narrow energy region between 780 keV and 855 keV was performed, which resulted in the 3.5σ significance of presence of CNO neutrino events. After combining the CNO flux with other solar neutrino fluxes, the low-metallicity (SSM B16-AGSS09met) hypothesis is disfavoured with a significance of 2.1σ. An improved measurement of CNO solar neutrino by including most recent data and the more robust implications on solar physics will be discussed in next section.

4.4 Updated CNO measurement

This section is devoted to the improved measurement of CNO solar neutrinos using *Phase-III final* dataset, composing of data collected between January 2017 and October 2021. With respect to the dataset used in Sec. 4.3, an additional dataset from March 2020 to October 2021 is used. Furthermore, the dataset of six months in 2016 is excluded due to a relative high amount of decaying convective ^{210}Po during this

period [181], just following the thermal insulation campaign. The live-time of *Phase-III final* dataset amounts to 1453.51 days. The energy region corresponds to 320 - 2640 keV (136 - 954 N_h^{norm}), which is same as the energy range used in the CNO analysis described in Sec. 4.3.

4.4.1 *pep*-ν constraint

To break the spectral degeneracy of CNO-ν and *pep*-ν, a constraint on *pep*-ν rate is applied. The *pep* solar neutrino rate is determined using the solar luminosity constraint, the theoretical *pp/pep* flux ratio, the global analysis of all solar data and considering MSW effect on the neutrino propagation and the errors on the most recent oscillation parameters. The ratio of *pp* and *pep* neutrino fluxes is determined from nuclear physics as the processes producing *pp* and *pep* neutrinos have same nuclear matrix element. Imposing the luminosity constraint [182] and using the global fit on all independent experimental solar data [183], the precision level of *pep* neutrino rate is $\sim$1%. Taking into account the additional uncertainties due to oscillation parameters [184] and neutrino propagation in matter, the *pep* neutrino rate is obtained at 1.4% precision level [185]. The final value of *pep*-ν constraint is (2.74 ± 0.04) cpd/100 t.

4.4.2 ^{210}Bi constraint

To break the spectral degeneracy of CNO-ν and ^{210}Bi background, a constraint on ^{210}Bi rate is obtained, through the measurement of minimum ^{210}Po rate in the low polonium field (LPoF). The low polonium field (LPoF) is a region where ^{210}Po rate is the lowest with a little contribution from its convective component (Sec. 3.1.4 and 3.1.5). Ideally, if the convective component of ^{210}Po is not present in LPoF, one could provide the measurement on ^{210}Bi rate through the measurement of minimum ^{210}Po rate in LPoF.

Data selection and fit equation: The data, with MLP < 0.3 and $150 < N_{pe}^{\delta geonorm} < 270$, is selected to have a maximal ^{210}Po contribution. The final fit region has a mass of about 20 t. The data selection criteria is based on a figure of merit method. To determine the minimum rate of ^{210}Po ($R(^{210}Po_{min})$) in LPoF, a paraboloid equation in 2D assuming the rotational symmetry along x-y plane, is used to fit the selected data:

$$f(\theta) = (R(^{210}Po_{min})\epsilon_\alpha\epsilon_E) \cdot [1 + \frac{\rho^2}{a^2} + \frac{(z - z_0)^2}{b^2}] + \beta_{leak}, \tag{4.1}$$

where β_{leak} is the rate of leaked β events due to MLP selection, ϵ_α and ϵ_E are the α-efficiency of MLP < 0.3 selection and the energy efficiency, respectively, a and b are the shape parameters along the paraboloidal axes, z_0 is the vertical position of minimum and $\rho^2 = x^2 + y^2$. The assumption of rotational symmetry in the x-y plane in the 2D paraboloid fit has been checked by performing 3D ellipsoid fit [174]. The parameter ϵ_α is estimated using a pure MC sample of ^{210}Po events by selecting the events in an energy range of $150 < N_{pe}^{\delta geonorm} < 270$. It is estimated to be 96.5%. The parameter β_{leak} represents the β leakage rate due to MLP < 0.3 selection (see Sec. 3.2.2).

β leakage determination: To determine the value of β_{leak}, a fit based approach using 2 different types of modelling are adopted:

- **Method 1: Gaussian and exponential fit**: Here, the ^{210}Po data, obtained using the MLP cut, is fitted using the ROOT based likelihood method. Here, a combined Gaussian and exponential function is used as a simplified model:

$$y = N_1 \cdot e^{k_1 x} + N_2 \cdot e^{\frac{-(x-\mu)^2}{2\sigma^2}}, \tag{4.2}$$

where fit parameters: N_1, N_2, k_1, μ, and σ are free to vary. Here, an exponential function models the fact that MLP efficiency has exponential energy dependence, as found by the calibration studies [186, 187]. The Gaussian function models the spectral shape of α events. Figure 4.3a shows the best fit result in the energy range of $140 < \mathrm{N}_{pe}^{geonorm} < 295$. By integrating $N_1 \cdot e^{k_1 x}$ in $150 < \mathrm{N}_{pe}^{geonorm} < 270$ and taking into account the exposure, the β_{leak} is calculated. Here, the systematic uncertainty is evaluated by varying fit energy range. The range of lower bound is (140-150) $\mathrm{N}_{pe}^{geonorm}$ due to presence of pileup at < 140 $\mathrm{N}_{pe}^{geonorm}$. Moreover, the range of upper bound is (270-300) $\mathrm{N}_{pe}^{geonorm}$ due to the fact that the MLP efficiency model are only tested to be consistent with a single exponential within 300 $\mathrm{N}_{pe}^{geonorm}$.

- **Method 2: Fit using Borexino's analytical PDFs**: In this approach, the ^{210}Po data is fitted with the analytical PDFs (described in [173]) in $\mathrm{N}_{pe}^{geonorm}$ variable using the bx-Goostats framework [180]. The motivation to perform fit using analytical PDFs is that since Borexino MC is tuned with N_h as an energy observable and the N_{pe} energy estimator is used for the ^{210}Bi constraint analysis, the analytical PDFs which were developed in N_{pe} [159] is used here. The combined fit model can be represented as follows:

$$y = N_3 \cdot \mathrm{AnaBeta}(x) \cdot e^{kx} + N_4 \cdot \mathrm{AnaAlpha}(x), \tag{4.3}$$

where fit parameters: N_3, N_4 are free to vary and k is fixed to a value based on a likelihood scan. AnaAlpha(x) is analytically derived ^{210}Po PDF in $\mathrm{N}_{pe}^{geonorm}$ variable. AnaBeta(x) is analytically derived PDF of β events obtained by summing PDFs of species lying in the ^{210}Po region using weights according to the SSM predicted solar neutrino rates or the independently determined rates of backgrounds. The term e^{kx} takes into account the exponential dependence of the MLP efficiency for β events. Figure 4.3b shows the fit result in the energy range of $150 < \mathrm{N}_{pe}^{geonorm} < 280$. The choice of energy range and k contributes to the systematic uncertainty . Hence, the systematic error is evaluated by varying energy range as in previous method, while a negative log-likelihood (or $\Delta\chi^2$) scan as shown in Fig. 4.3c, is performed to evaluate systematic error due to fixed k. Figure 4.3d shows the variation of β_{leak} as a function of k and the values of k within $\Delta\chi^2 = 1$ contributes to the systematic error on β_{leak}. Finally, using this approach, β_{leak} is estimated by counting number of β events in $150 < \mathrm{N}_{pe}^{geonorm} < 270$ and taking into account the exposure.

Table 4.2 summarizes the results from both the methods along with different sources of uncertainties. It can been be seen that the results on β_{leak} are in agreement with each other within the errors. Taking the average of the two methods and adding all errors, the final result on β_{leak} = (2.9 ± 0.3 (stat. + syst.)) cpd/100 t. This was used in eq. 4.1 to extract the minimum ^{210}Po rate in the LPoF [174]. The result on β_{leak} = (2.8 ± 0.2 (stat. + syst.)) cpd/100 t, obtained by X. Ding independently using a method based on a multivariate complementary fits in energy range $150 < \mathrm{N}_{pe}^{geonorm} < 1500$ with and without the MLP cut [187, 188] is in agreement within uncertainties.

Fit strategy and result: As LPoF slowly moves along the z-axis ($\lesssim$ 20 cm per month), particularly before 2020 due to the residual convective motions, the data in LPoF is aligned along z-direction every month using their centers z_0, which is extracted by

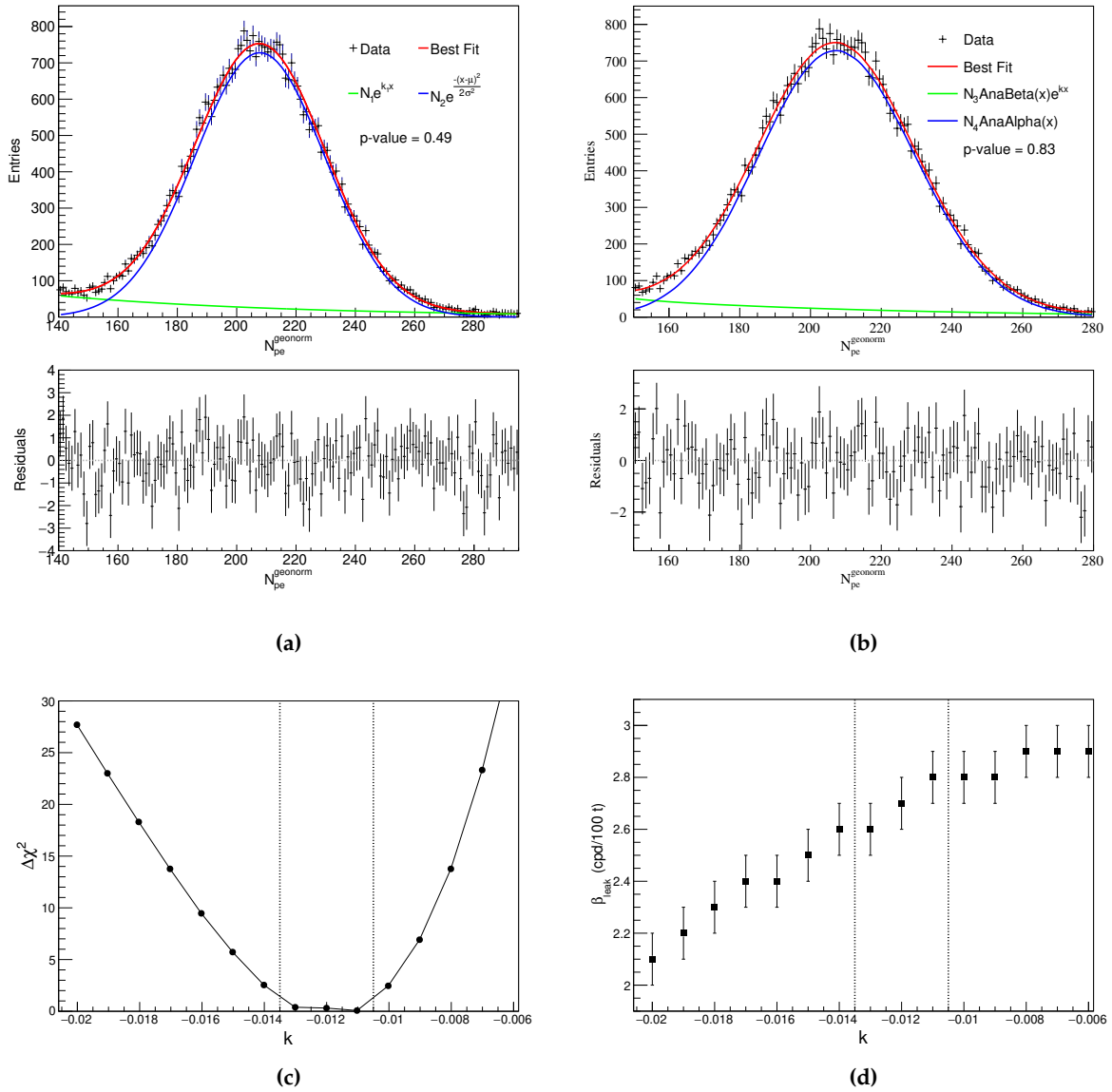

Figure 4.3: Extraction of β_{leak}: (a) **Method 1**: The fit of ^{210}Po data in Phase-III final period and selected with MLP < 0.3 (black points) using method 1 is shown. The energy range of the fit corresponds to $140 < N_{pe}^{geonorm} < 295$. Also, the best fit function (red curve) is shown. The best fit function consists of an exponential function (green curve) and Gaussian function (blue curve). The p-value = 0.49, which is extracted from the fit. **Method 2**: (b) The fit result with p-value = 0.83 in the energy range of $150 < N_{pe}^{geonorm} < 280$ using method 2 is shown. The fit is performed using ^{210}Po data, from Phase-III final period and selected with MLP < 0.3 (black points), with the best fit function (red curve). The best fit function consist of an analytical model of Borexino's energy response function: ^{210}Po PDF (blue curve) and β PDF with exponential damping due to energy dependence of MLP efficiency (green curve). (c) $\Delta\chi^2$ profile from the fit as a function of slope k of the exponential term in method 2. (d) The corresponding extracted β_{leak} values as a function of slope k of exponential term in method 2. The vertical lines in (c) and (d) represents the interval within $\Delta\chi^2 = 1$, used to evaluate the systematic error on β_{leak} for method 2.

fitting previous month data in larger volumes of about 70 t. The fit is performed using paraboloid equation 4.1 through ROOT likelihood approach or a paraboloid + spline function through Bayesian MultiNest algorithm [174, 181]. The cubic spline function, the piece-wise polynomials, take into account the shape complexity along z-axis compared to a simple paraboloidal shape. Figure 4.4 shows the LPoF centers z_0 from paraboloid fits with (white) and without (red) a cubic spline along the z axis on monthly data. One can see the stability of LPoF centres after 2020 and also, the

Method	β_{leak}	σ_{stat}	$\sigma_{low-bound}$	$\sigma_{up-bound}$	$\sigma_{exp-slope}$	Final β_{leak}
Method 1	2.9	± 0.1	$^{+0.0}_{-0.2}$	$^{+0.3}_{-0.2}$	-	2.9 ± 0.3
Method 2	2.8	± 0.1	$^{+0.0}_{-0.1}$	$^{+0.0}_{-0.0}$	$^{+0.0}_{-0.2}$	$2.8\ ^{+0.1}_{-0.2}$

Table 4.2: The final result on β_{leak} obtained from method 1 and 2 separately including all different sources of uncertainty.

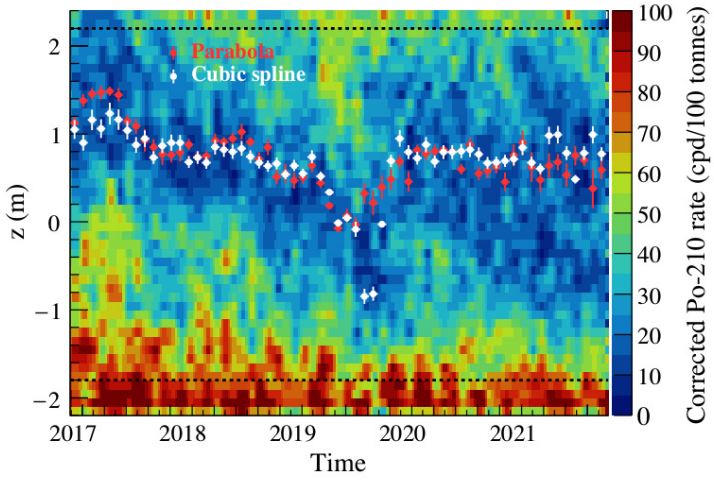

Figure 4.4: ^{210}Po rate in the detector as a function of time in the Phase-III final period, in cylindrical z-slices of 0.1 m height and radius $\rho^2 = (x^2 + y^2) < 2\,\mathrm{m}^2$. The black dashed horizontal lines represent the z-cut of fiducial volume used in the analysis. In addition, the LPoF centers z_0 from monthly paraboloid fits with (white) and without (red) a cubic spline along the z axis are also displayed. From [3].

LPoF area in the blue region has also enlarged. Then, the final fit is performed on the whole aligned data in around 20-25 t using the same approach and depending on the fit method.

After incorporating various systematic sources in the final fit, such as choice of the fit parameters, the beta-leakage, and averaging results from different fit models, the ^{210}Po rate in LPoF is determined to be 10.8 ± 1.0 cpd/100 t. Since we can not exclude that the residual convective component of ^{210}Po is not present, this minimum rate of ^{210}Po rate is considered as an upper limit on ^{210}Bi rate.

^{210}Bi homogeneity: The fiducial volume used in CNO analysis is $\sim$3 times bigger than the LPoF region. The upper limit on ^{210}Bi rate can be used from a smaller volume to the entire fiducial volume of CNO analysis under the assumption that ^{210}Bi is uniform in the fiducial volume. It is necessary to verify the assumption of ^{210}Bi spatial uniformity in order to extrapolate the upper limit on ^{210}Bi rate in fiducial volume. The ^{210}Bi non-uniformity could exists due to the possibility of ^{210}Pb leaching off of the nylon vessel. Moreover, the spatial distribution of ^{210}Bi was non-uniform in the detector in Phase-II, after the purification campaign, as the cleanest part of the scintillator was concentrated on the top [2]. To test the radial and angular homogeneity of ^{210}Bi in the fiducial volume used in CNO analysis in Phase-III final period, the analysis is performed by selecting β-like events in the energy interval $150 < \mathrm{N}_{pe}^{geonorm} < 471$, where ^{210}Bi contribution is maximal. The radial homogeneity was studied by dividing fiducial volume into iso-volumetric shells and a fit is performed on the data using a linear function with respect to radius r with a constant rate and variable rate with slope. The fit results in a constant rate of β-like events and a slope. Attributing all variations of

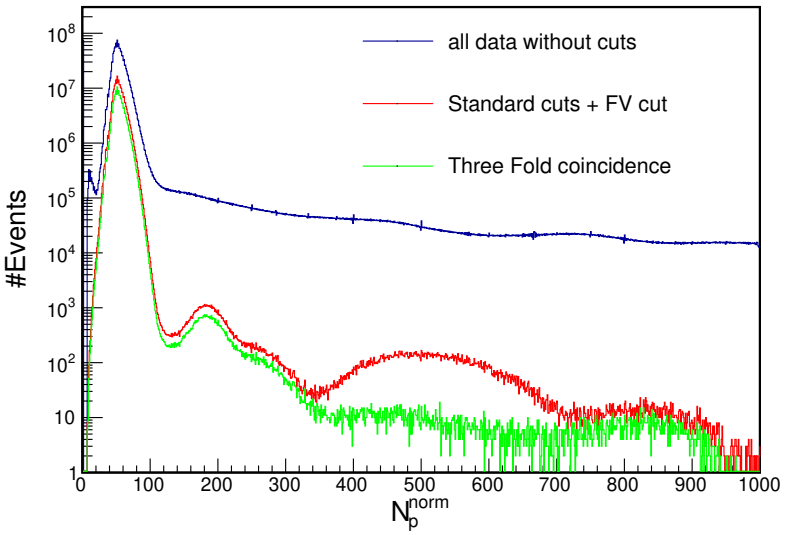

Figure 4.5: The energy spectra of Phase-III final data in normalized N_{pmts} energy variable without any cuts (in blue), after all the standard cuts listed in Sec. 3.2.4 and a fiducial volume cut of R<2.8 m & -1.8 m < z < 2.2 m (in red). The TFC-subtracted energy spectra (in green) is also shown.

β-like events to ^{210}Bi and using energy efficiency of ^{210}Bi, the error from radial homogeneity alone is 0.46 cpd/100 t. To study angular homogeneity, the spatial coordinates of data is projected on a spherical surface, where an event is assigned a index according to its spherical coordinates. The power spectra from data is computed and it is compared to power spectra of randomly generated white noise. The data power spectra is compatible with the white noise within 2σ and posing an error of 0.52 cpd/100 t. The total error of 0.68 cpd/100 t is also included as the major systematic uncertainty to upper limit on ^{210}Bi rate [189].

To conclude, the constraint on ^{210}Bi rate is R(^{210}Bi) $\leq 10.8 \pm 1.0$ cpd/100 t, applied as upper limit in the spectral fit of Phase-III final dataset. Now, the rate and the uncertainty is lower than the previous limit discussed in Sec. 4.3. The reasons include the removal of 2016 data with high ^{210}Po rate and addition of more data corresponding to stable period after February 2020. However, this is still in agreement with previous results within 1σ range of uncertainties.

4.4.3 Production of data and MC PDF inputs for final fit

Data: As discussed in Sec. 3.1.2, the data acquisition of Borexino is organized in 6 hours long *runs*. The runs from each week are combined in files called *DSTs*. Then, each dst goes through series of selection cuts listed in Sec. 3.2.4 with pepFV cut and TFC application. The energy spectra before TFC application, splitted energy spectra into TFC-subtracted and TFC-tagged data in different energy estimators and radial distributions of data are saved. Then, a final rootfile is produced by adding all the weekly dsts and several parameters related to live-time of data, exposure, number of channels, TFC performance parameters etc are calculated. Figure 4.5 shows the effect of standard selection cuts on the energy spectra of Phase-III final data. In this figure, the non-statistical features in the data without cuts (in blue) is due to the so-called *masking* effect, which is discussed later in this subsection.

MC PDFs: All solar neutrino and background components are first simulated using dedicated generators or standard Geant4 classes in the MC software [175]. The energy spectra of recoiled electron events in the solar neutrino generator are calculated

using the predicted solar neutrino flux and the primary neutrino spectra, which are taken from http://www.sns.ias.edu/∼jnb/. The electron survival probability of electron solar neutrinos [190] and the energy dependence of the $\nu_e - e$ and $\nu_{\mu,\tau} - e$ elastic scattering cross-sections including radiative corrections at next-to-leading order [191] are also computed and used. Finally, the electron recoil energy is sampled from the computed energy distribution of recoiled electron [175]. To produce the simulation of CNO-ν events, the contribution of ^{13}N, ^{15}O, and ^{17}F solar neutrinos from the CNO cycle (see Sec. 2.1) is simulated, taking into account their weighted sum according to the SSM predictions. The Borexino experiment is not sensitive to ^{13}N, ^{15}O, and ^{17}F solar neutrinos individually and the systematic effects arising from taking their weighted sum is negligible [159].

Each species is simulated with statistics of 50-2000 times larger than the expected counts, to avoid the effect of statistical fluctuation in the final PDFs. The generational volume for most of the species is a sphere of radius 3.75 m, which lies inside the IV containing LS. Figure 4.6a shows the comparison of true spatial distribution of generated events in comparison to the shape of IV in the first week of January 2017. Most of the species are generated to be uniformly distributed, except for ^{210}Po and the external γ backgrounds. ^{210}Po is not uniformly distributed inside the detector and therefore, the spatial distribution for ^{210}Po simulation follows the distribution in the so-called Polonium-maps. Polonium-maps are the reconstructed spatial distribution of data, after the application of MLP cut and an energy cut where the ^{210}Po contribution is maximal. The external γ backgrounds are generated on SSS and the PMTs' surfaces to perform the propagation of γ in a realistic way. As discussed in Sec. 4.3, the region of interest is 320 - 2640 keV (136 - 954 N_h^{norm}), the simulation of all species lying in this energy region are simulated.

Then, the physical processes after the event generation are simulated, as described in Sec. 3.2.5. The parameter, quantum efficiency (QE), is defined as the probability of conversion of the incident photons on PMT into photoelectrons. It is an crucial parameter to ensure the precise simulation of the experimental data and its initial value was used based on the pre-installation measurements. The QE value can change with time with respect to the initial values due to the deteriorating functionality and dying of PMTs. It is not possible to monitor the QE directly after the PMTs have been installed. One of the parameter, that is monitored in Borexino, is the so-called effective quantum efficiency (EQE), which accounts for all the sources that influence the photoelectrons production such as variations in the light yield and properties of electronic channel. This parameter was re-tuned in the Monte Carlo for the Phase-III final analysis. Using standard candles such as ^{210}Po, one can track the reconstructed energy scale with respect to time. The discrepancy between data and MC at a level of $>$1% was observed, starting from the year 2019. The reason of this problem was associated to dying of PMTs in the subset of 900 (*B900*) PMTs [192] in the recent years, which are used in the evaluation of QEs in MC [193]. This PMT selection is performed using ^{14}C events due to the unavailability of calibration source after 2009 and ^{14}C fulfills the criteria of an ideal standard candle for these studies. For the analysis in the next sections, a new subset of relatively good quality 700 PMTs, the so-called *C700*, was selected in all phases and the new inputs to *bxelec* were calculated [194]. Using these new inputs, an improved MC simulation was performed. The precision level of agreement between data and improved MC are investigated using cosmogenic neutrons as the standard candles and is found to be within 1% level which is taken as systematic error, which will be described in Sec. 4.4.6.

The output of MC simulations of all species are processed by the same reconstruction algorithms, that are also used for the real data. This leads to the production of files corresponding to each runs. Each file also undergoes the same series of standard

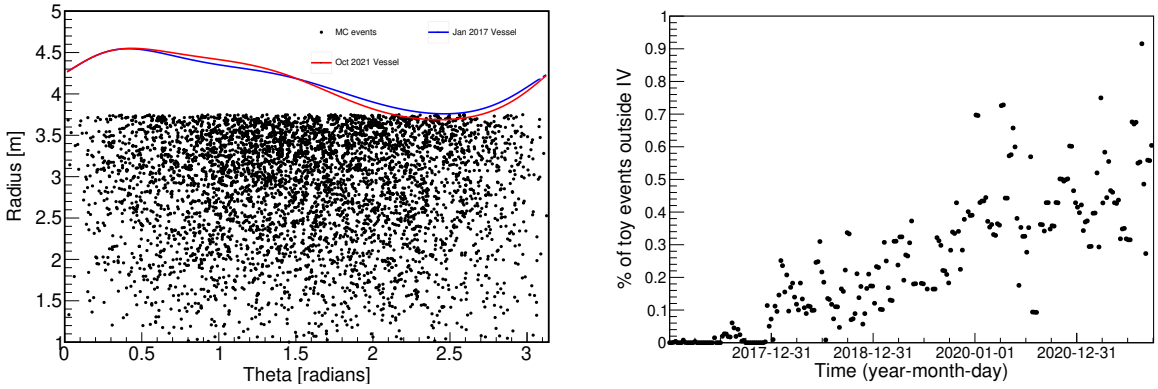

(a) **(b)**

Figure 4.6: (a) The comparison of true position of simulated CNO-ν events (black points) and the IV shape (blue curve) in polar coordinates, where both distributions corresponds to 1st January 2017. The IV shape corresponding to 3rd October 2021 is also shown in red. (b) The time evolution of fraction of toy events generated in a sphere of radius R<3.75 m and lying outside the IV.

selection cuts and pepFV cut, which were also applied on the data. The files of all runs corresponding to the Phase-III final period are summed together to obtain the PDF histograms of each species that are used for the final fit. The next step of PDF production is the normalisation of histograms with the trigger efficiency factor, crucial for species with a part of their energy spectrum lying below trigger threshold. This normalisation factor (f_N) is defined as the ratio of the number of reconstructed and triggered events in pepFV (N_{recoFV}) to the number of events generated in the pepFV (N_{genFV}):

$$f_N = \frac{N_{recoFV}}{N_{genFV}}. \tag{4.4}$$

For the uniform species, N_{genFV} is usually calculated as:

$$N_{genFV} = N_{genTOT}\frac{V_{FV}}{V_{gen}}, \tag{4.5}$$

where N_{genTOT} is the total number of generated events, V_{FV} and V_{gen} represent the volume of pepFV and the spherical generation volume of radius 3.75 m , respectively. Since the radius of IV is reducing in the southern part of the detector (see $\theta \sim$2.5 radians in Fig. 4.6a), a part of the spherical generation volume of radius 3.75 m would lie outside IV in the latest period. The MC software confines the generation region inside IV, i.e it does not simulate the true event vertex outside the IV, even if the generation volume lie outside IV for the corresponding run. Since the shape of IV is continuously changing, the increasing part of generation volume lies outside IV over the time, only in the Phase-III final period. Therefore, the effect of changing generation volume should be taken into account in eq. 4.5. Using a toy study, where the uniformly distributed random position were generated within sphere of radius 3.75 m and the fraction of events lying outside the IV is calculated and plotted for each week. As shown in Fig. 4.6b, only $\lesssim$1% of the generated uniform events lie outside the IV. In order to take this effect into account for uniform species, N_{genFV} is now calculated as:

$$N_{genFV} = V_{FV} \cdot \sum_{i}^{runs} \frac{N^i_{gen}}{V^i_{gen}} \quad ; \quad V^i_{gen} = (1 - x^i)\frac{4}{3}\pi(3.75)^3, \tag{4.6}$$

where N^i_{gen} is the number of generated events in each run i, and V^i_{gen} is the corrected

Specie	f_N (before)	f_N (after)	Relative difference (%)
^{7}Be-ν	0.850	0.848	0.24
pep-ν	0.925	0.922	0.32
CNO-ν	0.857	0.855	0.35
^{210}Po	0.999	0.999	0
^{210}Bi	0.829	0.827	0.24
^{85}Kr	0.823	0.821	0.24
^{11}C	0.987	0.985	0.20
^{10}C	0.994	0.991	0.30
^{6}He	1.00	0.997	0.30
^{8}B	0.961	0.959	0.21
Ext ^{40}K	0.740	0.740	0
Ext ^{208}Tl	0.832	0.832	0
Ext ^{214}Bi	0.786	0.786	0

Table 4.3: Value of normalisation factors f_N for all simulated species before and after correction in V_{gen} in eq. 4.6.

generation volume, which is calculated with the fraction of toy events lying outside the IV, x^i. Table 4.3 shows the values of f_N for each species using N_{genFV} in eq. 4.5 and eq. 4.6. It can be seen from Table 4.3, that the effect on the trigger efficiency is $\leq$0.35%, which is smaller than its precision level of $\sim$1% . The non-uniform species such as ^{210}Po and external γ backgrounds are not affected because N_{genFV} in their case is calculated as:

$$N_{genFV} = N_{genTOT}\frac{N_{FV}}{N_{IV}}, \tag{4.7}$$

where N_{FV} and N_{IV} represents the number of events from data lying in the fiducial volume (FV) and Inner Vessel (IV), respectively. Their normalisation factor is also shown in Table 4.3.

Masking effect

For performing the spectral fit (Sec. 4.4.5), the inputs are produced in the normalised energy estimators (Sec. 3.2.1), to take into account the decreasing number of PMTs over time. The normalization to 2000 PMTs is performed on an event-by-event basis, where the energy estimator, N_p^m or N_h^m is a integer value and the factor $f_{eq} = 2000/N_{live}$ is a rational number. When the product of N_h^m (or N_p^m) and f_{eq} is input to a data or PDF histogram with a bin width of 1, this results in the non-statistical fluctuations between the close bins. This effect of fluctuation is referred to as *masking* effect [195,196] and the PDFs obtained with normalised energy estimator are termed as *masked PDFs*. The masked PDFs can be smoothed ("unmasked") or the features as in data can be reproduced in unmasked PDFs by dividing or multiplying a distribution, respectively.

This distribution is called the *mask* (h_{mask}) and is produced using the distribution of live PMTs h_{live} with bins n_{hlive}:

$$h_{mask} \rightarrow \forall_{i=1,j=1}^{2000,n_{hlive}} Fill\left(\frac{2000*i}{\text{bincenter}^j(h_{live})}, \text{bincontent}^j(h_{live})\right), \tag{4.8}$$

where i, j corresponds to each bin of h_{mask} and h_{live} , respectively.

4.4.4 Spectral fit technique

A multivariate spectral fit technique is utilized to fit collected data with the PDFs of various solar neutrino and background species, obtained from the MC simulations. Here, a total binned likelihood function is defined using multiple likelihoods, containing the information from energy distributions and radial distributions. Then, the total likelihood using information from the TFC splitted energy spectra (tagged and subtracted) and the radial distribution of the events is maximised. The total likelihood function is calculated as the following:

$$\mathcal{L}(\vec{k}|\vec{\theta}) = \mathcal{L}_{\text{sub}}^{\text{TFC}}(\vec{k}|\vec{\theta}) \cdot \mathcal{L}_{\text{tag}}^{\text{TFC}}(\vec{k}|\vec{\theta}) \cdot \mathcal{L}_{\text{radial}}(\vec{k}|\vec{\theta}). \tag{4.9}$$

The $\vec{\theta}$ represents the set of parameters with respect to which likelihood is maximised, which are the interaction rates of each species. Here, $\vec{k}$ represents the set of experimental data used to calculate the likelihood. Each likelihood term related to energy distributions splitted by TFC : $\mathcal{L}_{\text{sub}}^{\text{TFC}}(\vec{k}|\vec{\theta})$ and $\mathcal{L}_{\text{tag}}^{\text{TFC}}(\vec{k}|\vec{\theta})$, is calculated as standard Poissonian likelihood:

$$\mathcal{L}^{\text{TFC}}(\vec{k}|\vec{\theta}) = \prod_{i=1}^{N} \frac{\lambda_i(\vec{\theta})^{k_i}}{k_i!} e^{\lambda_i(\vec{\theta})}, \tag{4.10}$$

where the product runs for each bin i of total number of bins (N) in the spectrum and k_i are the number of entries of measured events in i^{th} bin. The λ_i parameter is the expected number of entries for the bin i given $\vec{\theta}$. The energy range of the fit is 136 - 954 N_h^{norm}. In the fit, the rate of most of the species is free to vary. The events in TFC-tagged and TFC-subtracted spectrum are independent. The fit rate of all species are common in both the tagged and subtracted spectrum except the cosmogenic backgrounds such as ^{10}C, ^{11}C, and ^{6}He and also, ^{210}Po, which is non-uniformly distributed throughout the FV. For latter species, the fit rates are different in the two spectra.

For performing the radial fit, the radial distribution of TFC-subtracted data events in energy range 500 - 900 N_h^{norm} are produced. As the radial fit is performed to disentangle the external backgrounds from the data, the fit uses reference distribution of 2 components: uniform and non-uniform. The non-uniform component is obtained from the MC simulations of external backgrounds and the uniform component is the radial distribution of simulated β^-like species. The likelihood $\mathcal{L}_{\text{radial}}(\vec{k}|\vec{\theta})$ is calculated using a scaled Poissonian likelihood as following:

$$\mathcal{L}_{\text{radial}}(\vec{k}|\vec{\theta}) = \prod_{i=1}^{N_{rad}} \frac{a\lambda_i(\vec{\theta})^{k_i}}{k_i!} e^{a\lambda_i(\vec{\theta})}, \tag{4.11}$$

where the product goes over each bin i of N_{rad} bins in the radial distribution and a is

a scaling factor, calculated using normalization to the total number of entries in measured distribution as:

$$N_{entries} = a \sum_{i=1}^{N_{rad}} \lambda_i(\vec{\theta}). \tag{4.12}$$

This normalization is done because there exists a correlation between energy and radial distributions due to the presence of same entries.

The rates of solar neutrino or the background can also be constrained in the fit using a penalty term multiplied to eq. 4.9. There are two types of penalty term applied in spectral fit:

- Symmetric Gaussian constraint with mean and sigma determined from independent measurement of the rate, which is used to apply constraint on *pep* solar neutrino rate.
- Asymmetric half Gaussian term to impose an upper limit, where the value of parameter of interest is left to vary between 0 and the value of upper limit, which is used to apply constraint on ^{210}Bi rate.

4.4.5 Fit results

The fit results using the TFC-subtracted and TFC-tagged energy spectra, as well as the radial distributions are shown in Fig. 4.7a and 4.7b, following the technique described in the Sec. 4.4.4 and using the bxGoostats framework [180]. Table 4.4 shows the list of species, their configuration in the fitting procedure and the extracted interaction rate from the fit. The *p-value* of fit is 0.2, showing that the agreement between the data and the fitted model is good.

Now, the scan of CNO-ν rate is performed to obtain the log-likelihood profile, $ln\mathcal{L}$ (dotted curve in Fig. 4.8). The CNO rate obtained from the profile is $6.6^{+2.0}_{-0.7}$ cpd/100 t, with statistical error only. The asymmetric shape of the profile is due to the ^{210}Bi upper limit as it impacts only the left part of the CNO profile. Now, the uncertainties from the systematic effects, described in the Sec. 4.4.6, are injected using a folding procedure. In this procedure, the log-likelihood profile is converted to a probability density function (pdf):

$$\text{pdf} = e^{\frac{\Delta\chi^2}{2}} \quad ; \quad \chi^2 = -2\Delta ln\mathcal{L}. \tag{4.13}$$

The pdf is convolved with an asymmetric Gaussian to take into account the asymmetric systematic error [197], which is evaluated to be +0.5 and -0.4 cpd/100 t. All the systematic effects included here, are summarized in Sec. 4.4.6. The final CNO-ν rate is obtained by taking the maximum of convolved pdf as the central value and confidence intervals (C.I.) are estimated using the 68% quantile of convolved PDF starting from the tail from both ends. The convolved pdf is then converted back to the log-likelihood profile, as the black solid line shown in Fig. 4.8. The final result on CNO-ν rate is $6.7^{+2.0}_{-0.8}$ cpd/100 t, including systematic and statistical uncertainties. The no-CNO signal hypothesis is rejected with about 7σ significance, estimated from the log-likelihood profile with $\Delta\chi^2 \approx 49$ at CNO rate = 0 cpd/100 t. Using the electron density in LS, neutrino oscillation parameters [198] and considering MSW effect in matter, the measured flux of CNO-ν on Earth is $6.6^{+2.0}_{-0.9} \times 10^8$ cm^{-2} s^{-1}.

4.4.6 Systematic uncertainties

Various systematic sources are investigated that contributes in the result on CNO solar neutrinos [199]. They are listed as following:

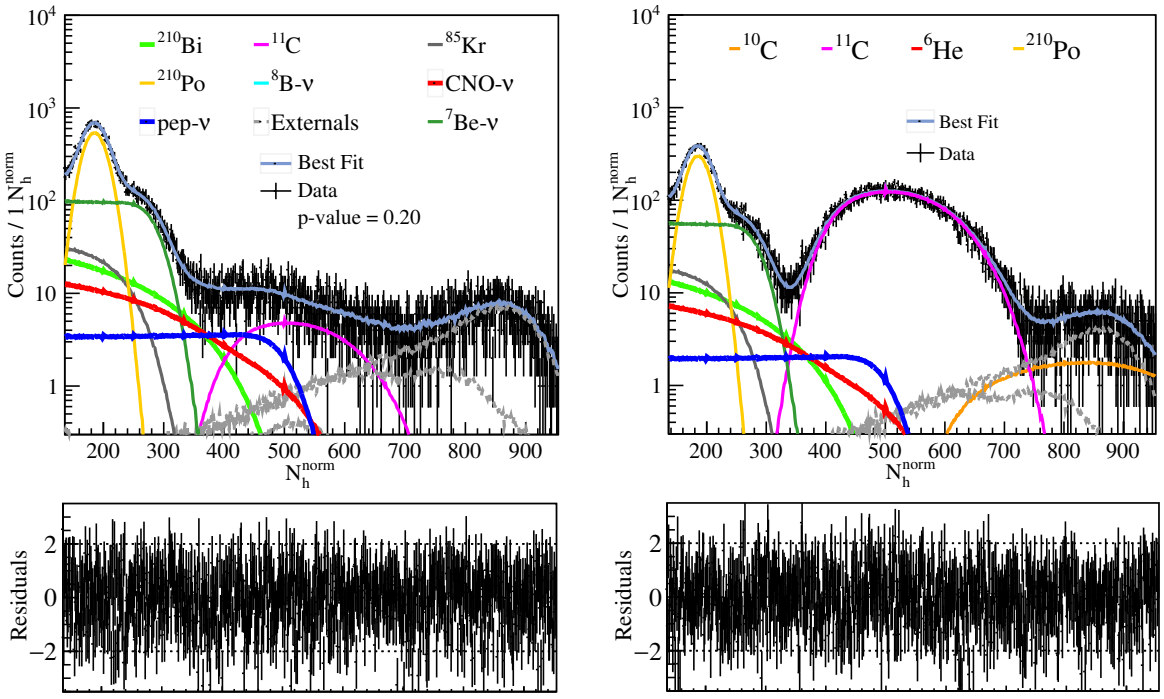

(a)

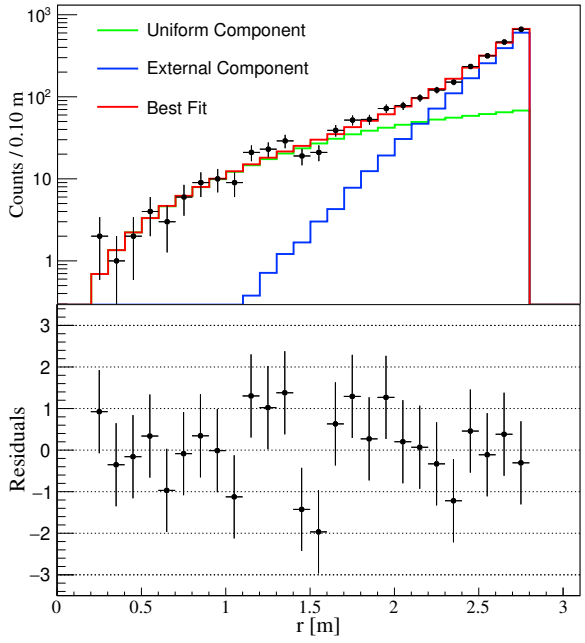

(b)

Figure 4.7: (a) The multivariate fit of Phase-III final dataset with different spectral components in the TFC-subtracted (left) and TFC-tagged (right) spectra in the N_h^{norm} variable, along with the fit residuals below. In upper plots, the data is shown as black points and the light blue line represents the total fit function. The CNO-ν spectrum is shown in bold red line. (b) Radial distribution of events in the multivariate fit: the distribution in green shows the uniform component from internal backgrounds and the solar neutrinos, while the blue distribution represents non-uniform contribution from the external backgrounds. The black points represent the data distribution and the best fit model is shown in red. The residuals from the fit are also shown.

Fit configuration : The systematic error associated to fitting configuration is estimated by performing about 650 multivariate fits by varying minimum and maximum range in energy and radial distributions as well as their binning and comparing the resulting log-likelihood profiles. No impact on the CNO profile was seen and therefore,

Species	Configuration	Extracted Rate (cpd/100 t)
^{7}Be-ν	free	46.90 $\pm$ 1.10
pep-ν	penalty	2.738 $\pm$ 0.040
CNO-ν	free	6.62 $\pm$ 0.87
^{210}Po (TFC-tagged)	free	39.47 $\pm$ 0.47
^{210}Po (TFC-subtracted)	free	40.60 $\pm$ 0.39
^{210}Bi	upper limit	11.05 $\pm$ 0.97
^{85}Kr	free	11.50 $\pm$ 1.60
^{11}C (TFC-tagged)	free	71.09 $\pm$ 0.51
^{11}C (TFC-subtracted)	free	1.580 $\pm$ 0.096
^{10}C	free	1.56 $\pm$ 0.28
^{6}He	free	0.00
^{8}B	fixed	0.46
Ext ^{40}K	free	1.40 $\pm$ 1.20
Ext ^{208}Tl	free	5.91 $\pm$ 0.24
Ext ^{214}Bi	free	3.80 $\pm$ 0.53

Table 4.4: The extracted rates and their statistical error only, obtained from the multivariate fit in bx-Goostat framework for all species, along with their configuration for Phase-III final data.

no systematic error contributes in the final result of CNO solar neutrinos.

^{210}Bi shape : The choice of reference shape of ^{210}Bi spectrum, based on the different measurements [200], contributes as systematic error of 18%.

Shift in energy scale of ^{11}C and ^{210}Po : The relative energy scale of ^{11}C (e^{+} - like) and ^{210}Po (α-like) events with respect to the electron energy scale needs to be tuned in Borexino MC. The energy distributions of almost pure ^{210}Po and ^{11}C events in data, selected using MLP and TFC techniques with strict thresholds, are compared with the MC PDFs in N_h^{norm}. This allows to determine the value, by which energy scale of ^{11}C and ^{210}Po PDFs needs to be shifted [179]. The estimated shift values are: ^{11}C = +9.5 $\pm$ 0.7 N_h^{norm} and ^{210}Po = +0.33 $\pm$ 0.14 N_h^{norm}. The central values are fixed during the multivariate fit and the errors contribute as systematic uncertainties.

Detector stability and uniformity : In order to track light yield stability and study non-uniformity of energy response in Borexino, the cosmogenic neutrons events are selected using trigger TT128 and are analyzed. The cosmogenic neutrons are captured on the scintillator hydrogen emitting 2.2 MeV γ's. The peak position of its energy spectrum in data and MC is studied with respect to the time and space inside the detector.

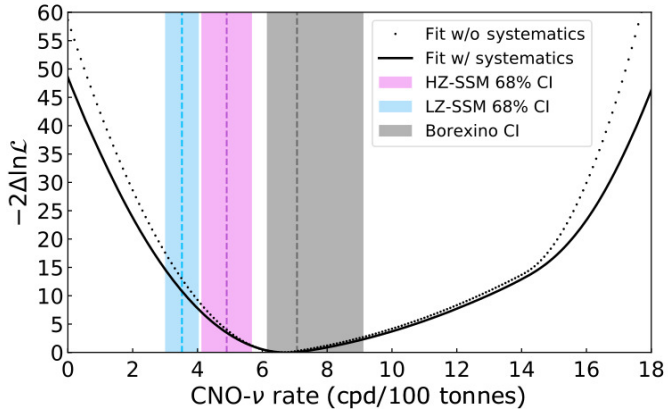

Figure 4.8: The negative log-likelihood (-2Δ ln$\mathcal{L}$) profile as a function of CNO-ν rate. The black dotted line shows the profile as obtained from multivariate fit without folding with systematic error, while the black solid line is the profile after including systematic uncertainties. The gray band shows the 68% confidence intervals (C.I.) of the CNO-ν rate measurement in Phase-III final period, including systematic uncertainties. The blue and pink bands represent 68% C.I. for the low-metallicity (LZ) SSM B16-AGSS09met predictions [(3.52 ± 0.52) cpd/100 t] and the high-metallicity (HZ) SSM B16-GS98 predictions [(4.92 ± 0.78) cpd/100 t], respectively. From [3].

The inaccuracies accounting for the spatial non-uniformity and the stability in detector response are 0.06% and 0.32% , respectively.

Detector non-linearity : The non-linearity of detector response in data and MC has been studied using calibration sources and the associated inaccuracies are 0.084%.

In order to determine the effect of these systematic sources on the CNO-ν rate, a toy MC method was used. In this method, 10,000 simulated data-sets were produced without and with the deformations of above mentioned magnitudes of each systematic sources. Both data-sets are fitted using standard PDFs with no deformations and the distribution of CNO-ν rate is obtained for both configurations. The widening of the distribution is taken as the systematic error.

4.4.7 Implications on solar physics

Global analysis of neutrino data

A global analysis of all neutrino data is performed by collecting and combining all results from various neutrino experiments and extracting the maximum amount of information about neutrino fluxes and oscillation parameters [201]. In order to so, a χ^2 comparison of data results from all the solar-ν experiments (Chapter 1) including Borexino (Phase-II and new CNO results), and the KamLAND [202] experiment is carried out with their respective theoretical expectations. The free parameters are the oscillation parameters (Δm^2_{21}, θ_{12}) and the neutrino fluxes (Φ_i), taking into account both the experimental and theoretical errors as well as the cross-correlations between different parameters error, while θ_{13} is fixed to value in [203] as it has a negligible impact on the analysis. The resulting χ^2 is then marginalized over each parameter of fit, obtaining χ^2 projection of interested parameter. The best fit results for oscillation parameters are: $\Delta m^2_{21} = 7.50^{+0.17}_{-0.18} \times 10^{-5}$ eV^2, $\theta_{12} = 0.43^{+0.04}_{-0.02}$. Figure 4.9 shows the results of this global analysis in parameter space of Φ_B-Φ_{Be}, Φ_B-Φ_{Be}, and Φ_{Be}-Φ_{CNO} and their 1σ regions in gray color. In the green color, the output of the analysis is shown when only Borexino and KamLand experiments results are included. Unshaded elliptical region shows the predictions from the high-metallicity SSM B16-GS98 (red) and

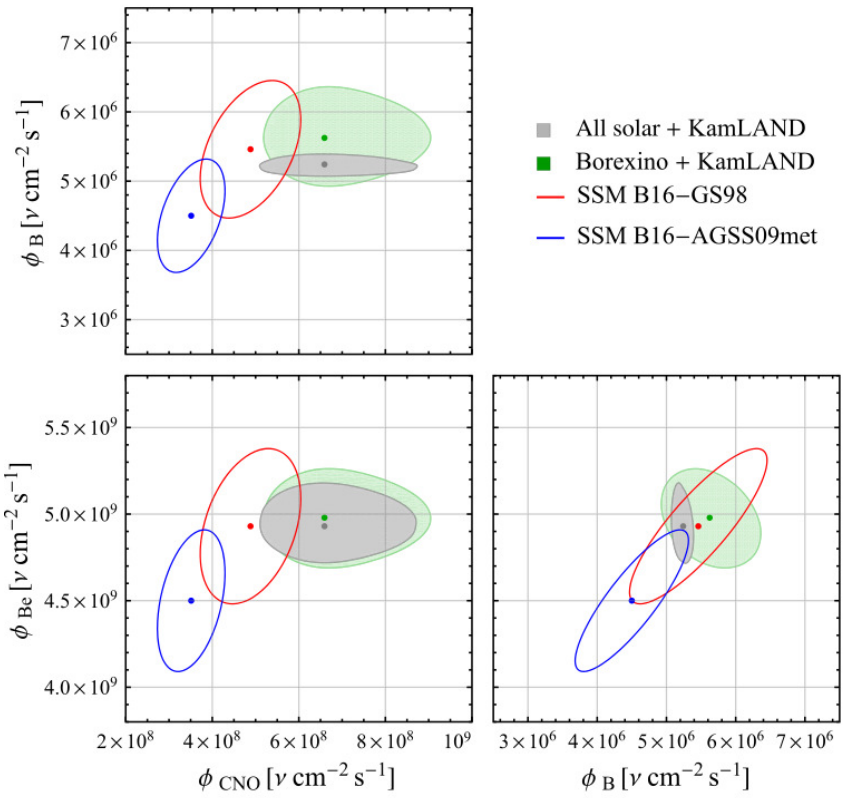

Figure 4.9: The global analysis results where 1σ regions allowed by all solar neutrino experiments and KamLAND reactor data (gray) in planes of Φ_B-Φ_{Be}, Φ_B-Φ_{Be}, and Φ_{Be}-Φ_{CNO} are shown. The KamLAND reactor $\bar{\nu}_e$ data is used to better constrain Δm^2_{21}. The 1σ regions allowed by Borexino only + KamLAND (green) are also shown. The 1σ predictions of high-metallicity SSM B16-GS98 and low-metallicity SSM B16-AGSS09met are shown in red and blue ellipses, respectively. From [3].

the low-metallicity SSM B16-AGSS09met (blue). One can see that both results are in small tension with SSM low-metallicity AGSS09met predictions. To have quantitative comparison of compatibility, the p-value between theoretical predictions and analysis results is computed [204]. The comparison between the global analysis data results and Borexino only (without including CNO solar neutrino measurement) with the SSM B16-AGSS09met predictions yields a p-value of 0.327 and 0.231, respectively. After including CNO solar neutrino results in the global analysis and in Borexino only, the p-value reduces to 0.028 and 0.018, respectively. On the other hand, the comparison between the global analysis data results and Borexino only (with including CNO solar neutrino measurement) with the SSM B16-GS98 predictions yields a p-value of 0.462 and 0.554, respectively. This shows that all solar neutrino fluxes, including CNO-ν, are in agreement with the high-metallicity SSM B16-GS98 predictions, while they have a moderate tension with the low-metallicity SSM B16-AGSS09met predictions.

Frequentist hypothesis test

A frequentist hypothesis test of the SSM B16-AGSS09met vs SSM B16-GS98 models is also performed, which has been mentioned in Sec. 4.2. The test statistics t, in the hypothesis test, is based on the log-likelihood ratio between SSM B16-AGSS09met and SSM B16-GS98 assumption. The PDF of t is built using the MC method, by generating thousands of toy results on ^{7}Be, ^{8}B, and CNO solar neutrino and assuming SSM B16-GS98 hypothesis to be true. Then, t is estimated for each generated toy set [1]. This step is repeated again, assuming now SSM B16-AGSS09met to be true. By comparing the actual Borexino results with the built distributions of t, it was concluded that the

Borexino data disfavors SSM B16-AGSS09met at 3.1σ level, as an alternative to SSM B16-GS98 [3].

Determination of C and N abundance

The measurement of CNO neutrinos is used to study the Sun's chemical composition by determining the abundance of Carbon (C) and Nitrogen (N) in the Sun. The information on the Sun's metallicity problem is also obtained, for the first time by Borexino [205] using CNO-ν measurement. The idea is as follows: all solar neutrino fluxes depend on the subset of SSM parameters, the so-called *environmental parameters*, indirectly through the core temperature (T_c), which is an implicit function of those parameters. The *environmental parameters* include the solar age, solar luminosity, radiative opacity, diffusion length and metallicity, that are calibrated according to the spectroscopic measurement of the Sun's photosphere. The other set of SSM parameters are the nuclear S-factors of the nuclear fusion reactions in the Sun. The approximation of neutrino flux (Φ_i) dependence on T_c is given by the SSM power law with index τ_i, specific to the neutrino flux of interest. For ^{8}B, which is extremely sensitive to T_c, the dependence can be expressed as :

$$\frac{\Phi_B}{\Phi_B^{SSM}} \propto \left(\frac{T_c}{T_c^{SSM}}\right)^{\tau_B}. \tag{4.14}$$

Here, "SSM" indicates the value of SSM predictions. The similar expression can also be made for CNO neutrinos, for example ^{15}O, where in addition to its flux dependence on T_c, it also features a direct dependence on the abundance of C and N (relative to hydrogen) in the solar core n_{CN} due to the presence of "metals" C and N, catalyzing the CNO cycle:

$$\frac{\Phi_O}{\Phi_O^{SSM}} \propto \frac{n_{CN}}{n_{CN}^{SSM}} \times \left(\frac{T_c}{T_c^{SSM}}\right)^{\tau_O}. \tag{4.15}$$

By taking the weighted ratio with factor of k, we obtain:

$$\frac{\Phi_O/\Phi_O^{SSM}}{(\Phi_B/\Phi_B^{SSM})^k} \propto \frac{n_{CN}}{n_{CN}^{SSM}} \times \left(\frac{T_c}{T_c^{SSM}}\right)^{\tau_O - k\tau_B}. \tag{4.16}$$

However, in reality, the neutrinos are produced in an extended Sun's core region, where the temperature and chemical composition profile vary. In addition, the temperature and the CN abundance profile are not direct inputs of SSM. Therefore, an explicit dependence of a given neutrino flux Φ_i on each SSM input parameter j, in the form of the SSM power law, is made:

$$\frac{\Phi_i}{\Phi_i^{SSM}} = \prod_j^{\text{C,N}} x_j^{\alpha(i,j)} \times \prod_j^{\text{env}} x_j^{\alpha(i,j)} \times \prod_j^{\text{nucl}} x_j^{\alpha(i,j)} \times x_{\text{diff}}^{\alpha(i,\text{diff})}, \tag{4.17}$$

where x_j represents the SSM parameter normalized for their nominal values. Here, $\alpha(i,j)$ denotes the logarithmic derivatives of the given neutrino flux with respect to the SSM parameter:

$$\alpha(i,j) = \frac{\partial \ln(\Phi_i/\Phi_i^{SSM})}{\partial \ln x_j}, \tag{4.18}$$

which is calculated numerically [206]. In eq. 4.17, the SSM inputs are group into four, including Carbon and Nitrogen (C,N) abundance and nuclear reaction cross-section (nucl). The environmental parameters (env) are also taken into account, where the diffusion parameter is treated explicitly. This is due to the fact that change in the diffusion

will affect the temperature stratification in the Sun as well as it also impact the chemical composition profile of the Sun. Using eq. 4.17, it is now possible to express the left hand side of eq. 4.16 as a function of the SSM parameters. In the weighted ratio, the value of k is 0.769, which is obtained by taking the SSM B16-GS98 as reference such that it minimizes the impact of environmental parameters on the flux ratio. Using the uncertainties of each SSM input parameter and the difference in chemical abundance by GS98 and AGSS09met as an additional uncertainty,:

$$\frac{\Phi_O/\Phi_O^{SSM}}{(\Phi_B/\Phi_B^{SSM})^{0.769}} = \frac{N_{CN}}{N_{CN}^{SSM}}[1 \pm 0.097(\text{nucl.}) \pm 0.005(\text{env}) \pm 0.027(\text{diff})] \tag{4.19}$$

is obtained. The terms in square brackets quantify the contribution of nuclear, environmental, and diffusion uncertainties to the total error budget. The symbol N_{CN} represent the extrapolated CN abundance in the Sun's photosphere from its core, that allows us to have a direct comparison with the Sun's photosphere spectroscopic analysis. Plugging the ^{8}B-ν measurement from the aforementioned global analysis of all solar neutrino experiments and the extracted flux of ^{15}O from CNO measurement with the assumption of SSM ratio between ^{13}N and ^{15}O fluxes and taking SSM B16-GS98 as reference, we get:

$$\frac{N_{CN}}{N_{CN}^{SSM}} = 1.35 \times (0.96)^{-0.769} \times [1^{+0.303}_{-0.136}(\text{CNO}) \pm 0.097(\text{nucl.}) \pm 0.023(^8\text{B}) \pm 0.005(\text{env}) \pm 0.027(\text{diff}) \pm 0.022(^{13}\text{N}/^{15}\text{O})].$$

The final value of N_{CN} is $(5.78^{+1.86}_{-1.00})\times10^{-4}$, which is the first determination of CN abundance in the Sun using the solar neutrinos. Figure 4.10 shows the comparison of CN abundance in the Sun with the spectroscopic measurements of the Sun's photosphere. Our measurement is in good agreement with the high-metallicity compilations (MB22 [141] and GS98), while featuring a $\sim 2\sigma$ tension with low-metallicity ones (AGSS09met, C11 [139] and AAG21 [140]). This analysis is repeated again by changing the reference to SSM B16-AGSS09met and the fully compatible value is obtained, as shown in white cross in Fig. 4.10.

4.5 Summary

Borexino has successfully performed the complete spectroscopy of solar neutrinos originated from both the fusion processes inside the Sun: *pp*-chain and CNO cycle. After the first detection of CNO solar neutrinos in 2020, Borexino has provided an improved uncertainty of $^{+30\%}_{-12\%}$ on the measurement of CNO solar neutrinos flux in 2022. This analysis was performed on dataset starting from January 2017 until the end of data taking in October 2021. This analysis does not utilize the 2016 dataset in Phase-III period unlike the analysis performed in 2020, in order to remove the contribution of high amount of convective ^{210}Po in 2016, thereby making it possible to determine the constraint on the rate of its parent ^{210}Bi with lower uncertainty as compared to the previous analysis. My contributions to this analysis include the determination of value of a parameter included in the model used to determine ^{210}Bi constraint. I have also been responsible for the production of real and simulated data distributions and perform final spectral fits using these distributions. Now, the CNO-ν detection significance has increased to about 7σ significance. This new result is also included in the global analysis of all solar-ν and KamLAND reactor data. The resulting solar neutrino fluxes

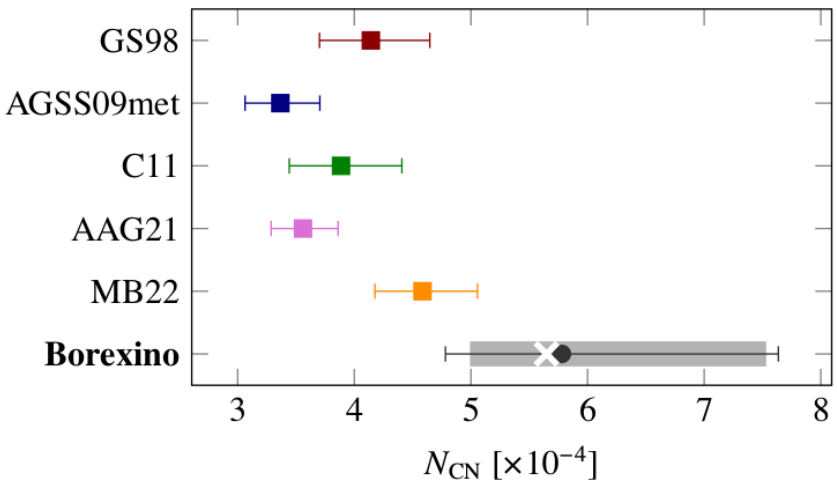

Figure 4.10: The comparison of Carbon (C) + Nitrogen (N) abundance with respect to the Hydrogen (H) in the Sun's photosphere, N_{CN}, from spectroscopy (squares) and from the measurement of CNO solar neutrino flux by Borexino (circle). The gray band shows the uncertainty range due to the precision of CNO measurement. The white cross marks the result of the same study repeated after changing the reference SSM from the B16-GS98 to B16-AGSS09met. From [3].

are found to be in agreement with high-metallicity SSM B16-GS98, while a moderate tension with low-metallicity SSM B16-AGSS09met is observed. Using a frequentist hypothesis test, it was found that CNO, ^{7}Be and ^{8}B neutrinos fluxes by Borexino disfavors SSM B16-AGSS09met at 3.1σ level as an alternative to SSM B16-GS98. Furthermore, the CNO-ν measurement together with ^{8}B-ν flux from global analysis has been used to determine the C and N abundance in the Sun. The determination of C and N abundance in the Sun is performed for the first time using solar neutrinos. When comparing the C and N abundance determined using this method with the independent spectroscopic measurements of solar photosphere, the results agrees very well with the high-metallicity values (GS98 [136], MB22 [141]), while it features a $\sim$2σ tension with the low-metallicity values (AGSS09met [138], C11 [139], AAG21 [140]). A further precise CNO neutrino measurement has been performed using a combined directional and spectral fit technique, which will be discussed in the next chapter.

Chapter 5

Directional measurement of solar neutrinos in Borexino

In this chapter, the directional analysis of low-energy solar neutrinos using Cherenkov photons with the Borexino experiment is described [4–6]. The motivation to study the directionality of solar neutrinos is covered in Sec. 5.1. The *Correlated and Integrated Directionality* (CID) method, developed and used for the directional analysis of solar neutrino in Borexino, is discussed in Sec. 5.2 in detail. Section 5.3 is dedicated to the description of the strategy for the Monte Carlo PDFs production in order to perform the fit and the fit strategy is discussed in Sec. 5.4.

Section 5.5 is devoted to the first directional measurement of sub-MeV solar neutrinos in a liquid scintillator detector [4, 5]. This analysis is performed in an energy region of ^{7}Be shoulder and provides a proof-of-principle of the CID method. The data selection used for this analysis is described in Sec. 5.5.1. Section 5.5.2 discusses the optimisation of fit configurations and the selection of PMTs with the correct time behaviour. The calibration of group velocity for Cherenkov photons using the γ calibration sources is discussed in Sec. 5.5.3. Section 5.5.4 describes all sources of the systematic uncertainties, and Sec. 5.5.5 summarizes the final results. My contribution to this analysis comprises the optimisation of binning of the distributions used in the fit, development of a toy simulation method to investigate the systematic effects associated to the simulation of background events. I also contributed in the preparation of the publications [4, 5].

Section 5.6 is dedicated to the CNO-ν measurement by exploiting the Cherenkov light using CID. This analysis has been performed without an external constraint on the ^{210}Bi rate, which is different from the spectral analysis performed in Chapter 4. This analysis uses an energy region which is independent from the one used for the ^{7}Be CID analysis. All selection cuts are summarized in Sec. 5.6.1. Section 5.6.2 discusses the optimisation of different fit configurations for this analysis and the selection of PMTs with correct time behaviour. Here, the calibration of group velocity for the Cherenkov photons is performed using ^{7}Be solar neutrinos, as described in detail in Sec. 5.6.3. Section 5.6.4 describes all sources of systematic uncertainties. Section 5.6.5 summarizes the final results, which are then combined with the multivariate fit, as reported in Sec. 5.6.6. My contribution to this analysis comprises the optimisation of the fit inputs, estimation of the expected number of neutrino events and performing analysis for the calibration of group velocity of Cherenkov photons in the ^{7}Be-ν edge region, evaluation of the systematic uncertainties, performing final CID fits as well as analysis checks, and co-writing the publication [6].

5.1 Motivation to study directionality in liquid scintillator experiments

As seen in Chapter 1, either water Cherenkov or liquid scintillator (LS) detectors exist as the current generation experiments for the measurement of solar neutrinos. Although the emission of the directional Cherenkov light in water Cherenkov detectors provides an aid in the background suppression and particle identification, the water Cherenkov detectors have a relatively small light yield at MeV energies, and a detection threshold at higher energies. For example, in Super Kamiokande, the light yield is 34 photoelectrons at 3.5 MeV [207]. On the other hand, the LS detectors have a higher light yield, good energy resolution and a lower energy threshold to detect the solar neutrinos. As discussed in Chapter 3, the light yield in Borexino is $\sim$500 photoelectron at 1 MeV, and an effective low energy threshold of 0.19 MeV has been used for the solar neutrino spectroscopy [1]. Since in LS detectors, the dominant scintillation light are emitted isotropically, the directional analysis of solar neutrinos on an event-by-event basis can not be performed.

In order to combine the advantages of both detector types, there has been an increased interest in the recent years to develop the hybrid detection techniques. The motivations for such interests include the measurement of CNO solar neutrinos [208], as well as the search for neutrinoless double beta decay where the solar neutrinos act as the backgrounds [209]. To achieve this goal of a hybrid detector, some of the ongoing activities are as follows:

- Development of new target materials, such as water based LS [164], slow LS [165] or nano-crystal doped LS [166].
- Developing fast-photo sensors to achieve the time separation of Cherenkov and scintillation light [167].
- Spectral photon sorting by wavelength using the dichroic reflectors [168].
- New analysis techniques [210, 211].

These efforts have been investigated using the small-scale experiments such as the CHESS experiment [212], FlatDot detector [213], and ANNIE [214]. For the large scale detectors, the feasibility of hybrid detectors has been studied using the Monte Carlo simulations [169, 208]. In this chapter, the first measurement of sub-MeV (^{7}Be and CNO) solar neutrinos exploiting the directional Cherenkov light, using a newly developed analysis technique called *Correlated and Integrated Directionality* (CID) method [4, 5] with the Borexino experiment, is discussed.

5.2 Correlated and Integrated Directionality (CID) technique

Solar neutrino with energy E_ν scatters off electrons elastically in the liquid scintillator detectors by an angle θ_e and transfers energy T_e, as discussed in Chapter 1. The relation between θ_e, E_ν, and T_e is given by eq. 2.18. For relatively high values of T_e, the electron is scattered in the forward direction. If the velocity of recoiled particle v is greater than the speed of light c_n in LS with the refractive index n, the recoiled electron emits Cherenkov radiation in a cone in its velocity direction. The scintillation photons are also emitted isotropically, when the recoiled electron deposits its energy in LS target. All the photons are detected by the PMTs.

The basic principle of *Correlated and Integrated Directionality* (CID) method is illustrated in Fig. 5.1. In CID, the direction of early photons of an event is correlated to the initial direction of solar neutrino, by calculating the cosine of α angle for each detected

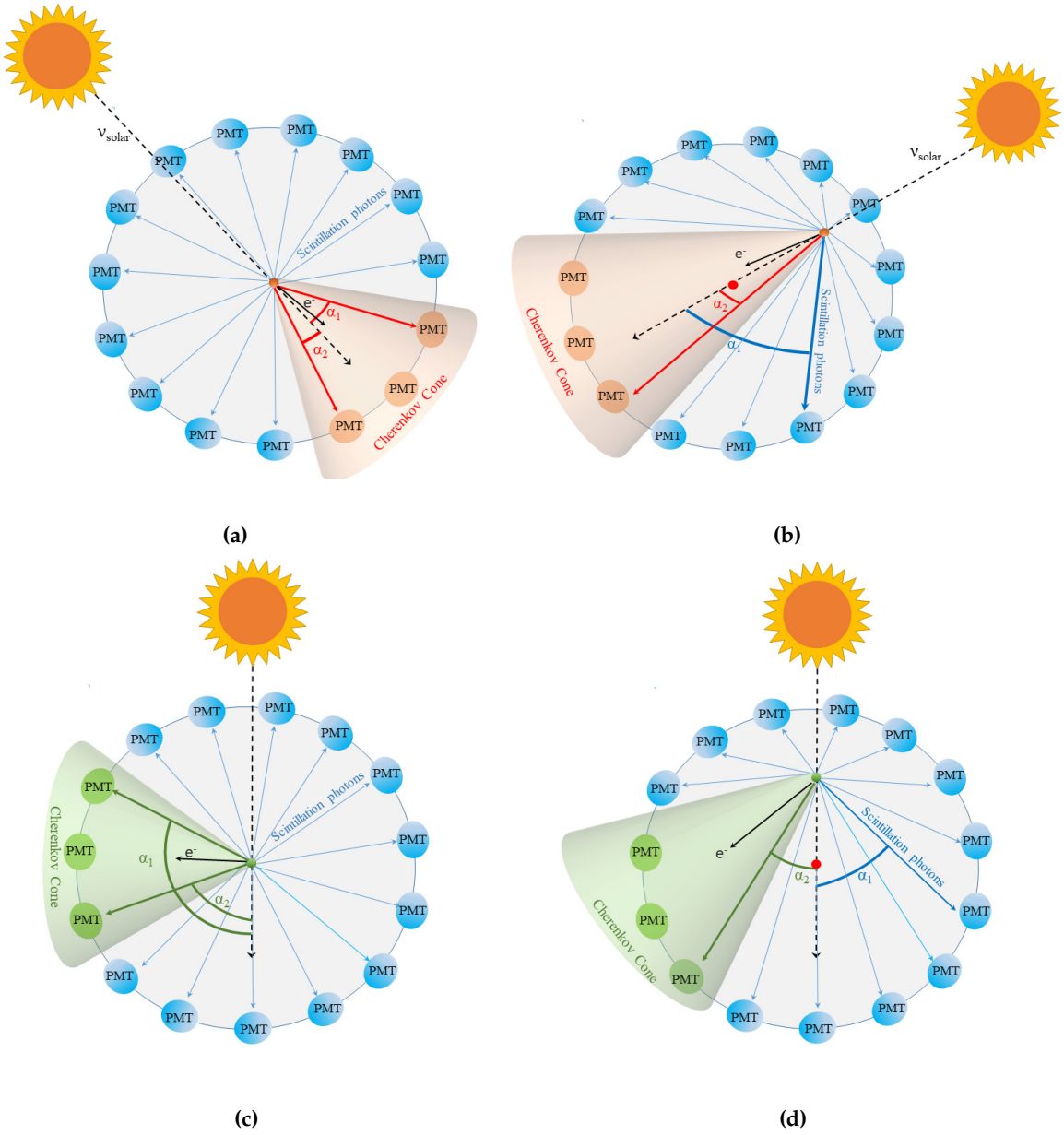

Figure 5.1: Schematic representation of the CID angle, expressed by the angle α between the Sun's position in Borexino's coordinates and the direction of emitted photons, which is given by the reconstructed vertex and hit PMT position. (a) Electron recoiled by a solar neutrino at the detector center produces the Cherenkov photons (red arrows) in a cone (orange cones) pointing forward in the direction of the Sun and the isotropic scintillation photons (blue arrows). α_1 and α_2 are the directional angles of the first and second detected photons of the event, respectively. The Cherenkov photons and the PMT hits, that are triggered by them, are correlated to the incoming direction of the solar neutrinos. (b) It is also possible that the first detected photon in an solar neutrino event is a scintillation photon, therefore not correlated to the direction of the solar neutrino, and the second detected photon is a Cherenkov photon. In addition, this event happens off-center. (c) An electron from the intrinsic radioactive background also produces a Cherenkov photons (green arrows) and isotropic scintillation photons (blue arrows). As before, α_1 and α_2 are the directional angles of the first and second photons of the background event, respectively. Here, the Cherenkov photons have no correlation to the Sun's direction. (d) Background event similar to (c), but this is an event happening off-center, where the first photon is a scintillation photon and the second detected photon is a Cherenkov photon. Used in [4,5].

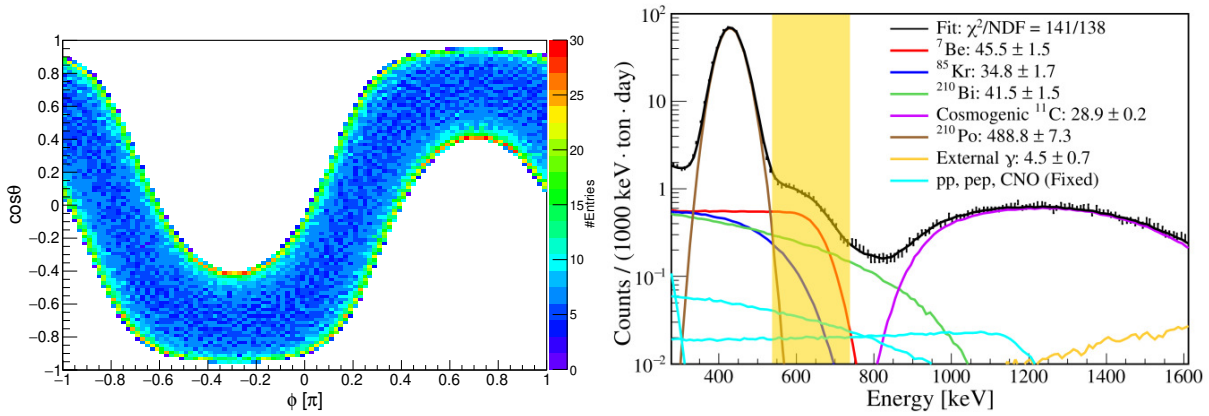

(a) **(b)**

Figure 5.2: (a) The solar neutrino direction distribution in $(\phi, \cos\theta)$ space in Borexino coordinate system, corresponding to 1 year time period with an time interval of ∼15 min. (b) The spectral fit of energy distribution of Phase-I data. Along with the fitted data, the PDFs of different components of the solar neutrinos and backgrounds are shown [159]. The energy region used for the CID analysis in Phase-I is shown in yellow band. From [4, 5].

photon. Here, α is defined as the angle between the incoming solar neutrino direction and the photon direction. The photon direction is given by the reconstructed position of the event and the hit-PMT position. By doing so for all detected events, the $\cos\alpha$ distribution is produced. The $\cos\alpha$ distribution consists of contributions from both the directional Cherenkov and isotropic scintillation photon hits. The $\cos\alpha$ distribution of solar neutrino events will have a characteristic peak at positive $\cos\alpha$ values due to the contribution of Cherenkov photon hits, which is correlated to the Sun's position. For background events, the $\cos\alpha$ distribution is expected to be flat in an ideal scenario, as the event direction as well as the direction of all photons are not correlated to the solar direction. As the scintillation photons are dominant in LS detectors (>99% of the total optical photons), an event-by-event directional reconstruction is not possible, unlike the water Cherenkov detectors. It is now possible to exploit the $\cos\alpha$ distribution to statistically separate the solar neutrino signal events from the data by using the directional Cherenkov information. However, the CID technique alone is not enough to distinguish between several kinds of solar neutrinos in Borexino.

Solar direction in Borexino

The solar neutrino direction is given by the position of the Sun, calculated for each detected event in real time. The Sun's position is determined for the event trigger time and the Borexino's geographical coordinates. Then, it is converted to Borexino's spherical coordinate system. The solar direction is defined in $(\phi, \cos\theta)$, where θ is the azimuthal angle and ϕ is the polar angle. Figure 5.2a shows the solar direction distribution in Borexino's spherical coordinate system, for a 1 year time period. The Sun's position, as seen by Borexino, is not uniformly distributed in all directions, as shown in Fig. 5.2a.

N^{th} hit method

As it is already mentioned, the $\cos\alpha$ distributions of early hits are exploited in the CID technique. This is due to the fact that the sub-dominant Cherenkov photons are emitted earlier in time, with respect to the slower and dominant scintillation photons, and therefore, the directional information is mostly contained in the early hits. A time cut (in units of nanoseconds) could be applied to maximise the sensitivity to Cherenkov

photons. However, the small systematic differences between data and MC hit time distributions for a large statistics of events, particularly at the early times, make it difficult to select the Cherenkov photons using an absolute hit-time cut [5]. Therefore, the so-called N^{th} hit method is adopted, that takes into account the relative timing of the hits. For each event, the PMTs hits are sorted in time with respect to the reconstructed start time of the event. In addition, the Time-of-Flight (ToF) subtraction is also performed so that the distribution is comparable for events at center as well as near to the edge of fiducial volume. Here, the ToF is calculated as:

$$\mathrm{ToF} = n_{\mathrm{eff}} \cdot \frac{d_{\mathrm{PMT}}}{c}, \tag{5.1}$$

where d_{PMT} is the distance between the reconstructed event vertex and the PMT that detected the hit and c is the speed of light in vacuum. The effective refractive index of Borexino LS n_{eff}, represents the average group velocity of all optical photons in the detectable wavelength range in Borexino LS.

These relatively ordered hits in time are then classified as the 1^{st} hit, 2^{nd} hit and so on, up to the total number of hits for each event. Each of these hits are referred to as the so-called N^{th} hit. The CID $\cos\alpha$ distributions are produced for each N^{th} hit, for all detected data and simulated solar neutrino and background events. Thus, the $\cos\alpha$ distribution of each N^{th} hit has entries equal to the total number of events. A cut on the maximum N^{th} hit is optimised for the CID analysis to maximise the relative contribution of Cherenkov photons, which will be discussed in Sec. 5.5.2 and 5.6.2. The benefit of using the N^{th} hit method is that the absolute average differences in the hit time distribution between data and MC are effectively resolved, and a precise knowledge of the absolute hit time is not required. Then, the data $\cos\alpha$ distributions of all selected N^{th} hits are fitted simultaneously with the MC PDFs of solar neutrino signal and background, using the strategy described in Sec. 5.4.

The n_{eff} parameter in eq. 5.1, was initially tuned on Borexino's position reconstruction algorithm (see Sec. 3.2.1) such that the correct reconstruction of the event positions of calibration source is performed [172]. Therefore, an improved estimation using ^{14}C-^{222}Rn calibration source at different detector locations has been performed [215], in order to take into account the hit time properties of photons which is crucial for the CID analysis. This analysis was performed on the PMT hit time distributions of the extracted ^{214}Po events from the calibration source. The extracted n_{eff} values are (1.6631 $\pm$ 0.0005) for data and (1.6531 $\pm$ 0.0003) for MC. These results are in agreement within the instrumental error on the measured refractive index and the difference in data and MC values is also compatible within this error.

5.3 Monte Carlo production for CID

In Borexino MC (Sec. 3.2.5), the Cherenkov photons, necessary to perform the CID analysis, are simulated according to the Frank–Tamm formula [175]. Their spectrum as well as their velocity in the liquid scintillator depend on the wavelength-dependent refractive index $n(\lambda)$. The wavelength spectrum detected by the PMTs according to the MC is shown in Fig. 5.3a. Both scintillation (blue) and Cherenkov (red) spectra start sharply at 370 nm. This is due to the absorption of the light in the scintillator and its re-emission by the PPO. The Cherenkov light with a wavelength $\lambda < 370$ nm are absorbed and re-emitted as the scintillation light. There has been no dedicated calibration in Borexino for the Cherenkov light, as it has been observed that the unabsorbed Cherenkov light has only a negligible influence on the Borexino's position reconstruction and other algorithms, as well as the spectroscopic analyses.

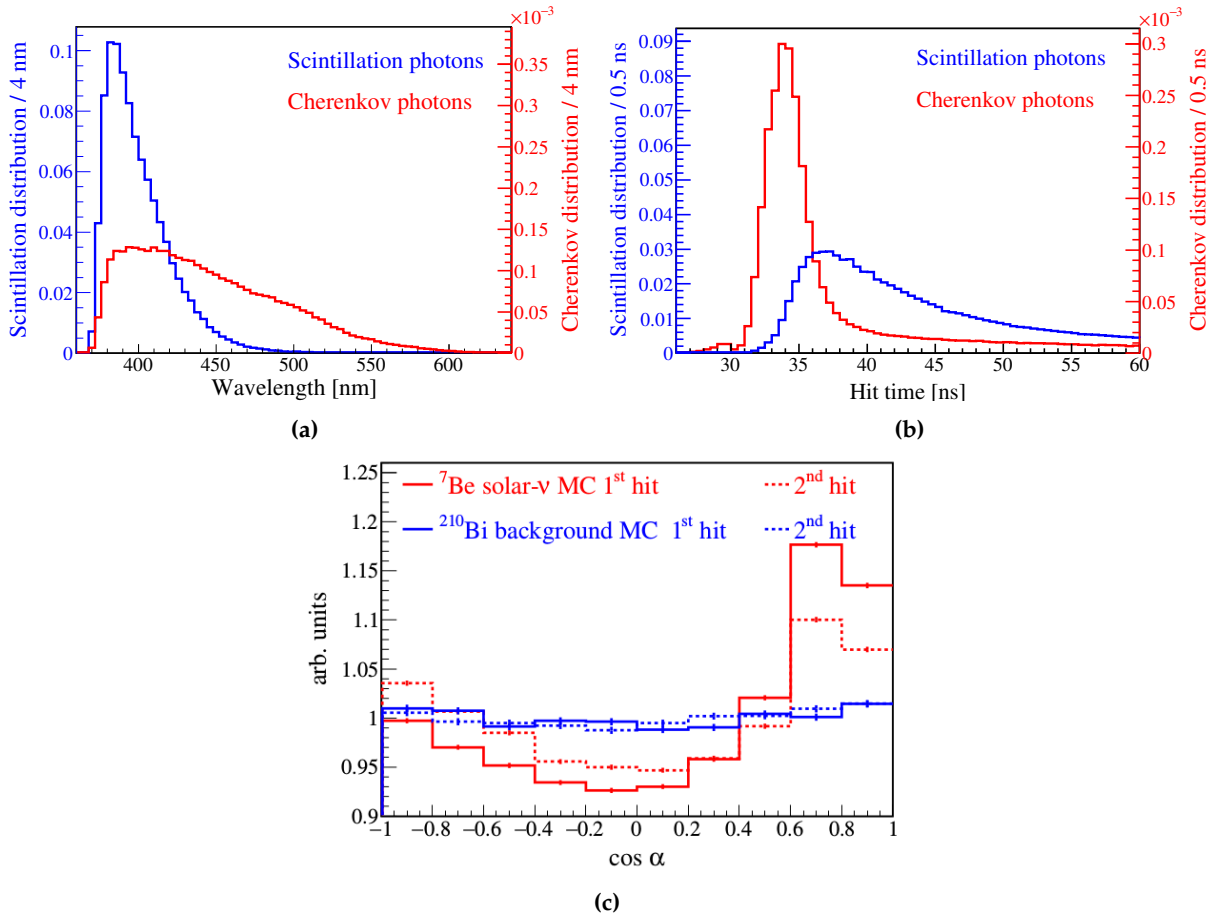

Figure 5.3: (a) The wavelength spectra of scintillation (blue) and Cherenkov (red) photons as detected by the PMTs in Borexino MC, including all the effects of absorption and re-emission. (b) The hit-time distributions, corrected with the Time-of-Flight for the simulated ^{7}Be solar neutrino recoil electrons, as described in Sec. 5.5.1. In (a) and (b), the left y-axis shows the scintillation light (blue), normalized to 1 and the right y-axis shows the Cherenkov light (red), normalized to the number of Cherenkov hits relative to the scintillation hits, which is ∼0.35%. (c) The cos α distributions for MC events of ^{7}Be solar neutrinos (red) and ^{210}Bi background (blue) in ^{7}Be-ν energy region, as shown in Sec. 5.5.1. The histograms are normalized to have the same area. As it can be seen, the first hit of ^{7}Be MC has more directional information than the second hit due to a larger Cherenkov contribution in the first hit. For the ^{210}Bi background MC, there is no dependence on the Nth hit, as the direction of photon hits of background events are uncorrelated to the Sun's position [5].

The Cherenkov light is emitted instantaneously, while the scintillation light emission follows a multi-exponential decay time where the fastest component has 1.6 ns [175]. This intrinsic time distribution is affected by various optical processes during the light propagation, Transition Time Spread (TTS) of the PMTs, as well as the precision of the PMT time calibration. The ToF corrected PMT hit time distribution of Cherenkov and scintillation photons, as obtained from the ^{7}Be-ν MC after the full simulation and reconstruction chain, is shown in Fig. 5.3b. The time axis is normalized such that the beginning of the scintillation time profile corresponds to the ToF of photons from the center of the detector. The expected ratio between all the detected Cherenkov and the scintillation hits in the ^{7}Be-ν energy region is ∼0.35%.

The Borexino MC is used to produce the CID cos α PDFs for both the solar neutrino signal and for the radioactive backgrounds. The recoil electrons of solar neutrinos are simulated according to their theoretical energy spectrum and the angle relative to the neutrino direction (eq. **??**). The signal and background MC simulations are performed on an event-by-event basis. For each individual data event, which corresponds to a certain position of the Sun, 200 MC events are simulated within a sphere of radius =

15 cm around the reconstructed data event position and with the distribution of PMTs, that were active as in the data. The advantage of this procedure is that the possible hit patterns of the active PMTs relative to the position of the Sun and the event position are correctly taken into account in the MC production. This procedure is repeated for each event twice: once assuming it is the neutrino signal and once assuming it is the radioactive background, according to their spectral shape within the selected energy regions. The systematic uncertainty associated to this procedure, due to any possible bias in the selection of events' positions, has also been studied and are discussed later. Figure 5.3c shows the CID $\cos\alpha$ distributions for the first two N^{th} hits of the solar neutrino and background events, simulated using MC in the ^{7}Be-ν energy region (see Sec. 5.5.1).

5.4 Fit strategy

After producing the $\cos\alpha$ distributions of each N^{th} hit in the data as well as the MC solar neutrino and background components, a χ^2 fit is performed to extract the total number of solar neutrino events, $N_{solar-\nu}$ from the data. The strategy is to simultaneously fit the data $\cos\alpha$ distributions of each hit, up to the optimised maximum N^{th} hit, N^{th} hit(max), with the $\cos\alpha$ distributions of the corresponding N^{th} hit of the simulated solar-ν and background events. The χ^2 is defined as follows:

$$\chi^2 = \sum_{n=1}^{N^{th}\text{-hit(max)}} \sum_{i=1}^{\text{bins}} \left[\frac{\{\cos\alpha^D_{n,i} - norm \cdot \cos\alpha^M_{n,i}(N_{solar-\nu},\, gvc_{ch},\, \Delta r_{dir})\}^2}{norm \cdot \cos\alpha^M_{n,i} + norm^2 \cdot \cos\alpha^M_{n,i}} + \frac{\{gvc_{ch} - gvc^{result}_{ch}\}^2}{\{\sigma(gvc^{result}_{ch})\}^2} \right], \quad (5.2)$$

where n, i represent the indices for N^{th} hit and number of bins, that run from 1 to the selected N^{th}-hit(max) and total numbers of bins, respectively. The $\cos\alpha$ values of i^{th} bin and n^{th} hit of the data and the MC model are given by $\cos\alpha^D_{n,i}$ and $\cos\alpha^M_{n,i}$, respectively. The term *norm* is the scaling factor between the simulated MC statistics and number of events in the data, N_{data}. The term "$norm^2 \cdot \cos\alpha^M_{n,i}$" accounts for the finite statistics of MC. Since the model is built using the distributions of both signal S and background B, the representation $\cos\alpha^M_{n,i}$ is given by:

$$\cos\alpha^M_{n,i} = \frac{N_{solar-\nu}}{N_{data}} \cdot \cos\alpha^S_{n,i}(\Delta r_{dir},\, gvc_{ch}) + \left(1 - \frac{N_{solar-\nu}}{N_{data}}\right) \cdot \cos\alpha^B_{n,i}. \quad (5.3)$$

In the fit, $N_{solar-\nu}$ is the parameter of interest, which is free to vary. In addition, there are two parameters, Δr_{dir} and gvc_{ch}, that affect $\cos\alpha$ distributions of solar-ν only and are treated as nuisance parameters. As a result, a three dimensional χ^2 profile is obtained. In order to take into account the nuisance parameters, χ^2 is minimised over Δr_{dir} and gvc_{ch}, for each value of $N_{solar-\nu}$. The parameters, Δr_{dir} and gvc_{ch}, represent the event position reconstruction bias and an effective correction on the group velocity of Cherenkov photons, respectively. The parameter Δr_{dir} is free to vary, while gvc_{ch} is constrained using a pull term, as can be seen in eq. 5.2.

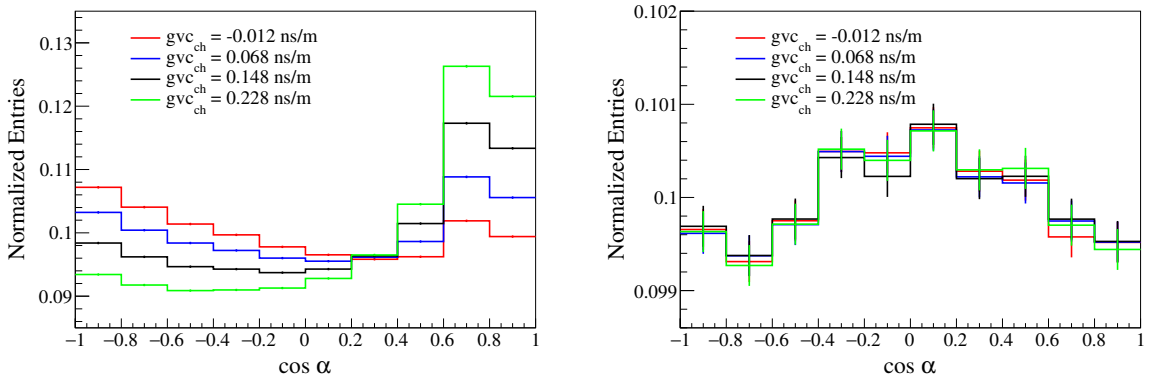

Figure 5.4: (a) Effect of varying effective correction of the group velocity for Cherenkov photons (gvc_{ch}) on the signal $\cos\alpha$ PDFs for N^{th} hit = 1 and fixed Δr_{dir} = 2.0 cm. (b) Effect of varying gvc_{ch} on the background $\cos\alpha$ PDFs for N^{th} hit = 1. All $\cos\alpha$ PDFs correspond to Phase-II and are obtained in ^{7}Be-ν energy region, discussed in Sec. 5.5.1.

Nuisance parameters

There are two nuisance parameters in the fit, Δr_{dir} and gvc_{ch}, which are described as follows:

Effective correction of the group velocity for Cherenkov photons (gvc_{ch}): This parameter takes into account the small differences in the relative hit time distribution between scintillation and Cherenkov photons in data, relative to the one in MC. In Borexino, the effective wavelength spectrum of detected Cherenkov photons has not been measured before, and the wavelength dependent refractive index in MC also has a finite accuracy. Since the wavelength distribution differs for Cherenkov and scintillation photons as shown in Fig. 5.3a from MC, their average group velocity, $\overline{v_g}$ can be different in data and MC. Therefore, we apply a correction in MC so that the relative group velocities of Cherenkov and scintillation light, $\Delta\overline{v_g}$ in data and MC are in agreement:

$$\Delta\overline{v_g}(Data) = \Delta\overline{v_g}(MC). \tag{5.4}$$

The correction is applied in MC on the PMT hit time for Cherenkov photons as follows:

$$\begin{aligned} t^{\text{ToF}}_{\text{corr}} &= t^{\text{ToF}}_{\text{MC}} - (gvc_{\text{ch}} \cdot L_{\text{true}}), \\ &= t^{\text{ToF}}_{\text{MC}} - \left(\frac{\Delta n_{\text{ch}}}{c} \cdot L_{\text{true}}\right), \end{aligned} \tag{5.5}$$

where $t^{\text{ToF}}_{\text{MC}}$ is the normal hit time (after ToF subtraction) of the Cherenkov photons in MC, $t^{\text{ToF}}_{\text{corr}}$ is the corrected hit time (and ToF subtracted) of the Cherenkov photons, and L_{true} is the MC photon track length. The gvc_{ch} parameter has the units of ns m^{-1} and can further be expressed as a function of effective change in the refractive index Δn_{ch} at a particular wavelength.

The gvc_{ch} parameter influences the shape of signal PDFs, as shown in Fig. 5.4a. This is because varying gvc_{ch} changes the ratio of Cherenkov photons arriving in the early hits as this correction is applied to the simulated Cherenkov photons only. Therefore, the calibration of this parameter in MC is necessary, which has been performed using

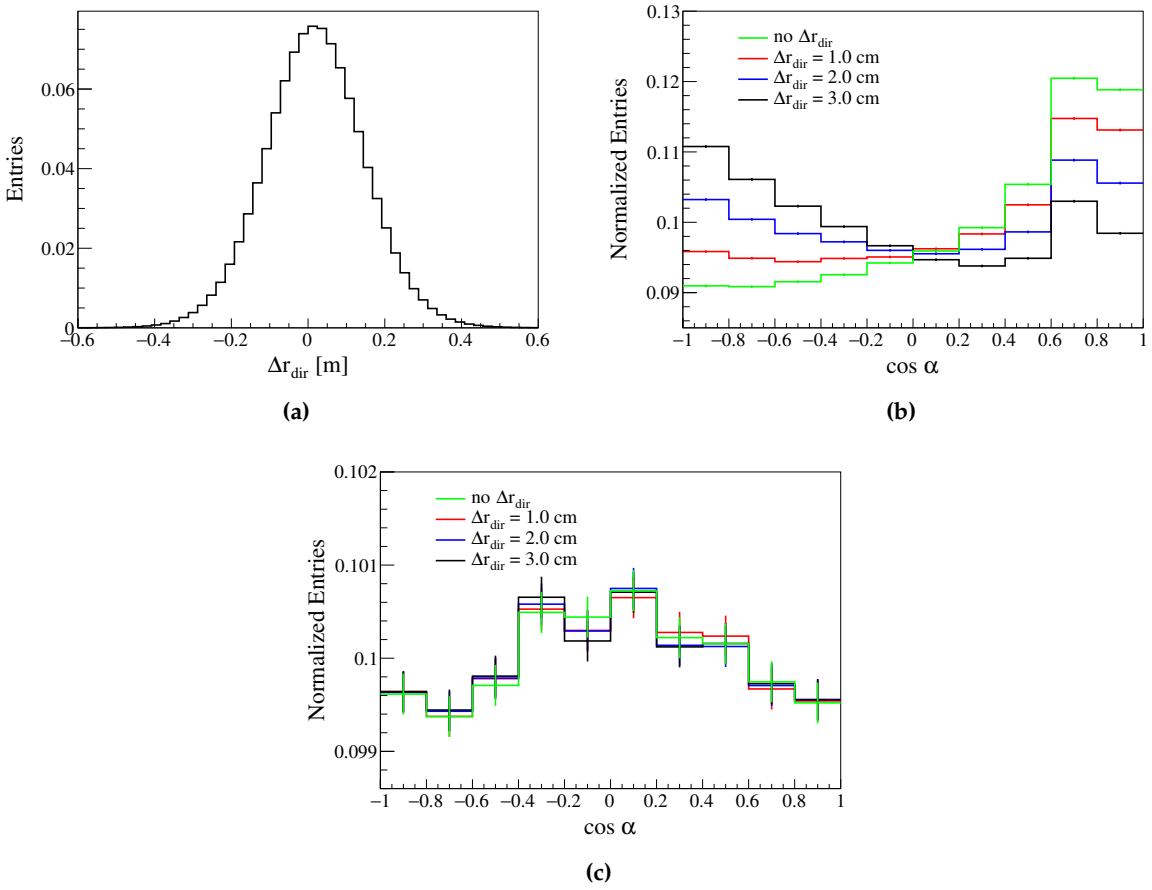

Figure 5.5: (a) The distribution of the bias Δr_{dir}, obtained from many MC recoil electron events. (b) Effect of varying event vertex mis-reconstruction (Δr_{dir}) on the signal $\cos\alpha$ PDFs for N^{th} hit = 1 and a fixed gvc_{ch} = 0.068 ns/m. (c) Effect of varying Δr_{dir} on the background $\cos\alpha$ PDFs for N^{th} hit = 1. All these distributions correspond to Phase-II and are obtained in ^{7}Be-ν energy region, discussed in Sec. 5.5.1.

γ calibration sources (Sec. 5.5.3), as well as using ^{7}Be solar neutrinos (Sec. 5.6.3). However, it does not impact the shape of backgrounds PDFs, as can be seen in Fig. 5.4b. It is to be noted that this systematic difference in data and MC for the sub-dominant Cherenkov light does not influence the spectral analysis, which was discussed in the previous Chapter.

Event vertex mis-reconstruction (Δr_{dir}): In MC, it is observed that the reconstructed position of an event is slightly shifted towards the true direction of the recoiled electron. The position reconstruction algorithm of Borexino determines the most likely vertex of the event using the hit time PDFs of the detected hits on the PMTs. The early hits tend to pull reconstructed position of the corresponding event towards their own direction and the Cherenkov photons arrive to the PMTs, on average, at earlier times with respect to the scintillation photons, as well as they are emitted in the initial direction of electron. Since the direction of all photon hits in the CID analysis is calculated using the reconstructed event position, the reconstructed photon direction is also biased. In addition, the ToF subtraction, before the relative ordering of hits, is also performed using the reconstructed event vertex for all detected hits. This gives rise to an indirect effect of the Cherenkov photons. The bias $\Delta r^{i}_{\text{dir}}$ is calculated for each event as follows:

$$\Delta r^{i}_{\text{dir}} = \left(\vec{r}^{\,i}_{\text{rec}} - \vec{r}^{\,i}_{\text{true}}\right) \cdot \vec{d}^{\,i}_{\text{true}}, \tag{5.6}$$

where $\vec{r}^{\,i}_{\text{true}}$ is the true position of an event i, the true direction of the simulated recoil electron is $\vec{d}^{\,i}_{\text{true}}$, and the reconstructed position is $\vec{r}^{\,i}_{\text{rec}}$. A distribution of the bias Δr_{dir} is obtained from many MC recoil electron events, as shown in Fig. 5.5a. Then, the mean Δr_{dir} of the distribution is extracted.

As the direction of Cherenkov photon hits of solar neutrinos are correlated to the Sun's position, the impact of vertex bias is seen for the solar-ν events only. The influence of Δr_{dir} parameter on the shape of CID $\cos\alpha$ distributions of the signal is shown in Fig. 5.5b. One can see that it impacts the slope at negative $\cos\alpha$ values. In the Borexino MC, its value is estimated to be $\sim$2 cm and $\sim$3 cm in the selected region of interest for the ^{7}Be-ν and CNO-ν analysis, respectively. These values are relatively small, as compared to the position resolution in Borexino (Sec. 3.2.1) and therefore, not relevant for the spectral analysis. Moreover, varying Δr_{dir} parameter does not impact the shape of background events' $\cos\alpha$ distributions, as shown in Fig. 5.5c. Due to lack of the dedicated calibrations, its value is unknown in the data and can be different in data and MC due to the differences in the underlying hit time distributions. So, Δr_{dir} is treated as a free nuisance parameter in the fit.

5.5 Directional analysis of ^{7}Be solar neutrinos

This section provides proof of principle of the CID method, that is, to use directional Cherenkov hits for the detection of sub-MeV neutrino events in Borexino. Therefore, the CID analysis is performed in an energy window of $\sim$(0.5 - 0.8) MeV, that lies around the Compton-like edge of the ^{7}Be neutrinos, where the contribution from the sub-MeV solar neutrino events is maximal. Here, the effective correction of the group velocity for Cherenkov photons (gvc_{ch}) is determined using the γ calibration sources, which were deployed in Borexino during Phase-I and thus, the full analysis is done in Phase-I (Sec. 5.5.3). By doing CID analysis on the first two hits of selected events in this energy region, the detection of sub-MeV solar neutrinos with $>5\sigma$ significance is carried out. In addition, a measurement on the number of solar neutrinos in the region of interest is performed, including all systematic effects in Phase-I. These results are then used to infer the interaction rate of ^{7}Be solar neutrinos in Borexino, after the subtraction of other subdominant solar neutrinos lying in this energy window. For the other phases, the exclusion of background hypothesis only is also provided, as will be discussed in Sec. 5.5.5.

5.5.1 Data selection

For the directional analysis of ^{7}Be solar neutrinos, the selection criteria for all phases of Borexino detector until February 2020 is studied. The standard selection cuts are applied on the dataset of each phase, as described in Sec. 3.2.4, in order to veto the muons and the cosmogenic backgrounds as well as to reduce the contribution from backgrounds coincidences and noise events. The additional cuts, that are applied to obtain high statistics and a good ratio of solar neutrino signal with respect to the radioactive backgrounds in the detector, are listed as follows:

- **Fiducial Volume (FV)** : The enlarged fiducial volumes of spherical shape with R $<$ 3.3 m and mass 132.1 t (for Phase-I and Phase-II), and R $<$ 3.0 m and mass 99.3 t (for Phase-III) are chosen. Note that this fiducial volume is larger than the one applied in the spectroscopic analysis of Borexino, as the pepFV is used in the spectral fit analyses (Chapter 4).

  The choice of spherical shape of the fiducial volume, with respect to the asymmetrical shape of pepFV, is motivated by studying the effects on the shape of $\cos\alpha$

Phase	Fiducial volume	Energy cut	Total Events	Signal to total ratio
Phase-I	R < 3.3 m	$225 < N_h^{geonorm} < 305$	19904	51%
Phase-II	R < 3.3 m	$210 < N_h^{geonorm} < 310$	29686	76%
Phase-III	R < 3.0 m	$200 < N_h^{geonorm} < 320$	19893	81%

Table 5.1: Summary of data selection cuts for the CID analysis in the ^{7}Be edge region and the total number of events in data of each phase. The last column reports the expected ratio of signal to the total number of events in ROI. Here, the rate predictions of solar neutrino events is taken from high-metallicity SSM B16-GS98 (Table 5.3), and the trigger and energy efficiencies are calculated using the Borexino MC energy PDFs.

distribution of backgrounds using toy MC simulations. The procedure of toy MC studies is described in Sec. 5.5.4 and the influence of shape of fiducial volume on $\cos\alpha$ distribution of backgrounds is shown in Fig. 5.10a. As can be seen, the choice of a spherically asymmetric fiducial volume can lead to the deviation of background distribution shape from an ideal flat distribution and thus, a spherical fiducial volume is chosen. Moreover, a spherical fiducial volume also benefits from a large event statistics. A larger FV can be used for the CID analysis because the energy region of interest is lower than the typical energy region of the external γ backgrounds, which also dominates at larger radii and the end cap regions outside pepFV..

- **Energy cut** : In order to maximise the number of solar neutrino events over the total events, a Region of Interest (ROI) of approximately 0.5-0.8 MeV is chosen for all the phases. This region lies around the ^{7}Be Compton-like edge as shown in Fig. 5.2b and has a dominant contribution from ^{7}Be solar neutrinos, which is the main signal in this ROI. It also has a sub-dominant contribution from *pep* and CNO solar neutrinos and the contribution from ^{8}B solar neutrinos is negligible. In this ROI, the ^{210}Po, ^{210}Bi and ^{85}Kr contribute as the backgrounds. Here, the $N_h^{geonorm}$ (Sec. 3.2.1) is used as the energy variable, since it takes into account the non-uniformity due to the dead PMTs position. Table 5.1 reports the optimised energy cuts, using the strategy described below.
- **Pulse shape discrimination cut**: The α/β discrimination technique is used to reject the non-uniform ^{210}Po α background events lying in ROI. The events with MLP parameter $>$0.3 are chosen for this analysis.

The upper threshold of ROI and the radius of fiducial volume cut have been chosen simultaneously, based on the energy spectra of data via studying event rate in different radial shells with respect to pepFV [216]. This optimisation is based on the fact that the presence of only non-uniform external γ backgrounds can increase the event rate in the detector, with respect to the pepFV and in the higher energy regions. This strategy results in a high statistics of the data events, without compromising on the signal to background ratio. The lower energy cut is optimised through a *Figure of Merit* (FOM) estimation using the MC energy PDFs, after fixing the above mentioned higher energy and the radial cut:

$$\mathrm{FOM} = \frac{N_{\mathrm{solar}-\nu}}{N_{\alpha-\mathrm{bckg}} + \sqrt{(N_{\mathrm{solar}-\nu} + N_{\beta-\mathrm{bckg}})}}, \tag{5.7}$$

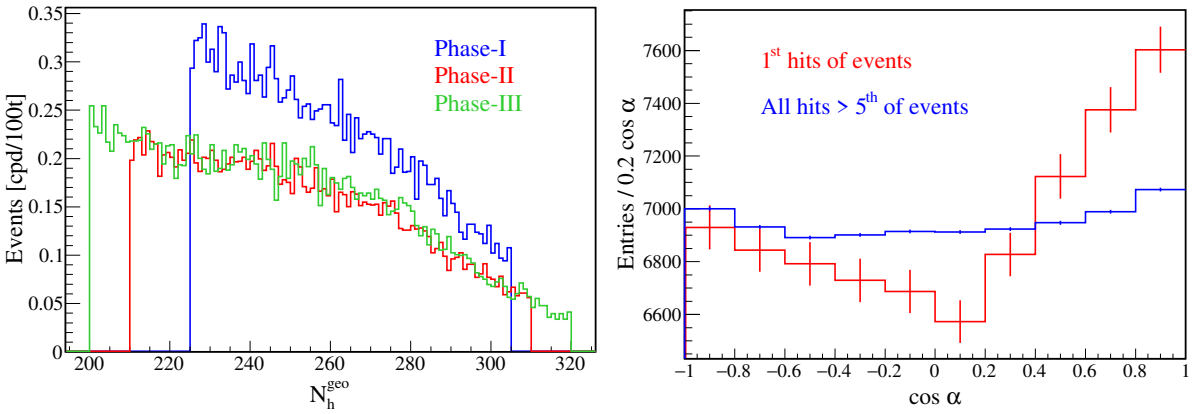

(a) **(b)**

Figure 5.6: (a) Energy distributions of the data events in ^{7}Be ROI for CID analysis, after applying selection cuts in Phase-I (blue), Phase-II (red), and Phase-III (green) [5]. (b) The CID $\cos\alpha$ distribution of 1st hit (in red) and >5th hits (in blue) data in ROI for Phase-I+II+III after relative time ordering, as described in Sec. 5.5.2, where both distributions are normalized to the same statistics [5].

where $N_{\text{solar}-\nu}$ is the total number of expected solar neutrino events (^{7}Be, CNO, and *pep*), $N_{\alpha-\text{bckg}}$ is the number of residual ^{210}Po events after MLP cut and taking into account the energy-dependent efficiency of the MLP variable, and $N_{\beta-\text{bckg}}$ is the sum of the β-decay background components (^{210}Bi and ^{85}Kr). The square root in the denominator is used to account for the Poisson statistical errors. However, the residual ^{210}Po background is taken out of the square root to give more weight to this background and suppress it strongly.

Table 5.1 summarizes the fiducial volume and energy cuts for all phases, including the total number of data events, after application of these selection cuts. It also reports expected ratio of the solar neutrino events to the total number of all events in ROI, using the rate predictions of solar neutrino events from high-metallicity SSM B16-GS98, as well as the trigger and energy efficiencies from Borexino MC energy PDFs. The energy distribution of selected data events is shown in Fig. 5.6a. The $\cos\alpha$ distributions of time ordered 1st hit (in red) and >5th hits (in blue) of all selected data events in combined Phase-I+II+III after time of flight (ToF) correction, is shown in Fig. 5.6b. One can clearly see the peak at $\cos\alpha > 0$ for 1st hit (red) due to significant contribution of Cherenkov photons, while for all later hits (blue), no directional peak is visible, as the isotropic scintillation photons are dominant. The blue distribution is non-flat, due to the effects described in Sec. 5.5.4.

The ^{7}Be solar neutrinos are the dominant signal ($\sim$89% of the total neutrino signal) in the selected ROI. So, the MC PDF for ^{7}Be solar neutrino is used as the signal PDFs for the further analysis in ROI. Other sub-dominant solar neutrinos, CNO and *pep* neutrinos contribute at a level of $\sim$7% and $\sim$4% of the total neutrino signal in ROI. The difference between $\cos\alpha$ distributions of different solar neutrinos in the ROI has been found to be negligible, which could be present as a result of the dependence of neutrino-electron scattering angle on the energy of scattered electron as well as the neutrino energy. For the backgrounds, the β-decaying ^{210}Bi events are simulated. As all the backgrounds are isotropic and not correlated to the Sun's position, the PDFs of all other backgrounds are found to have the same shape. The ^{210}Po events, which are non-uniformly distributed in the detector, are suppressed by MLP cut because the non-uniformity in the position distribution of events can lead to the differences in the backgrounds' $\cos\alpha$ distribution (see Sec. 5.5.4).

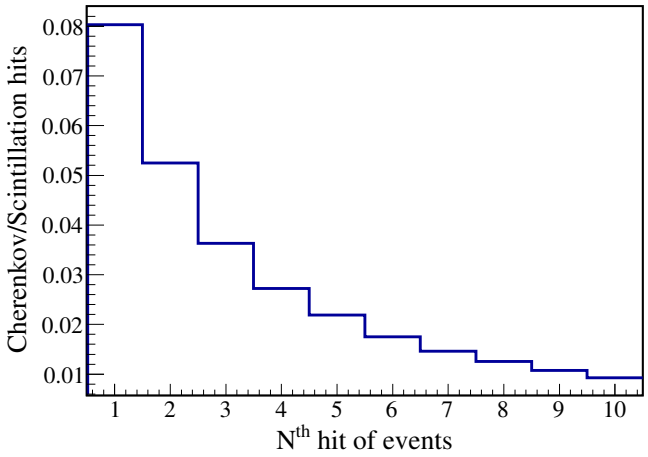

Figure 5.7: Detected Cherenkov to the scintillation photon hits ratio as a function of the N^{th} hits of ^{7}Be MC events [5].

5.5.2 Analysis Criteria

N^{th} hit selection

A cut on the N^{th} hit, N^{th}-hit(max) is selected in order to maximise the amount of Cherenkov photons for the CID analysis. Figure 5.7 shows the ratio of Cherenkov to scintillation light as a function of N^{th} hit of all the events in ROI, discussed in Sec. 5.5.1. As it can be seen, the early hits have the highest sub-dominant Cherenkov contribution, followed by a steady decrease in the ratio for the later hits. A χ^2 test between $\cos\alpha$ PDFs of each N^{th} hit of MC signal and the background ones is performed for fixed nuisance parameters. It has been found that the first hit of all events has the highest directional information, while the 2^{nd} hit also has some sensitivity to the directional differences between the signal and background MC PDFs [174, 215]. The χ^2 distribution is observed to be flat for N^{th} hit > 4. The N^{th}-hit(max) = 2 is chosen for the analysis and due to the possible systematic bias in the final result as a function of N^{th}-hit(max), the choice of N^{th}-hit(max) is considered for the systematic uncertainty in Sec. 5.5.4.

Selection of number of bins

A dedicated study for the selection of number of bins is necessary, in order to have optimal information in the distributions used for the fit. Having relatively small or large number of bins can smear out or decrease the impact of the directional information in the $\cos\alpha$ distributions and hence, can influence the expected precision on the parameter of interest. Therefore, the number of bins of the $\cos\alpha$ distributions in eq. 5.2 is optimised using a MC based pseudo-experiment approach. In this approach, the pseudo-datasets are created by sampling the solar neutrino (^{7}Be) and background (^{210}Bi) $\cos\alpha$ PDFs with certain values of nuisance parameters. The total number of events in these pseudo-datasets is set to be the same as the data statistics, and the contribution of solar neutrino events is taken from the expected signal to total events ratio. Both pseudo-data and MC $\cos\alpha$ PDFs are created with different number of bins. For each binning, 10,000 pseudo-datasets are fitted with the MC PDFs of signal and background events using χ^2 defined in eq. 5.8. In this equation, the number of solar neutrino events, $N_{\mathrm{solar}-\nu}$ is free to vary, while the nuisance parameters are fixed in the

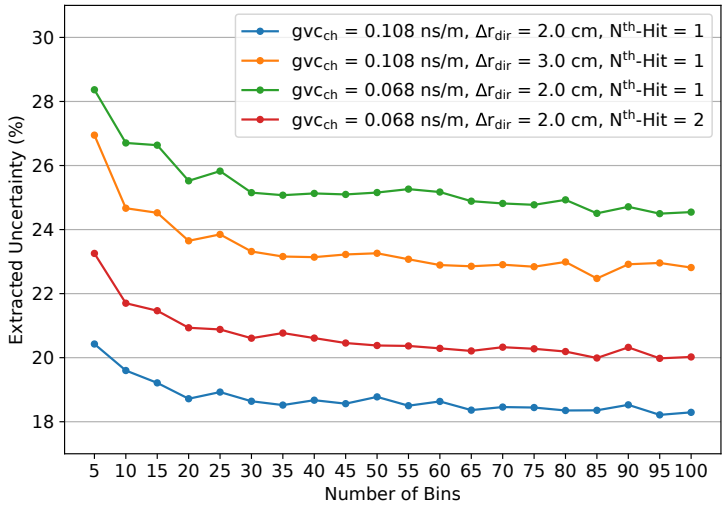

Figure 5.8: The distributions of the extracted uncertainty (%), defined as the ratio of Root Mean Square (RMS) of the $N_{\text{solar}-\nu}$ distribution to the injected value of $N_{\text{solar}-\nu}$ in Phase-I, as a function of the number of bins in the $\cos\alpha$ histograms of pseudo-data and MC PDFs. $N_{\text{solar}-\nu}$ is injected with the expected value in Phase-I. The $N_{\text{solar}-\nu}$ distribution is extracted from the fit of pseudo-data and MC PDFs, where the total number of events in pseudo-data is same as in the real data, with different injected values of parameters: gvc_{ch} and Δr_{dir}. The fit is performed using χ^2 defined in eq. 5.8, where $N_{\text{solar}-\nu}$ is the only free parameter and other fit parameters are fixed to their injected values. The distributions in different colors represent different fit configurations. In all cases, the extracted uncertainty decreases for the number of bins <30, while for later bins, the distributions do not show strong dependence on the number of bins.

fit to their injected values. The χ^2 is defined as:

$$\chi^2(N_{\text{solar}-\nu}) = \sum_{n}^{\text{N}^{\text{th}}\text{hit}} \sum_{i}^{\text{bins}} \left[\frac{\{\cos\alpha_{n,i}^{PD} - norm \cdot \cos\alpha_{n,i}^{M}(N_{\text{solar}-\nu})\}^2}{norm \cdot \cos\alpha_{n,i}^{M} + norm^2 \cdot \cos\alpha_{n,i}^{M}} \right], \tag{5.8}$$

where n, i represent the indices for the N^{th} hit and the number of bins, respectively. The $\cos\alpha$ values of i^{th} bin and n^{th} hit of the pseudo-data and the MC model are given by $\cos\alpha_{n,i}^{PD}$ and $\cos\alpha_{n,i}^{M}$, respectively.

For each configuration, we obtain a best fitted $N_{\text{solar}-\nu}$ value. A distribution of extracted $N_{\text{solar}-\nu}$ is produced from 10,000 fits, and the mean as well as the Root Mean Square (RMS) of this distribution are extracted for each configuration. Overall, a negligible bias of $< 0.5\%$ has been observed in the extracted mean $N_{\text{solar}-\nu}$ with respect to the injected value for all cases. The relative uncertainty (%), defined as the ratio of the RMS of the distribution to the injected $N_{\text{solar}-\nu}$, is also extracted.

Figure 5.8 shows the extracted uncertainty of the $N_{\text{solar}-\nu}$ distribution as a function of the number of bins, considering the total number of events and the expected signal ratio in Phase-I. Different trends represent different values of the injected nuisance parameters and the applied N^{th} hit cut. As can be seen from the figure, until about 30 bins, the distributions of the uncertainty on the extracted $N_{\text{solar}-\nu}$ show a strong dependence on the number of bins, while for later bins, the distributions become almost steady as a function of the number of bins. For example, for the injected values of $\text{gvc}_{\text{ch}} = 0.068\ \text{ns}\,\text{m}^{-1}$ and $\Delta r_{\text{dir}} = 2.0\,\text{cm}$, using only 1^{st} hit of the events, the extracted uncertainty decreases from $\sim$28% at 5 bins to about 25% at ≥ 30 bins. This is expected, as there is a loss of information if the number of bins is too small. A similar trend can

also be seen in the distributions, obtained with other injected values of nuisance parameters and N^{th} hit cut. It can also be observed that the extracted precision worsens with increasing Δr_{dir}, or with decreasing gvc_{ch} or N^{th} hit. This is expected because the more Cherenkov information is present in the $\cos\alpha$ distributions, the more sensitive the fit is to extract the number of solar neutrino events. For performing the CID analysis in ROI in Phase-I, a binning of 60 is chosen to avoid too few bins based on the above pseudo-experiments, as well as too large number of bins that can lead to few entries per histogram bin. As the analysis with >30 bins are expected to give a comparable precision and due to the possible systematic differences in the final result as a function of binning, the choice of number of bins between 30 to 100 bins is included as a systematic uncertainty (Sec. 5.5.4).

PMT selection and time calibration

In Borexino, the time equalization of the PMTs are performed weekly using laser calibration [172]. It has been found using the ^{14}C-^{222}Rn calibration source that there exists sub-nanosecond time differences between different PMTs in the data, necessary to take into account for the CID analysis. This means that some PMTs in data can observe early hits relative to the other PMTs due to an intrinsic time behaviour of the PMTs. If it is also not reproduced in MC, this could result in the fit bias and therefore, this effect should be corrected. In order to investigate this, the distance dependent hit time distributions for each PMTs in calibration data are constructed. These distributions are fitted with a bi-exponentially modified Gaussian distribution, which results in a distribution of mean hit time as a function of the distance from PMT to the source location. The data PMTs exhibited a hit time offset with respect to all the averages PMT hit time of about 0.3 ns [215], which corresponds to the standard deviation of the distribution of relative hit time offset. This behaviour is not present in the MC simulation. Thus, the differences between each PMT time constant and the mean of all PMTs time constants is then applied in data before time sorting of the photon hits, in addition to the ToF subtraction to ensure the accurate timing behaviour of the photon hits. In addition, when the number of 1^{st} hits is plotted as a function of PMTs number for all events for data and MC, it has been found that some PMTs in data show a deviation from the average number of hits. This behaviour is not observed in MC and therefore, the PMTs, whose hit behaviours are correctly reproduced in MC simulation as in data, are selected for the CID analysis. This is crucial for the directionality analysis as it uses the early hits, and any bias in the observed number of early hits can lead to the biased results. In order to ensure the compatibility of the number of early hits on the PMTs in data and MC, a subset of PMTs is selected, using the ratio of data hits to the MC hits (normalized to the data statistics) for each PMT. If the number of hits in MC is within 68% Poissonian C.I. of the data hits for a certain PMT, then the PMT is selected to be used in CID analysis [174, 215].

5.5.3 Calibration for Cherenkov photons using γ-sources

For CID analysis in the ^{7}Be edge energy region, the calibration data from γ sources [172], are used to estimate the systematic group velocity correction gvc_{ch} which is needed to be applied in MC for Cherenkov photons. As discussed in Sec. 5.4, this is necessary because the difference in relative group velocity of Cherenkov to scintillation photons in data with respect to the ones in MC can lead to a biased Cherenkov to scintillation hits ratio in the early hits and thus, can result in the bias of the fit results.

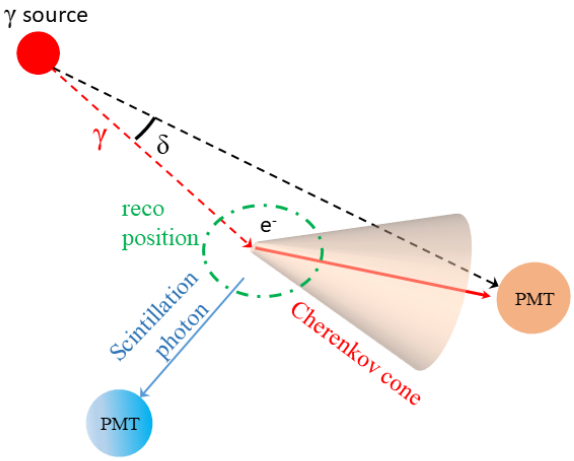

Figure 5.9: Schematic representation of the $\cos\delta$ angle, used in the calibration of group velocity correction $\mathrm{gvc_{ch}}$ for the Cherenkov photons in MC using the γ- sources. The direction of γ, emitted from the source (in red circle) is shown in red dashed line. The Compton scattered electron (e^-) emit Cherenkov photon (orange solid line) in a cone (orange cone), which is correlated to the direction of γ. The scintillation photon (solid blue line) is also shown to be emitted in the direction uncorrelated to the direction of γ. The δ angle corresponds to the angle between the reconstructed γ direction, based on the reconstructed position (green dashed circle), and the direction of the hit using the source location and the PMT position. Used in [5].

The MeV γs interact in Borexino liquid scintillator via Compton scattering on the multiple electrons, before they are absorbed in the scintillator. These scattered electrons excite the scintillator molecules, and the isotropic scintillation photons as well as sub-dominant Cherenkov photons are emitted. Similar to the CID analysis, a correlated angular distribution is also defined here, since the initial direction of Compton electrons and hence, the Cherenkov photons direction is also correlated to the initial γ direction.

$$\cos\delta_i = \frac{\left(\vec{r}_i^{\,\mathrm{PMT}} - \vec{r}_{\mathrm{source}}\right)\cdot\left(\vec{r}_{\mathrm{rec}} - \vec{r}_{\mathrm{source}}\right)}{\left|\left(\vec{r}_i^{\,\mathrm{PMT}} - \vec{r}_{\mathrm{source}}\right)\right|\left|\left(\vec{r}_{\mathrm{rec}} - \vec{r}_{\mathrm{source}}\right)\right|}. \tag{5.9}$$

The directional angle $\cos\delta$ of the PMT hits, used for this calibration, is calculated using the position of the PMT that detected the hit i, $\vec{r}_i^{\,\mathrm{PMT}}$ and the reconstructed position of the γ event $\vec{r}_{\mathrm{rec}}$. Here, $|\,(\vec{r}_{\mathrm{rec}} - \vec{r}_{\mathrm{source}})\,|$ is the reconstructed gamma direction, based on the reconstructed event position and the source location $\vec{r}_{\mathrm{source}}$. It is mathematically expressed in eq. 5.9. The angle δ is illustrated in Fig. 5.9.

Here, the analysis uses calibration data from the ^{54}Mn and ^{40}K gamma sources, with Q-values of 0.834 MeV and 1.460 MeV, respectively. In order to select the events arising from the source, a radial cut of $<$0.8 m, with respect to the source location, is applied. The energy regions of $290 < N_h < 350$ and $480 < N_h < 600$ are also chosen for the ^{54}Mn and ^{40}K gamma sources, respectively. As in the CID analysis, the PMT hits of all selected events are sorted in time after the ToF correction. The first 3 hits are selected based on a $\Delta\chi^2$ difference between ^{40}K PDFs with different values of $\mathrm{gvc_{ch}}$. Now, the $\cos\delta$ histograms of ^{40}K data is fitted with the MC PDFs, where $\mathrm{gvc_{ch}}$ is the free fit parameter. As ^{40}K has more Cherenkov photons, it has a larger sensitivity for the $\mathrm{gvc_{ch}}$ fit. In this analysis, it has been found that the direction mis-reconstruction of γ poses the largest systematic uncertainty. This is due to the different underlying hit time distributions of data and MC in the first few nanoseconds, which is used in the position reconstruction. This will result in the different reconstructed positions of γ events with same true positions. This means that the photons with same direction will

also be reconstructed differently in the data and MC. A modified position reconstruction PDF, which is a function of hit time, was produced, that takes into account the time differences between data and MC using a first Gaussian derivative function. The parameters of the Gaussian derivative function are selected separately for the data and MC, such that the resulting different modified position reconstruction PDFs produce $\cos\delta$ distributions of ^{54}Mn data and MC, that are in agreement with each other under certain conditions ($\chi^2/ndf < 1.5$). The selection of derivative function parameters under this condition contribute to the systematic uncertainty. Other systematic effects include the choice of energy cut and N$^{\text{th}}$ hit cut. The final result is $\text{gvc}_{\text{ch}} = 0.108 \pm 0.006$ (stat.) $\pm$ 0.039(syst.) ns m^{-1}. This is an effective correction and it changes the timing of Cherenkov photons relative to the scintillation photons. Considering the refractive index of $\approx$1.55 @400 nm wavelength, this correction corresponds to only about 2%. The gvc_{ch} is a sub-nanosecond effect and it depends on the overall timing behaviour of the whole detector. As the calibration of the detector using γ sources was performed in mid-2009, this result is considered reliable for Phase-I only and for the later phases, it is not possible to exclude the change in detector response over time with sub-nanosecond precision [174, 215].

5.5.4 Systematic errors budget

In addition to gvc_{ch} and Δr_{dir}, that contribute as the major systematics of the CID analysis, there are other smaller systematic uncertainties for the ^{7}Be solar neutrino CID analysis. In this analysis, not only $N_{\text{solar}-\nu}$ is extracted but also the ^{7}Be interaction rate (R(^{7}Be)), after subtracting the contributions of other solar neutrino events from $N_{\text{solar}-\nu}$. These systematic uncertainties can be categorized into two: (1) systematic error on $N_{\text{solar}-\nu}$, (2) systematic uncertainty from the estimation of R(^{7}Be) only. The uncertainties, that falls in the first category, are:

Choice of N$^{\text{th}}$ hit: As described in Sec. 5.5.2, the analysis is performed on the first two hits of the selected events. After performing the fit on $\cos\alpha$ distributions with different cuts on N$^{\text{th}}$ hit = 2, 3, and 4, the systematic uncertainty has been estimated to be 4.8% by conservatively taking the difference between the maximum and minimum fit results.

Choice of number of bins: As seen in Sec. 5.5.2, the analysis with >30 bins are expected to give a comparable precision and 60 bins are selected for this analysis. By performing CID analysis with different binning and conservatively taking the difference between the maximum and minimum fit results as systematic error, the uncertainty associated to binning choice has been estimated to be 4.2%.

Selection of PMTs: As discussed in Sec. 5.5.2, a selection based on the number of first hits contributed by each PMT, was applied such that they are in statistical agreement between data and MC. The method of PMTs selection gives a systematic uncertainty of 5.9% by varying Poissonian C.L. from 68% to 95%.

The uncertainties that falls in the second category are:

Exposure: The uncertainty on the exposure is dominated by the precision of the position reconstruction, using which the events lying inside the fiducial volume are selected. This effect has been studied using calibration sources [172]. The maximum

uncertainty on the position of the fiducial volume has been found to be 5 cm [78]. Considering a nominal spherical fiducial volume of 3.3 m, this results in an uncertainty of 4.6%. In addition, the MLP variable contribute to an uncertainty of 1.0%.

CNO and *pep* neutrino rates: As CNO and *pep* solar neutrinos also contribute in the ROI, the conversion of $N_{\text{solar}-\nu}$ to $R(^7\text{Be})$ requires the subtraction of their contributions. The interaction rates of CNO and *pep* solar neutrino differ for high-metallicity (HZ) SSM B16-GS98 and low-metallicity (LZ) SSM B16-AGSS09met predictions. In this analysis, the rates from HZ predictions are used and the difference between HZ and LZ predictions are included as the systematic uncertainty (+2.5%). In addition, taking into account the theoretical errors results in the 1.5% relative uncertainty on the number of ^{7}Be neutrinos. The total uncertainty on $R(^7\text{Be})$ due to the assumptions of the CNO and *pep* neutrino rates is $^{+2.9}_{-1.5}$%.

There are some systematic effects that were studied and found to be negligible for this analysis. They are described in detail as the following:

CNO and *pep* neutrino spectral shapes:

The systematic uncertainty due to differences in the $\cos\alpha$ shapes of the CNO and *pep* solar neutrinos in the ROI, according to eq. 2.18, has been studied using the MC simulation and has been found to be negligible. This implies that the CID method alone is not able to differentiate between ^{7}Be, CNO, and *pep* neutrinos in the ROI in Borexino, and only the sum of their contributions can be measured.

Effects on background $\cos\alpha$ distribution

The $\cos\alpha$ distributions of the background events are not entirely flat. The background events have no correlation to the Sun's position, so their $\cos\alpha$ distributions are expected to be flat. Therefore, it is crucial to investigate the underlying reasons which can cause non-flatness in the observed MC background distributions. Using a toy simulation, it has been found that several effects can contribute to this: (1) an asymmetrical fiducial volume cut (2) non-uniform distribution of PMTs and number of live PMTs, and (3) non-uniform background distribution. These effects were studied by developing a C++/ROOT based toy MC framework, which I performed. In this simplified framework, only the geometrical conditions of the detector, such as the observed Sun's position relative to the Borexino detector's coordinates, the event positions, and the distribution of PMTs inside the detector, are implemented. Here, no timing information is taken into account, and random PMTs are chosen to simulate the hit direction as would be in reality for the backgrounds. Therefore, only the effects relevant for backgrounds are studied here. To obtain the $\cos\alpha$ distribution, the angle between simulated solar direction and the direction of PMT hit with respect to the generated event position is calculated. Using this approach, the ideal detector conditions, where all events are present uniformly inside a spherical volume of the detector and the detector has 100% PMT coverage, is first simulated. In these conditions, an ideal flat $\cos\alpha$ distribution of background events is expected, as they have no correlation with the Sun's position. Then, one effect is applied at a time.

The effect of using an asymmetrical fiducial volume cut (pepFV) can be seen in Fig. 5.10a. This has been removed by employing a spherical fiducial volume, as previously explained in Sec. 5.5.1. The next possible source is the non-uniform distribution of the data events. Figure 5.11 shows the spatial distribution of data events in Phase-I and their comparison with uniformly distributed toy events. As can be seen, the data

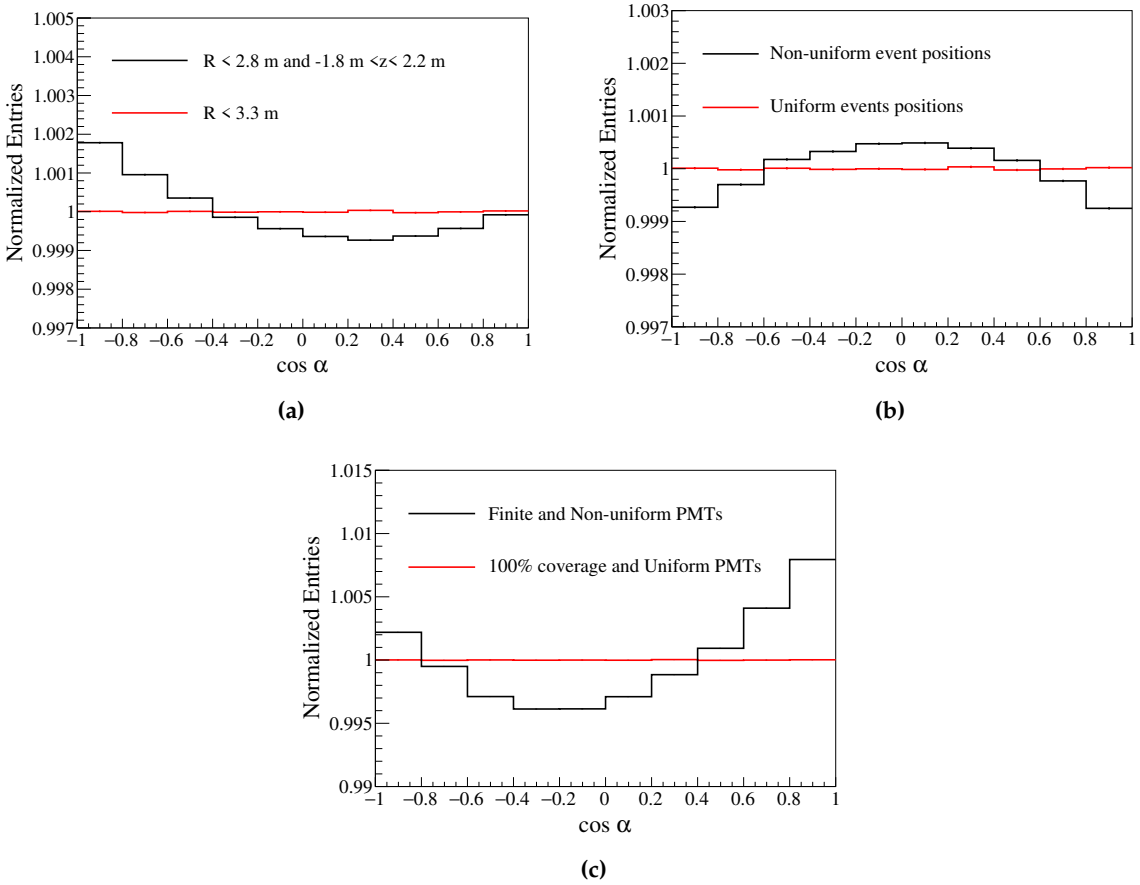

Figure 5.10: Effects on the $\cos\alpha$ distributions of background events, which are simulated using a toy MC approach where only the geometrical conditions of the detector, such as the observed Sun's position relative to the Borexino detector's coordinates, generated event positions, and the distribution of PMTs inside the detector are taken into account. The distribution of ideal conditions is shown in red, where uniformly distributed events in a spherical volume and the uniform PMTs with 100% coverage are simulated. The different effects, applied at a time, are shown in black: (a) an asymmetrical fiducial volume cut, (b) non-uniform event distribution which is sampled from Phase-I data distribution, and (c) non-uniform distribution of PMTs and number of live PMTs corresponding to a run in Phase-1. Each distribution is normalized to 1 and has the statistics of about $\sim 10^{10}$ entries.

distributions are not fully compatible with distributions of uniformly generated toy events, which could be due to the possible non-uniformity of background events. Figure 5.10b depicts the comparison of $\cos\alpha$ distribution using the uniformly generated toy events and the non-uniform event distribution, which are sampled from the Phase-I data spatial distribution. It can be seen that the maximum effect is at the level of $< 0.1\%$ for Phase-I, thus negligible within the statistics of data and MC.

The non-uniform distribution of PMTs in the detector as well as their finite amount that results in <100% detector coverage, also lead to a non-flat $\cos\alpha$ distribution of the background events. This effect in comparison to the ideal conditions is shown in Fig. 5.10c, where the live PMTs position distribution corresponding to a run in Phase-I is simulated. This effect is the dominant and lead to a non-flat CID distribution of the background MC. Since the distribution of PMTs in each phase is perfectly reproduced by the full MC, this effect does not contribute to the systematic uncertainty.

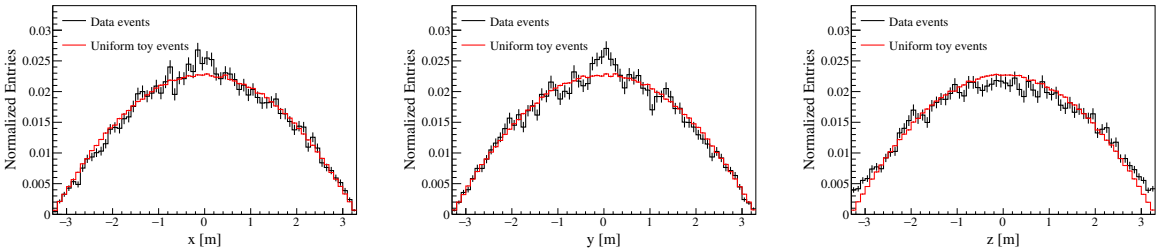

Figure 5.11: The reconstructed position distribution of selected data events (black points) in ROI for Phase-I in Cartesian coordinates: x (a), y (b), and z (c). The red distributions shows the spatial distribution of uniformly generated toy events inside a sphere of radius 3.3 m.

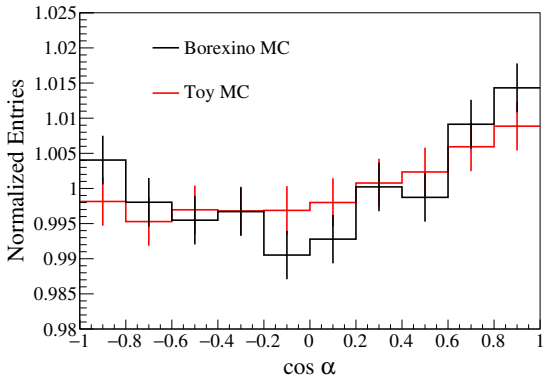

Figure 5.12: The $\cos\alpha$ distributions of the background events, which are simulated using Borexino MC in black and the toy MC approach in red, are shown. In toy approach, only the geometrical conditions of the detector such as the observed Sun's position relative to the Borexino detector's coordinates in Phase-I, uniformly distributed event positions, and the distribution of live PMTs in Phase-I inside the detector, are taken into account. The statistics of toy MC and Bx MC simulated events are simulated to be the same.

MC production method

As discussed in Sec. 5.3, about 200 events are simulated in MC per data event, once as a signal and once as a background, in a sphere of radius 15 cm around the reconstructed event position with corresponding Sun's position and live PMT distribution. Since the $\cos\alpha$ calculation depends on the event positions, the MC PDFs are also produced using the uniformly sampled event positions and their shape has been found to be in agreement with the PDFs produced using reconstructed vertex of data events. Figure 5.12 shows the comparison of $\cos\alpha$ distributions from ^{210}Bi MC (black) and the toy MC (red) described above, where only geometrical conditions related to Sun's position and PMTs position as in Phase-I data, as well as uniformly distributed toy events with the MC statistics, are simulated. It can be seen that the two distributions are compatible with each other. In addition, it is also unknown that how many data events are actually the true neutrino or background event and can cause systematic effect for the choice of position for the simulation. In order to investigate this, a set of large number of MC histograms are produced, each corresponding to a random selection of expected number of signal/background events from data. The data is analyzed again with these sets and the systematic uncertainty arising from this method is found to be negligible [217]. These studies show that the MC production method is robust and do not have any associated systematic uncertainty regarding the choice of event position, whether all uniform or a subset of data event positions.

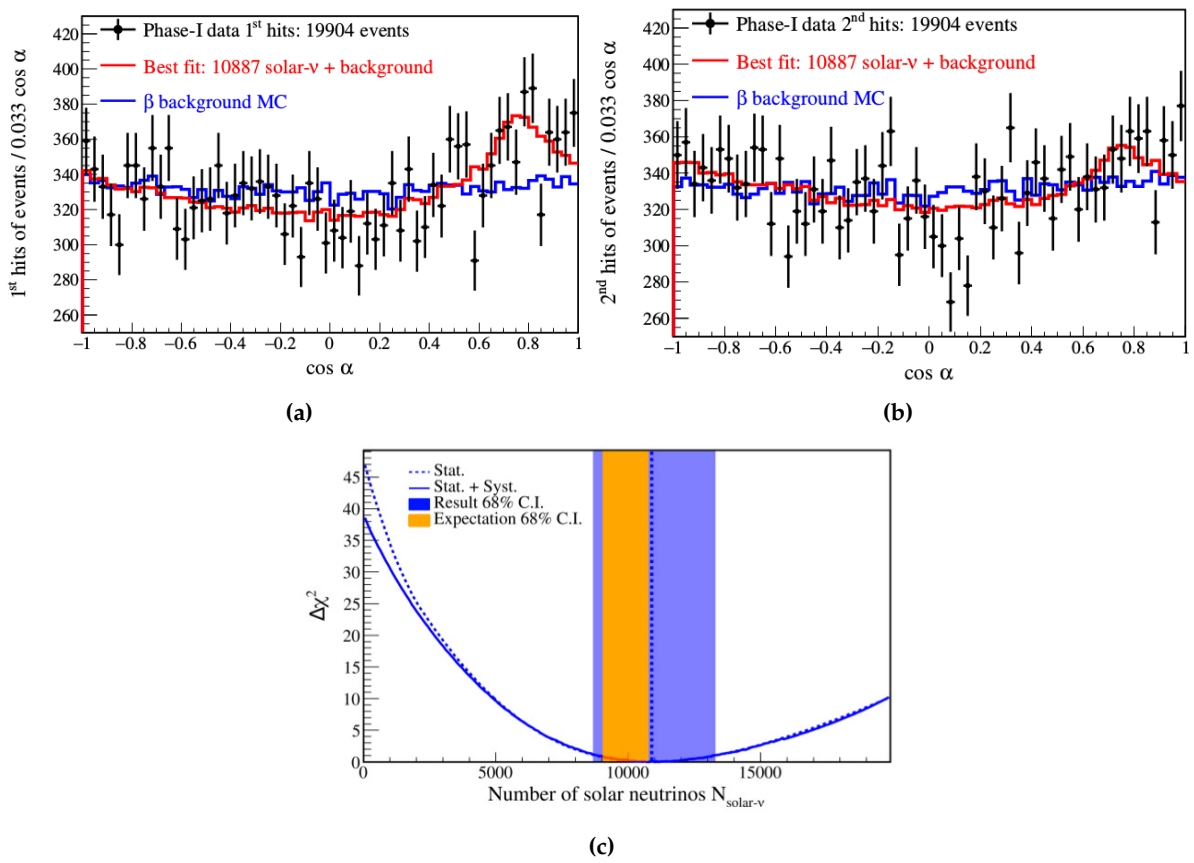

Figure 5.13: The $\cos\alpha$ distributions of the (a) first and (b) second hits of all selected events in Phase-I (black points), compared with the best fit curve (red) for the resulting $N_{\text{solar}-\nu}$ = 10887. All distributions are normalized to the data statistics. It can be inferred that the data points cannot be explained by the background-only hypothesis (blue). (c) The $\Delta\chi^2$ profiles from of the fit of the first and second hits of all the selected events in Phase-I, as a function of $N_{\text{solar}-\nu}$ with (blue solid curve) and without (blue dotted curve) the systematic (Syst.) uncertainties. The no-neutrino signal hypothesis ($N_{\text{solar}-\nu}$=0) can be rejected with $\Delta\chi^2 > 25$ or $> 5\sigma$ significance. The blue shaded band represents the 68% C.I. on $N_{\text{solar}-\nu}$ and the best fit value is shown as a vertical blue dotted line. The 68% C.I. of the expected $N_{\text{solar}-\nu}$ using high-metallicity (HZ) SSM B16-GS98 predictions is shown as a shaded orange band [4,5].

Therefore, the total systematic uncertainty on the directional measurement of number of solar neutrinos ($N_{\text{solar}-\nu}$) in the ^{7}Be edge region and the ^{7}Be interaction rate are estimated to be 6.9%, and $^{+8.8}_{-8.4}$%, respectively.

5.5.5 Results

This section discusses the results of CID analysis on the data events in the ROI discussed in Sec. 5.5.1. Here, the measurement on the number of solar neutrinos using CID method is provided for Phase-I period only, since the calibration of effective group velocity correction for the Cherenkov photons is performed in Phase-I. The remaining phases are used to provide only the exclusion of the null hypothesis of no-neutrinos. The fit strategy, as discussed in Sec 5.4, is adopted to perform the fit on the first and second PMT hits of all selected events (19904 in Phase-I) to obtain the number of solar neutrinos $N_{\text{solar}-\nu}$, which consists of ^{7}Be+*pep*+CNO neutrino events.

The results of the CID analysis in ^{7}Be edge energy region are shown in Fig. 5.13. It can be seen that the best fit $\cos\alpha$ distribution (red) is well in agreement with the first (Fig. 5.13a) and second (Fig. 5.13b) hits of the selected data events (black), while the background curve only (blue) is incompatible with the data. We now obtain a $\Delta\chi^2$ profile (dotted blue curve) as a function of $N_{\text{solar}-\nu}$ for the first two hits of each event.

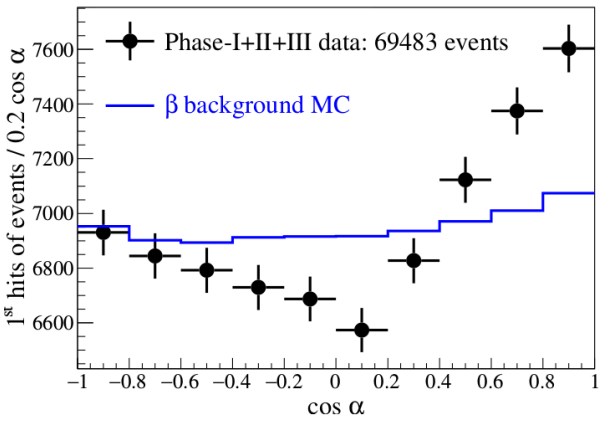

Figure 5.14: The cos α distribution of the first hits of the selected data (black points) in combined Phase-I+II+III period. The comparison with the background MC PDF, normalized to the statistics of data, is shown in blue curve. It can be seen that the data cannot be explained with a background-only hypothesis [5].

The χ^2 profile has been further smeared with the systematic uncertainties, described in Sec. 5.5.4. The $\Delta\chi^2$ profiles without (dotted blue curve) and with (solid blue curve) systematic uncertainty as a function of $N_{\text{solar}-\nu}$ are shown in Fig. 5.13c. From the fit, the $\chi^2/ndf = 124.6/117$ and a p-value=0.3 are obtained. The measured number of solar neutrinos $N_{\text{solar}-\nu}$ in the ROI is:

$$N_{\text{solar}-\nu} = 10887^{+2386}_{-2103}(\text{stat.}) \pm 947(\text{syst.}).$$

The expected value of $N_{\text{solar}-\nu}$ using high-metallicity (HZ) SSM B16-GS98 predictions is 10187^{+541}_{-1127} events. The 68% C.I. of the result corresponding to $\Delta\chi^2 = 1$ and the expectations are shown as the blue and orange bands, respectively, in Fig. 5.13c.

As the nuisance parameters $gv_{\text{ch}}^{\text{corr}}$ and Δr_{dir} does not influence the cos α distribution of the background, the profile becomes steeper for a larger background contribution. This is the reason for the asymmetry of the $\Delta\chi^2$ profile. Since the pure background hypothesis can be excluded with $\Delta\chi^2 > 25$, this corresponds to a $>5\sigma$ detection of sub-MeV solar neutrinos using their directional Cherenkov light with the CID method.

The statistical uncertainty (+2386, -2103) on the final measurement is arising from the combination of the statistics of data and the effect of the nuisance parameters in the fit. Using MC studies, the expected statistical uncertainty on $N_{\text{solar}-\nu}$ is found to be $\pm$1523 events, when the nuisance parameters are fixed. The uncertainty from the lack of a dedicated e^- Cherenkov calibration can then be estimated as (+1837, -1450) events.

The result on the ^{7}Be interaction rate, using measured $N_{\text{solar}-\nu}$ from Phase-I, after fixing the contributions of the CNO and *pep* solar neutrinos from the SSM predictions and including the systematic uncertainties due the detection efficiency, exposure, and the difference between the HZ and LZ predictions of CNO and *pep* neutrinos:

$$R(^7\text{Be}) = 51.6^{+13.9}_{-12.5}\,(\text{stat.} + \text{syst.})\,\text{cpd}/100\text{t}.$$

Figure 5.14 shows the test regarding the background-only hypothesis on the summed data of all three Borexino phases. The data in each phase undergoes the selection cuts corresponding to each phase, as discussed in Sec. 5.5.1. It can be seen that a pure background MC PDF does not agree with the first hits of the data. Since Cherenkov light from the background is uncorrelated to the solar direction, this comparison does not depend on a Cherenkov calibration. The χ^2 between the data and the MC β background PDF gives a p-value$<3\times10^{-7}$ (χ^2/ndf = 95.5/9 for 10 bins). This shows that the background-only hypothesis is incompatible with our data with a significance $>5\sigma$

and a detection of solar neutrinos is performed only using their directionality, without any Cherenkov calibration.

These results on the ^{7}Be-ν rate measurement have shown the proof of principle for the CID method. The CID method can be further combined with the multivariate spectral fit discussed in Chapter 4 for a joint analysis. This is done for the CNO solar neutrinos measurement, as will be described in the next section.

5.6 Directionality analysis of CNO solar neutrinos

This section is devoted to the measurement of CNO solar neutrinos using CID method. Here, the analysis is performed in an energy region of 0.85 MeV $-$ 1.3 MeV, as shown in Fig. 5.15. This energy region has been optimised for the CNO-ν analysis, nevertheless, the contribution from *pep*-ν is dominant. While the measurement of ^{7}Be solar neutrino interaction rate was possible only in Phase-I, the CNO measurement can now be performed in all phases. This is possible due to the development of the strategy to calibrate gvc_{ch} using the ^{7}Be shoulder data. This is done by performing the CID analysis in the same RoI as in the previous section. Here, the number of solar neutrinos, dominantly ^{7}Be-ν, is constrained to the average of high-metallicity SSM B16-GS98 and low-metallicity SSM B16-AGSS09met predictions. The obtained gvc_{ch} correction is then used in the CID analysis in a fully independent energy region for the CNO-ν measurement. With this new strategy, the effective correction of the group velocity of Cherenkov light in the MC, gvc_{ch} can be calibrated on the same data taking period as the one used for the CNO analysis. The details of gvc_{ch} calibration using ^{7}Be-ν energy region are discussed in Sec. 5.6.3. Here, the MC production of neutrino and background PDFs, as well as performing the data fit follows the strategy described in Sec. 5.3 and Sec. 5.4, respectively. Since Cherenkov and scintillation photons cannot be distinguished in the data, only the 1$^{\text{st}}$ and 2$^{\text{nd}}$ hits of each event were used in Sec. 5.5, which have the largest probability of all hits to be Cherenkov hits. For the analysis presented in this section, the directional information contained in the first several hits ($\sim$15), is fully exploited. This choice uses direct and indirect information (see Sec. 5.4) from Cherenkov photons and is supported by the sensitivity studies and the Monte Carlo simulations, as will be described in Sec. 5.6.2. The various systematic effects relevant for the CNO-ν analysis using CID method are discussed in Sec. 5.6.4. The CID fit results on the CNO measurement, after taking into account all systematics and calculating a Bayesian posterior distribution, are reported in Sec. 5.6.5. The results from the directional analysis of CNO solar neutrinos are then combined with the standard multivariate analysis performed on Phase-III data [218], to obtain an improved measurement of the CNO neutrino interaction rate, as summarized in Sec. 5.6.6. These results are published in [6].

5.6.1 Data selection

For the CID measurement of CNO solar neutrinos, the entire Borexino dataset until the end of its data taking (2007-2021) is used. Two analyses have been performed in parallel: for Phase-I (May 2007 to May 2010, 740.7 days) and Phase-II+III (December 2011 to October 2021, 2888.0 days). The reason is that this allows the comparison of gvc_{ch} obtained using the γ-sources from calibration (Sec. 5.5.3) with the one obtained in Sec. 5.6.3. Also, the analyses of two independent datasets allow for the investigation of any variation of the detector response over time.

The selection cuts are: $R_{\text{FV}} < 3.05$ m and $340 < \text{N}_h^{\delta^{geonorm}} < 520$ for Phase-I, and $R_{\text{FV}} < 2.95$ m and $340 < \text{N}_h^{\delta^{geonorm}} < 515$ for Phase-II+III. Here, the strategy for optimising region of interest for the CNO-ν measurement (RoI_{CNO}) is based on the same

Phase	Fiducial volume	Energy cut	Total Events	Signal to total ratio
Phase-I	R < 3.05 m	$340 < N_h^{geonorm} < 520$	2990	22%
Phase-II+III	R < 2.95 m	$340 < N_h^{geonorm} < 515$	5974	40%

Table 5.2: Summary of fiducial volume and energy cuts for the CID analysis in region of interest for the CNO-ν measurement (RoI_{CNO}) and the total number of events in Phase-I and Phase-II+III data after application of all cuts. The last column reports the expected ratio of signal to the total number of events in RoI_{CNO}. For this, the rate predictions of solar neutrino events is taken from the high-metallicity SSM B16-GS98 expectations and the trigger and energy efficiencies are calculated using the Borexino MC energy PDFs.

FOM method [216], discussed in Sec. 5.5.1. In addition, all other cuts that include the muon veto and data quality cuts have been applied as discussed in Chapter 3. The TFC algorithm (Chapter 3) is also applied to suppress the ^{11}C background in the RoI_{CNO}, preserving the exposure with a signal survival fraction of 55.77% $\pm$ 0.02% for Phase-I and 63.97% $\pm$ 0.02% for Phase-II+III. Therefore, the overall exposures for this analysis are: 740.7 days $\times$ 104.3 t $\times$ 55.77% for Phase-I and 2888.0 days $\times$ 94.4 t $\times$ 63.97% for Phase-II+III. The total exposure of Phase-II+III (477.81 years $\times$ t) is about four times larger than that of Phase-I (118.04 years $\times$ t). All these cuts ensure a maximal signal to background ratio for the CNO analysis. The RoI_{CNO} is illustrated for the Phase-II+III dataset in a yellow band in Fig. 5.15.

In addition to CNO-ν, the RoI_{CNO} consists of *pep*-ν and ^{8}B-ν as the signal. The *pep*-ν has the dominant contribution with about $\sim$64% of the total number of solar neutrino events in RoI_{CNO}. The contribution of CNO-ν and ^{8}B-ν the RoI_{CNO} is $\sim$33% and $\sim$2.5% of the total number of solar neutrino events, respectively. The remaining negligible contribution is from ^{7}Be-ν. The ^{210}Bi decay, cosmogenic ^{11}C, and external γ events contribute as the backgrounds in RoI_{CNO}. As the emission of secondary particles of these backgrounds have no correlation with the Sun's position, the differences in the shape of $\cos\alpha$ distributions of ^{210}Bi and ^{11}C backgrounds in RoI_{CNO} have been found to be negligible. The effect on the shape of $\cos\alpha$ distributions of external γ backgrounds due to their radial dependence is also studied, as will be described in Sec 5.6.4. Therefore, the $\cos\alpha$ distributions of *pep*-ν and ^{210}Bi background with their spectral shape in RoI_{CNO} are used as the signal and background PDFs, respectively, using the procedure described in Sec. 5.3. The difference in the shape of $\cos\alpha$ distributions of different solar neutrinos in RoI_{CNO} is included as the systematic uncertainty in Sec 5.6.4.

5.6.2 Analysis criteria

Number of bins

Similar to Sec. 5.5.2, the number of bins for CID analysis in RoI_{CNO}, is also selected using the MC based sensitivity approach so that the information in the expected $\cos\alpha$ distributions is optimal. Here, the pseudo-datasets are created by sampling *pep* solar neutrino and ^{210}Bi background MC PDFs, and the contribution of solar neutrino events is fixed according to the expected signal-to-total ratio (Table 5.2). The total number of events in these pseudo-datasets is set to be the same as the data statistics in Table 5.2. Figure 5.16 shows the extracted uncertainty of the $N_{\mathrm{solar}-\nu}$ distribution in RoI_{CNO} as a function of the number of bins, considering the total number of events and the expected signal ratio in Phase-II+III. This study is performed for different values of injected nuisance parameters and the N^{th} hit cuts with high Cherenkov ratio. It is observed that until $\sim$40 bins, the distributions of the uncertainty on the extracted

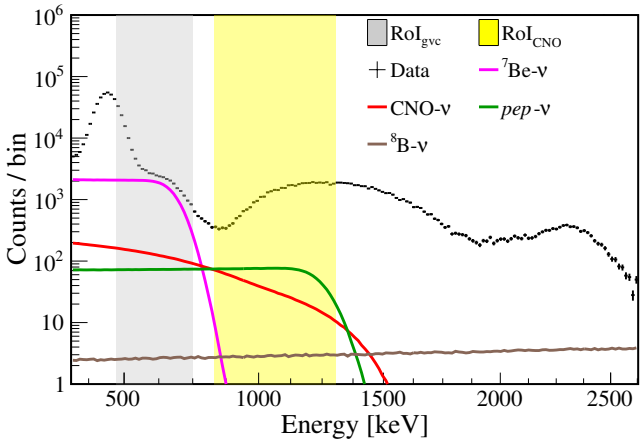

Figure 5.15: Illustration of the two RoIs, on the energy spectrum of the Phase-II+III data in the fiducial volume of 2.95 m radius. The Monte Carlo PDFs of different solar neutrino components are scaled to the high-metallicity SSM B16-GS98 predictions. The grey band shows the ^{7}Be-ν edge region, used for the estimation of gvc_{ch} correction (RoI_{gvc}). The CNO region, used to measure the CNO-ν rate, is shown in yellow band (RoI_{CNO}). Used in [6].

$N_{\text{solar}-\nu}$ have a decreasing trend, while for larger binning, the extracted uncertainty of the $N_{\text{solar}-\nu}$ almost stabilizes. A similar trend can also be seen in the distributions, obtained by injecting other values of nuisance parameters and using N^{th} hit cut = 2. A bias of $< 0.5\%$ has been observed in the extracted mean $N_{\text{solar}-\nu}$ with respect to the injected value, which is negligible within the statistical error. For Phase-I, the similar observations have been made on the extracted precision $N_{\text{solar}-\nu}$ as function of the number of bins, where the extracted uncertainty decreases until ∼40 bins, while it almost stabilizes for larger binning. For performing CID analysis in RoI_{CNO}, a binning of 60 is chosen for all phases, in order not to have less number of bins where the expected sensitivity in RoI_{CNO} worsens. Therefore, the choice of the number of bins, between 40 and 100, is studied for the systematic uncertainty (Sec. 5.6.4).

Improved selection of N^{th} hit range

For performing the CID analysis in RoI_{CNO}, the selection of N^{th} hit cut or N^{th}-hit(max) is investigated using the MC based sensitivity approach, as described in Sec. 5.5.2. Here, the uncertainty of the $N_{\text{solar}-\nu}$ distribution in RoI_{CNO} is extracted as a function of N^{th} hit, for the fixed values of gvc_{ch} and Δr_{dir}. Figure 5.17a shows the extracted uncertainty of the $N_{\text{solar}-\nu}$ distribution in RoI_{CNO} as a function of the N^{th} hit cut, considering the total number of events and the expected signal ratio in Phase-II+III. It can be seen from the figure that the extracted uncertainty improves as a function of increasing N^{th} hit cut in the toy CID analysis. For example, the extracted uncertainty is about 28% using N^{th} hits up to 2, while it drops to ∼18% for N^{th} hit cut = 15, followed by a steady trend at later hits for gvc_{ch} = 0.108 ns/m and $\Delta\text{r}_{\text{dir}}$ = 3.0 cm. The reason is that the Δr_{dir} parameter induces the slope at negative $\cos\alpha$ values, as discussed in Sec. 5.4. As a result, the signal and background MC $\cos\alpha$ histograms are still different from each other for the first few hits, as well as even for later hits ($5 \lesssim \text{N}^{\text{th}}$ hit $\lesssim 20$), where the contribution of direct Cherenkov hits becomes negligible relative to the scintillation hits, as shown in Fig. 5.17b. The much later hits consist of delayed scintillation photons, that have undergone various optical process during their propagation inside the detector. A few cm of bias does not influence the $\cos\alpha$ distributions of these noisy hits and their shape is compatible with the backgrounds distributions. Figure 5.17c shows

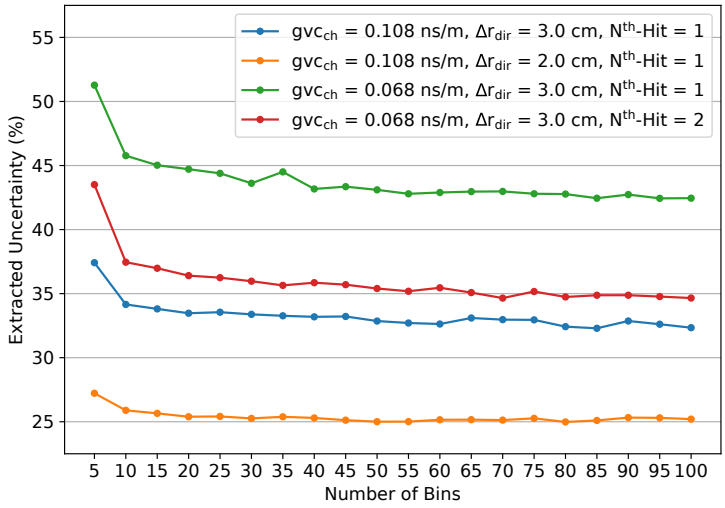

Figure 5.16: The distributions of the extracted uncertainty (%), defined as the ratio of Root Mean Square (RMS) of the $N_{\text{solar}-\nu}$ distribution to the injected value of the expected $N_{\text{solar}-\nu}$ in Phase-II+III, as a function of number of bins in $\cos\alpha$ histograms of pseudo-data and MC PDFs in RoI_{CNO}. The $N_{\text{solar}-\nu}$ distribution is extracted from the fit of the MC based pseudo-experiments. The total number of events in pseudo-data is the same as in real data, with fixed and different injected values of nuisance parameters (gvc_{ch} and $\Delta\text{r}_{\text{dir}}$) to investigate their impact. The fit is performed using χ^2 defined in eq. 5.8, where $N_{\text{solar}-\nu}$ is the only free parameter and up to N^{th} hit = 1 or 2. It can be seen that the extracted uncertainty have a decreasing trend for number of bins $\lesssim$40, while for later bins, the distributions do not show a strong dependence on the number of bins.

the comparison between the MC $\cos\alpha$ distributions of different N^{th} hits of simulated *pep*-ν events, as well as with the $\cos\alpha$ distribution of ^{210}Bi events simulated in RoI_{CNO}. It can be observed that the later hits (N^{th} hit = 5, 17) still have the directional information and are different from background distribution. This directional information, due to Δr_{dir}, decreases as function of increasing N^{th} hit, and the PDF corresponding to much later hit (N^{th} hit = 40) of *pep*-ν is in agreement with the ^{210}Bi PDF. For the Phase-I, the similar observations have been made using the same toy study with the expected signal contribution in this period, where the extracted precision improves significantly as function of N^{th} hit cut, that is, from about 60% using N^{th} hits up to 2, to $\sim$42% for N^{th} hit cut $=$ 15, for fixed values of gvc_{ch} = 0.108 ns/m and $\Delta\text{r}_{\text{dir}}$ = 3.0 cm. Figure 5.17a also illustrates the possible impact of varying values of nuisance parameters. By changing the Δr_{dir} value from 3.0 cm (blue) to 2.0 cm (orange), the overall sensitivity improves due to an increase in the Cherenkov peak in the first hits (see Fig.5.5b). However, the dependence on the N^{th} hit cut also decreases, compared to the slope at N^{th} hit cut $\gtrsim$ 5 in the blue distribution, as a result of a decrease in the slope at negative $\cos\alpha$ values. When gvc_{ch} is lowered (green) while keeping Δr_{dir} fixed, the first few hits are impacted due to a fewer Cherenkov photons, but the overall trend in the slope of the distribution in green is similar to the blue distribution as the Δr_{dir} value is the same. Therefore, it can be concluded that by using several early hits, instead of only 2 hits, it is expected that the CID sensitivity improves due to the presence of directional information in these hits of the signal $\cos\alpha$ distributions.

For the CID analysis in RoI_{CNO}, the first hits up to the N^{th}-hit(max) $=$ 15, 17 are used for Phase-I and Phase-II+III, respectively, in order to use all direct Cherenkov information and indirect Cherenkov information from $\Delta\text{r}_{\text{dir}}$ and to keep contribution small from the delayed hits with no Cherenkov information [219]. This selection is based on investigating the directional differences between 10^4 $\cos\alpha$ distributions of

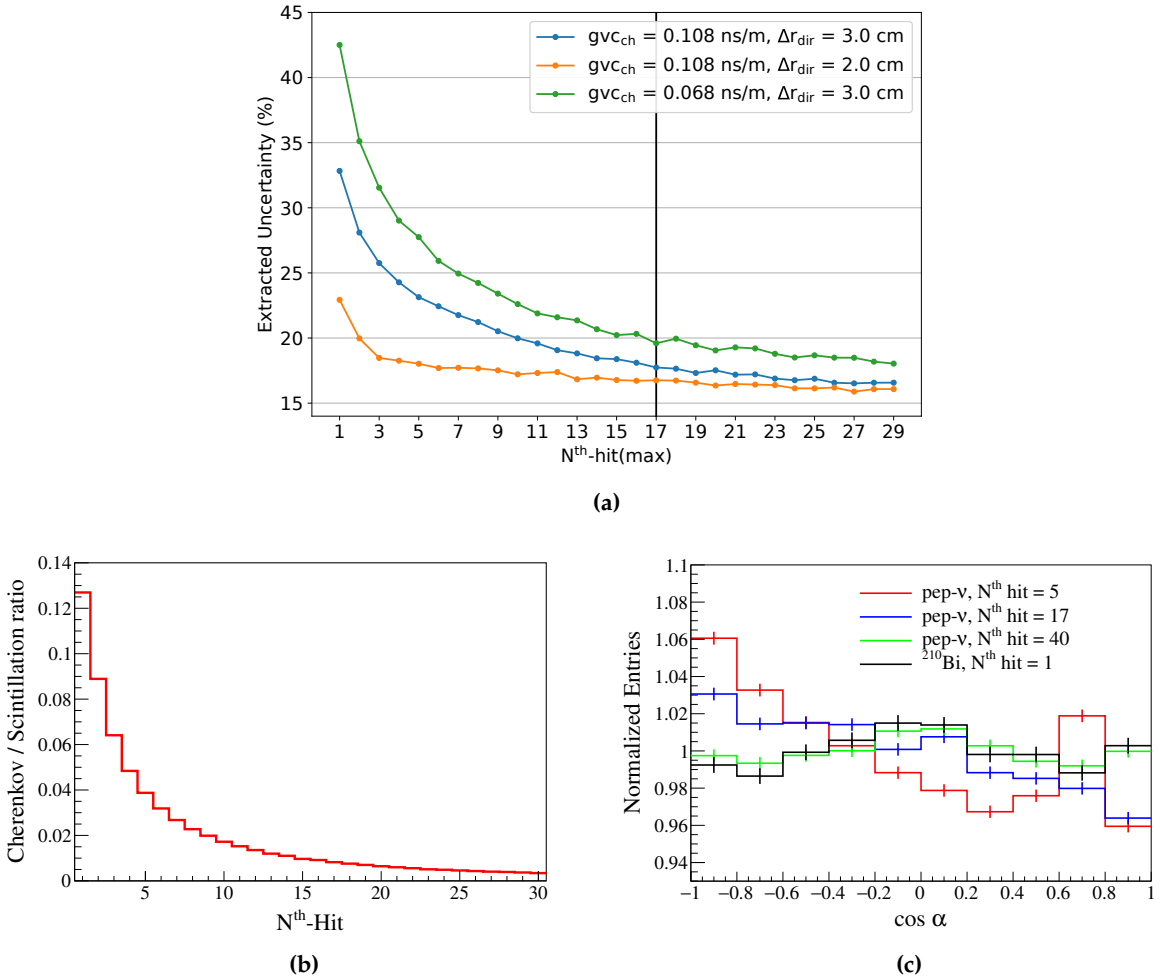

Figure 5.17: (a) The extracted uncertainty (%) on $N_{\text{solar}-\nu}$ from the MC based sensitivity studies in Phase-II+III, as a function of the N$^{\text{th}}$-hit(max) in the CID analysis of pseudo-data and MC PDFs in RoI$_{\text{CNO}}$. In the MC based pseudo-experiments, the total number of events in pseudo-data is the same as in the real data, with fixed and different injected values of nuisance parameters (gvc$_{\text{ch}}$ and Δr_{dir}). The fit is performed on pseudo-data using the χ^2, defined in eq. 5.8, where $N_{\text{solar}-\nu}$ is the only free parameter. It can be seen that the extracted uncertainty improves significantly as a function of the N$^{\text{th}}$ hit cut in the CID analysis. The vertical line represents the N$^{\text{th}}$-hit(max) = 17, optimised for the CID analysis in Phase-II+III. (b) Detected Cherenkov to scintillation photon hits ratio as a function of each N$^{\text{th}}$ hit, for all simulated events of the *pep* solar neutrinos in Phase-II+III in RoI$_{\text{CNO}}$ [6]. (c) Comparison between the shapes of MC cos α distributions of different N$^{\text{th}}$ hits of simulated *pep*-ν events (red, blue, and green) which are simulated in RoI$_{\text{CNO}}$. The N$^{\text{th}}$ hit = 5 (red) correspond to little direct Cherenkov contribution, have directional information from the Δr_{dir} parameter. This directional information decreases as a function of increasing N$^{\text{th}}$ hit, which is shown for N$^{\text{th}}$ hit = 17 (blue), due to optical processes in LS during propagation of the delayed hits. As shown for the N$^{\text{th}}$ hit = 40 (green), the indirect information is not visible and the shape of cos α distribution of *pep* solar neutrinos is compatible with the shape of ^{210}Bi cos α distribution (black). This is performed for Phase-II+III period and with gvc$_{\text{ch}}$ = 0.108 ns/m and Δr$_{\text{dir}}$ = 3.0 cm. Here, the distributions correspond to MC statistics and are normalised to 1.

each N$^{\text{th}}$ hit of the signal and background PDFs, with data statistics for the expected value of nuisance parameters. For this, a $\Delta\chi^2$ test is performed between the sampled cos α distributions of the signal and background PDFs for each N$^{\text{th}}$ hit, and an averaged $\Delta\chi^2$ from 10^4 comparisons is obtained as a function of N$^{\text{th}}$ hit. It is observed that until N$^{\text{th}}$ hit $\approx$15 (17) for Phase-I (Phase-II+III), averaged $\Delta\chi^2$ is greater than zero. The averaged $\Delta\chi^2$ as a function of N$^{\text{th}}$ hit in RoI$_{\text{CNO}}$ for Phase-II+III is shown in Fig. 5.18. This means that there exist directional differences between the signal and background

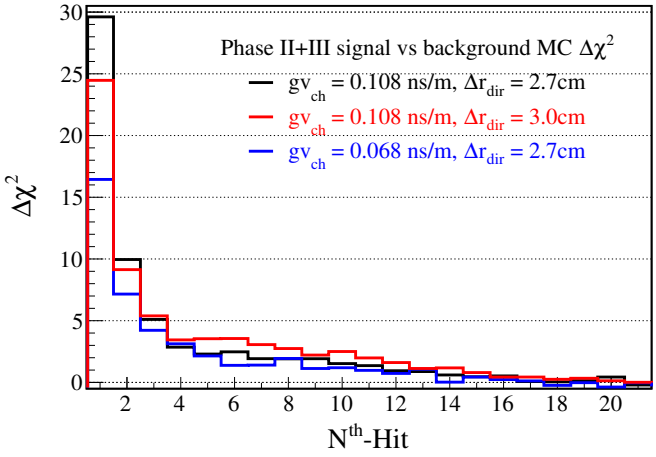

Figure 5.18: $\Delta\chi^2$ between the neutrino signal and background MC $\cos\alpha$ distributions in RoI_{CNO} of the Phase-II+III period for different selections of nuisance parameters. From [6, 219].

PDFs on average, until N^{th} hit $\approx$15 (17) for the Phase-I (Phase-II+III) with data statistics. From Fig. 5.17a, it can also be seen that there is almost no effect of Δr_{dir} on sensitivity results for N^{th} hit$\gtrsim$17. This choice on the N^{th} hit cut is attributed to the systematic uncertainty.

PMT selection and time calibration

As discussed in 5.5.2, some data PMTs show the time misbehaviour and have over-selection of the number of 1$^{\text{st}}$ hits, not reproduced in the MC. In Sec. 5.5.2, the data PMTs' time behaviour was investigated and corrected using the sources from the calibration performed in 2008-2009 and can therefore be considered reliable only for Phase-I. Also, the PMTs were deselected based on the statistical agreement (68% C.L) between only the first hits in data and MC. This is a conservative method as it does not take into account the overall PMT hit time properties and is likely to over-reject the non-misbehaving PMTs.

Since all phases are utilised for the CID analysis in RoI_{CNO}, a method based on the ^{11}C tagged data in an energy region of $350 < N_h^{geonorm} < 700$ is utilised. As a result, the same data-taking period can be used in this method as well as for the CID analysis. In addition, the ^{11}C data is independent from the data used for the CID analysis. Moreover in this method, the PMTs with overall hit time misbehaviour as well as the misbehaviour in early hits are deselected. For each PMT, the ToF corrected hit time distributions are built separately for Phase-I, Phase-II, and Phase-III, and these distributions are fitted with a bi-exponentially modified Gaussian function. This function consists of parameters such as the amplitudes A_1 and A_2, τ_1 and τ_2 as the exponential time constants, and μ and σ as the Gaussian mean and standard deviation. The test statistic for the fit is based on a Poissonian likelihood. The distributions of the best fit results of these model parameters as well as the test statistics, the fit uncertainty on μ, $\Delta\mu$, and the early hits over total ratio, are extracted. Then, the PMTs are deselected, based on the difference between their fit parameters and their mean values with respect to the chosen cut values. As the chosen cut values can result in the possible bias of PMTs selection, which can influence the CID analysis since it depends on the PMTs distribution, the systematic uncertainty associated to the selection of PMTs is discussed in Sec. 5.6.4.

It is also observed that the μ distribution of data PMTs cannot be explained from the statistical uncertainty from the fit of the PMT hit time distribution. The data PMTs

have an offset relative to each other, following a distribution with a standard deviation of 0.3 ns, and this offset has been measured with an uncertainty of up to ± 0.1 ns. This value is fully compatible with the one obtained in Sec. 5.5.2. It was not found to be the case in the MC, where the PMT hit time distribution of the simulated ^{11}C events were analyzed in the same way. Consequently, the data PMTs are corrected with a relative offset, which is the difference between μ and the averaged μ, in order to have same PMT time behaviour in data and MC. And the fit error $\Delta\mu$ is propagated in the analysis chain, as this relative offset is known with a finite precision. This is done by performing CID analysis 1000 times, where each time, the time correction of the PMTs are modified with a Gaussian smearing with $\Delta\mu$ as the standard deviation [215], as will be discussed in Sec. 5.6.4.

5.6.3 Calibration for Cherenkov photons using ^{7}Be solar neutrinos

Data selection

Since the sub-nanosecond stability of the detector time response cannot be guaranteed for long periods, and no more calibrations have been performed after 2009, a method to calibrate the gvc_{ch} on the ^{7}Be shoulder data has been developed. This is done by using the fiducial volumes, MLP parameter cuts, and energy cuts on the data until the end of Borexino data taking, as those listed in Sec. 5.5.1. This energy region will be referred to as RoI_{gvc}. The RoI_{gvc} is illustrated for the Phase-II+III dataset in grey band in Fig. 5.15. It can be seen that the two energy regions, used to calibrate gvc_{ch} and to measure the CNO-ν, are fully independent. Nevertheless, this calibration has been found to be justified according to the MC studies, as the wavelength distribution of the detected Cherenkov photons, produced by electrons from RoI_{gvc} and RoI_{CNO}, are in the agreement with each other [220]. Here, we perform the CID analysis on the ^{7}Be shoulder data in Phase-I and Phase-II+III, so that the gvc_{ch} can be calibrated on the same data taking period as the one used for the CNO analysis. Furthermore, the obtained gvc_{ch} can also be compared with the value estimated from γ-sources in Sec. 5.5.3.

Fit strategy

The fit procedure, to obtain gvc_{ch} in the ^{7}Be shoulder region, follows the similar strategy as discussed in Sec. 5.4. However, since gvc_{ch} is now the parameter of interest, the modified χ^2 is defined as follows:

$$\chi^2 = \sum_{n=1}^{\text{N}^{\text{th}}\text{-hit(max)}} \sum_{i=1}^{\text{bins}} \left[\frac{\{\cos\alpha^D_{n,i} - norm \cdot \cos\alpha^M_{n,i}(N_{\text{solar}-\nu},\, \Delta r_{\text{dir}},\, \text{gvc}_{\text{ch}})\}^2}{norm \cdot \cos\alpha^M_{n,i} + norm^2 \cdot \cos\alpha^M_{n,i}} \right] - 2\ln\left(P(N_{\text{solar}-\nu})\right). \tag{5.10}$$

The $\cos\alpha^M_{n,i}$, for n$^{\text{th}}$ hit and i$^{\text{th}}$ bin, is modeled as eq. 5.3. The selected number of bins is 60 (Sec. 5.5.2). The values of N$^{\text{th}}$-hit(max) are the same as the values used in RoI_{CNO} for each phase, studied using the sensitivity and MC studies as in RoI_{CNO}. The number of neutrino events $N_{\text{solar}-\nu}$ and Δr_{dir} are treated as the nuisance parameters, and $N_{\text{solar}-\nu}$ is constrained in each phase, using the probability distributions based on SSM expectations. For this, the neutrino prior probability distribution $P(N_{\text{solar}-\nu})$ is given by the sum of the Gaussian probability distributions (φ) with the mean ($N_{^7\text{Be}}$, N_{pep}) and the standard deviations ($\sigma_{^7\text{Be}}$, σ_{pep}) from the high-metallicity (HZ) SSM B16-GS98

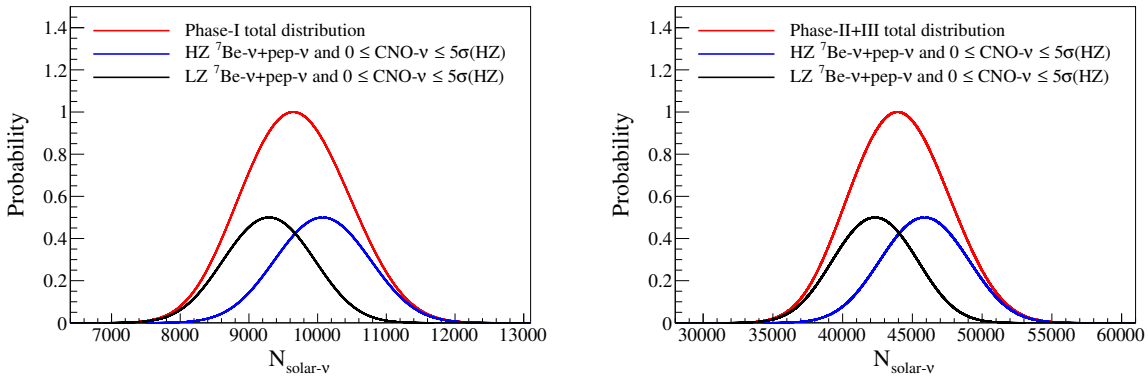

Figure 5.19: The probability distributions of expected $N_{\text{solar}-\nu}$, $P(N_{\text{solar}-\nu})$ in Phase-I (a) and Phase-II+III (b). The distribution in black and blue correspond to the probability distributions, calculated using expected number of ^{7}Be-ν and *pep*-ν events in RoI$_{\text{gvc}}$ from the high-metallicity (HZ) SSM B16-GS98 only and the low-metallicity (LZ) SSM B16-AGSS09met only predictions in eq. 5.11, respectively. The red distribution is calculated using both high-metallicity (HZ) SSM B16-GS98 and low-metallicity (LZ) SSM B16-AGSS09met predictions on the expected number of ^{7}Be-ν and *pep*-ν events in RoI$_{\text{gvc}}$ in eq. 5.11. In all these distributions, a uniform probability distribution of number of CNO-ν events between 0 to the HZ-SSM CNO expectation taking into account its 5σ error, is used for convolution. The total probability distribution (red) is then used in eq. 5.10. These distributions include systematic uncertainties arising from the exposure, during the conversion of rate to number of events.

and low-metallicity (LZ) SSM B16-AGSS09met predictions in RoI$_{\text{gvc}}$, as well as taking into account the expected statistical uncertainty. In this way, both HZ and LZ SSMs are equally treated. The resulting distribution is then convoluted with a uniform distribution of CNO-ν, denoted by f, between zero and the HZ-SSM CNO expectations taking into account the 5σ error, $N^{\text{HZ}}_{\text{CNO}} + 5\sigma^{\text{HZ}}_{\text{CNO}}$:

$$
\begin{aligned}
P\left(N_{\text{solar}-\nu}\right) &= \int_t \left[\varphi_{\text{HZ-SSM}}\left(N_{\text{solar}-\nu} - t\right) + \varphi_{\text{LZ-SSM}}\left(N_{\text{solar}-\nu} - t\right)\right] \cdot f(t)\, dt, \\
\varphi_{SSM}(x) &\propto \exp\left(-\frac{1}{2}\frac{\left(x - \left(N_{^7\text{Be}} + N_{pep}\right)\right)^2}{\sigma^2_{^7\text{Be}} + \sigma^2_{pep}}\right), \\
f(t) &= \begin{cases} 1 & \text{if } 0 \leq t \leq N^{\text{HZ}}_{\text{CNO}} + 5\sigma^{\text{HZ}}_{\text{CNO}}. \\ 0 & \text{otherwise .} \end{cases}
\end{aligned}
\tag{5.11}
$$

By assigning a uniform probability to CNO-ν counts, a potential correlation of the gvc$_{\text{ch}}$ calibration and the subsequent measurement of the CNO-ν rate using this gvc$_{\text{ch}}$ constraint, is avoided. Figure 5.19 shows the neutrino prior probability distribution $P(N_{\text{solar}-\nu})$ in red for both Phase-I and Phase-II+III, calculated using eq. 5.11 and is used in eq. 5.10. Table 5.3 summarizes the expected number of different solar neutrinos along with their theoretical uncertainties, that are used to estimate the neutrino probability distributions in Fig. 5.19.

Results on the group velocity correction

Figure 5.20 shows the illustration of the best fit results for the summed hits in Phase-I (top) and Phase-II+III (bottom), relative to a pure background hypothesis (blue). For the early hits (left), the direct Cherenkov light causes the peak seen for $\cos\alpha > 0$ and

Solar -ν	Phase-I	Phase-II+III
^{7}Be [counts]	9060 $\pm$ 530 (HZ)	41153 $\pm$ 2405 (HZ)
	8270 $\pm$ 483 (LZ)	37563 $\pm$ 2196 (LZ)
pep [counts]	424 $\pm$ 6 (HZ)	1962 $\pm$ 27 (HZ)
	430 $\pm$ 6 (LZ)	1989 $\pm$ 26 (LZ)
CNO [counts]	705 $\pm$ 112 (HZ)	3341 $\pm$ 532 (HZ)
	505 $\pm$ 75 (LZ)	2393 $\pm$ 357 (LZ)

Table 5.3: Expected number of solar neutrinos in $\mathrm{RoI}_{\mathrm{gvc}}$, which are used in eq. 5.11. The calculations use the rate predictions and errors from [221], that uses the flux predictions from the SSM B16-GS98 and the SSM B16-AGSS09met.

the influence of Δr_{dir} induces the negative slope for $\cos\alpha < 0$, which can be seen in the best fit (red) distributions. For later N^{th} hits (right), the Cherenkov peak washes away, whereas the indirect impact of the Cherenkov hits on the position reconstruction bias Δr_{dir} makes it still possible to distinguish between the neutrino signal and background.

The compatibility between the data and the MC model, considering all selected hits, is good: $\chi^2/\mathrm{ndf} = 874.9/897$, p-value = 0.70 for Phase-I and $\chi^2/\mathrm{ndf} = 1036.2/1017$, p-value = 0.33 for Phase-II+III. The illustrations of the best fit results for some individual hits in Phase-I and Phase-II+III are shown in Appendix A. The χ^2/ndf and p-values have also been investigated for the individual N^{th} hits $\cos\alpha$ histograms, to investigate the fit performance. For all cases, the best fit MC model $\cos\alpha$ distribution is always in agreement with the data. The effective calibration of the Cherenkov light as a result of the CID analysis on the ^{7}Be edge is $\mathrm{gvc}_{\mathrm{ch}} = (0.140 \pm 0.029)\,\mathrm{ns\,m^{-1}}$ for Phase-I and $\mathrm{gvc}_{\mathrm{ch}} = (0.089 \pm 0.019)\,\mathrm{ns\,m^{-1}}$ for Phase-II+III. These $\mathrm{gvc}_{\mathrm{ch}}$ values for Phase-I and Phase-II+III differ by less than 1.5σ. Both values are in agreement with the calibration performed using a ^{40}K γ source, as shown in Fig. 5.22. These results include the non-negligible systematic uncertainties, which are summarized below:

Exposure: Since the $\mathrm{gvc}_{\mathrm{ch}}$ calibration is performed using the constraint on the expected number of all solar neutrino events, which is converted from the rate using exposure, the systematic uncertainties associated to exposure should be taken into account. The systematic uncertainty on the determination of fiducial mass and on the fraction of solar neutrinos in the RoI is evaluated. The error related to fiducial mass is evaluated to be $\binom{+0.2}{-1.2}$ for all phases using the calibration sources. Here, the edge of FV are sampled according to the offsets between reconstructed event position and the true position of ^{222}Rn+^{14}C calibration source. The new obtained volumes are compared to the nominal values. The systematic uncertainty associated to α/β discrimination method (Sec. 5.5.4) is also taken into account. The systematic error due to energy efficiency is evaluated to be 1.3% for Phase-I and 0.9% for Phase-II+III using the toy-MC method. In this method, the edge of selected energy cut is randomly sampled taking into account the uncertainty on detector response and the new efficiencies are compared to the nominal values [215]. These errors are added in quadrature with the total uncertainty in the neutrino prior probability distribution.

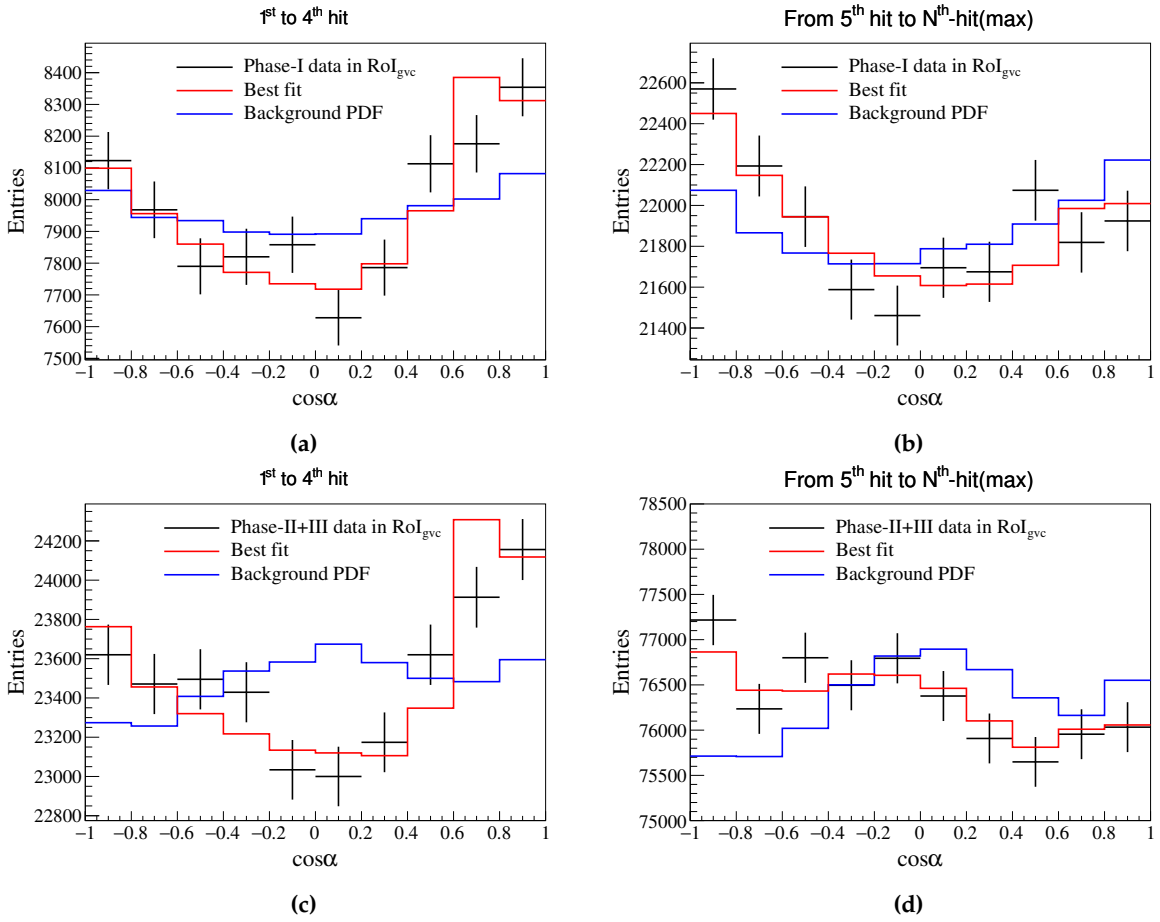

Figure 5.20: Illustration of the best fit results in RoI_{gvc} for summed N^{th} hits in Phase-I (top) and Phase-II+III (bottom). The sum of $\cos\alpha$ distributions of the first four hits in (a) and (c) show the direct Cherenkov peak as well as the effect of Δr_{dir} parameter. The sum of $\cos\alpha$ distributions from 5^{th} hit to N^{th}-hit(max) in (b) and (d) show the indirect effect of Cherenkov photons, Δr_{dir} parameter only (Sec. 5.4). The CID data is shown in black points and the best fit distribution is shown in red. For comparison, the background PDF (blue), scaled to to the total number of events, is also shown.

PMT time correction: The systematic error on the PMT time correction in data should be taken into account as the relative offset of the PMTs is known within a finite precision (Sec. 5.6.2). Therefore, the uncertainty of the PMT time correction, estimated using ^{11}C events, is propagated through the entire analysis chain. This is done by performing CID analysis 1000 times where in each analysis, the time correction includes a Gaussian smearing with the standard deviation of the time offset. By doing χ^2 fit using eq. 5.10 in each analysis, this results in the distribution of best fitted values of gvc_{ch}, which is shown in Fig. 5.21a. The standard deviation of this distribution resulted in the systematic uncertainty of 3.7% for Phase-I and 2.1% for Phase-II+III. For illustration, the obtained 100 χ^2 profiles are shown in Appendix C.

In order to incorporate this systematic effect in the final gvc_{ch} results, the $\Delta\chi^2$ profile as a function of gvc_{ch} averaged over 1000 fits is produced, which is shown in Fig. 5.21b for Phase-II+III, and the final result of gvc_{ch} is obtained using this averaged $\Delta\chi^2$ profile for each period.

5.6.4 Systematic errors budget

Similar to Sec. 5.5.4, the systematic uncertainties for the CID analysis in RoI_{CNO} is also associated to the extraction of total number of solar neutrinos and the conversion to

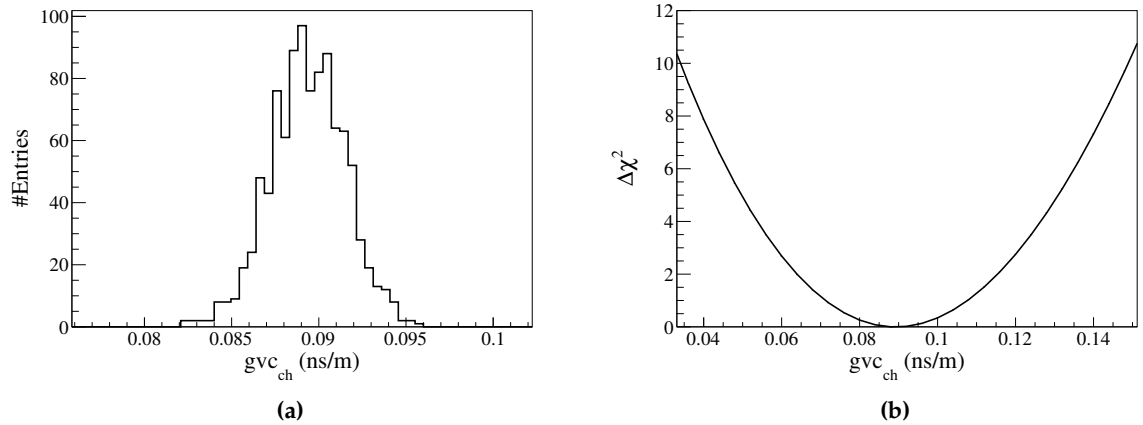

(a) (b)

Figure 5.21: (a) The distribution of gvc_{ch} for Phase-II+III, from 1000 fits after propagating the uncertainty of the PMT time correction through the entire analysis chain. (b) The $\Delta\chi^2$ profile as a function of gvc_{ch} for Phase-II+III, including the uncertainty of the PMT time correction.

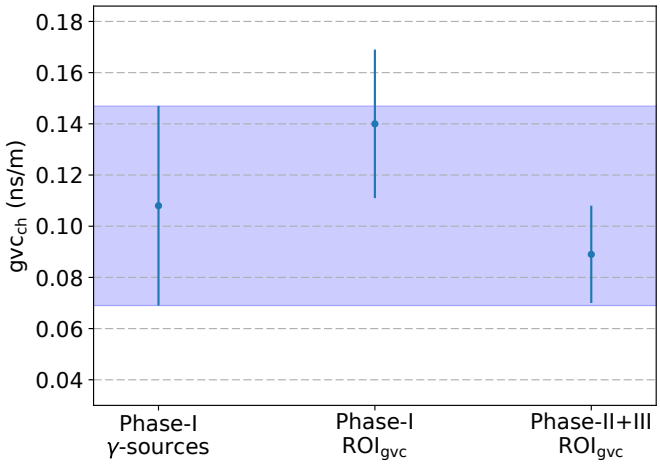

Figure 5.22: The comparison of gvc_{ch} values obtained from the calibration γ-sources (= $(0.108 \pm 0.039)\,\mathrm{ns\,m^{-1}}$) in Phase-I, with the results obtained by doing CID analysis in RoI_{gvc}, which lies in ^{7}Be-ν shoulder region, in Phase-I (= $(0.140 \pm 0.029)\,\mathrm{ns\,m^{-1}}$) and Phase-II+III (= $(0.089 \pm 0.019)\,\mathrm{ns\,m^{-1}}$). The blue band represents the 68% C.I on gvc_{ch} values, obtained from calibration γ-sources (Sec. 5.5.3). It can be seen that the gvc_{ch} values, obtained using the CID analysis in RoI_{gvc} in Phase-I and Phase-II+III, are in agreement with the gvc_{ch} that is estimated using a ^{40}K γ source.

CNO-ν rate after subtraction of the non-CNO solar neutrinos. The systematic uncertainties associated to $N_{solar-\nu}$ are as follows:

PMT time correction: As discussed in Sec. 5.6.2, the relative offset between the PMTs is corrected in data using ^{11}C events and has a finite precision. The uncertainty of the PMT time correction is propagated through the entire analysis chain in order to investigate the systematic differences in the final results, following the procedure discussed in Sec. 5.6.3. By performing 1000 χ^2 fits, described in Sec. 5.4, this results in the distribution of best fitted $N_{solar-\nu}$ values, as shown in Fig. 5.23a and the standard deviation of this distribution resulted in the systematic uncertainty of 4.2% for Phase-I and 2.4% for Phase-II+III. For illustration, the obtained 100 χ^2 profiles are shown in Appendix C. In order to incorporate this systematic error in the final results on $N_{solar-\nu}$, the $\Delta\chi^2$ profile as a function of $N_{solar-\nu}$ averaged over 1000 fits is produced, which is

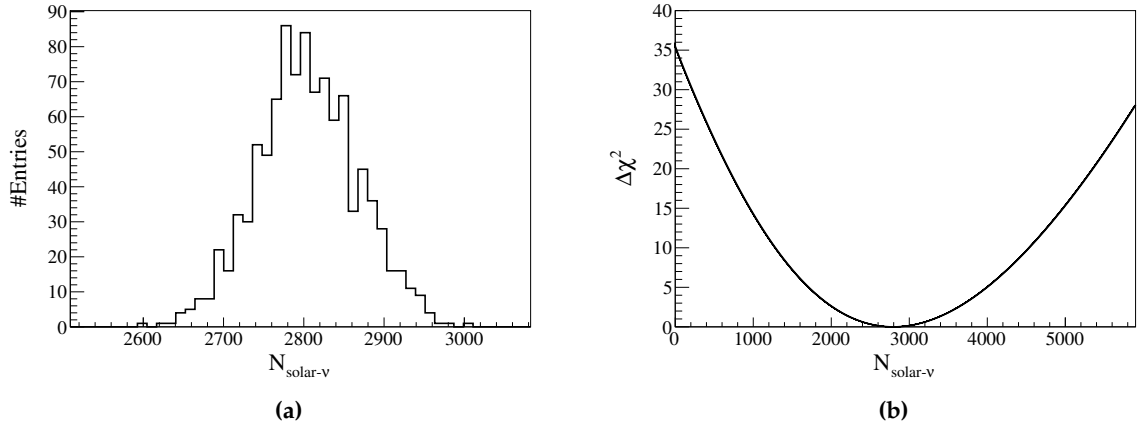

Figure 5.23: (a) The distribution of $N_{solar-\nu}$ in Phase-II+III, after propagating the uncertainty of PMT time correction through the entire analysis chain. (b) The $\Delta\chi^2$ profile as a function of $N_{solar-\nu}$ for Phase-II+III, including the uncertainty of the PMT time correction.

shown in Fig. 5.23b for Phase-II+III and the final result of $N_{solar-\nu}$ is obtained using this averaged $\Delta\chi^2$ profile.

MC production: As described in Sec. 3.2.5, the signal and background MC PDFs are produced on an event-by-event basis. Since it is not known which data events corresponds to the true neutrino events, this could result in an additional systematic uncertainty for the production of the signal MC through the particular choice of the event positions. This is estimated by producing the signal MC $\cos\alpha$ distributions by randomly selecting the expected number of signal events from data in each phase and analyzing the data again with these $\cos\alpha$ histograms. Due to the optimally large statistics of events in Phase-II+III, the subsets of $\cos\alpha$ histograms were similar in shape and the systematic uncertainty is negligible for Phase-II+III. However, this effect is found to have a contribution to the systematic uncertainty of 2.2% in the RoI_{CNO} of Phase-I [220].

CNO-ν vs *pep*-ν spectral shape: Since the spectral shape of the CNO-ν and *pep*-ν events are different in RoI_{CNO}, the Cherenkov to scintillation hits ratio is also different. The expected Cherenkov to scintillation hits ratio for *pep*-ν events (0.475%) is found to be higher than for CNO events (0.469%) in RoI_{CNO} from MC. Moreover, the angular distribution of recoiled electrons by CNO-ν and *pep*-ν is also different due to its dependence on the energy distributions of both the neutrino and the recoiled electron. Since the final fit is performed with the *pep*-ν MC, the CID analysis is performed again with the CNO-ν MC PDFs to estimate the systematic uncertainty of 2.2% for Phase-I and 2.0% for Phase-II+III [215].

The systematic uncertainties associated to the extraction of CNO-ν rate, after the subtraction of non-CNO solar neutrinos from $N_{solar-\nu}$, is as follows:

Constraint on non-CNO neutrinos: The CID analysis is only sensitive to the measurement of the total number of solar neutrinos $N_{solar-\nu}$. The contributions from different solar neutrino species can not be differentiated. Therefore, it is necessary to subtract the non-CNO neutrinos in the RoI_{CNO}. The ^{8}B solar neutrino is constrained using the high precision flux measurement of Super-Kamiokande experiment and its rate in Borexino corresponds to 0.42 ± 0.002 cpd/100 t, which is much smaller than the expected rates of other solar neutrinos [215]. In addition, the number of ^{7}Be and *pep*

Solar -ν	Phase-I	Phase-II+III
^{7}Be [counts]	1.0 ± 0.1 (HZ)	10.0 ± 0.6 (HZ)
	0.9 ± 0.1 (LZ)	9.0 ± 0.5 (LZ)
pep [counts]	406.0 ± 6.0 (HZ)	1513.0 ± 21.0 (HZ)
	411.0 ± 6.0 (LZ)	1534.0 ± 20.0 (LZ)
^{8}B [counts]	15.9 ± 0.3	59.0 ± 1.0

Table 5.4: Expected number of solar neutrinos in RoI_{CNO} in Borexino, which are used for the subtraction of non-CNO solar neutrinos to obtain N_{CNO}. The calculation used for ^{7}Be and *pep* solar neutrinos rate predictions in Borexino are taken from [221], that uses the flux predictions from the SSM B16-GS98 and the SSM B16-AGSS09met models. The estimation of number of ^{8}B solar neutrino events uses the high precision flux measurement of Super-Kamiokande and its rate in Borexino corresponds to 0.42 ± 0.002 cpd/100 t [215].

neutrinos are constrained by both SSM B16-GS98 (HZ) and the SSM B16-AGSS09met (LZ) predictions taking into account their theoretical errors, as listed in Table 5.4. It can be seen that the contribution of ^{7}Be-ν is practically negligible and the *pep* neutrino rate is constrained with about 1.4% precision.

Source of uncertainty	Phase-I	Phase-II+III
For N_{ν}		
PMT time corrections	4.2%	2.4%
Low number of signal events	2.2%	–
CNO-ν vs. *pep*-ν MC	2.2%	2.0%
For N_{CNO}		
Non CNO-ν constraint	4.6%	1.8%
For R_{CNO}		
Fiducial mass	$\binom{+0.2}{-1.2}$ %	$\binom{+0.2}{-1.2}$ %
Fraction of CNO-ν in RoI	1.4%	1.4%

Table 5.5: Systematic uncertainties, relevant in RoI_{CNO}, on the number of solar neutrino events $N_{solar-\nu}$ in RoI_{CNO}, relative to the best fit value. The uncertainty from non CNO-ν rate constraint is relevant only for N_{CNO}. The last two rows are relevant only for the CNO-ν rate (R_{CNO}) calculation.

Exposure: Since the expected number of non-CNO neutrino events are constrained in the analysis, which are converted from the rate using exposure, the systematic uncertainties associated to exposure should be taken into account. The determination of systematic uncertainty associated to the fiducial mass and the fraction of solar neutrinos in RoI_{CNO} is based on the toy-MC studies, already described for RoI_{gvc} in Sec. 5.6.3. The error related to fiducial mass is evaluated to be $\binom{+0.2}{-1.2}$ for all phases and the error related to energy efficiency is evaluated to be 1.4% for all phases [215]. The error of

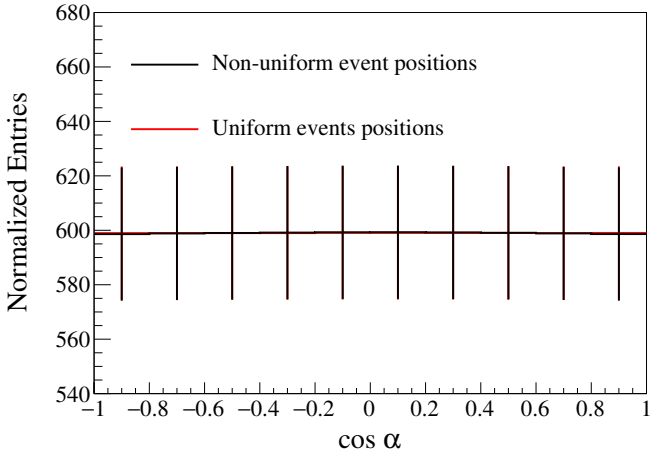

Figure 5.24: Effect on the shape of $\cos\alpha$ distribution in the presence of the external γ background events. These distributions are simulated using a toy MC approach, where only the geometrical conditions of the detector such as the observed Sun's position relative to the Borexino detector's coordinates in Phase-II+III, generated event positions, and the distribution of PMTs inside the detector is taken into account. The distribution of ideal conditions is shown in red, where uniformly distributed events in a spherical volume and uniform PMTs with 100% detector coverage are simulated. The distribution for non-uniform events, which is sampled from the Phase-II+III data distribution with $N_h^{geonorm}$>750, is shown in black. Here, the two distributions almost overlap each other. Each distribution is normalized to the Phase-II+III data statistics.

0.02% associated to TFC application in RoI_{CNO} is also taken into account.

The sources, that contribute negligible systematic error on the final result, are as follows:

Non-uniform backgrounds: As we have seen in Chapter 4, the external γ background events are not present uniformly inside the detector. They have an exponential radial dependence, so their $\cos\alpha$ distributions, which are not simulated in MC, can contribute as a systematic source. Using the toy MC described in Sec. 5.5.4, it has been discussed that the non-uniform position of events can also cause the deviation of the shape of $\cos\alpha$ distribution from its ideal flat shape. Here, using the same method, the comparison is done between the $\cos\alpha$ distributions of uniform and non-uniformly distributed toy events. The spatial distribution of toy events is based on the data events selected in fiducial volumes (Sec. 5.6.1) and energy with $N_h^{geonorm}$>750 (see Fig. 4.7a), where contribution from the external γ background events is maximal. The comparison of $\cos\alpha$ distributions, produced for $\sim 10^9$ statistics and is normalized to the data statistics, is shown in Fig. 5.24. It can be seen that the difference in the shape of the distribution in the two cases is negligible within the statistics of data. The same conclusion has been made when the two distributions with data statistics are simulated and are compared.

Binning, N^{th} hit cut, and PMT selection: As discussed in Sec. 5.6.2, the selection of binning and N^{th} hit cut can result in possible systematic differences in the final results, as there is a possible range of equally valid values from MC studies to use in the CID analysis. For this purpose, a toy MC method is used where the pseudo-datasets, with randomly selected nuisance parameters and the number of physically allowed solar neutrino events, are created. Firstly, these datasets are constructed with the default values of binning and N^{th} hit cut. Then, they are fitted in the same way as the data.

If the best fit values of toy analyses are same as in data results taking into account the systematic error of PMT time offset correction, the 1000 fits are performed again for each varying values of binning and N^{th} hit cut of the same sampled dataset. Then, the resulting distributions of the number of solar neutrinos for each varied binning or N^{th} hit cut are used to statistically compare the data results obtained using default and varied selection values. Similar strategy has also been adopted for studying systematic effects of PMT selection, which is performed by analyzing overall hit time properties of the data PMTs using an enriched sample of ^{11}C events as well as using the relative contribution to the early hits in data and MC (Sec. 5.6.2). For this, the pseudo-datasets and PDFs with events corresponding to different PMT selections, including the default one, are built. By performing the fit with default selection of PMTs and saving toy fit results as in data, the 1000 fits are performed again for each varied PMT selection on the same events. Then, the resulting distributions of the number of solar neutrinos for varied PMT selection are used to statistically compare the data results from default and varied selections. It has been observed that the difference in the data results obtained in varied selection of binning, N^{th} hit cut, and PMTs, with respect to the ones obtained with nominal values, are statistically likely to occur. Thus, the default selected binning, N^{th} hit cut, and PMTs can be used without having any systematic effects in the final results [215]. In addition, the statistically incompatible number of 1^{st} hits is also investigated between data and MC PMTs [220]. It has been found that for only a few PMTs ($\sim$5-8 for all phases) in data, 1^{st} hits are not in statistical agreement and its effect on the final results has been found to be negligible as compared to the statistical and other systematic errors.

Strategy for injection of systematics

As already mentioned before, the error associated to the relative PMT hit time correction is included in the analysis, using the averaged $\Delta\chi^2$ profile over multiple fits, where each profile is obtained by modifying the time correction of PMTs with Gaussian smearing. In order to inject other non-negligible systematics, the probability distribution of $N_{\text{solar}-\nu}$, N_{CNO}, or CNO-ν rate obtained in Sec. 5.6.5, is convoluted with the systematic uncertainties, where all the contributing errors are added in quadrature.

The subtraction of the number of *pep*, ^{7}Be, and ^{8}B neutrino events from the $N_{\text{solar}-\nu}$ is done through the convolution of the $N_{\text{solar}-\nu}$ probability distribution with the predicted $P(N_{pep+^8\text{B}+^7\text{Be}})$ probability distribution, as expressed in eq. 5.12:

$$P(N_{\text{CNO}}) = P(N_{\text{solar}-\nu}) * P(-N_{pep+^8\text{B}+^7\text{Be}}). \tag{5.12}$$

The $P(N_{pep+^8\text{B}+^7\text{Be}})$ probability distribution is a Gaussian distribution, with mean corresponding to the SSM predicted number of *pep*-ν and ^{7}Be-ν and the estimated ^{8}B neutrino counts in Borexino using Super-Kamiokande measurement, as discussed before. The standard deviation is the theoretical and statistical errors on the expected number of *pep*, ^{7}Be, and ^{8}B neutrino events, summed in quadrature. The result of convolution is the probability distribution on CNO neutrino events $P(N_{\text{CNO}})$, which is used to obtain the final CNO-ν rate measurement.

5.6.5 CNO measurement with CID

Now, the results on the measurement of CNO solar neutrinos with CID, using the full Borexino live time from May 2007 to October 2021, is obtained. The gvc_{ch} values, presented in Sec. 5.6.3, are used as independent pull terms in the eq. 5.2 for the fit in RoI_{CNO} of the respective phases. Using the fit strategy discussed in Sec. 5.4, the

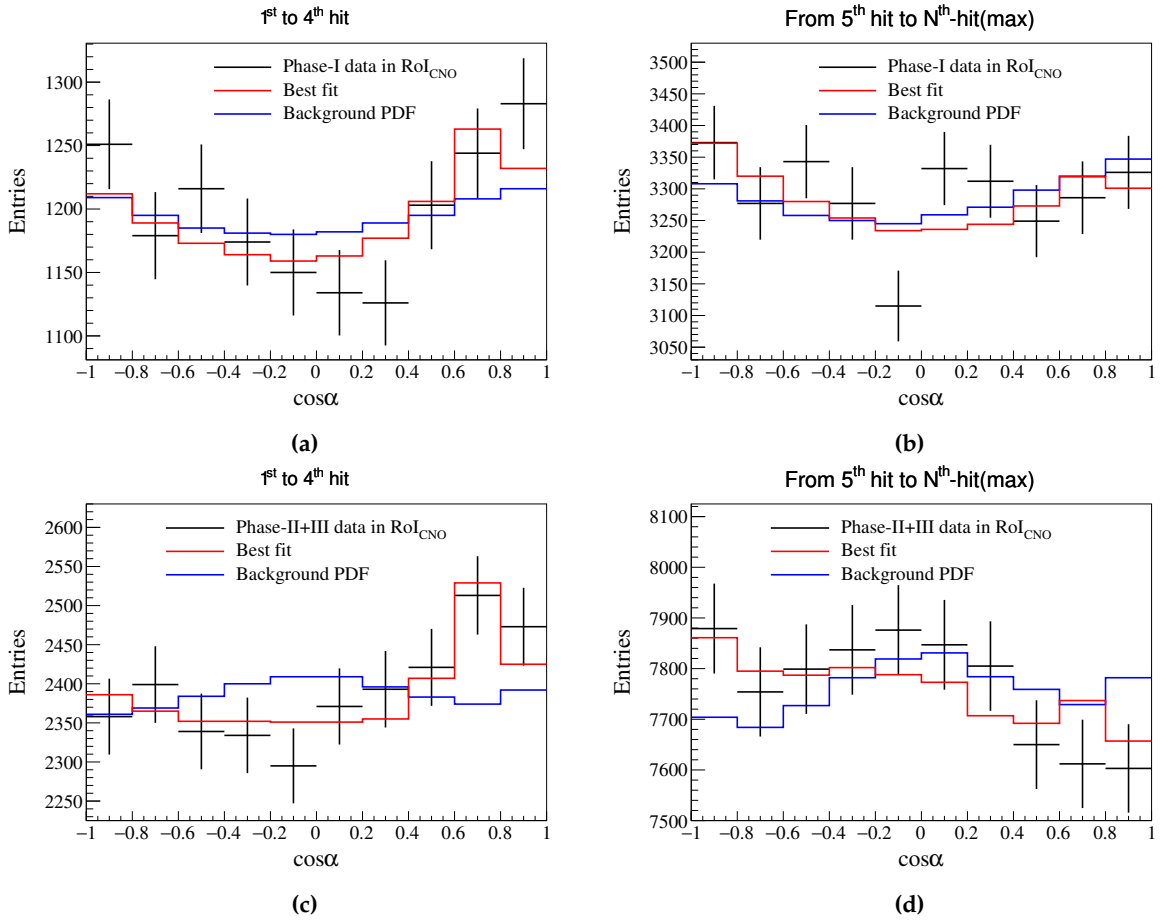

Figure 5.25: Illustration of the best fit results in the $\mathrm{RoI_{CNO}}$ for summed $\mathrm{N^{th}}$ hits in Phase-I (top) and Phase-II+III (bottom). The sum of $\cos\alpha$ distributions of the first four hits in (a) and (c) show the direct Cherenkov peak as well as the effect of $\Delta\mathrm{r_{dir}}$ parameter. The sum of $\cos\alpha$ distributions from 5^{th} hit to $\mathrm{N^{th}}$-hit(max) in (b) and (d) show the indirect effect of Cherenkov photons, $\Delta\mathrm{r_{dir}}$ parameter only (Sec. 5.4). The CID data is shown in black points and the best fit distribution is shown in red. For comparison, the background PDF (blue), scaled to to the total number of events, is also shown.

best fit values obtained for the number of solar neutrinos in $\mathrm{RoI_{CNO}}$ are $N_{\mathrm{solar}-\nu} = 691^{+235}_{-224}$ (stat) for Phase-I and $N_{\mathrm{solar}-\nu} = 2828^{+518}_{-494}$ (stat) for Phase-II+III, without the inclusion of any systematic uncertainties or corrections. The fits are good with $\chi^2/\mathrm{ndf} = 884.8/897$, p-value = 0.61 for Phase-I and $\chi^2/\mathrm{ndf} = 1000.7/1017$, p-value = 0.64 for Phase-II+III. The MC model is able to reproduce the data $\cos\alpha$ distribution, which has also been investigated for the individual $\mathrm{N^{th}}$-hits $\cos\alpha$ histograms.

To show that the early hits have the Cherenkov peak and the later hits show the impact of Δr_{dir}, the sum of the early first to fourth $\mathrm{N^{th}}$-hits and the sum of the later $\mathrm{N^{th}}$-hits from the fifth hit to $\mathrm{N^{th}}$-hit(max), are illustrated in Fig. 5.25 for Phase-I (top) and Phase-II+III (bottom). The illustrations of the best fit results for some individual hits in Phase-I and Phase-II+III are shown in Appendix B.

Fit response bias correction

A toy MC analysis is performed to investigate the bias in the fit response of the strategy used in the CID analysis, where $\mathrm{gvc_{ch}}$ and Δr_{dir} are treated as nuisance parameters in the fit. It has been found that the number of solar neutrinos in $\mathrm{RoI_{CNO}}$ show a small systematic shift between the injected number of neutrinos and their corresponding best fit values, in the case of a small signal ratio as well as the small data event statistics. This fit response bias is induced by two nuisance parameters ($\mathrm{gvc_{ch}}$, Δr_{dir}) because

they only impact the shape of the neutrino signal MC $\cos\alpha$ distribution, but not that of the background. In the case of low event statistics, the purely statistical fluctuations of the data $\cos\alpha$ distribution can be better accommodated with the change in shape of neutrino signal MC $\cos\alpha$ distribution by nuisance parameters, which in turn influences the best fit value of the number of neutrino events. This results in the observed fit response bias. This effect has been found to be present in $\mathrm{RoI}_{\mathrm{CNO}}$. However, it is negligible in $\mathrm{RoI}_{\mathrm{gvc}}$, due to large event statistics and a good signal to total ratio in $\mathrm{RoI}_{\mathrm{gvc}}$ [215]. This means that in $\mathrm{RoI}_{\mathrm{CNO}}$, the direct likelihood profile interpretation from CID analysis is not optimal for obtaining final results.

A Bayesian approach has been utilised to unfold for fit response bias [222] and estimate the correct intervals on the final results. The Bayes theorem can be written as [223]:

$$P(\theta|x) \propto L(x|\theta) \cdot \pi(\theta), \tag{5.13}$$

where θ represents all associated parameters of the model and x represents the available data. $L(x|\theta)$ is the likelihood for the data given θ, which can be obtained by comparing the data with model whose parameters are given by θ. Here, $\pi(\theta)$ represent the prior distributions of θ, representing one's degree of belief for θ before performing the measurement. $P(\theta|x)$ is the posterior probability distributions of parameters θ given data x, which represents the degree of belief that θ is true given the data. In Bayesian approach, the statistical inference is based on the posterior probability distribution.

Here, the Bayesian posterior distribution of $N_{\mathrm{solar}-\nu}$ is built using a MC acceptance-rejection sampling method [215, 222, 223]. The Bayesian approach has some advantages, which involve easier physical interpretation of the results and the treatment of physical limits such as $N_{\mathrm{solar}-\nu}$ can not be negative. Here, the treatment of nuisance parameters by using them as prior distributions over all possible range of values and the inclusion of systematic errors as well as subtraction of non-CNO solar neutrinos are also straightforward. In this method, the pseudo-data inputs are created from the MC signal for the injected parameters $N^{\mathrm{sim}}_{\mathrm{solar}-\nu}$, $\mathrm{gvc}^{\mathrm{sim}}_{\mathrm{ch}}$, and $\Delta r^{\mathrm{sim}}_{\mathrm{dir}}$, and the background $\cos\alpha$ distributions. These parameters are sampled from their prior distributions. The prior distribution for the $N_{\mathrm{solar}-\nu}$ is chosen to be uniform within allowed physical limits, i.e, between zero and the total number of selected data events (see Table 5.2), the prior distribution of Δr_{dir} is also uniform between 0.0 and 6.0 cm, and the prior distribution of $\mathrm{gvc}_{\mathrm{ch}}$ is given by the measurement in $\mathrm{RoI}_{\mathrm{gvc}}$. Due to limited computational resources, the MC signal $\cos\alpha$ distributions for the injected parameter are created using the interpolation method [215].

Then, the fit is performed in the same way as for the real data, and this results in the best fit values, given by $\left(N^{\mathrm{fit}}_{\mathrm{solar}-\nu}, \mathrm{gvc}^{\mathrm{fit}}_{\mathrm{ch}}, \Delta r^{\mathrm{fit}}_{\mathrm{dir}}\right)$. A multivariate Gaussian probability distribution is defined, which is given by $\mathrm{P}_{\mathrm{accept}}(N_{\mathrm{solar}-\nu}, \mathrm{gvc}_{\mathrm{ch}}, \Delta r_{\mathrm{dir}})$, with mean value at the best fit values from the real data and a standard deviation from the systematic uncertainty of the PMT time corrections, as it has been propagated through the whole analysis chain. A distribution using the injected values of $\left(N^{\mathrm{sim}}_{\mathrm{solar}-\nu}, \mathrm{gvc}^{\mathrm{sim}}_{\mathrm{ch}}, \Delta r^{\mathrm{sim}}_{\mathrm{dir}}\right)$ is built from 20k pseudo-experiments. In the resulting distribution, each injected value of the fit parameters is saved with a probability of $\mathrm{P}_{\mathrm{accept}}(N^{\mathrm{fit}}_{\mathrm{solar}-\nu}, \mathrm{gvc}^{\mathrm{fit}}_{\mathrm{ch}}, \Delta r^{\mathrm{fit}}_{\mathrm{dir}})$, given by the best fit result of the pseudo-data. This is done for the values of best fit parameters which are compatible with the data result, otherwise they are rejected. The resulting distributions of the true values for $\left(N_{\mathrm{solar}-\nu}, \mathrm{gvc}_{\mathrm{ch}}, \Delta r_{\mathrm{dir}}\right)$ then correspond to their Bayesian posterior distributions. The resulting distribution is then marginalized over nuisance parameters to obtain the posterior probability distribution as a function of $N_{\mathrm{solar}-\nu}$.

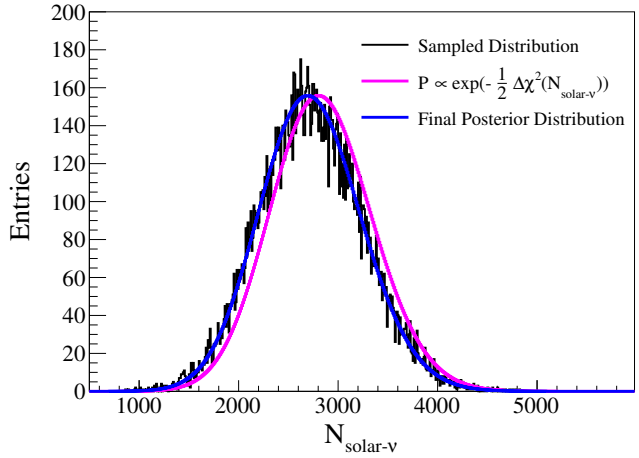

Figure 5.26: Correction of the fit response bias for Phase II+III in the RoI_{CNO}. The posterior distribution of 20k pseudo-data analyses, selected through the toy MC rejection sampling, is shown in black. The data fit result, i.e. the likelihood $P(N_{\text{solar}-\nu})$ given by the $\Delta\chi^2$ profile of eq. 5.2 and averaged over 1000 fits with different PMT time offsets is shown in violet. The blue distribution corresponds to the posterior distribution that includes only the systematics from the PMT time alignment correction.

The fit response bias is illustrated in Fig. 5.26 for Phase II+III. The likelihood distribution $P(N_{\text{solar}-\nu}) \propto \exp\left(-\frac{1}{2}\Delta\chi^2(N_{\text{solar}-\nu})\right)$ given by the χ^2 fit of data with eq. 5.2 and averaged over the 1000 fits with different PMT time offsets is shown in pink. The black distribution is given by the simulation of 20k pseudo-data analyses, selected through the rejection sampling MC described above. The blue distribution is the resulting posterior distribution after bias correction. The blue distribution is produced by shifting $P(N_{\text{solar}-\nu})$ by a value, so that it is in agreement with the black rejection sampled distribution, as the black sampled distribution could be produced for a finite number of simulations. It can be seen from the Fig. 5.26 that the overall shape of blue distribution, produced after the shift, is in agreement with the black distribution. For Phase-I, the shift is found to be -50 ± 4 events and for Phase-II+III, the shift is -109 ± 4 events.

Final results on CNO with CID

The posterior distribution of $N_{\text{solar}-\nu}$ is then convoluted with the systematic uncertainties described in Sec. 5.6.4. The posterior distributions $P\left(N_{\text{solar}-\nu}\right)$ in Phase-I and Phase-II+III, including all systematics and the fit response bias correction, are shown in Fig. 5.27a. The resulting number of solar neutrinos detected in the RoI_{CNO} is:

$$N_{\text{solar}-\nu} = 643^{+235}_{-224}\,(\text{stat})^{+37}_{-30}\,(\text{sys}) \;\text{ for Phase-I;}$$

$$N_{\text{solar}-\nu} = 2719^{+518}_{-494}(\text{stat})^{+85}_{-83}(\text{sys}) \;\text{ for Phase-II+III.}$$

These results include all systematics relevant for $N_{\text{solar}-\nu}$ and the fit response bias correction. The quoted central values and systematic uncertainties are based on the posterior distributions using an 68% equal-tailed credible interval (CI) before and after convolution. In equal-tailed CI, the median of the posterior distribution is quoted as the central value and the left and right extremes with ∼16% and ∼84% probabilities contribute to the errors. The one-sided zero neutrino hypothesis can be excluded with probabilities: $P(N_{\text{solar}-\nu} = 0) = 2.8 \times 10^{-5}$ ($\sim 4.2\sigma$) for Phase-I, and $P(N_{\text{solar}-\nu} = 0) = 6.4 \times 10^{-11}$ ($\sim 6.5\sigma$) for Phase-II+III.

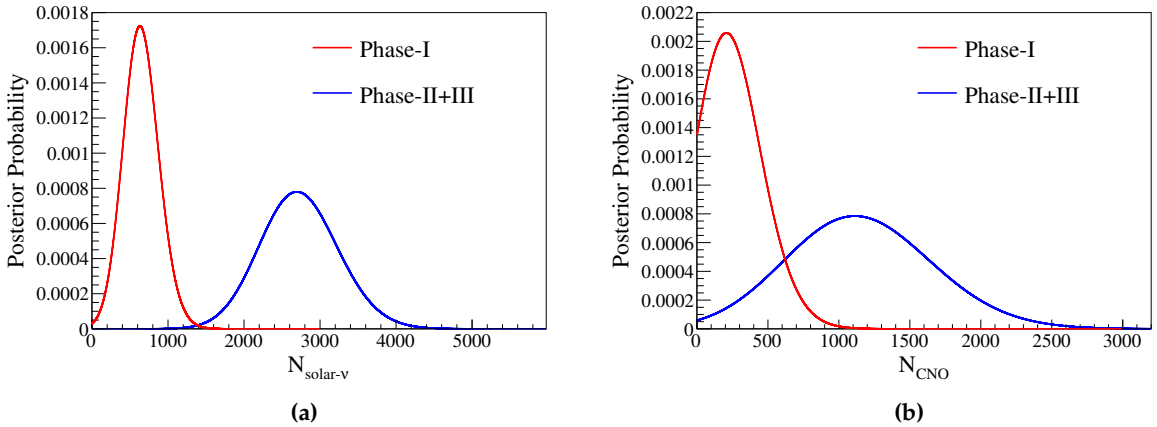

Figure 5.27: (a) The CID measured posterior probability distributions for the number of solar neutrinos $N_{\text{solar}-\nu}$ in the RoI_{CNO} for Phase-I (red) and Phase-II+III (blue). All systematic effects are included. (b) The CID measured posterior probability for the number of CNO-ν events N_{CNO} in the RoI_{CNO}, after constraining *pep* and ^{8}B neutrinos for Phase-I (red) and Phase-II+III (blue). All systematic effects are included.

The resulting number of solar neutrino events $N_{\text{solar}-\nu}$ in the RoI_{CNO} is converted into the number of CNO neutrinos detected in the same energy region, after constraining the contributions from non-CNO solar neutrinos, as discussed in Sec. 5.6.4, without any prior knowledge of the backgrounds. The CID measurement for the number of CNO-ν events are:

$$N_{\text{CNO}} = 270^{+218}_{-169}\,(\text{stat})^{+33}_{-25}\,(\text{sys}) \;\text{ for Phase-I;}$$

$$N_{\text{CNO}} = 1146^{+518}_{-486}\,(\text{stat})^{+92}_{-89}\,(\text{sys}) \;\text{ for Phase-II+III,}$$

where the uncertainties correspond to equal-tail 68% C.I. within the physical boundaries, including all systematics. The posterior distributions $P\,(N_{\text{CNO}})$ in Phase-I and Phase-II+III, including all systematics, are shown in Fig. 5.27b. The probability, that exactly zero CNO-ν events contribute to the measured data CID $\cos\alpha$ distribution, is $P(N_{\text{CNO}} = 0) = 1.35 \times 10^{-3}$ for Phase-I and $P(N_{\text{CNO}} = 0) = 5.87 \times 10^{-5}$ for Phase-II+III. It has been observed that Phase-I and Phase-II+III do not show different behavior for the full CID analysis chain and therefore, the independent results of Phase-I and Phase-II+III can be combined through the convolution of both posterior distributions :

$$P\,(N_{\text{CNO}})^{\text{I+II+III}} = P\,(N_{\text{CNO}})^{\text{I}} * P\,(N_{\text{CNO}})^{\text{II+III}}\,. \tag{5.14}$$

For the combined phases, the probability that exactly zero CNO-ν events contribute to the measured data $\cos\alpha$ distribution is $P(N_{\text{CNO}} = 0) = 7.93\times10^{-8}$. This corresponds to the exclusion of the zero-CNO hypothesis at about 5.3σ credible interval for the combined Phase-I and Phase-II+III. The estimated number of CNO solar neutrinos is:

$$N_{\text{CNO}} = 1436^{+560}_{-525}\,(\text{stat + sys}) \;\text{ for Phase-I+II+III,}$$

where the uncertainties correspond to equal-tail 68% C.I. within the physical boundaries, including all systematics. The CNO-ν rate probability density function, shown in Fig. 5.28, is calculated from the measured posterior distribution of CNO-ν events by using exposure in the respective phases. The final CID result for the CNO-ν rate, using the full dataset of Phase-I + Phase-II+III, is:

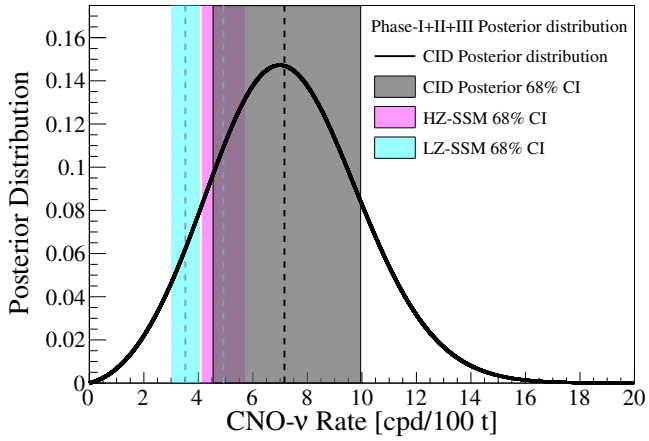

Figure 5.28: The combined CID Phase-I + Phase-II+III CNO-ν rate posterior distribution is shown in black. The blue, violet, and grey bands show the 68% CI, for the low-metallicity SSM B16-AGSS09met ((3.52 ± 0.52) cpd/100 t), the high-metallicity SSM B16-GS98 ((4.92 ± 0.78) cpd/100 t) predictions, and the combined CID result in Borexino, respectively. All systematic effects are included. From [6].

$$\begin{aligned} R^{\mathrm{CID}}_{\mathrm{CNO}} &= 7.2 \pm 2.5\ (\mathrm{stat}) \pm 0.4\ (\mathrm{sys})\ ^{+1.1}_{-0.8}\ (\mathrm{nuisance})\ \ \mathrm{cpd/100\,t}, \\ &= 7.2^{+2.8}_{-2.7}\,(\mathrm{stat+sys})\ \ \mathrm{cpd/100\,t}, \end{aligned}$$

where the uncertainties correspond to equal-tail 68% C.I. and include all systematics. The quoted statistical uncertainty corresponds to a hypothetical, perfect calibration of these CID nuisance parameters. These CID results are well in agreement with both the HZ-SSM prediction of (4.92 ± 0.78) cpd/100 t ($0.6\,\sigma$) and the LZ-SSM prediction (3.52 ± 0.52) cpd/100 t ($1.1\,\sigma$).

5.6.6 Combined CID and multivariate fit

The result from the CID analysis is now combined with the multivariate fit on Phase-III (Chapter 4), by including the posterior distributions of solar neutrinos from the CID analysis, shown in Fig. 5.27a after statistical subtraction of the subdominant ^{8}B neutrinos. The CID neutrino posterior distributions are included as the external likelihood terms in the multivariate likelihood minimization procedure [218]. These distributions correspond to two pull terms, which constrain the number of CNO and *pep* neutrino events: the first one is related to the Phase-I ($\mathcal{L}^{\mathrm{P-I}}_{\mathrm{CID}}$), while the second one refers to Phase-II+III datasets ($\mathcal{L}^{\mathrm{P-II+III}}_{\mathrm{CID}}$). The overall combined likelihood is as follows:

$$\mathcal{L}_{\mathrm{MV+CID}} = \mathcal{L}_{\mathrm{MV}} \cdot \mathcal{L}_{\mathrm{pep}} \cdot \mathcal{L}_{^{210}\mathrm{Bi}} \cdot \mathcal{L}^{\mathrm{P-I}}_{\mathrm{CID}} \cdot \mathcal{L}^{\mathrm{P-II+III}}_{\mathrm{CID}}, \tag{5.15}$$

where the first three terms correspond to TFC subtracted/tagged energy and radial distributions (Sec. 4.4.4), the constraint on *pep* solar neutrino $\mathcal{L}_{\mathrm{pep}}$ (Sec. 4.4.1), and ^{210}Bi constraint $\mathcal{L}_{^{210}\mathrm{Bi}}$ (Sec. 4.4.2), respectively. Here, an improved approach is used that couples the one-dimensional Poisson likelihood for the TFC-Tagged dataset with a two-dimensional one (energy and radius) for the TFC-subtracted, to enhance the separation between signal and backgrounds. The energy range of the fit is 0.32 MeV − 2.64 MeV and all species are free to vary in the fit, except ^{8}B solar neutrino which is fixed according to HZ-SSM expectations.

The multivariate fit has a p-value of 0.2, showing the agreement between the model and data. The negative log-likelihood profile as a function of the CNO rate is shown in

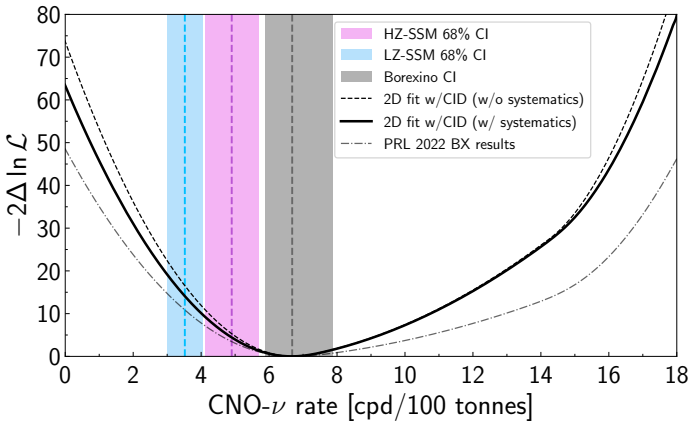

Figure 5.29: The negative log-likelihood ($-2\Delta \ln \mathcal{L}$) profile as a function of CNO-ν rate, obtained from the spectral fit combined with the CID analysis constraint, with and without convolution with the systematic uncertainties (black dashed and solid lines respectively). The grey dash-dotted line shows the same profile obtained in Chapter 4. The blue, violet, and gray bands show 68% confidence intervals (CI) for the low-metallicity SSM B16-AGSS09met (3.52 ± 0.52 cpd/100 t) and the high-metallicity SSM B16-GS98 (4.92 ± 0.78 cpd/100 t) predictions, and the new Borexino result including systematic uncertainty, respectively [6, 218].

Fig. 5.29. The solid and dashed black lines show the results from combined CID and spectral fit with and without systematic uncertainty, respectively. The result, without CID constraint from Chapter 4, is included as grey dash-dotted line. The CNO interaction rate is extracted from the 68% quantile of the likelihood profile convoluted with the systematic uncertainties described in Sec. 4.4.6, as $R^{\mathrm{MV+CID}}(\mathrm{CNO}) = 6.7^{+1.2}_{-0.8}$ cpd/100 t. The no-CNO hypothesis is excluded with about 8σ significance, and the resulting CNO flux at Earth is $\Phi(\mathrm{CNO}) = 6.7^{+1.2}_{-0.8} \times 10^8\,\mathrm{cm}^{-2}\,\mathrm{s}^{-1}$.

Using the same procedure as in Sec. 4.4.7, the abundance of C + N with respect to H in the Sun, $\mathrm{N_{CN}} = 5.81^{+1.22}_{-0.94} \times 10^{-4}$. This error includes both the statistical uncertainty due to the CNO measurement and the systematic errors (Sec. 4.4.7). Similar to the previous results, this result is in agreement with the high-metallicity compilations (MB22 [141] and GS98), while featuring a $\sim 2\sigma$ tension with low-metallicity ones (AGSS09met, C11 [139] and AAG21 [140]) [6].

5.7 Summary

In summary, this chapter has introduced a novel technique called Correlated and Integrated Directionality (CID) method, that is used to not only provide the first ever directional measurement of sub-MeV solar neutrinos in liquid scintillator detectors with Borexino experiment, but also the CNO-ν measurement has been performed using this technique. In this method, the event by event directional reconstruction is not possible as the scintillation photons are dominant. In CID, the early photon hits in time of each selected event are correlated to the well-known solar position using the hit-PMT position and the reconstructed event position. This produces an angular distribution, which is used to statistically infer the number of solar neutrinos in a region of interest.

The first directional measurement of sub-MeV solar neutrino is performed in an energy window of $\sim$(0.5-0.8) MeV, that lies around the ^{7}Be-ν shoulder. For the Phase-I of Borexino experiment, where the calibration of effective group velocity correction for Cherenkov photons is possible using γ-sources, the proof of concept of this method is provided. Here, the null hypothesis of no solar neutrinos in the region of

interest, by fitting CID distributions of the first 2 hits, is excluded with >5σ significance by purely using their directionality. The inferred total number of solar neutrino (^{7}Be+*pep*+CNO) events using CID is $10887^{+2386}_{-2103}(\text{stat.}) \pm 947(\text{syst.})$. The expected value using SSM predictions is 10187^{+541}_{-1127} events, where the uncertainty includes the difference between low-metallicity SSM B16-AGSS09met and high-metallicity SSM B16-GS98 models. Thus, the CID measurement is well in agreement with the SSMs. The result on the ^{7}Be interaction rate, after fixing the contributions of the CNO and *pep* solar neutrinos from the SSM predictions and including the systematic uncertainties is $51.6^{+13.9}_{-12.5}$ (stat. + syst.) cpd/100t. In addition, the test regarding the background-only hypothesis on the summed data of all the three Borexino Phases is also performed. The background-only hypothesis is found to be incompatible with the data with a significance of >5σ. In addition, a detection of solar neutrinos is performed only using their directionality, without any Cherenkov calibration. I contributed to this analysis by optimising the number of bins of the cos α distributions used in the fit and by developing a toy simulation method that has been used to investigate the systematic effects concerning background events' simulation. I also worked towards the preparation of the publications [4, 5].

As said, CID technique is also applied to the CNO-ν analysis in an energy region of about (0.85 - 1.3) MeV. Here, the evidence of CNO solar neutrinos is extracted using the entire Borexino dataset, thanks to the calibration of effective group velocity correction for Cherenkov photons using ^{7}Be solar neutrinos. The calibration is performed using CID analysis on ^{7}Be-ν edge region, where the number of solar neutrinos is treated as a nuisance pull term in the fit. Then, using the calibration results on the group velocity correction for Cherenkov photons, the number of solar neutrino events in the CNO energy region is obtained by fitting the CID angular distributions of the selected first several hits. Using a Bayesian posterior distribution and constraining non-CNO solar neutrinos, the exclusion of the zero-CNO hypothesis is provided at about 5.3σ credible interval for all combined phases. The final CID result for the CNO-ν rate, using the full dataset of Borexino is $7.2^{+2.8}_{-2.7}$ cpd/100 t. This method has provided an alternative approach with respect to the standard multivariate analysis (Chapter 4) as well as provided the measurement of CNO neutrinos without the help of ^{210}Bi constraint. My contribution to this analysis comprises the optimisation of the fit inputs, estimation of the expected number of neutrino events and performing analysis for the calibration of group velocity of Cherenkov photons in the ^{7}Be-ν edge region, evaluation of the systematic uncertainties, performing final CID fits as well as analysis checks, and co-writing the publication [6]. By combining the CID results with the standard multivariate fit performed on Phase-III data, the improved measurement of the CNO neutrino rate in Borexino is also obtained. Using the combined approach, the CNO interaction rate is $6.7^{+1.2}_{-0.8}$ cpd/100 t and the significance against the absence of a CNO signal is about 8σ. The determination of C+N abundance using this result, is found to be compatible with SSM B16-GS98 metallicity measurements.

These results have not only shown the proof of principle for the CID method but also demonstrated a combined solar neutrino analysis approach using CID and the multivariate spectral fit, discussed in Chapter 4. The future liquid scintillator experiment such as JUNO, can be benefited using CID without any need of specialised hardware or LS mixtures. The sensitivity of CID could be improved by performing a dedicated e^- Cherenkov calibration, in order to reduce the major uncertainties arising from the position reconstruction bias and the Cherenkov group velocity correction.

Part III

The JUNO Experiment

Chapter 6

Introduction to JUNO Experiment

The Jiangmen Underground Neutrino Observatory (JUNO) [100] is a next generation neutrino experiment, which is under construction in Southern China and is expected to complete its construction at the end of 2024. This chapter provides a comprehensive overview of the JUNO experiment as well as summarizes its various physics goals. Section 6.1 first describes the experimental site and the structure of the detector. This section also summarizes the goals and structure of the two satellite detectors, OSIRIS and TAO. Moreover, the future calibration programs and the expected radiopurity level of the detector are also discussed. The dedicated Monte Carlo software framework used in all JUNO analyses and the various stages of simulation are described in Sec. 6.2. Section 6.3 reports the main physics goal, the determination of the neutrino mass ordering, of JUNO as well as its capability for extended physics programs, including solar neutrinos, geoneutrinos, supernova neutrinos, etc.

6.1 JUNO detector

The Jiangmen Underground Neutrino Observatory (JUNO) [100] is a multi-kiloton liquid scintillator detector under construction in an underground laboratory with a vertical overburden of $\approx$ 650 m ($\approx$ 1800 m water equivalent) in Jinji town in Guangdong province in Southern China. The geographic location of the JUNO experiment is 112°31′05" E and 22°07′05" N. The JUNO detector is located at a distance of 52.5 km from both the Yangjiang and the Taishan nuclear power plants (NPPs). This baseline is optimized to have the best sensitivity for the JUNO's primary goal, *i.e.*, the determination of the neutrino mass ordering (NMO) using reactor antineutrinos. The Yangjiang NPP has six reactor cores, where the thermal power of each core is 2.9 GW_{th}. The Taishan NPP has two cores in operation, each with 4.6 GW_{th} thermal power. The total thermal power of both NPPs is 26.6 GW_{th}. The reactors are commercial light-water reactors, where the fissions of the four isotopes in fuel, ^{235}U, ^{238}U, ^{239}Pu, and ^{241}Pu, occur. Other than Daya Bay nuclear complex, located at 215 km distance from the JUNO detector and whose cores only contribute about 6.4% of the reactor antineutrino events, there is no other or planned NPP within a radius of 500 km around the JUNO's experimental site. To achieve its main goal, JUNO requires a large target mass and an excellent energy resolution, which offer further opportunities for a variety of topics in the areas of neutrino and astroparticle physics (Sec. 6.3).

A schematic sketch of the JUNO detector's design is shown in Fig. 6.1. It consists of a Central Detector (CD) [224], containing 20 kt of liquid scintillator mixture in a spherical acrylic vessel with a diameter of 35.4 m and a thickness of 120 mm. This huge volume makes JUNO the largest liquid scintillator (LS) detector ever built. The liquid scintillator mixture is composed of linear alkylbenzene (LAB) as the detection medium, 2.5 g/L of 2,5-diphenyloxazole (PPO) as the scintillation fluor, and 3 mg/L of p-bis-(o-methylstyryl)-benzene (bis-MSB as a wavelength shifter. This recipe has been optimized in dedicated studies with a Daya Bay detector [225]. JUNO's LS will be purified before filling to improve its radiopurity levels and transparency. The light

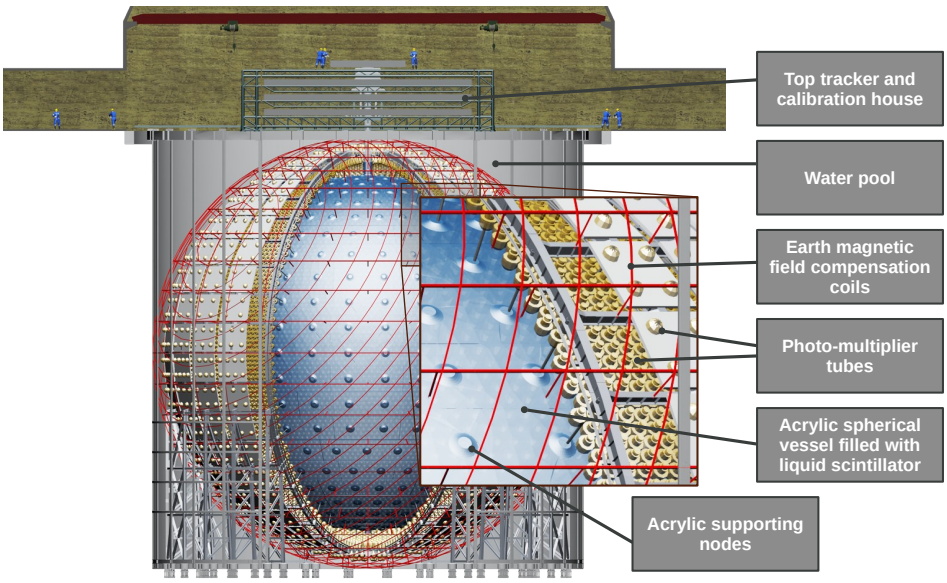

Figure 6.1: Schematic sketch of the main JUNO detector. From [7].

yield of JUNO LS is high, with about 10,000 photons per MeV. Combining this with all the detector parameters, the predicted overall yield is about 1600 photoelectrons per MeV [226]. The light attenuation length is greater than 20 m at 430 nm in order to make up for the huge CD dimensions, and the LS density is $0.856\,\mathrm{g/cm^3}$. Before filling, the liquid scintillator of JUNO will be purified using distillation, water extraction, and stripping plants to improve its radiopurity.

The acrylic vessel is supported by a spherical stainless steel (SS) structure via 590 connecting bars. The scintillation light emitted due to energy depositions in the liquid scintillator is detected by 17,612 20-inch PMTs, or the so-called *Large PMTs (LPMTs)*, and 25,600 3-inch PMTs, or the so-called *Small PMTs (SPMTs)*. There are two types of LPMTs based on the manufacturing companies: Northern Night Vision Technology Co. (NNVT) and Hamamatsu. The 5000 PMTs correspond to Hamamatsu or dynode PMTs, and the remaining 12,612 PMTs are the NNVT PMTs or the Microchannel Plate (MCP) PMTs. The PMTs are mounted on the SS structure facing the acrylic sphere. This provides a large photo coverage (75.2% for 20-inch PMTs and 2.7% for 3-inch PMTs), which is necessary to collect a large number of photoelectrons per unit of deposited energy. These unique features of JUNO lead to an unprecedented energy resolution for a liquid scintillator detector of $\approx 3\%\sqrt{E(\mathrm{MeV})}$, at the price of a large dark noise rate of about 30 kBq. The dark counts are typically caused by thermionic emission of electrons in the photo cathode or dynode of the PMT. The space between SS and the acrylic vessel is filled with water and serves as a buffer volume.

The CD is placed inside a cylindrical water pool (WP) with a diameter of 43.5 m and a height of 44.0 m, filled with 35 kt of ultra-pure water. The WP shields the CD against external fast neutrons and gammas. It also acts as a Cherenkov veto for cosmic muons, with a flux of about $0.004\,\mathrm{m^{-2}s^{-1}}$ and a mean energy of 207 GeV. The muons passing through water produce Cherenkov light, which are detected by 2,400 20-inch PMTs installed on the outer surface of the SS structure. The SS structure has an inner diameter of 40.1 m with 30 pairs of legs attached to the floor of WP. The WP walls and the SS support structure are coated with Tyvek reflective foil to increase light collection efficiency. On the top of the WP, a Top Tracker (TT) is placed to precisely measure the tracks of a sub-sample of the crossing muons. It consists of a plastic scintillator array, formerly used in the Target Tracker of the OPERA experiment [227].

The analog signal from each PMT is fed to front-end electronics, where it is amplified and converted to digital signal with a 12 bit and 1 GS/s custom FADC. After

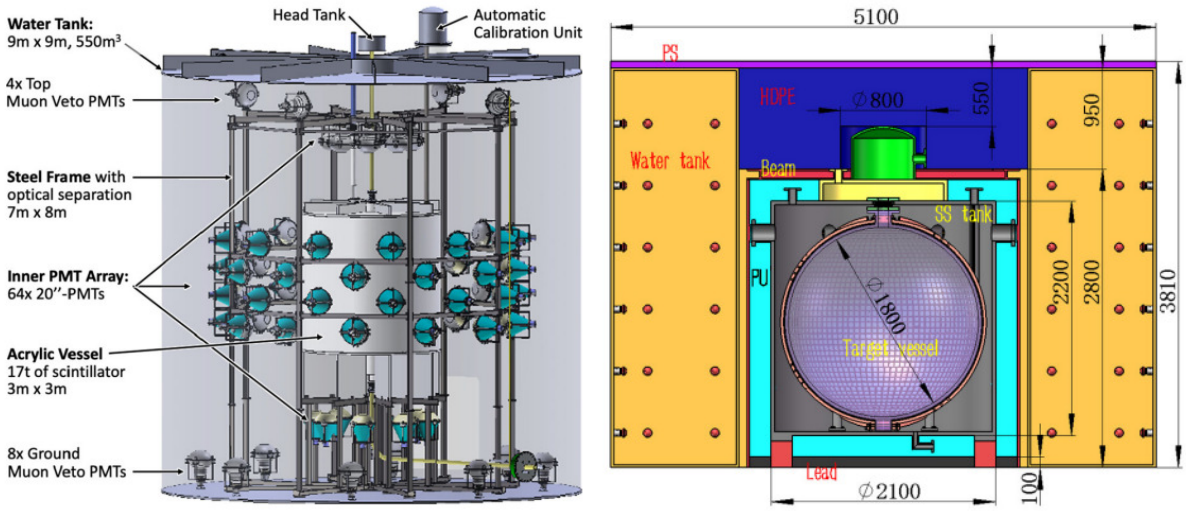

Figure 6.2: Schematic layout of OSIRIS (left) and TAO (right) detectors. From Refs. [228] and [66], respectively.

further processing of digitized PMT waveform and the trigger validation, the PMT data is saved to data acquisition (DAQ) system. Due to the enormous size of JUNO, it is expected that about 40 GB/s triggered waveform data will be read out by DAQ from all PMTs in the CD and WP, which could lead to a storage challenge. Therefore, an Online Event Classification (OEC) algorithm will be used to reduce the data rate by processing waveform data such that only relevant information of the relevant events is recorded. The working condition of the detector will also be monitored in real-time. All raw data will be recorded with a rate of about 2 PB per year to the IHEP data center resources, which will be replicated at other sites to perform analysis by the entire JUNO collaboration.

Sub-detectors: OSIRIS and TAO

The JUNO experiment consists of two additional detectors: the Online Scintillator Internal Radioactivity Investigation System (OSIRIS) [228] and the Taishan Antineutrino Observatory (TAO) [66]. Figure 6.2 shows the schematic diagrams of OSIRIS (left) and TAO (right).

The OSIRIS detector will monitor the JUNO LS radiopurity during the filling of the JUNO CD and provide confirmation of the proper operation of the purification plants. This detector contains 18 t of LS in a cylindrical acrylic vessel with a height and diameter of 3 m. The acrylic vessel is mounted inside a steel tank with a height and diameter of 9 m to shield against external radiation. The scintillation light is collected by 64 20-inch PMTs mounted to a stainless steel frame surrounding the acrylic vessel at a distance of 1.3 m facing towards the vessel. About 12 20-inch PMTs are directed outwards and act as a muon veto detector. These inner and outer PMTs are optically separated by a PET foil installed on the stainless-steel frame. The expected light yield is about 275 photoelectrons at 1 MeV, which corresponds to an energy resolution of about 6% at 1 MeV for the inner detector. It has been optimized to screen LS to the purity levels of U/Th decay chains within days for a contamination level of 10^{-15}g/g and 2-3 weeks for 10^{-16}g/g. It can also provide limits on other intrinsic backgrounds [228]. The construction of OSIRIS has been completed and currently, the calibration data is being taken and understanding of backgrounds is ongoing [229].

TAO is a satellite experiment that will be placed at about 44 m distance from one of the two cores of Taishan NPP, while the distance is about 217 m from the other

core [230]. The goal of this detector is to measure the reactor antineutrino spectrum with a sub-percent energy resolution. This will provide a reference spectrum for JUNO in order to eliminate the model dependence in NMO analysis and benchmark measurements to test nuclear databases. It consists of CD with a spherical acrylic vessel of 1.8 m in inner diameter holding 2.8 ton of Gadolinium-doped LS (GdLS). The acrylic vessel will be surrounded by a spherical copper shell with a diameter of 1.884 m and will support about 4000 silicon PMTs (SiPM) providing almost full coverage. The detector operates at -50°C to lower the dark noise of SiPM to an acceptable level. The expected energy resolution is better than 2% at 1 MeV. The CD is surrounded by water tanks equipped with 3-inch PMTs to veto cosmic muons. The TAO detector will be covered on top by layers of High Density Polyethylene (HDPE) to provide a shield against external radioactivity. The HDPE shielding is covered by a plastic scintillator layer on top for tagging cosmic muons [66].

Calibration

Multiple calibration systems based on different calibration sources have been designed and developed to calibrate the detector and to understand the non-uniformity and non-linearity of its response with better than 1% precision [231]. A laser source will be deployed to calibrate PMT timing response. Various radioactive γ sources ranging from about 662 keV to a few MeV and neutron sources to calibrate energy response are considered from the point of view of JUNO's main goal. There are three calibration systems: Automatic Calibration Unit (ACU), Guide Tube system (GT), and Cable Loop System (CLS), that will be used in JUNO in order to place a source along the central axis of the CD, on a circle at the LS-acrylic boundary, and in the region in between on an vertical plane, respectively. A Remotely Operated under-LS Vehicle (ROV) can be deployed inside the LS for a full volume scan if desired. The calibration operation will be carried out through an acrylic chimney, which connects the CD to the outside from the top. The calibration program is foreseen in three frequency categories: comprehensive calibration, where all the sources will be deployed at the start of the experiment and then, a few times throughout the JUNO lifetime, the weekly calibrations using neutron and laser sources to track changes in the detector properties, and a monthly calibration to perform calibration in a limited number of positions using both laser and neutron sources. The calibration sources such as ^{226}Ra, ^{241}Am, and ^{222}Rn, covering energy range below 662 keV useful for the solar neutrino analysis, are being studied [232,233].

Radiopurity levels

In order to reach its ambitious physics goals, the contamination levels of backgrounds in the scintillator and all detector components should be kept at very low levels in JUNO. The background levels are especially crucial for the solar neutrino analysis, where neutrino elastic scattering events are indistinguishable on an event-by-event basis from the background ones, which will be discussed in Chapter 7. This is in contrast to the IBD channel used for NMO analysis, where a space-time coincidence technique using prompt-delayed signal can be applied to identify the signal and therefore, a lower limit on the radioactive background level for the solar neutrino analysis, compared to the NMO analysis, is typically required.

Dedicated efforts are being made to keep the radiopurity levels of JUNO high, which is necessary for all physics programs of JUNO. This includes selection of the radiopure materials, transportation of LAB in cleaned tanks and its storage, as well as development of a combined system of LS purification plants and monitoring using OSIRIS. The production, storage and construction protocols of all JUNO materials are

carefully performed to avoid possible contamination of the material surfaces. A constant monitoring of PMT glass radiopurity during its production has been performed. The screening and quality control of acrylic has been done using a neutron activation analysis and ICP-MS techniques. The cleanliness of the environment during installation and vessel filling is also being controlled, since the acrylic will be exposed to the air for a limited time before filling with the LS. The JUNO MC simulation framework (see Sec. 6.2) is used to check the impact of any modification or upgradation on the JUNO background budget and the study shows that JUNO can achieve the background count rate, targeted for the NMO analysis. More details on the strategies of background control in JUNO can be found in Ref. [234].

The purification procedure include passing JUNO LS through the alumina columns (to improve the transparency), distillation (to remove heavy radio-impurities and to further improve optical properties), water extraction (to remove radioisotopes from U/Th chains and ^{40}K introduced by PPO and bis-MSB), and steam stripping (to remove gaseous impurities, such as ^{85}Kr and ^{222}Rn). This purification procedure will be performed on the scintillator during filling. Later on, if required, the JUNO design permits to perform further purification campaigns using water extraction and steam stripping in a closed loop [100]. Since the LS will be extensively purified during filling, the purification efficiency is hard to predict accurately. Therefore, different assumptions on the background levels has been made concerning internal backgrounds (see Sec. 2.5) in JUNO, relevant for the solar neutrino analysis, which is the main focus of this thesis:

1. The *High Background* scenario corresponds to the minimum radiopurity requirements needed for the NMO measurement [228]. Preliminary tests performed with the purification plant prototypes demonstrate that the High Background scenario can be reached.

2. The *Medium Background* scenario corresponds to a factor 10 improvement with respect to the High background scenario for all isotopes. It is not guaranteed that the scintillator can be purified down to these radiopurity levels.

3. The *Low Background* scenario corresponds to a factor 10 improvement with respect to the Medium Background scenario for all isotopes, except for ^{210}Pb and ^{85}Kr, for which the improvement is only by a factor 5.

4. The *Very Low Background* scenario corresponds to the radiopurity levels reached on ^{40}K, ^{85}Kr, ^{232}Th chain, and ^{238}U chain by the Borexino experiment in the Phase-III in the fiducial volume [1,2,173]. Note that this scenario is considered only as a best-case scenario reference, since the JUNO central detector's size would make it very difficult (if not impossible) to reach this level of radiopurity.

The list of all contaminants, with their concentrations and corresponding count rates in JUNO for each radiopurity scenario, can be found in Table 6.1. In this table, the count rate without assuming any energy threshold, R and in the energy region of interest ROI of (0.45-1.6) MeV, R^{ROI} (see Chapter 7) is provided. In this table, ^{210}Pb decay chain, which can be found out of equilibrium with respect to the parent ^{238}U decay chain, is included. As discussed in Sec. 2.5, ^{210}Pb is not a problematic background for solar neutrino analysis. However, the isotopes belonging to ^{210}Pb decay chain, ^{210}Bi and ^{210}Po represent major background for solar-ν analysis. The isotope ^{210}Po can also be present out-of-equilibrium with both ^{238}U and ^{210}Pb chains and this case will be studied separately in Chapter 7. Since JUNO LS is organic and is derived from petroleum, ^{14}C is also present in JUNO LS, constantly produced by cosmic rays impinging on ^{14}N in the atmosphere. Results from previous experiments based on the

	^{40}K	^{85}Kr	^{232}Th chain	^{238}U chain	^{210}Pb chain
	High Background scenario				
$c\,[\frac{g}{g}]$	1×10^{-16}	4×10^{-24}	1×10^{-15}	1×10^{-15}	5×10^{-23}
$R\,[\frac{cpd}{kt}]$	2289	5000	3508	15047	36817
$R^{ROI}\,[\frac{cpd}{kt}]$	1562	705	2100	7368	17269
	Medium Background scenario				
$c\,[\frac{g}{g}]$	1×10^{-17}	4×10^{-25}	1×10^{-16}	1×10^{-16}	5×10^{-24}
$R\,[\frac{cpd}{kt}]$	229	500	351	1505	3682
$R^{ROI}\,[\frac{cpd}{kt}]$	156	70	210	737	1727
	Low Background scenario				
$c\,[\frac{g}{g}]$	1×10^{-18}	8×10^{-26}	1×10^{-17}	1×10^{-17}	1×10^{-24}
$R\,[\frac{cpd}{kt}]$	23	100	35	150	736
$R^{ROI}\,[\frac{cpd}{kt}]$	16	14	21	74	345
	Very Low Background scenario				
$c\,[\frac{g}{g}]$	2×10^{-19}	8×10^{-26}	5.7×10^{-19}	9.4×10^{-20}	5×10^{-25}
$R\,[\frac{cpd}{kt}]$	4.2	100	2	1.4	347
$R^{ROI}\,[\frac{cpd}{kt}]$	2.9	14	1	1	163

Table 6.1: Summary of internal background levels in different radiopurity scenarios, without assuming any energy threshold (R) and in the energy region of 0.45 MeV - 1.6 MeV (R^{ROI}), which is used in Chapter 7. The rates corresponding to ^{232}Th and ^{238}U chains are obtained by summing up the contributions of all daughters in the chain under the assumption of secular equilibrium. The last column reports the contribution of ^{210}Pb, assuming it will be out-of-equilibrium with respect to the ^{238}U chain [235]. Note that in the Very Low background scenario the ^{40}K, ^{232}Th, and ^{238}U contaminations are set to the upper limit found by Borexino [1, 2, 173]. The rates are reported in cpd/kt units, which are counts per day per kiloton of LS.

organic liquid scintillator show that the expected concentration of ^{14}C is in the range of 10^{-17}–10^{-18} g/g [236, 237]. These assumptions on the internal background levels will be used for the solar neutrino analysis, which will be described in Chapter 7.

Cosmic muons and cosmogenic backgrounds are significantly reduced in JUNO as it is located in an underground laboratory with a vertical overburden of $\approx$ 650 m. Furthermore, the residual muons will be effectively detected and tracked using WP and TT. Many of the cosmogenic backgrounds are short-lived and can be fully removed by a simple time veto cut around the muon track. However, the cosmogenic isotopes, ^{11}C, ^{10}C, and ^{6}He, are long-lived isotopes with non-negligible rates, and are relevant for solar neutrino analysis in the scope of this thesis. The expected cosmogenic isotope rate in JUNO is obtained by scaling the reference experimental measurements from KamLAND [238] and Borexino [239, 240]:

Isotope	R^{ref} [cpd/kt]	R^{JUNO} [cpd/kt]	$\langle R^{JUNO} \rangle$ [cpd/kt]	$\langle R^{JUNO} \rangle_{ROI}$ [cpd/kt]
^{11}**C**	$R_{Bx} = 274 \pm 3$ $R_{KL} = 1106 \pm 8$	1890 ± 199 1959 ± 254	1916 ± 157	1761 ± 144
^{10}**C**	$R_{Bx} = 6.2 \pm 2.2$ $R_{KL} = 21.1 \pm 1.8$	41.4 ± 15.3 36.5 ± 5.7	37.1 ± 5.3	0.25 ± 0.04
^{6}**He**	$R_{Bx} = 11.1 \pm 4.5$ $R_{KL} = 15.4 \pm 2$	74 ± 31 26.6 ± 4.9	27.8 ± 4.8	12.7 ± 2.19

Table 6.2: Summary of cosmogenic background contributions, crucial for the solar neutrino analysis described in the next Chapters. The interaction rates of cosmogenic backgrounds in KamLAND (R_{KL}) [238] and Borexino (R_{Bx}) Phase-I [239, 240] are reported in the first column. The expected JUNO production rate evaluated from the scaling method (eq. 6.1), using Borexino and KamLAND results separately, are displayed in the second column. The rates, average of the scaled results, without assuming any energy threshold ($\langle R^{JUNO} \rangle$) and in the energy region of 0.45 MeV - 1.6 MeV ($\langle R^{JUNO} \rangle_{ROI}$), are reported in the third and fourth column respectively [235].

$$R^{JUNO} = R^{ref} \cdot \left(\frac{\bar{E}_{\mu}^{JUNO}}{\bar{E}_{\mu}^{ref}} \right)^{\alpha} \cdot \frac{\Phi(\mu)^{JUNO}}{\Phi(\mu)^{ref}} \cdot \frac{\epsilon_C^{JUNO}}{\epsilon_C^{ref}}, \tag{6.1}$$

where α is the spectral index of the energy dependence of the isotope production yield as measured by KamLAND [238]. The $\bar{E}_{\mu}$ is the average muon energy, $\Phi(\mu)$ is the incoming total muon flux, and ϵ_C is the mass fraction of carbon atoms corresponding to JUNO and the reference (ref) experiment. The selection efficiencies of all three experiments are assumed to be comparable. For JUNO, the value of $\bar{E}_{\mu}$, $\Phi(\mu)$, and ϵ_C are 209.2 ± 6.4 GeV, $10.8 \pm 1.1\, m^{-2}\, h^{-1}$, and 0.8792, respectively. The expected rates, estimated using eq. 6.1 and exploiting the Borexino and KamLAND results separately, are displayed in the second column of Table 6.2. For each cosmogenic isotope, the weighted average of these rates is used to calculate the JUNO expected cosmogenic rates: the values in the full energy range and in the energy region of 0.45 MeV - 1.6 MeV (see next Chapter), are reported in the last two columns. The most crucial cosmogenic background for the solar neutrino analysis in JUNO is ^{11}C . It can be effectively identified using the threefold-coincidence (TFC) algorithm, which is described in Chapter 3.

The elastic scattering (ES) process has no intrinsic threshold, in contrast to the inverse beta decay process (IBD) which is the main channel of interaction of antineutrinos in JUNO. Therefore, the reactor antineutrinos which interact through the elastic scattering process also contribute as a crucial background, especially for the solar neutrino analysis. I estimated the ES interaction rate of antineutrinos, by taking its spectrum from Ref. [49], which is shown in Fig. 6.3. Considering 26.6 GW thermal power of reactors and 52.5 km baseline, the flux of reactor antineutrinos at JUNO detector is estimated to be $(1.5 \pm 0.1) \times 10^7\, cm^{-2} s^{-1}$. This exploits the fission fraction [49] for isotopes (^{235}U, ^{238}U, ^{239}Pu, and ^{241}Pu), and their energy released per fission [241], which is tabulated in Table 6.3. Considering the cross section of elastic scattering for antineutrinos on electrons [142] and the survival probability of reactor antineutrinos [50] with oscillation parameters [36] in eq. 2.20, the rate of background events induced by antineutrinos is calculated to be 1.4 ± 0.1 cpd/kt without any energy cut and 0.52 ± 0.02 cpd/kt in the energy region of (0.45-1.6) MeV. When comparing the antineutrino interaction rate with the expected rate of solar neutrinos (Sec. 6.3) and the radioactive and cosmogenic backgrounds, the contribution of antineutrino background is found to be negligible for the solar neutrino analysis.

Isotope	Fission fraction	Energy per fission [MeV]
^{235}U	0.56	202.36 ± 0.26
^{238}U	0.07	205.99 ± 0.52
^{239}Pu	0.31	211.12 ± 0.34
^{241}Pu	0.06	214.26 ± 0.33

Table 6.3: The fission fraction [49] and the energy released per fission [241] for isotopes ^{235}U,^{238}U, ^{239}Pu, and ^{241}Pu, used in the nuclear power plants (NPPs).

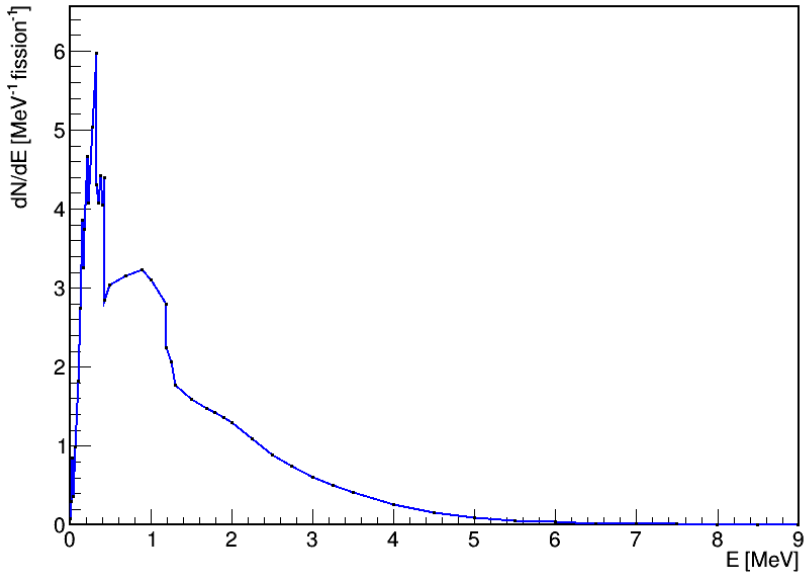

Figure 6.3: The reactor antineutrino spectrum plotted from Ref. [49].

6.2 Simulation framework

JUNO's simulation software framework has been developed based on the Geant4 simulation tool-kit and the SNiPER (Software for Non-collider Physics Experiment) framework [242, 243]. It consists of various stages that include the physics generators, detector simulation (DetSim), electronic simulation (ElecSim), waveform reconstruction (Calib), and event reconstruction. For performing studies involving various neutrino signals and backgrounds as well as single particles, physics generators are used to produce events with necessary information of particles, such as time, position and momentum. The DetSim stage takes into account the accurate detector geometry based on Geant4 framework. In this stage, all particle interaction processes inside the LS and the generation and propagation of optical photons according to a LS optical model take place. When these optical photons reach the PMT, a PMT optical model in DetSim describes the light interactions with PMT window and its detection on the PMTs. All useful information including true energy, true position of the events as well as the PMT hit time and number of photo-electrons are saved in a root file.

ElecSim takes DetSim output as the input and model the responses of PMT and detector readout electronics. ElecSim includes the effects such as dark-noise, afterpulsing, as well as Transit Time Spread (TTS). It generates the analog signal pulse, track through the digitization process to produce the so-called waveforms, and simulates the event trigger. The output of ElecSim is designed to represent the output of DAQ in JUNO. If required, the mixing of events from different DetSim sources with randomly arranged hits can also be done in ElecSim. If no mixing is performed, one can assign each ElecSim event to a DetSim event and extract its true information. In the Calib (or

the calibration) stage, the charge and time from each PMT waveform are reconstructed by deconvoluting PMT waveform with the single photoelectron PMT response to remove high-frequency electronic noise. At the event reconstruction stage, the vertex and energy of an event are reconstructed by taking reconstructed PMT charges and hit times as the inputs and performing a likelihood fit with charge-time PDFs given the observed information [244]. The last two stages follow the procedure that will also be adopted during the data taking of JUNO.

6.3 Physics goals

Neutrino Mass Ordering determination: In Chapter 1, the neutrino mass ordering problem has already been discussed. The determination of neutrino mass ordering is the main physics goal of the JUNO experiment. This measurement is planned by studying small spectral distortion caused by the mass splitting (Δm^2_{31} and Δm^2_{32}) driven oscillation pattern (eq. 1.15) of the reactor antineutrinos energy spectrum [50, 245], as shown in Fig. 6.4. Therefore, it is crucial to achieve an excellent energy resolution and large statistics in JUNO, in order to determine NMO by precisely measuring oscillated antineutrino spectrum. Unlike other experiments that rely on the NMO dependence of matter effects, JUNO measurement is based on the vacuum oscillations and does not depend on unknown CP-violating phase and the octant of θ_{23}, which makes it an unique experiment.

JUNO is located at a distance of 52.5 km, equally from both the Yangjiang and the Taishan NPPs, which is required for the NMO determination to avoid cancellation of the oscillation dephasing effect and have the best sensitivity for the NMO determination. It detects reactor antineutrinos $\bar{\nu}_e$ from the NPPs, located at about 53 km, via the Inverse Beta Decay (IBD) reaction on protons in the liquid scintillator, $\bar{\nu}_e + p \rightarrow e^+ + n$. This provides an excellent tool to identify the signal via the space-time coincidence of the *prompt* and *delayed* signals, which is a powerful handle to reject background events. The positron quickly deposits its kinetic energy in the scintillator and annihilates into two 0.511 MeV γs, which generates scintillation and Cherenkov photons, providing a prompt signal. The delayed signal is caused by 2.2 MeV or 4.95 MeV gamma following the neutron capture after scattering, with mean lifetime of about 200 μs, on a proton ($\sim$99% probability) or carbon nucleus ($\sim$1% probability), respectively. The antineutrino energy threshold of IBD reaction is 1.8 MeV and the deposited energy of the prompt signal is approximately equal to E_ν - 0.78 MeV, where E_ν is the antineutrino energy. The backgrounds for the NMO analysis constitute: 1) the accidental backgrounds, which are the random coincidence of different backgrounds, 2) β+n decays from cosmogenic ^{9}Li/^{8}He, 3) fast neutrons, which are the energetic neutrons caused by cosmic muons passing through the detector and its surrounding rocks, 4) ^{13}C(α, n)^{16}O backgrounds, formed by the interactions of α particles from U/Th-chain with ^{13}C in LS, where the radiation from ^{16}O excitation state mimics as the IBD prompt signal and the neutron capture forms delayed signal, 5) geoneutrinos, 6) atmospheric neutrinos, and 7) the electron antineutrinos from distant (>300 km) reactors as they provide no information on NMO. The expected IBD signal counts correspond to about 47 events per day and the expected background counts is about 4 events per day, after all data selection cuts are applied to identify IBD events as well as to reduce the backgrounds.

The sensitivity to NMO is obtained by using a χ^2 test-statistics between measured and the predicted number of neutrino events with oscillations, where various updated systematic contributions related to reactor uncertainty, the detector response, background shapes and rates, and oscillation parameters, are included as nuisance parameters. The procedure is to fit the spectrum first assuming normal ordering (NO) or

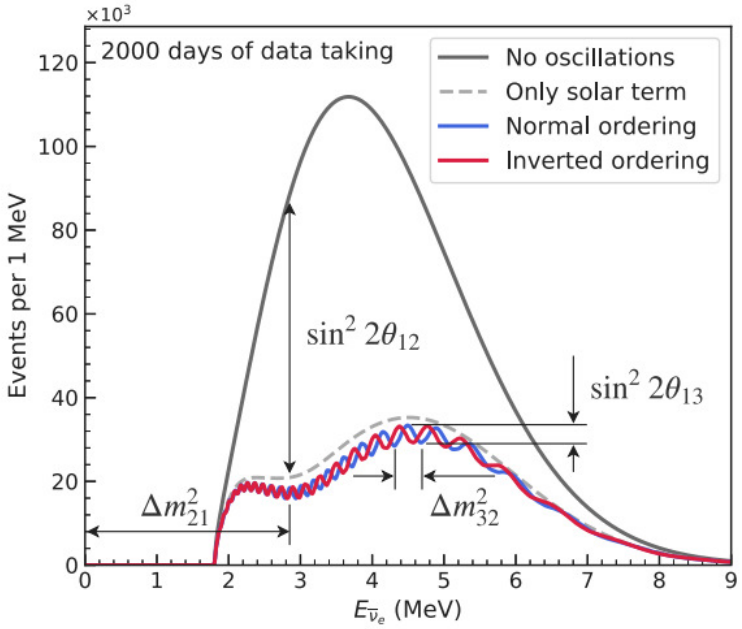

Figure 6.4: Expected reactor antineutrino spectrum at the JUNO detector taking into account the IBD cross-section and assuming 2000 days of data taking. The unoscillated spectrum is shown in black solid line. The grey dashed spectrum takes into account the oscillation due to solar term (Δm^2_{21} and $\sin^2\theta_{12}$) only, that is, using $\sin^2\theta_{13}$ =0 in the reactor antineutrino survival probability. The blue and red curves show the oscillated spectrum at JUNO, assuming normal and inverted ordering of neutrino masses, respectively. From [100].

inverted ordering (IO) with the chi-squared method. Then, the difference of the chi-squared minima, $\Delta\chi^2_{\rm MO} = |\chi^2_{\rm min}({\rm NO}) - \chi^2_{\rm min}({\rm IO})|$, is taken as a measure of median NMO sensitivity using Asimov data. Using this approach, a joint analysis of JUNO and TAO detectors has been performed to incorporate the constraints on reactor antineutrino shape in determining the total sensitivity. The median sensitivity to reject the wrong mass ordering is found to be 3σ with an exposure of 6.5 years $\times$ 26.6 GW thermal power, assuming NO is true. If IO is true, the median sensitivity is 3.1σ under the same exposure [230].

Precision measurement of neutrino oscillation parameters: JUNO can observe the effects of oscillations driven by both solar and atmospheric oscillation parameters simultaneously on the reactor antineutrinos, as shown in Fig. 6.4. The analysis includes most recent information about the experimental site location and overburden, detector response, backgrounds, and the constraint on reactor antineutrino spectral shape expected from TAO. With six years of data taking, JUNO can determine the parameters Δm^2_{31}, Δm^2_{21}, and $\sin^2\theta_{12}$ with a precision of 0.2%, 0.3%, and 0.5%, respectively. The precision on $\sin^2\theta_{13}$ is not expected to improve with respect to the current knowledge [245].

Solar neutrinos: Thanks to its high mass and excellent energy resolution, JUNO will have great potential for the solar neutrino measurements, provided the radioactive background is kept under control and the detector response is fully understood. The main channel for the detection of solar neutrinos in the JUNO detector is the elastic scattering off electrons. As discussed above, the backgrounds for the solar analysis include the intrinsic natural radioactivity in LS, external γ backgrounds from surrounding detector materials, and decay of isotopes created by cosmic muons passing through the detector. By choosing a fiducial volume, the external backgrounds can be

	Solar-ν	^{7}Be	*pep*	CNO
HZ-SSM	Φ [10^8 cm^{-2} s^{-1}]	49.3(1±0.06)	$1.44(1 \pm 0.009)$	$4.88(1 \pm 0.11)$
	R [cpd/kt]	489 ± 29	28.0 ± 0.4	50.3 ± 8.0
	R^{ROI} [cpd/kt]	142.5 ± 8.3	17.1 ± 0.2	16.6 ± 2.6
LZ-SSM	Φ [10^8 cm^{-2} s^{-1}]	45.0(1±0.06)	$1.46(1 \pm 0.009)$	$3.51(1 \pm 0.10)$
	R [cpd/kt]	447 ± 26	28.4 ± 0.4	36.0 ± 5.3
	R^{ROI} [cpd/kt]	130.0 ± 7.5	17.3 ± 0.2	11.9 ± 1.8
Borexino results	Φ [10^8 cm^{-2} s^{-1}]	$49.9 \pm 1.1^{+0.6}_{-0.8}$	$1.27 \pm 0.19^{+0.08}_{-0.12}$ (LZ) $1.39 \pm 0.19^{+0.08}_{-0.13}$ (HZ)	$6.6\ ^{+2.0}_{-0.9}$

Table 6.4: Fluxes Φ and interaction rates R in the entire energy range for the ^{7}Be, *pep*, and CNO solar neutrinos. The first and second row show B16-SSM [137] predicted fluxes and the corresponding expected rates R in JUNO, according to the high-metallicity HZ and low-metallicity LZ hypothesis, respectively. The expected rates R^{ROI} in visible energy range of (0.45-1.6) MeV, that corresponds to a region of interest (ROI) chosen in Chapter 7, are also shown. The last row reports the current best experimental results for the ^{7}Be and *pep* [173] and CNO [3] neutrinos obtained by the Borexino experiment (note that the *pep* results slightly depend on the HZ/LZ SSM predictions used for constraining CNO neutrino flux in the fit in Borexino), as summarized in Chapter 4.

suppressed to a negligible level. The cosmogenic background events can be reduced using the TFC algorithm.

In JUNO, ^{8}B solar neutrinos can be measured in the energy range above 2 MeV, due to dominant cosmogenic ^{11}C decays at lower energy range. The expected ^{8}B rate in JUNO from the elastic scattering channel is about 4.4 cpd/kt assuming no energy threshold and about 2.9 cpd/kt in energy range above 2 MeV. About 60,000 signal events with a signal to background events ratio of 2:1 are expected in the energy range above 2 MeV, after all cuts are applied in ten years of data taking [246]. As a result of low threshold ^{8}B-ν measurement, JUNO can reject the absence of upturn in P_{ee} transition region with about 3σ significance including the systematic uncertainties, if $\Delta m^2_{21} = 7.5\times10^{-5} eV^2$. It is also expected that the day-night asymmetry measurement can be provided with about 0.9% precision in JUNO, which is better than the Super-K results (1.1%) [247]. Using spectral and the day-night asymmetry information, the oscillation parameter Δm^2_{21} can also be measured and the extracted precision is on the same level as the current global fit results [248]. In addition to the elastic scattering channel, JUNO also has a potential of detecting ^{8}B solar neutrinos through CC and NC interactions on ^{13}C. Therefore, it can provide model-independent measurement on ^{8}B solar neutrino flux using these interactions, that is, providing the total amount of neutrinos produced in the Sun without relying on the solar neutrino oscillations. The first model-independent measurement of ^{8}B solar neutrino flux has been provided by SNO, as discussed in Sec. 2.4 and JUNO will be the second one. About 6,000 CC and 3,000 NC signal events are expected in 10 years of data taking in JUNO. Performing a combined analysis in all three detection channels, the ^{8}B-ν flux, Δm^2_{21}, and $\sin^2\theta_{12}$ can be measured with a precision of about 5%, 8%, and 20%, respectively. When combining the results from SNO experiment, the ^{8}B-ν flux can be obtained with world's best precision of 3% [249].

JUNO will also be able to provide the measurement of solar neutrino fluxes in the energy range from 0.45 MeV to 1.6 MeV, including ^{7}Be, *pep*, and CNO solar neutrinos. It will detect these solar neutrinos via the elastic scattering channel. The expected

rates of ^{7}Be, *pep*, and CNO solar neutrinos in the entire range and in the energy window of (0.45-1.6) MeV are reported in Table 6.4. The precision of the solar neutrino measurement is highly dependent on the background levels in JUNO. The analysis of sensitivity to these neutrinos using energy spectral fit will be discussed in Chapter 7 in detail. There is also a possibility to perform combined directional and spectral fit for solar neutrinos in JUNO, which will be investigated in Chapter 8. JUNO's capability to detect day-night asymmetry and the gravity-driven modulations (g-mode) of the rate of ^{7}Be solar neutrino, dominant at sub-MeV energy region, has also been investigated [7]. After 10 years, JUNO will be able to improve the day-night modulation measurement by sub-percent precision in optimistic background scenarios, with respect to the current best measurement from Borexino ($\sim$1% precision) [250]. The current best limits concerning g-mode will be improved by one order of magnitude to reach percent level in JUNO, with respect to the current best measurement from SNO ($\sim$10% precision) [251]. The prospects of measuring *pp* solar neutrinos in JUNO is challenging due to the dominant contribution of ^{14}C background events and the pileup with itself or with other backgrounds, as well as the complications arising from the trigger threshold and energy response at low energies. This is currently under investigation, where machine learning approaches are being used to identify the pileup events [252].

Geoneutrinos: In JUNO, geoneutrinos will be detected via the IBD channel, which is also used for NMO analysis. It has a reaction threshold of 1.8 MeV and hence, only ^{238}U and ^{232}Th components can be measured in JUNO. Apart from the non-geoneutrino backgrounds discussed above for the NMO analysis, the reactor antineutrinos constitute the largest background for geoneutrinos analysis in JUNO. JUNO will detect unprecedented amount of geoneutrino events, which is about 400 events in 1 year, with respect to the previous experiments: KamLAND [79] and Borexino [78], discussed in Sec. 1.4. JUNO will be able to measure the total geoneutrino signal with about 10% and 8% precision in 6 and 10 years, respectively [253]. This is estimated using the sensitivity analysis where Th/U mass ratio is fixed and the uncertainty of geo and reactor neutrino shapes are included. In addition, JUNO has potential to measure the individual contributions from U and Th with a precision of about 30% and 35% in 10 years. More than 50% contribution to the total signal comes from the crust around JUNO in about 500 km range. Therefore, the study of refined geological models around JUNO is crucial for the estimation of JUNO's potential to separate the signal from Earth's crust and mantle. These studies are under investigation [253, 254].

Atmospheric neutrinos: JUNO can measure atmospheric neutrinos, which has not been performed before in a liquid scintillator experiment. JUNO have an expected count of 10 atmospheric neutrino events per day, arriving from all directions with energy ranging from 100 MeV to 10 TeV. JUNO can reach NMO sensitivity of about 1σ after 10 years, through measuring atmospheric neutrinos passing through the Earth (upward-going) [50]. The analysis uses energy and direction reconstruction algorithms as well as the neutrino particle identification techniques. The particle identification techniques in JUNO will also use the information from event topology to distinguish electron or muon-like events and to discriminate neutrino and antineutrino events. This will allow the reconstruction of oscillated spectrum of neutrinos and antineutrinos of different flavours. This is required for the NMO determination, as the contribution of the muon neutrino and antineutrino differ depending upon the true neutrino mass ordering due to the matter effects. New developments are being performed for the updated estimations with respect to the previous one [50], including the optimisation of the event selection cuts for more statistics and adopting the realistic neutrino

energy dependent neutrino directionality and efficiency of particle identification techniques [255, 256]. This analysis is complementary to the NMO determination from reactor antineutrino analysis and the NMO sensitivity in JUNO can be boosted using a combined analysis, which is also under evaluation.

Supernova neutrinos: JUNO can detect supernova neutrinos produced after the core-collapse of massive stars in our galaxy, already discussed in Sec. 1.4. The detection of supernova neutrinos in JUNO will take place through multiple channels, mainly IBD, elastic neutrino-electron scattering (ES), and the elastic neutrino-proton scattering (pES). For a supernova at a distance of 10 kpc, about 5000 IBD events, 300 ES and 2000 pES events are expected to be detected by JUNO. Additionally, the NC ($\sim$300 events) and CC ($\sim$200 events) interactions on ^{12}C in LS would also occur. It is also possible that JUNO will perform the first detection of neutrinos that are emitted before the core collapse (pre-SN neutrinos) through IBD and eES interactions. A real-time monitoring system has been designed in JUNO to provide early alerts that allows for prompt detection of pre-SN and supernova neutrinos with the largest possible statistics. JUNO has sensitivity to pre-SN and core-collapse supernova neutrinos detection upto a distance of about 1-2 kpc and 360-370 kpc, respectively, assuming a false alert rate of 1 per year and progenitor mass of 30 solar masses [82].

Diffuse supernova neutrino background (DSNB): JUNO will detect DSNB via the IBD channel. The most crucial background for the DSNB analysis is the NC interaction of atmospheric neutrinos with ^{12}C. Using a pulse-shape discrimination (PSD) method, the NC background can be reduced and an prompt energy window of roughly about 12 to 30 MeV can be chosen for the analysis, where the DSNB signal is expected to dominate. The low energy threshold is the result of the reactor antineutrinos spectrum which is dominant at energies $\lesssim$ 12 MeV. By performing an event counting analysis in the chosen energy window, JUNO can provide 3σ and $>5\sigma$ evidence of DSNB signal for 3 and 10 years of data taking and assuming the reference DSNB model parameters: average spectral energy of DSNB neutrinos to be 15 MeV, the black hole fraction of 0.27, and the present supernova rate of $1.0 \times 10^{-4}\mathrm{yr}^{-1}\mathrm{Mpc}^{-3}$ [93, 100].

Proton decay: In addition to the neutrino physics, JUNO can also contribute in the searches for proton decay, which will violate baryon number and provide an indirect experimental test of the Grand Unified Theories [36]. Using a simulation study, JUNO's sensitivity to proton decay ($p \to \bar{\nu}K^+$) searches has been investigated. JUNO will utilise a three fold coincidence feature in time to search for proton decay: a prompt signal from K^+ kinetic energy, a short delayed signal ($\tau = 12.38$ ns) from its decay daughters, and a long delayed signal ($\tau = 2.2\,\mu$s) from the energy deposit of the final Michel electron. The crucial backgrounds for this analysis are the atmospheric neutrinos and cosmic muons, as the deposited energy from the proton decay is expected to be larger than 100 MeV. Various selection cuts based on visible energy and the time correlation are applied to suppress the background levels. Taking into account the systematic uncertainties related to model inaccuracies and the background level, the sensitivity of JUNO is estimated to be 9.6×10^{33} years at 90% C.L for an exposure of 200 kt-years, assuming no proton decay events are observed. This is competitive with respect to the current best limit on proton lifetime and provide complementary search compared to the Super-K experiment [257, 258].

Dark matter search: JUNO is also expected to improve the current best limits on the dark matter self-annihilation rate by searching for the neutrinos originating from the

MeV dark matter (DM) annihilation ($\chi\chi \rightarrow \nu\bar{\nu}$) in the galactic halo. JUNO will detect DM annihilation neutrinos in the mass range of (15–100) MeV via the IBD signature. In order to avoid reactor neutrino background at lower mass range and to consider only direct annihilation channel for the production of neutrinos, the mass range of (15–100) MeV has been chosen. The dominant background for this analysis is the NC interaction of atmospheric neutrinos with ^{12}C nuclei and a PSD method is applied to reject these backgrounds. JUNO will provide an improved limit with respect to the current best limits by a factor of 2–10 for DM mass range of (15–100) MeV [259].

Chapter 7

Prospects for the spectroscopy of ^{7}Be, *pep*, and CNO solar neutrinos in JUNO

This chapter presents the JUNO's potential to perform the measurement of ^{7}Be, *pep*, and CNO solar neutrinos in a visible energy range from 0.45 MeV to 1.6 MeV. Thanks to its huge target size, it is expected that JUNO can provide unprecedentedly precise solar neutrino rate measurements. However, JUNO's sensitivity to solar neutrinos depends on the exact background levels. Since the exact radiopurity levels of JUNO are unknown, as discussed in Chapter 6, the sensitivity of JUNO for the solar neutrino measurement is explored in different background levels. Unlike IBD detection, where it is much easier to reject backgrounds, the solar neutrino detection takes place via elastic scattering of electrons in liquid scintillator and thus, the solar neutrino events are indistinguishable from background ones on an event-by-event basis. Here, the difference in the energy spectra of different species is utilized to extract the interaction rate of solar neutrinos in JUNO.

The motivation for the selection of chosen energy cut and fiducial volume cut are discussed in Sec. 7.1.1. The steps taken to perform sensitivity estimation are described in Sec. 7.1.2, following a MC based pseudo-experiment approach. The results associated to ^{7}Be, *pep*, and CNO solar neutrinos measurement in different background configurations and their comparison with the current best results are discussed in Sec. 7.2. My contribution to this analysis includes performing spectral fits in different radiopurity levels as a function of exposure in order to extract JUNO's sensitivity towards ^{7}Be, *pep*, and CNO solar neutrinos, as well as co-writing the article for publication [7].

7.1 Analysis strategy

This section is devoted to the description of strategy and methods, which are used to estimate JUNO's sensitivity to ^{7}Be, *pep*, and CNO solar neutrinos. Section 7.1.1 presents the energy region and fiducial volume selection for the sensitivity studies. The procedure and techniques used in the estimation of sensitivity is described in Sec. 7.1.2.

7.1.1 Selection cuts

The region of interest (ROI) chosen in this analysis corresponds to a visible energy range of (0.45-1.6) MeV, which mainly consists of ^{7}Be, *pep*, and CNO solar neutrinos. Events in this analysis are selected using the m_{NQE} variable, an energy estimator in JUNO, in the range of (650-2400) photoelectrons (p.e). It represents the total charge in all PMTs in a 280 ns signal window, taking into account the corrections related to the expected mean dark noise hits and non-uniformity of the detector energy response. The low energy threshold is chosen, in order to neglect the contribution from ^{14}C and its pileup events, which are dominant at low energies. A study shows that assuming a expected ^{14}C concentration of $\lesssim 10^{-17}$ g/g level based on the previous liquid scintillator experiments, the contribution of ^{14}C pileup is $\lesssim$0.1 cpd/kt in the chosen ROI, which

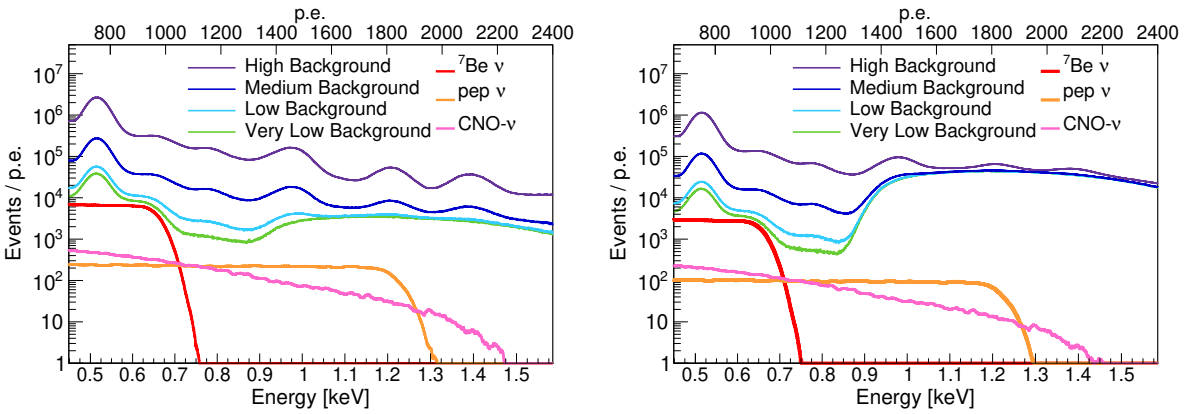

Figure 7.1: Energy spectra simulated for six years of data taking, which are used in the sensitivity analysis. The TFC-subtracted and TFC-tagged histograms are shown in the left and right panels. The datasets corresponding to four background scenarios: High Background (purple line), Medium Background (blue line), Low Background (light blue line), and Very Low Background (green line), are shown. The distributions of ^{7}Be, *pep*, and CNO neutrinos, scaled to SSM predictions, are shown as red, orange, and pink solid lines, respectively.

is extremely low with respect to other species and this analysis is robust [260]. In addition, a spherical fiducial volume (FV) with a radius of 14 m and a mass of 9.87 kt, is also chosen. The simulations of external γ's energy spectrum shows that a FV with r$\lesssim$15 m completely suppress the external γ background events, which dominate at energies above the end point of the analysis [246]. A fiducial volume of sphere with radius of 14 m is chosen for this analysis, also to avoid the systematic effect due to the position reconstruction of events.

7.1.2 Methods for sensitivity estimation

The neutrino-electron elastic scattering events are indistinguishable from the background events on an event-by-event basis in the liquid scintillator experiments. This is because they produce a single flash of light as the scintillation photons, which are dominantly emitted and do not have any directional information. However, the neutrino signal can be separated statistically from the data by fitting the energy distribution of data events with the model one, that consists of the sum of contributions from neutrinos and backgrounds. This strategy, to perform the solar neutrino spectroscopy, has already been discussed for Borexino in Chapter 4. There also exists a sub-dominant contribution from the directional Cherenkov photons, which can be used in the analysis as seen in Chapter 5, and this will be further discussed for JUNO in Chapter 8. In order to perform the sensitivity analysis in JUNO using the energy distributions, a MC based pseudo-experiment approach is adopted, where the toy datasets are fitted with the MC PDFs of all neutrino and background components, in order to obtain each species' rate and the statistical uncertainty. The complete procedure is described in detail below:

Monte Carlo and toy dataset production: The official Monte Carlo software in JUNO, described in Sec. 6.2, is used to simulate all the physics processes occurring in the JUNO detector. Using the JUNO MC software, the reference energy distributions (PDFs) of all neutrino signal and background events are obtained in reconstructed energy variable m_{NQE}. The solar neutrino events are generated through the dedicated physics generator in JUNO MC, taking the neutrino energy spectral shapes from http://www.sns.ias.edu/~jnb/ and the backgrounds ones are based on Geant4 [243]. All the neutrino signal and background components are simulated uniformly within a

	Number of events
^{7}Be	1.76×10^{6}
pep	1.05×10^{5}
CNO	1.81×10^{5}

Table 7.1: Expected number of solar neutrinos events after 1 year of data taking and with a fiducial volume of $R_{FV} = 14$ m, calculated using high-metallicity SSM predictions (see Table 6.4)

sphere of radius 15 m. For each species contributing to ROI, the number of simulated events is based on its expected rate in detector: SSM predictions of solar neutrino rate (Table 6.4) and the maximum expected background rate shown in Table 6.1 and Table 6.2. The output of the simulation is the PDF in the m_{NQE} variable for each species. Then, the PDFs are normalized according to the detection efficiency of the given species inside the fiducial volume, as not all the generated events of species, whose energy distribution extend to zero, are detected.

In order to estimate event statistics for the simulation, an exposure of 1 year of data taking with 100% duty cycle is assumed due to the enormous size of JUNO detector and limited computation resources. Due to the extremely large expected number of signal and background events, it is not possible to simulate PDFs with enough statistics for larger than 1 year of data taking. Consequently, the statistics in MC PDFs are expected to be the same order of magnitude or less with respect to the expected data events. This could result in the bias of the fit result, due to the statistical fluctuations in the PDFs. Not having enough statistics in the PDFs could create the spectral structures in PDFs as well as in the pseudo-data due to oversampling, which can artificially increase the sensitivity. In order to overcome this, a smoothing process on the PDFs is applied. The chosen smoothing algorithm is the *Savitzky Golay filter* [260, 261], which relies on the fit of adjacent data points with a low degree polynomial using the linear least square method, without smearing out the spectral features and keeping the difference between smoothed and original histograms under a threshold. This results in the creation of PDFs as if they were produced with the statistics higher than the actual simulated ones.

After smoothing of the PDFs, 10^4 pseudo-datasets are built by sampling the energy PDFs of all components. The sampling is Poissonian for each neutrino and background species with the mean taken as their expected individual contributions. The toy dataset is divided into two histograms: TFC-subtracted and TFC-tagged (see Sec. 3.2.3). The TFC algorithm performance parameters, namely Tagging Power (TP) and Subtracted Exposure (SE) are chosen to be similar to Borexino's TFC performance: TP = 0.90 and SE = 0.70. These values are taken into account to compute the total exposure and ^{11}C rate for each dataset. Figure 7.1 shows the generated datasets for six years of data taking in the different radiopurity levels, as well as ^{7}Be, *pep*, and CNO solar neutrino spectra that are normalized to their expected counts. The studies regarding CNO neutrinos are performed in two different ways. Firstly, the CNO is considered as a single species representing a weighted sum of all three components according to the SSM predictions, as used in Borexino in Chapter 4. Secondly, the individual ^{13}N and ^{15}O components are also considered, where the latter includes also sub-dominant ^{17}F neutrinos having a degenerate energy spectrum with ^{15}O. It can be observed in Fig. 7.1 that the shoulder-like spectral feature at $\approx$1000 p.e, due to ^{7}Be solar neutrinos, is present in the Very Low and Low Background scenarios, while for other background scenarios, there is no such feature due to the dominance of backgrounds. The PDFs of all species

in the ROI can be seen in Fig. 7.3, which shows the fit result obtained using the technique described below.

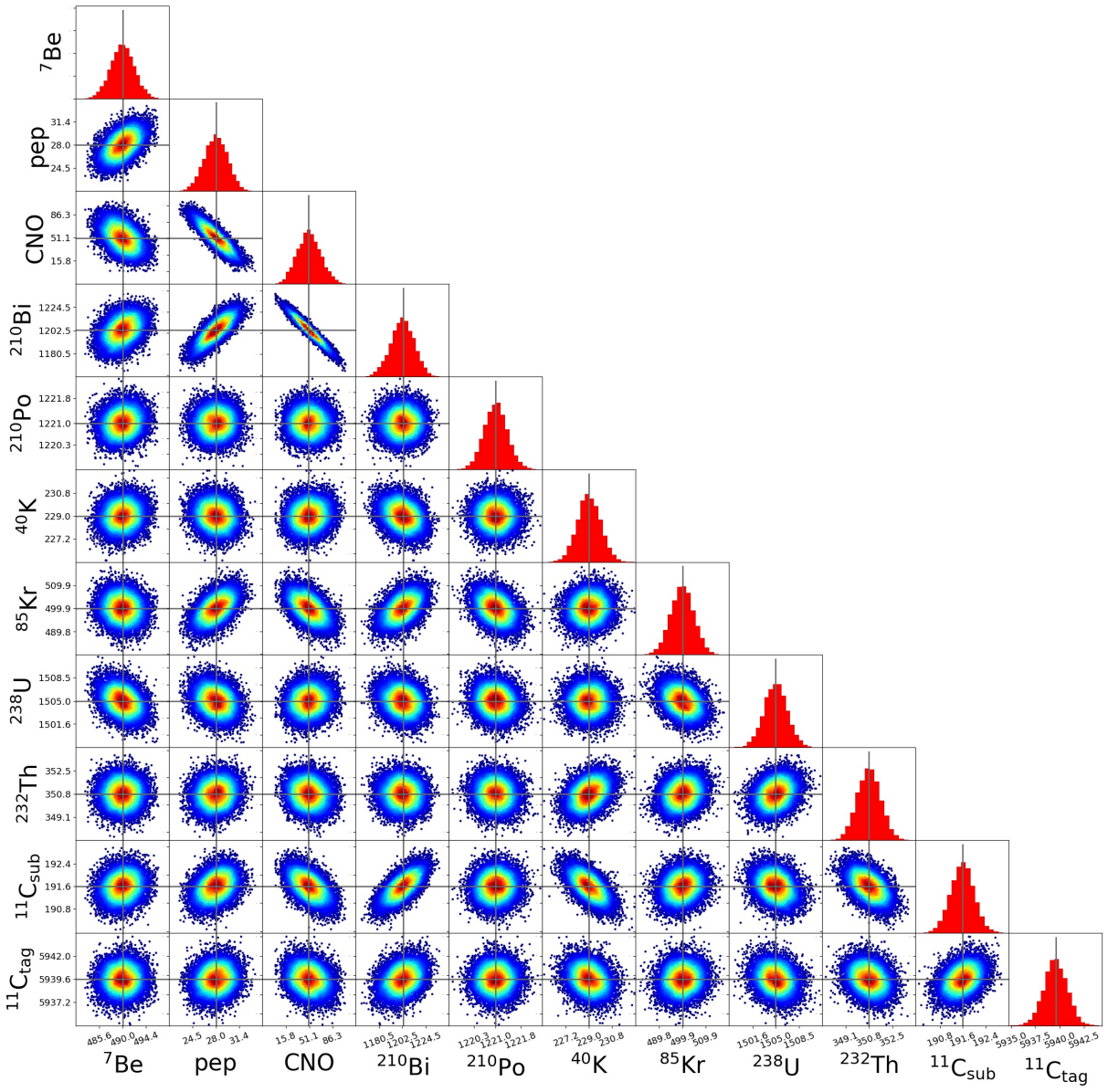

Figure 7.2: Correlation plots obtained by performing 10^4 fits in the Medium Background scenario for six years of data taking, where the rates of all species are free to vary. The red histograms show the distributions of the best fit reconstructed rates, expressed in cpd/kt. The non-diagonal frames report the correlation plots among the different species: the rates density increases going from blue to red color. From [7].

Multivariate fit: Similar to the fit technique described in Chapter 4, the generated TFC-tagged and TFC-subtracted datasets are fitted simultaneously with the MC PDFs using a binned likelihood test statistic. Consequently, the total likelihood is given by the product of TFC-subtracted and Tagged likelihoods, $\mathcal{L} = \mathcal{L}_{sub} \cdot \mathcal{L}_{tag}$ (see eq. 4.9). A dedicated software for the sensitivity studies of the solar neutrinos, named as *Jülich nUsol Sensitivity Tool (JUST)*, has been developed [262]. The fit parameters are the individual species rates. The TFC-subtracted and TFC-tagged datasets are statistically independent, while they have common fit parameters, which are the rates of the solar neutrinos and the internal backgrounds. Since ^{11}C rate is different in the two distributions due to the TFC algorithm, two independent parameters corresponding to the

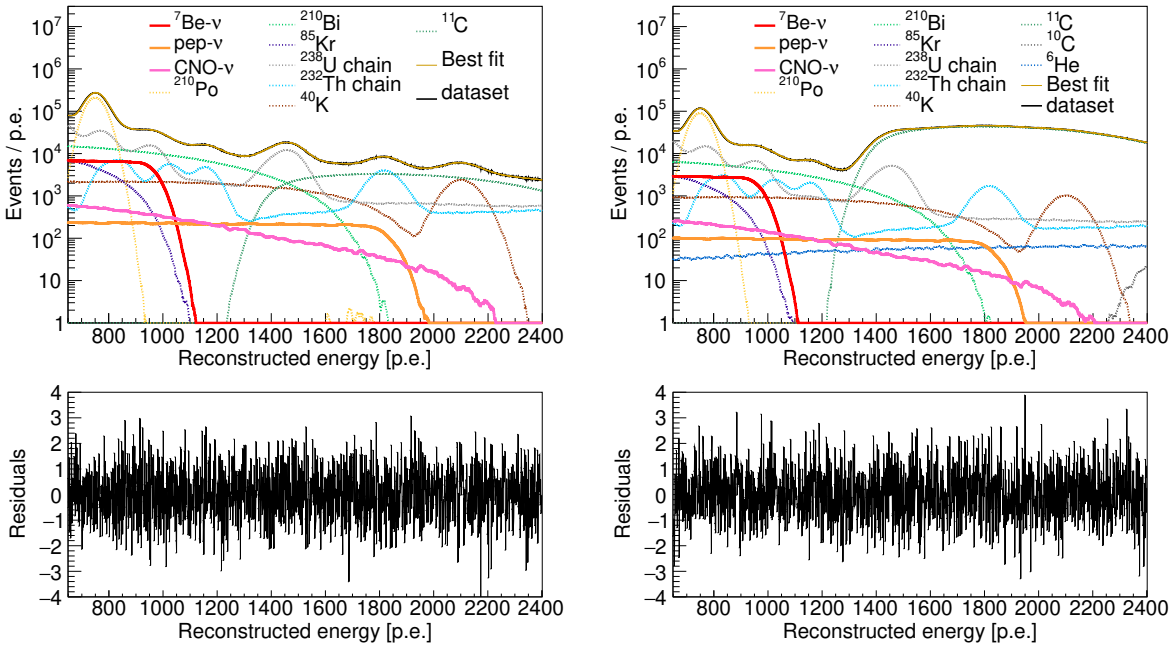

Figure 7.3: Multivariate fit example from the sensitivity analysis for Medium Background scenario with six years of data taking. The TFC-subtracted and TFC-tagged histograms are shown in the left and right panels, respectively. In the upper panels, the pseudo-datasets are shown in black and the best fit model is shown in a golden solid line. The solar neutrinos PDFs are shown in solid lines, while the backgrounds PDFs are shown in dotted lines. The bottom panels show the residuals of the fits.

^{11}C rate in the two distributions, are included in the likelihood. The other two relevant cosmogenic isotopes, ^{10}C and ^{6}He, are included in the TFC-tagged dataset only, due to their negligible contribution in the TFC-subtracted dataset. The output of the fit is the reconstructed rate of each species assuming no threshold efficiency. Note that in this analysis, the MC simulations are assumed to accurately reproduce the real detector response and the study of possible systematic errors, associated to the non-perfect knowledge of the detector energy response, is beyond the scope of this thesis.

Figure 7.2 shows an example analysis result from the sensitivity study and are obtained by performing 10^4 fits in the Medium Background scenario for 6 years of data taking. The fits are performed in the ROI, where all signal and background rates are free to vary. The red histograms represent the distributions of the species' reconstructed rates and the injected rates are shown in black vertical lines. The correlation plots between different species rates are also shown in this figure. It can be seen that there exist strong correlations between ^{210}Bi, *pep*, and CNO rates. Figure 7.3 shows the multivariate fit performed on one of the pseudo-datasets spectra out of 10^4 fits in the Medium Background scenario for 6 years of data taking. In the shown fits, no biases are observed. However, the biases can occur due to correlations in the cases, where the statistics is too low or the background is too high. In the cases, where the bias is too high, the sensitivity estimation is not done. However in some cases, the external constraints on some of the signal or background rates can be imposed to help the fit to extract unbiased species rates, as will be discussed in the next section.

Sensitivity extraction: The goal of this analysis is to estimate the achievable precision of ^{7}Be, *pep*, and CNO solar neutrino rates in JUNO, which are strongly affected by the exposure and the signal to background ratio. In order to quantitatively evaluate the JUNO's sensitivity to ^{7}Be, *pep*, and CNO solar neutrinos, the multivariate fits on a large number of pseudo-datasets are performed. From each fit, the rate of each species and

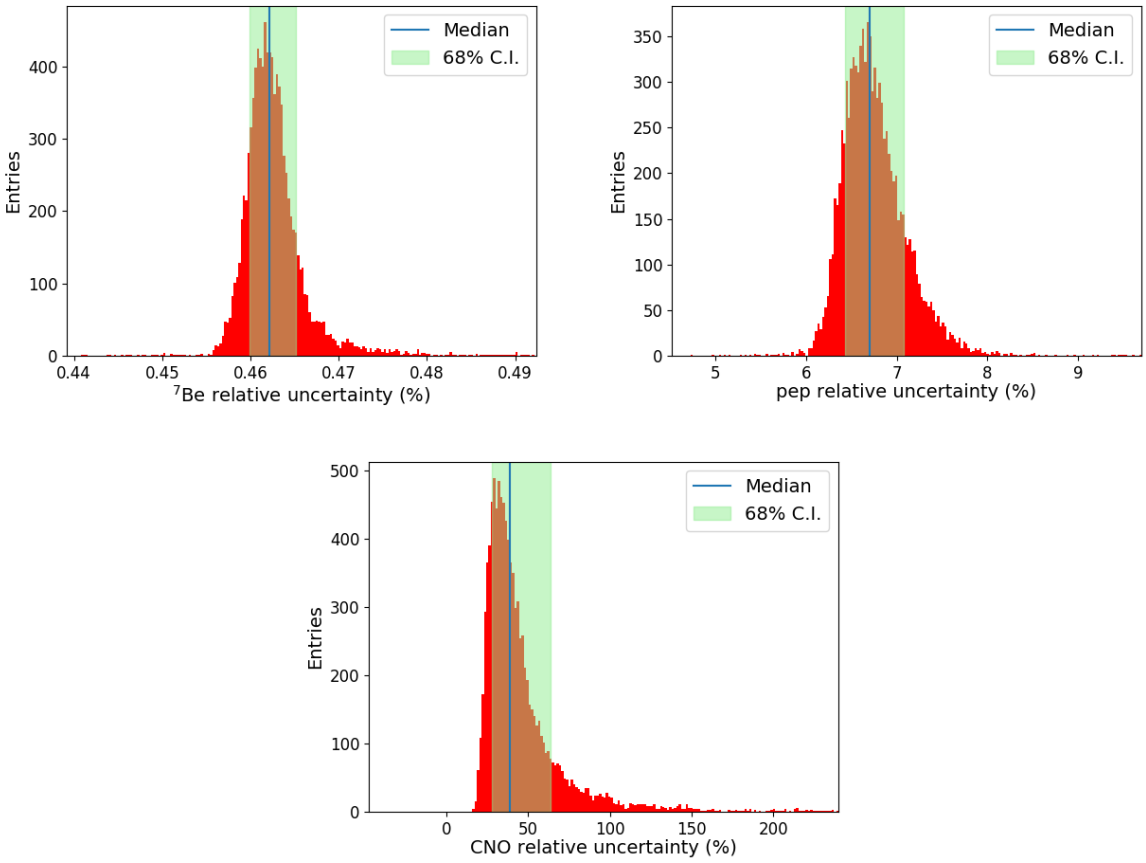

Figure 7.4: The distributions of relative uncertainty (%) of extracted solar neutrino rates are shown in red, which is defined as the ratio of rate uncertainty to the best fit rate extracted from each multivariate fit performed on 10,000 pseudo-datasets by leaving the rates of all species free to vary. The distributions are shown for the ^{7}Be (upper left), *pep* (upper right), and CNO (bottom) solar neutrinos in the Medium Background scenario with 6 years of data taking. The blue vertical line shows the median of the distribution, which is quoted as the sensitivity result, and the green band shows the 68% C.L. band extremes.

the rate uncertainty are extracted. Now, the distribution of the ratio of rate uncertainty to the extracted rate of species of interest is built from all fits. Then, the average relative uncertainty, which represents the sensitivity result, is quoted as the median of this distribution. The left and right errors on the final sensitivity result is taken as the distances between the median and the 68% C.L. band extremes. Figure 7.4 shows the relative uncertainty distributions in red for ^{7}Be, *pep*, and CNO solar neutrinos in the Medium Background scenario for 6 years of data taking. In this Figure, the blue vertical line represents the median of the distribution and the green band shows the 68% C.L. band extremes. Note that in this case, the rates of all species are free to vary. This method is adopted in order to take into account both the extracted rate and its error in each fit. This distribution carries the information about the possible large bias in the best fit rate and/or the possible fluctuation in the extracted error in some fits when it is not sensitive to a species. In addition, quoting the average uncertainty along with left and right errors, as the sensitivity results, will take into account the asymmetries in the distribution caused by the correlation of species rate.

7.2 Results

This section presents the results of the sensitivity analysis on ^{7}Be, *pep*, and CNO solar neutrinos. The precision of solar neutrino rates that JUNO can achieve, is studied in

various configurations, that is, as a function of time and different background levels. As described in the previous subsection, for a certain exposure and the background level, the multivariate fits of 10^4 pseudo-datasets with the MC PDFs are performed in the ROI of (650-2400) p.e. by exploiting differences in the energy spectra of neutrino and background components. Then, the distributions of relative uncertainty, defined as the ratio of extracted fit error on rate to the best fit rate for each species of interest, are built and their median are quoted as the sensitivity results. The sensitivity results are compared to the results from Borexino (Chapter 4) with and without including systematic uncertainties. Here, it is reminded again that the possible systematic uncertainties are not taken into account in this study as the systematic errors are not expected to be larger than in that of Borexino.

7.2.1 ^{7}Be solar neutrinos

Due to a high expected rate of ^{7}Be solar neutrinos (≈ 150 cpd/kt in the ROI) and the characteristic shoulder-like energy spectral shape, it is easier for the fit to disentangle the contribution of ^{7}Be solar neutrinos, even in the less exposure as well as in the High background scenario. Figure 7.5 (top left) shows the average relative error on the reconstructed ^{7}Be-ν rate as a function of data taking time (lower scale) and exposure (upper scale). The results from the Very Low, Low, Medium, and High Background scenarios are shown in green, light blue, blue, and purple solid lines, respectively. The best Borexino results, with and without including the systematic uncertainty (2.7% and 2.3%) [1] are represented as black dotted and solid horizontal lines, respectively. These trends follow a $a + b\epsilon^{-1/2}$ power law due to increasing statistics, where ϵ is the dataset exposure, a and b are the coefficients depending on the neutrino species and the background scenario. It can be seen that starting from 2 years of data taking, JUNO's results will be highly competitive in all background scenarios. They match or exceed the Borexino's best result depending upon the background scenarios. For longer data taking period, the relative statistical error on the extracted ^{7}Be rate will reach unprecedented levels, that is, $\approx$1.0% in the High Background scenario (worst radiopurity) to $\approx$0.15% in the Very Low Background case (best radiopurity).

The precision of ^{7}Be solar neutrinos can also be influenced by the presence of unforeseen levels of background and out-of-equilibrium components in the scintillator. The backgrounds that affect ^{7}Be results are ^{226}Ra, ^{210}Po, and ^{85}Kr, due to the overlap of their energy spectra with the ^{7}Be-ν spectrum. Therefore, the precision of ^{7}Be solar neutrinos is studied as a function of these backgrounds' levels for 6 years of data taking in order to have a sufficient exposure.

^{85}Kr (β-emitter) is one of the most crucial background for ^{7}Be-ν analysis, because its spectral shape is very similar to the ^{7}Be-ν spectrum and both spectra almost overlap. The ^{85}Kr contamination level is hard to predict a priori and could possibly be high. The reasons for the presence of high ^{85}Kr levels include the air-leak during filling, which could result in the absorption of ^{85}Kr by acrylic surface. This could emanate into the scintillator after the detector filling. Therefore, to study the effect of large contamination level of ^{85}Kr, extra contributions of ^{85}Kr with respect to the already included ^{85}Kr in each scenario are simulated, up to a value of 5×10^6 cpd/kt. The results on the precision of ^{7}Be solar neutrinos as a function of increasing ^{85}Kr rate are shown in Fig. 7.5 (bottom right). It can be seen that the ^{7}Be-ν relative uncertainty worsens for all scenarios as a function of increasing ^{85}Kr rate. If ^{85}Kr is kept below $\sim10^6$ cpd/kt, the ^{7}Be statistical error is still better than the best result from Borexino.

Another problematic background for ^{7}Be analysis is the contribution from out-of-secular-equilibrium ^{210}Po decay events. In this analysis, the supported ^{210}Po, which is in secular equilibrium with ^{238}U and ^{210}Pb decay chains, has been included. However,

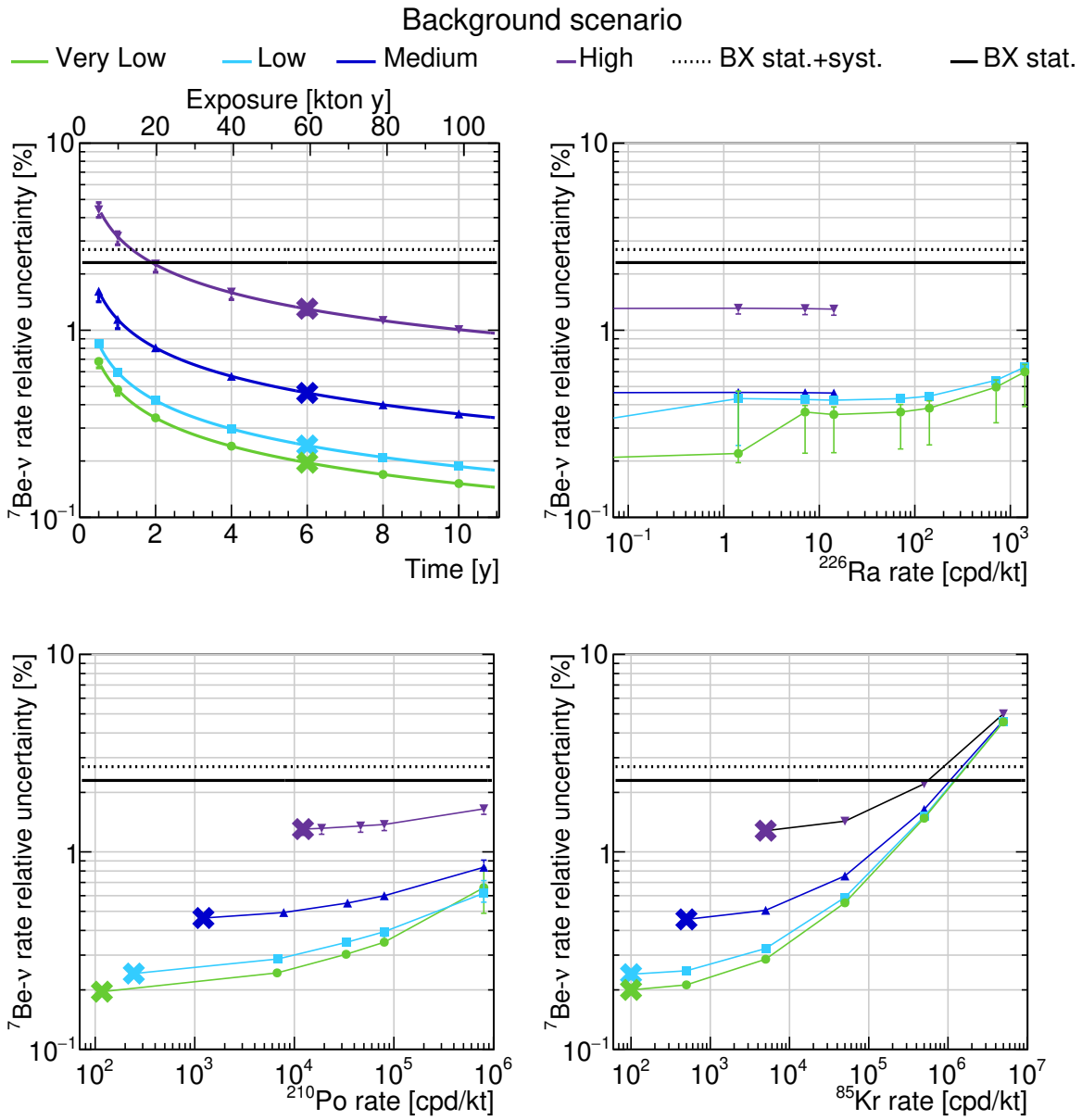

Figure 7.5: JUNO's sensitivity results to ^{7}Be solar neutrinos: Top left plot shows the relative uncertainties of ^{7}Be neutrino rate as a function of the exposure (upper axis) and data taking time in years (lower axis). Very Low, Low, Medium, and High Background scenario trends are shown in green, light blue, blue, and purple solid lines, respectively. The best Borexino results, with and without including the systematic uncertainty (2.7% and 2.3%) [173] are reported as black dotted and solid horizontal lines, respectively. Top right, bottom left, and bottom right plots show the relative uncertainty of ^{7}Be neutrino rate as a function of increasing rates of ^{226}Ra, ^{210}Po (expressed as the sum for ^{210}Po from ^{210}Pb and out of equilibrium component), and ^{85}Kr respectively, for 6 years of data taking. The bold cross markers correspond to the standard background scenarios for 6 years of data taking, i.e. High, Medium, Low, and Very Low with no extra contribution of backgrounds added. Concerning the top right plot, the standard background scenarios have no extra contamination of ^{226}Ra, therefore no cross is shown. From [7].

from the experience of both Borexino [159] and KamLAND [161] experiments, it is possible that a certain amount of ^{210}Po, which is out-of-secular-equilibrium with ^{238}U and ^{210}Pb decay chains, referred to as the unsupported ^{210}Po, will be present in the detector. The results from the study of impact of extra ^{210}Po contamination level on the ^{7}Be sensitivity is shown in Fig. 7.5 (bottom left). It can be seen that the ^{7}Be statistical precision in JUNO is still better than the current best results, even with extra ^{210}Po with total contamination up to $\sim 10^6$ cpd/kt ($\sim$10 times higher than one experienced

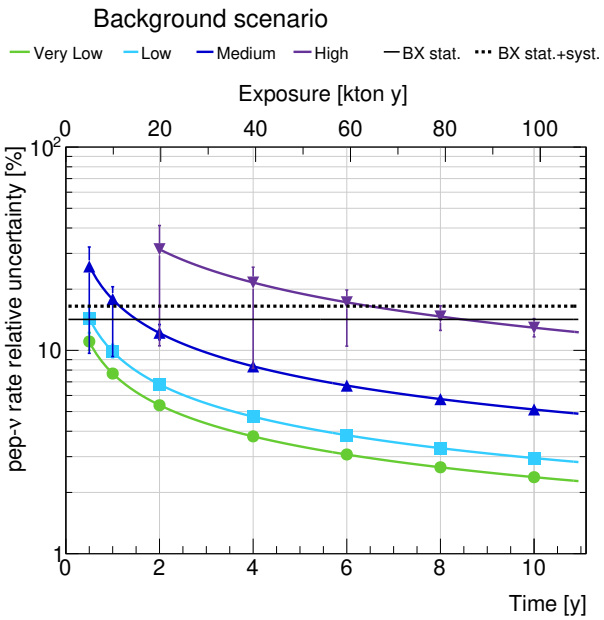

Figure 7.6: The relative uncertainty of *pep* neutrino rate as a function of the exposure (upper scale) and data taking time in years (lower scale). The distributions in green, light blue, blue, and purple solid lines represent the Very Low, Low, Medium, and High Background scenarios. The best results from Borexino, with and without including the systematic uncertainty (16.5% and 14.2%) [1] are reported as the black dotted and solid horizontal lines respectively. From [7].

initially in Borexino) [263].

^{226}Ra isotope, a sub-chain element in the ^{238}U decay chain, can be present in water or scintillator as the out-of-equilibrium component. Therefore, it is necessary to estimate the impact of possible extra levels of this isotope on the ^{7}Be sensitivity, which is shown in Fig. 7.5 (top right). For this study, the concentration level of ^{226}Ra is varied from $0.01c_{Ra}$ to $5c_{Ra}$, where c_{Ra} is ^{226}Ra contamination selected as the detector design requirement $c_{Ra}^{req.} = 5\times10^{-24}$g/g, corresponding to 142 cpd/kt rate for overall ^{226}Ra $\rightarrow$ ^{206}Pb decay chain. Starting from $0.5c_{Ra}$, the fit results start to be biased in the High and Medium Background scenarios. This implies that the fit is unable to disentangle ^{7}Be due to the increasing level of backgrounds that lie in the same energy region and thus, they are not shown here. In the Very Low and Low Background scenarios, the ^{7}Be precision slightly worsens for $c_{Ra} > c_{Ra}^{req.}$, nevertheless, it is still better than the current best results from Borexino [263]. Therefore, it can be concluded that the contamination level of ^{226}Ra isotope should be kept as minimum as possible to measure the precise ^{7}Be-ν rate in the Medium and High Background scenarios.

As discussed in Sec. 7.1.1, assuming the ^{14}C concentration level to be $\lesssim10^{-17}$ g/g, a typical contamination level from other liquid scintillator experiments, the contribution of its pileup is negligible in the ROI. This is because the single ^{14}C events and its multiple pileup (up to 3) do not lie in the ROI, and the quadruple pileup, which partly lies in the ROI, has a negligible contribution. However, the ^{14}C+^{210}Po pileup lies in ROI and can affect the measured precision on ^{7}Be solar neutrino rate. Assuming that the pileup rate can be constrained by making use of the pulse-shape discrimination techniques (for ^{210}Po) as well as data-driven and MC methods (for ^{14}C) adopted in Borexino [264], the measured statistical precision on ^{7}Be-ν rate is still competitive with the current best results from Borexino [260].

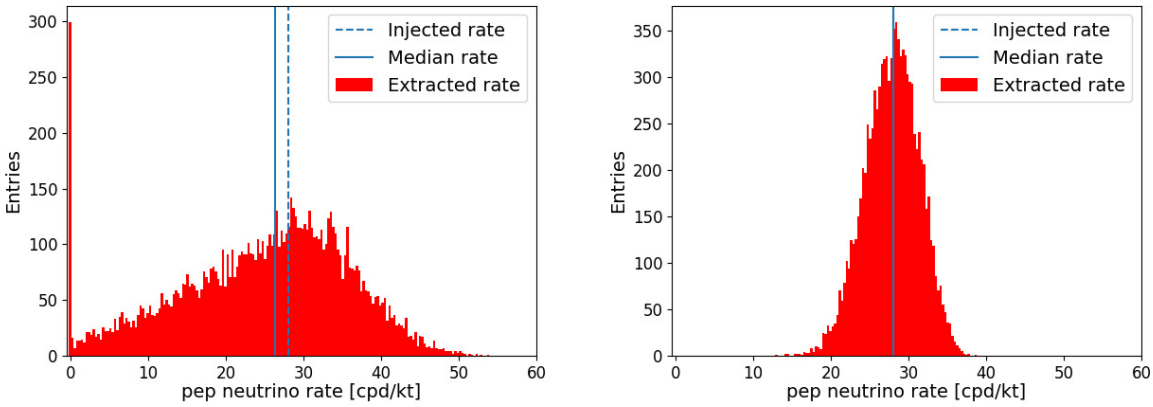

Figure 7.7: The distributions of the extracted *pep*-ν rates (red), obtained by performing multivariate fits on 10^4 pseudo-datasets and leaving the rates of all species free to vary with 0.5 year of data taking. Left and right plots show the distributions in the High and Low Background scenarios, respectively. The blue dashed lines represent the injected rate, while solid lines illustrate the medians of the distributions. It can be seen that in the High Background case, the extracted *pep*-ν rate is close to zero in many fits due to a poor signal to background ratio, which results in a bias and therefore, it is not shown in Fig. 7.6. However, this is not observed in the right plot, where the background levels are reduced. Note that the median rate is displayed here only for illustration purposes and it is not taken into account for the sensitivity results.

7.2.2 *pep* solar neutrinos

The *pep*-ν flux has been measured by the Borexino experiment with 17% precision [1, 173]. However, by including the solar luminosity constraint, the ratio of *pp* to *pep* neutrino rate, the global fit of solar neutrino data, and the oscillation parameters, the *pep*-ν flux is determined at 1.4% level as discussed in Sec. 4.4.1. It is important to directly measure *pep*-ν flux precisely in JUNO, in order to experimentally verify these theoretical and experimental information. However, there are some challenges in the *pep*-ν measurement. The *pep* neutrino flux is relatively low, approximately 50 times smaller than the ^{7}Be neutrino flux. Due to presence of backgrounds from the radioactive decays of ^{210}Bi and cosmogenic ^{11}C in the same energy region, this analysis is strongly influenced by these backgrounds. Furthermore, the similarity between *pep*-ν and CNO-ν spectral shapes as well as their comparable rates, also complicate the *pep*-ν measurement.

Similar to ^{7}Be neutrinos, the relative precision of *pep*-ν rate achievable in JUNO is also studied as a function of the exposure, as shown in Fig. 7.6. This is studied in all four background scenarios and leaving the rates of all species free to vary. In Figure 7.6, the current best results are also shown as the black dotted and solid horizontal lines, corresponding to with and without including systematic uncertainty (16.5% and 14.2%) [1], respectively. Overall, the precision of *pep*-ν measurement improves as a function of data taking time. It can be seen from the figure that more than 6 years are needed for JUNO in the High background scenario, in order to reach competitive precision with respect to the current best results. In other background scenarios, the relative statistical precision will match or exceed Borexino results after $\sim$1 year of data taking. Moreover, these results show that JUNO will be able to measure *pep*-ν flux without any constraint on CNO-ν, for the first time, while Borexino provided the *pep*-ν flux measurement by fixing CNO rate to the SSM predictions (see Sec. 4.2). In the High Background scenario, the sensitivity results for $<$ 2 years are not shown in Fig. 7.6, due to high bias observed in the reconstructed rates with respect to the injected *pep*-ν rate: for 0.5 year and 1 year of data taking, biases are about 6% and 3%, respectively. Here, the bias represent the difference between injected rate and median of extracted

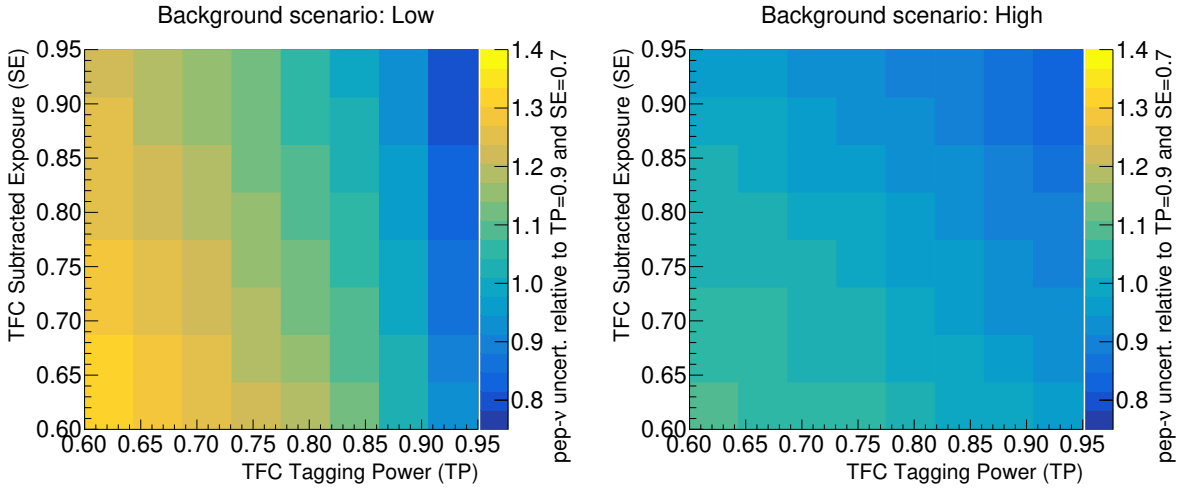

Figure 7.8: Impact of the TFC parameters on the *pep* neutrino rate uncertainty is shown as a function of the Tagging Power, TP (x-axis) and the Subtracted Exposure, SE (y-axis), after 6 years of data taking. The z-axis (color scale) represents the extracted *pep* neutrino uncertainties relative to the *pep* uncertainty when TP = 0.9 and SE = 0.7, corresponding to the ones achieved in Borexino TFC. The rate uncertainty increases going from blue to yellow tones. Low and High Background scenarios are shown in left and right plots, respectively. From [7].

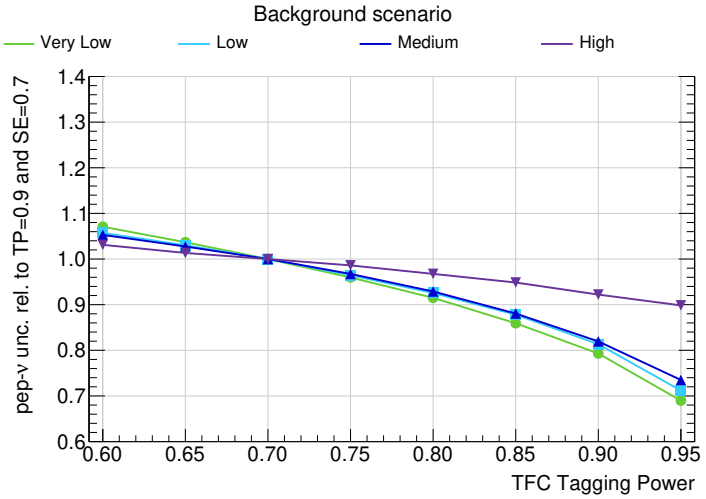

Figure 7.9: The *pep* neutrino rate relative uncertainty, normalized by the relative uncertainty obtained for the default TFC parameters (TP = 0.9 and SE = 0.7), is shown as a function of varying TP. Here, the SE is fixed to 0.7. The Very Low, Low, Medium, and High Background scenario trends are shown in green, light blue, blue, and purple solid lines, respectively. From [7].

rate distribution. Moreover, for 0.5 year in the High Background case, the extracted *pep*-ν rate is almost zero in many fits, as shown in Fig. 7.7 (left), as the spectral fit is not sensitive to *pep*-ν in this case due to poor signal to background ratio and insufficient exposure. However, this is not the case at low exposure for better radiopurity levels, as shown in Fig. 7.7 (right) for the Low Background scenario with 0.5 year of data taking time, where there is no peak for *pep*-ν rate ~ 0 cpd/kt and thus, no biases are observed.

As ^{11}C is one of the most important backgrounds for the *pep*-ν analysis, it is necessary to understand the impact of the TFC performance on the *pep*-ν sensitivity. As mentioned before, the performance parameters of the TFC in JUNO are assumed to be similar to the ones in Borexino. So, the 10^4 multivariate fits are performed for each TP and SE configuration between (60 - 95)%, considering 6 years of data taking in various radiopurity scenarios. The results from this study are shown in Fig. 7.8, for the Low and High Background scenarios, where the color scale represents the uncertainty of

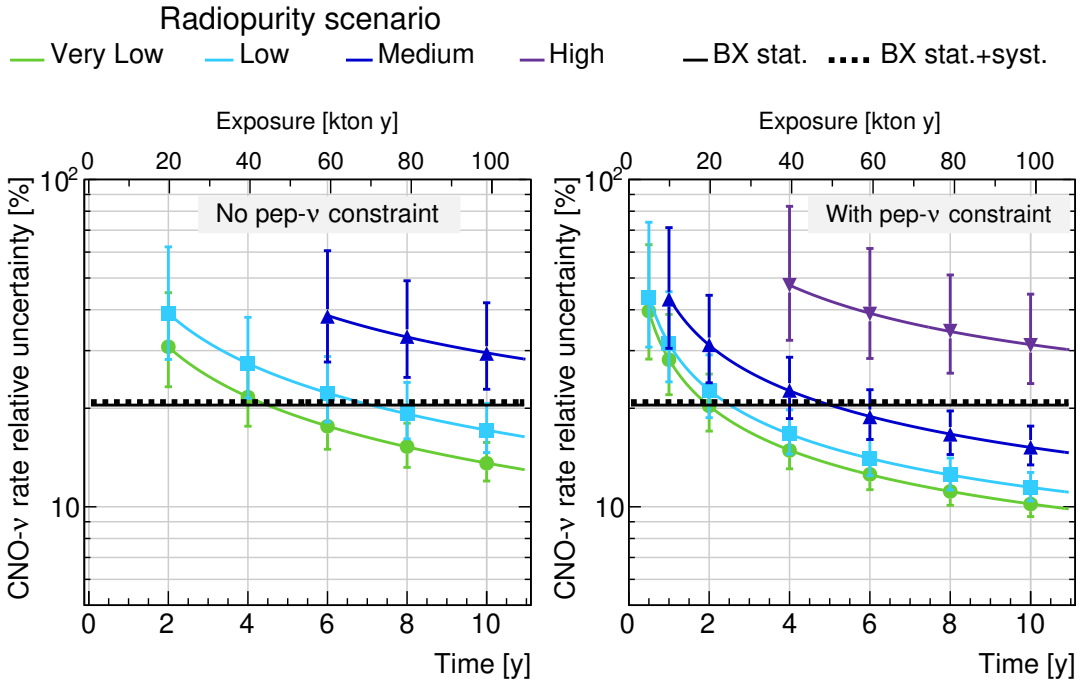

Figure 7.10: Expected relative uncertainty of the CNO rate as a function of exposure and time (in years). Left and right plots represent the results from multivariate fits without and with a constraint on the *pep* neutrino rate, respectively. Very Low, Low, Medium, and High background scenario trends are shown in green, light blue, blue, and purple solid lines, respectively. The Borexino results with and without the systematic uncertainties are reported as black dotted and solid horizontal lines, respectively. Here, each of these two errors is reported as an average of the left and right uncertainties [3]. Note that these Borexino results have been obtained by constraining the *pep* neutrino rate at 1.4% precision level, as well as using an upper limit on the ^{210}Bi rate. As discussed in the text, the fit produces a biased result on the CNO rate for the High Background scenario without constraining the *pep* rate, even after many years of data taking and therefore, the curve corresponding to the High Background scenario is not shown in the left plot. From [7].

pep-ν rate relative to the *pep*-ν error when TP = 0.9 and SE = 0.7. For the Low Background scenario, the *pep*-ν rate precision is almost doubled as a function of TP for a constant SE, while changing the SE has only a slight effect. This suggests that the ^{11}C tagging is more crucial than having more TFC subtracted exposure. The impact of the TFC-parameters decreases as the radiopurity scenarios worsens, as it can be seen in the right figure shown for High Background scenario. The impact of TP on the relative uncertainty of *pep*-ν rate, normalized to the *pep*-ν relative error with TP = 0.9 and SE = 0.7, is shown in Fig. 7.9 for all four radiopurity scenarios. In worse radiopurity scenarios, the internal backgrounds (^{238}U and ^{232}Th decay chains) increase to such a level that signal to background ratio is not anymore influenced by the TFC as well as ^{11}C is not a dominant source of background and thus, tagging of ^{11}C has a only mild impact on the *pep* neutrino rate precision.

7.2.3 CNO solar neutrinos

Similar to the sensitivity analysis for ^{7}Be and *pep* neutrinos, the relative uncertainty on the CNO neutrino rate in JUNO is also determined by performing multivariate fits of thousands of toy datasets with the MC PDFs, where the rates of all species are free to vary. Figure 7.10 (left) shows the relative statistical uncertainty on CNO rate, achievable in JUNO, as a function of the exposure in different background scenarios. The Borexino results with and without systematic errors are plotted as black dotted and solid horizontal lines, respectively. These Borexino results are obtained by constraining

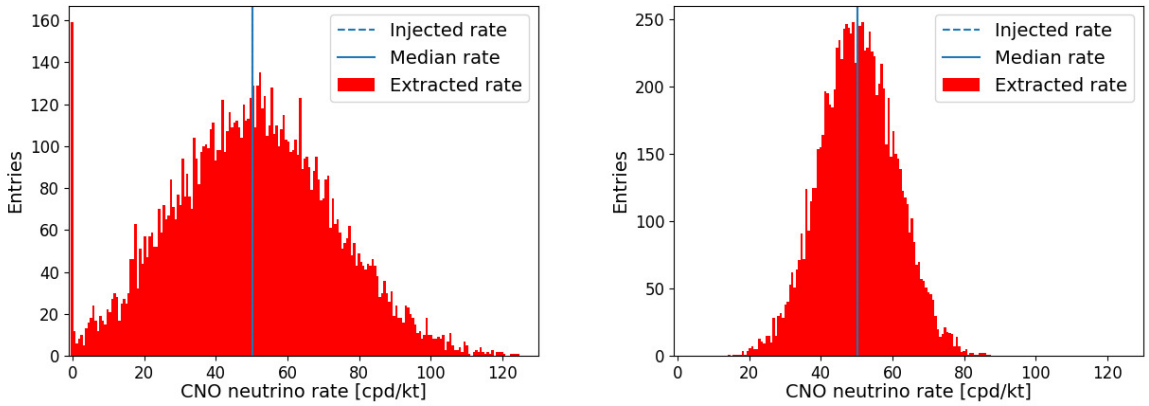

Figure 7.11: The distributions of the extracted CNO-ν rate (red), obtained by performing multivariate fits on 10,000 pseudo-datasets in the Medium Background scenario with 4 years of data taking. Left and right plots show the distribution obtained without and with the *pep*-ν rate constraint, respectively. The blue dashed line in each plot represents the injected rate, while the solid line illustrates the median of the distribution. In the left plot, it can be seen that the fit is not able to extract the CNO neutrino rate very well in this configuration, as not only the spread is large but also the extracted CNO neutrino rate is close to zero in many fits, although no bias in the obtained median of the distribution has been observed. Therefore, it is not shown in Fig. 7.10. However, the application of *pep*-ν constraint helps the fit to disentangle the fit as illustrated on the right plot.

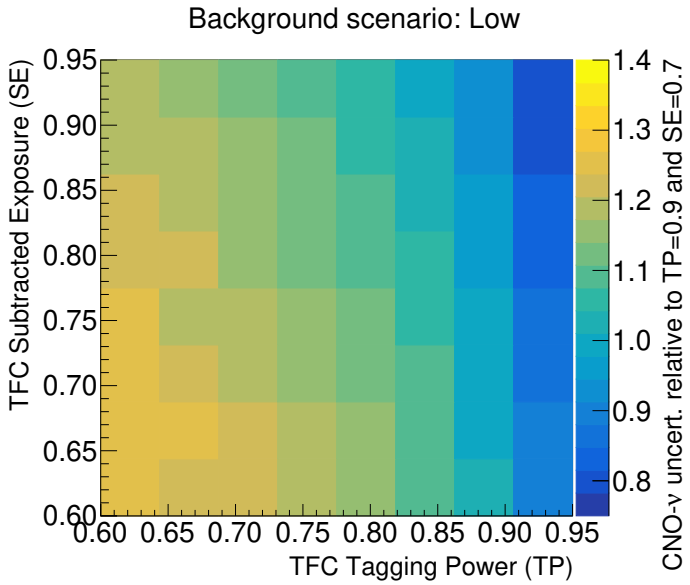

Figure 7.12: Impact of the TFC parameters on the relative uncertainty of the CNO neutrino rate is shown as a function of Tagging Power (x-axis) and Subtracted Exposure (y-axis), after 6 years of data taking in the Low Background scenario. The color scale represents the CNO neutrino rate uncertainty relative to the CNO rate uncertainty when TP = 0.9 and SE = 0.7. From [7].

the rates of ^{210}Bi and *pep* neutrinos and the errors are reported as the average of the left and right errors [3]. It can be seen that the CNO rate precision in JUNO overall improves as a function of data taking time, however, the sensitivity to CNO neutrinos is strongly dependent on the assumed radiopurity scenarios. In the Very Low and Low Background scenarios, JUNO will reach comparable precision as achieved by Borexino in about 4 years of data taking. However, in the Medium Background scenario (for <6 years) and the High Background scenarios, the fit outputs for CNO rate are affected as illustrated in Fig. 7.11 (left panel), where in many fits the extracted CNO neutrino rate is almost zero. This implies that in this configuration, the fit has a poor sensitivity

to CNO solar neutrinos due to its correlation with other species. Thus, they are not shown in Fig. 7.10.

In order to enhance the sensitivity on CNO neutrinos, it is important to reduce the correlations between CNO and *pep* neutrinos due to their spectral shape degeneracy, which can be done by constraining the *pep* neutrino rate at 1.4% precision level (Sec. 4.4.1). The relative statistical uncertainties on CNO rate, achievable in JUNO by imposing a constraint on the *pep* neutrino rate, as a function of the exposure in different background scenarios are shown in Fig. 7.10 (right). Now, the CNO sensitivity in JUNO greatly improves, for example, in Very Low, Low, and Medium Background scenarios, the relative precision on CNO rate reaches ≈10%, ≈12%, and ≈15% for >6 years of data taking, respectively. These results can be promising in order to solve the solar metallicity problem, if the systematic errors are kept under control. Moreover, the results on CNO neutrinos can be provided in the High background scenario for a long data taking period. At about 10 years, the CNO neutrino rate can be measured at about 31% level in the High background scenario. In addition, the extracted rates of CNO neutrino in the Medium Background scenario for <6years no longer show any strange behaviour, shown in Fig. 7.11 (right panel) as a result of the *pep*-ν constraint. Note that, these results have been obtained without imposing a constraint on the ^{210}Bi rate in the spectral fit, which was used in spectral fit in Borexino as discussed in Chapter 4. However, using more constraints such as the CID results, these results can be improved further, which will be discussed in the next Chapter.

As performed for the sensitivity study to *pep* neutrino, the precision of CNO neutrino rate is also studied as a function of TFC performance parameters, since the CNO spectrum highly overlaps with the ^{11}C one. This is studied by considering the fit configurations where all species are free to vary in all the background scenarios except in the High Background scenario, where the CNO results are biased even for the long data taking periods. Figure 7.12 shows the results on CNO rate uncertainty in different TP and SE relative to the values obtained when TP = 0.9 and SE = 0.7 (the nominal values) in the Low background scenario. The same conclusions has been achieved as for the *pep* neutrinos, that is, TP is more crucial than the SE to increase the ability of the fit to disentangle the CNO neutrinos rate.

7.2.4 ^{13}N and ^{15}O solar neutrinos

In the analysis above, the sum of contributions from ^{13}N, ^{15}O, and ^{17}F neutrinos in the CNO-cycle, fixed according to the SSM predicted values, was utilized. In JUNO, the sensitivity to individual components of CNO neutrinos is also studied, which has never been achieved in any experiment so far. In the Sun, the contribution of ^{17}F neutrinos is subdominant (∼1% of the total CNO flux) and its spectrum is fully degenerate with the ^{15}O spectrum. Therefore, the sensitivity studies for ^{13}N and ^{15}O solar neutrinos has been performed individually, where the ^{15}O study includes ^{17}F neutrino contribution [263]. The extraction of relative statistical precision of ^{13}N and ^{15}O rates has been performed in the two fit configurations: without and with the *pep* constraint, as a function of the data taking time or the exposure. The results are shown in Fig 7.13. It can be seen that JUNO will be sensitive to ^{13}N and ^{15}O neutrinos only in the Medium Background scenario for $\geq$6 years of data taking, without using the *pep* constraint. In the Low and Very Low Background scenarios, the detection is possible for $\geq$2 years, without using the *pep* constraint. There is no sensitivity to either of these neutrinos in the High Background scenario. Since the spectral shape of ^{15}O-ν and its end point is similar to the *pep* one, ^{15}O-ν rate is generally determined with a larger error compared to ^{13}N-ν rate. Therefore, the ^{15}O precision results are greatly affected by constraining *pep* neutrino rate, while ^{13}N ones are only slightly improved, as shown in the dotted

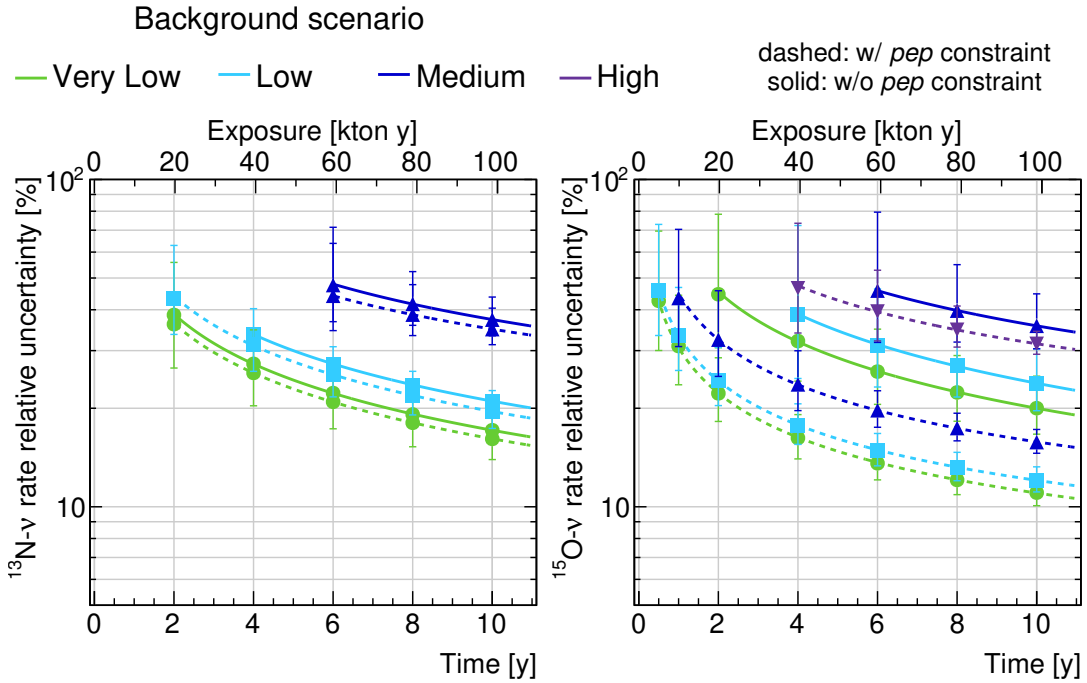

Figure 7.13: The relative uncertainty of ^{13}N (left) and ^{15}O (right) neutrino rates as a function of exposure and data taking time (in years), extracted from the multivariate fits of pseudo-datasets and using separate PDFs of ^{13}N and ^{15}O neutrinos from the CNO-cycle. Very Low, Low, Medium, and High Background scenario trends are shown in green, light blue, blue, and purple lines, respectively. The solid lines refer to the fit configurations, where all the species have been left free to vary. The dashed lines to the configuration, where the rate of *pep* neutrinos has been constrained. In the left plot, no results for the High Background scenario are shown due to the observed bias in the fit results. In the right plot, the results for the High Background scenario are shown only when the constraint on *pep* neutrino rate is applied. From [7].

lines in the Fig. 7.13. Moreover, the ^{15}O rate can now be measured in the High Background scenario when using a constraint on the *pep* neutrino rate.

7.3 Summary

In summary, this chapter has presented the solar neutrino sensitivity studies for ^{7}Be, *pep*, and CNO solar neutrinos in an visible energy range from 0.45 MeV to 1.7 MeV assuming different radiopurity levels. It is shown that JUNO will be able to measure solar neutrino rates with the uncertainties that are highly competitive with respect to the current state-of-the-art in the solar neutrino field. In particular, it can be concluded that in all considered background scenarios, JUNO will be able to measure ^{7}Be solar neutrinos with an unprecedented statistical precision after a few years of data taking with respect to the Borexino results. It is to be noted that the investigation of possible systematic errors, corresponding to the detector energy response, are beyond the scope of this work and their effect, as expected from the experience of Borexino, is much smaller as compared to the effect from the different background levels. After about 6 years, the *pep* neutrino measurement in JUNO will also be highly competitive in all background scenarios. For the first time, the *pep* neutrino rate can be measured without constraining the rate of CNO solar neutrinos, unlike performed in Borexino [1]. For the CNO solar neutrinos, the results are highly influenced by considering different background levels. However, using a constraint on the *pep* interaction rate at 1.4% level (Sec. 4.4.1), JUNO has a potential to reduce the Borexino's CNO neutrino measurement uncertainty after 6 years of data taking, to 12%-19% level depending upon the background scenario

assumed. These results have been obtained without applying a constraint on the ^{210}Bi rate in the spectral fit in JUNO, thanks to the large expected statistics of CNO neutrino as well as ^{210}Bi events in JUNO. The relevance of TFC performance parameters has also been studied for *pep*, and CNO solar neutrino measurement. Furthermore, JUNO has the potential to measure individually for the first time the rate of the two main components of the CNO flux, ^{13}N and ^{15}O solar neutrinos, except in case of the worst radiopurity scenario. My contribution to this analysis includes performing the spectral fits in different radiopurity levels and as a function of exposure in order to extract JUNO's sensitivity of ^{7}Be, *pep*, and CNO solar neutrinos, as well as co-writing the article for publication [7]. In conclusion, JUNO will play an important role in the solar neutrino physics by significantly reducing the uncertainties on the fluxes, which will provide insights to open issues in solar and neutrino physics.

Chapter 8

Feasibility studies for the directional analysis of solar neutrinos in JUNO

This chapter presents JUNO's potential to perform the measurement of ^{7}Be and CNO solar neutrinos exploiting the Correlated and Integrated Directionality (CID) method. As discussed in Chapter 5, in this method, the direction of early hits is correlated with the solar neutrino direction, resulting in an angular distribution which is used to statistically separate neutrino events from the background ones. Here, this analysis is carried out in two independent energy regions, where the contribution of ^{7}Be and CNO solar neutrinos is dominant, as discussed in Sec. 8.1.1. As the production of CID PDFs requires the directional information of solar neutrino events, which is currently not implemented in JUNO MC, the PDFs are produced using a combined JUNO MC and toy MC approach. This approach will include the directional information of solar neutrino event as well as the JUNO LS and PMTs' timing characteristics effectively for the simulation of Cherenkov contribution, which is crucial for the CID analysis.

The inputs, taking into account specific JUNO characteristics related to the hit time behaviour of photons in JUNO LS as well as of PMTs based on the JUNO MC, used in the toy MC simulation, is described in Sec. 8.1.2. The toy MC simulation constructs the PDFs utilising the information of geometrical conditions of the JUNO detector and simulating the physical processes in the detector, as reported in Sec. 8.1.3. The systematic effect of position reconstruction bias on the CID PDFs in JUNO has also been studied in Sec. 8.1.4. By performing the fit on pseudo-datasets created using CID PDFs as well as applying CID results as a constraint in the spectral fit discussed in the previous chapter, JUNO's sensitivity to solar neutrinos improves (Sec. 8.2) and the whole analysis chain can be adopted for future analysis with JUNO MC and the real data. These studies have been performed in the case of six years of exposure and the Medium Background scenario. My work includes the investigation of Cherenkov photon properties using JUNO MC software, the development of the toy MC framework, production of the CID PDFs, and the study of systematic effects in JUNO.

8.1 Strategy for directional analysis using CID method

This section describes the analysis strategy used for the CID analysis in JUNO. The CID analysis is carried out in two energy regions, 0.6 MeV - 0.75 MeV and 0.8 MeV - 1.4 MeV, where the contribution of ^{7}Be and CNO solar neutrinos is maximal, respectively. The *pep*-ν signal is not extracted using CID because the energy range of *pep*-ν overlaps with the energy range of other neutrino species of interest and it will be constrained in both ROIs to extract ^{7}Be and CNO solar neutrinos as only the total number of neutrinos is extracted using CID in a ROI. Moreover, the number of *pep* neutrino events is higher than CNO in ROIs and its rate is most precisely known as discussed before.

The strategy to create the CID angular PDFs in JUNO is described in detail further. As the current version of JUNO Monte Carlo software does not include the directional

information of solar neutrinos, this analysis is performed by producing CID PDFs using a two step procedure. As mentioned before, this approach include the directional information of solar neutrino event as well as JUNO's timing properties for simulating the Cherenkov contribution, which is crucial for the CID analysis. Firstly, the electrons, whose energy distribution is flat in the chosen energy windows, are simulated with JUNO MC, in order to extract the relative contribution of Cherenkov hits with respect to the Non-Cherenkov hits (hits from the scintillation photons, dark noise hits, and after pulse hits) including the timing behavior of the photons in the JUNO liquid scintillator as well as of the JUNO's PMTs (Sec. 8.1.2). The extracted information of relative Cherenkov hit contribution in time sorted hits is now given as an input to the toy MC simulation. The toy MC framework has been developed to construct the $\cos\alpha$ distribution on an N^{th} hit basis (see Sec. 5.2) for both solar neutrino and backgrounds, taking into account the various physical processes in JUNO, such as the neutrino direction from the Sun, energy and angular distribution of recoiled electron, event vertices, and PMTs' positions, etc, as will be described in Sec. 8.1.3. This procedure allows the inclusion of all JUNO characteristics crucial for the CID analysis in JUNO as realistic as possible. The next stage of CID analysis is planned using the PDFs produced from the Monte Carlo simulation software of JUNO, that will also take into account more effects such as the directional information of solar neutrinos, the scattering of electrons in LS, JUNO properties on a hit basis and so on. The effect of systematic contributions of CID, mainly position reconstruction bias, has also been studied in JUNO as will be discussed in Sec. 8.1.4.

8.1.1 Region of Interest

The CID analysis is performed in two independent energy Regions of Interests (ROIs), which will be referred to as the ^{7}Be ROI and the CNO ROI (see Fig. 8.1). They are selected in order to maximize the contribution of ^{7}Be and CNO solar neutrinos, respectively. Similar to Chapter 7, a spherical fiducial volume cut with a radius $R_{FV} = 14\,\mathrm{m}$ is chosen, which allows to neglect external backgrounds. The internal backgrounds (namely ^{85}Kr, ^{210}Bi, ^{40}K, ^{210}Po, and the radioactive isotopes in the ^{238}U and ^{232}Th decay chains), assuming the Medium Background scenario (see Chapter 6), account for $\sim$89% and $\sim$71% of the total events in the ^{7}Be and CNO ROIs, respectively. Furthermore, the cosmogenic ^{11}C background is present in the CNO ROI only, with an overlapping energy region with CNO-ν. Therefore, the Three Fold Coincidence (TFC) subtraction is assumed, with performance parameters of TP = 90% and SE = 70%, as discussed in Chapter 6. With the TFC algorithm, the contribution of ^{11}C events in the CNO ROI is approximately 27% of the total number of events. Considering all these effects, the percentages of total solar neutrino events are $\sim$11% and $\sim$2% in the ^{7}Be and CNO ROIs, respectively.

The ^{7}Be ROI spans from 0.6 MeV to 0.75 MeV, approximately corresponding to 880 and 1125 reconstructed photo-electrons (p.e.). The CNO ROI ranges from 0.8 MeV to 1.4 MeV, corresponding to about 1200 and 2125 reconstructed p.e. Figure 8.2 shows the types of neutrino species present in each ROI and their contribution relative to the total signal in the respective ROIs. In the ^{7}Be ROI, the signal comes from three solar neutrino species: ^{7}Be-ν (the dominant one, accounting for $\sim$83% of the total signal), *pep*-ν ($\sim$7%), and CNO-ν ($\sim$10%). In the CNO ROI, the signal is composed only of the *pep* ($\sim$70% of the total signal) and CNO ($\sim$30%) solar neutrinos, since the lower edge of this region is higher than the ^{7}Be-ν end point. The energy ranges of both regions were chosen qualitatively in order to maximize the amount of solar neutrinos and limit the contributions from crucial backgrounds (^{210}Po for the ^{7}Be ROI and ^{11}C for the CNO ROI).

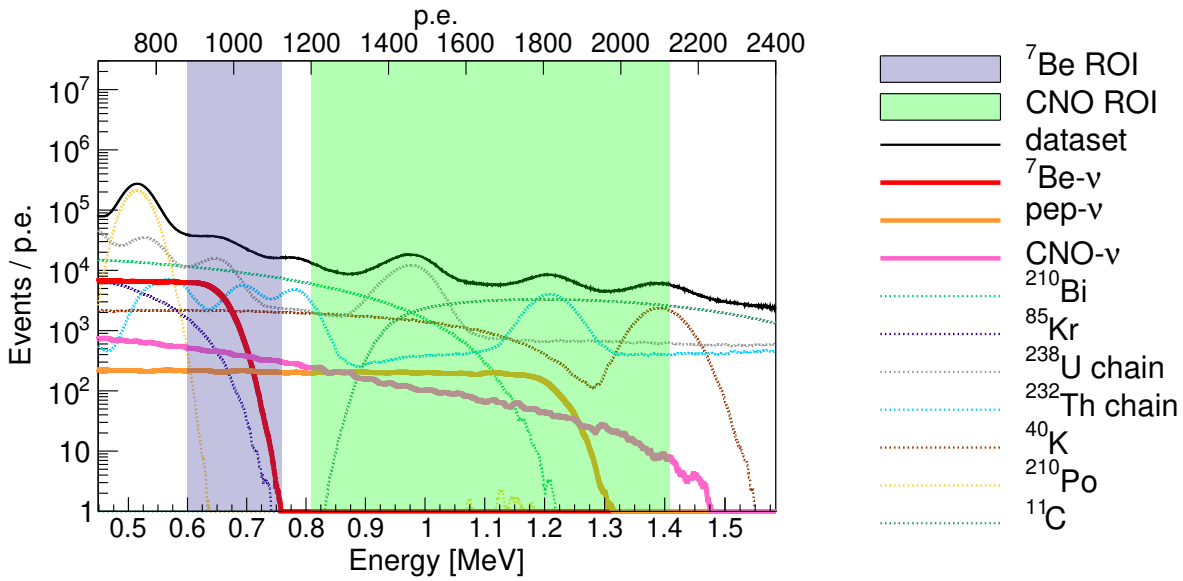

Figure 8.1: The energy distribution of pseudo-dataset (black), illustrating the ^{7}Be (blue band) and CNO (green band) Regions of Interest (ROIs) for the CID analysis in JUNO, assuming the Medium Background scenario and six years of data taking. The energy spectral shapes of ^{7}Be (red solid line), *pep* (orange solid line), and CNO (pink solid line) neutrinos, scaled to the number of events expected in six years of data taking, are drawn to visualize their contribution in the ROIs. Additionally, the energy spectral shapes of the backgrounds, assuming the Medium Background scenario and six years of data taking with Three Fold Coincidence (TFC) subtraction, are shown as dashed lines.

8.1.2 Inputs from JUNO Monte Carlo simulations

In order to study the properties of Cherenkov and scintillation photons in JUNO MC, the simulations of 100k electrons with a flat energy distribution is performed in both the ^{7}Be and CNO ROIs using the JUNO MC software (version J23.1.0-rc1). These simulations are performed at the DetSim and ElecSim levels (see Chapter 6) so that the true timing properties of photons and its propagation in the JUNO LS as well as the PMTs can be extracted. The events are simulated within a spherical volume of radius of 15 m and a fiducial volume cut with a radius $R_{FV} = 14$ m is applied. Events are selected based on their true interaction position. These simulations are crucial to extract the JUNO MC based inputs for the toy MC to construct the $\cos\alpha$ PDFs for CID analysis, taking into account the JUNO detector's characteristics. Figure 8.3a shows the wavelength distribution of detected Cherenkov and scintillation photons for all selected events in the CNO ROI in JUNO MC. Both scintillation (blue) and Cherenkov (red) photons' wavelength spectra start at about 400 nm, which is due to the absorption of light in LS and its re-emission by the LS. The Cherenkov photons with a wavelength $\lambda < 400$ nm are absorbed and re-emitted as the scintillation photons.

As previously discussed, the CID analysis is performed on the individual PMT hits, regardless of their origin of optical photons or the noise. All hits from simulated events are divided into following categories, according to their true JUNO MC information:

- **Cherenkov hits:** the hits caused by Cherenkov photons that have not been absorbed and re-emitted during their travel in LS.

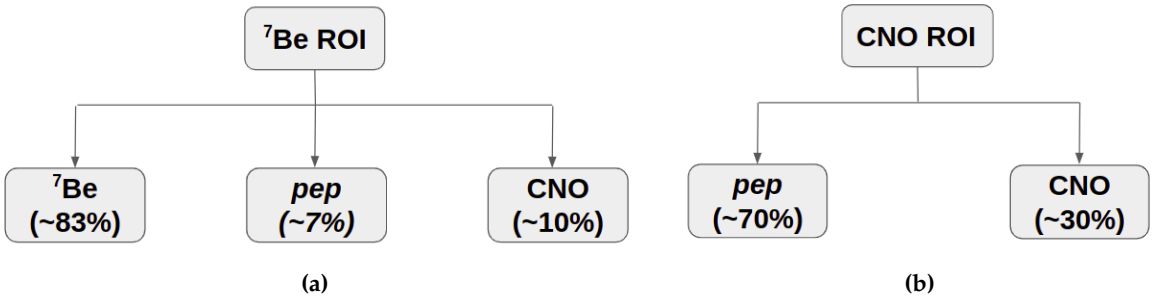

Figure 8.2: Block representation of the relative contribution of different solar neutrino species to the total solar neutrino signal in the (a) ^{7}Be ROI and (b) CNO ROI.

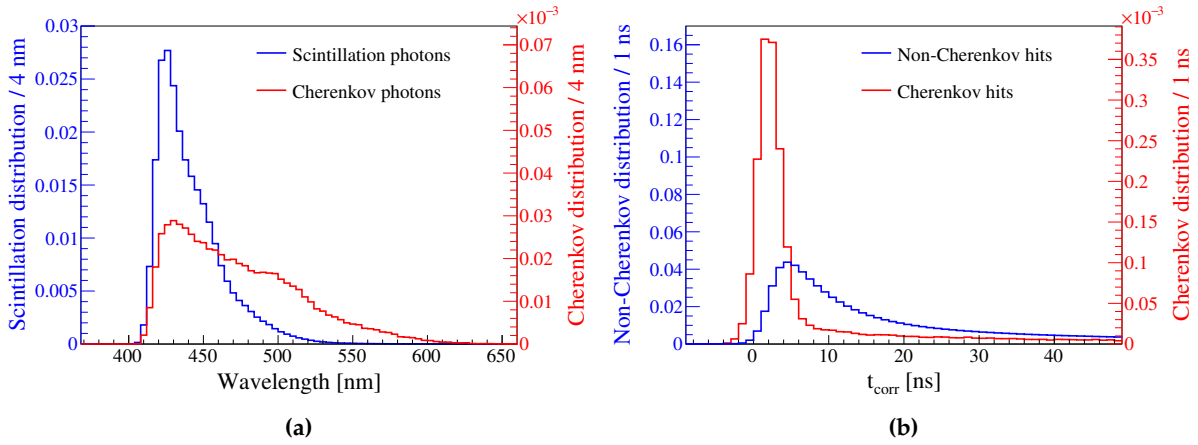

Figure 8.3: (a) The wavelength spectra of detected scintillation (blue) and Cherenkov (red) photon hits in JUNO MC, including the effects of absorption and re-emission in JUNO MC (version J23.1.0-rc1). (b) The distributions of the corrected hit-times t_{corr} on Hamamatsu PMTs in the CNO ROI for Cherenkov hits (in red) and Non-Cherenkov hits (in blue) from JUNO MC (version J23.1.0-rc1). The left y-axis refers to the Non-Cherenkov (the scintillation and noise hits) distribution, which has a unit normalization. The right y-axis refers to the Cherenkov distribution, whose normalization corresponds to 0.0023 (see Table 8.1), representing the fraction of Cherenkov hits. Both distributions extend to negative t_{corr} due to the TTS fluctuations.

- **Scintillation hits:** all other hits, including the ones originated from the scintillation light as well as the Cherenkov photons that were absorbed and then re-emitted in the isotropic direction.
- **Noise hits:** the hits caused by the PMT noise phenomena such as the dark noise and after pulses.

The scintillation and the noise hits are collectively referred to as the *Non-Cherenkov* hits. Here, only the hits on the LPMTs are analysed, as they contribute to the dominant geometric coverage of JUNO. Since the geometric coverage of SPMTs is only ∼3%, it is expected that their inclusion in the analysis would not substantially improve the results. Moreover, the investigation of light properties in JUNO MC is performed by selecting either Hamamatsu PMTs only or NNVT PMTs only, in order to take into account their different timing properties [265]. As the Cherenkov photons contribution in MC is highly sub-dominant (∼0.16% in ^{7}Be ROI and ∼0.25% in the CNO ROI) with respect to the scintillation photons, the N$^{\text{th}}$ hit strategy is adopted, as discussed in Chapter 5. For each detected hit of the event, the Time of flight (TOF) corrected hit-time t_{corr} is defined as follows:

$$t_{\text{corr}} = \text{hit-time} + \text{TTS} - \text{TOF}, \tag{8.1}$$

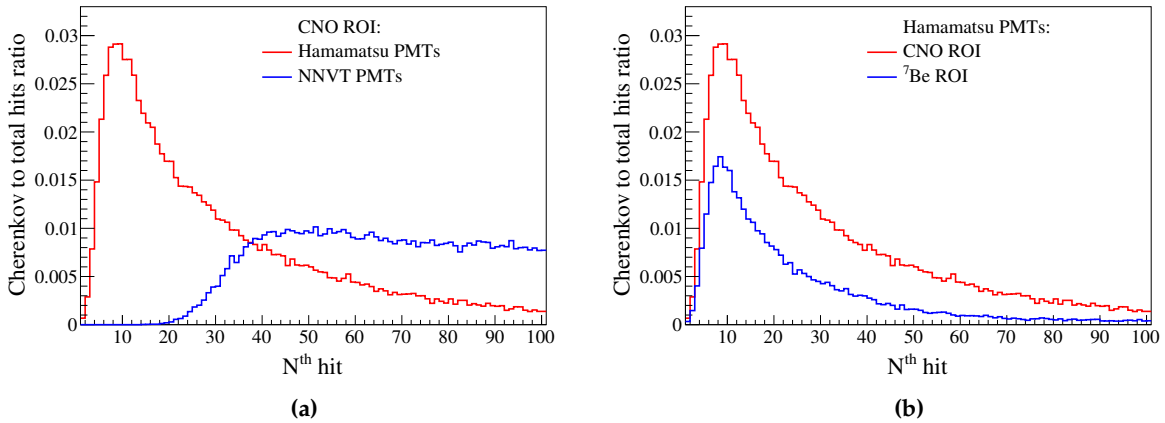

Figure 8.4: (a) The ratio of Cherenkov to total number of hits in the CNO ROI as a function of the N^{th} hit on Hamamatsu PMTs (in red) and on NNVT PMTs (in blue). The maximum Cherenkov to scintillation ratio is lower in blue distribution ($\sim$0.010 ns) as compared to the Hamamatsu PMTs ($\sim$0.029 ns). This is due to the presence of high dark noise and large TTS of NNVT PMTs, which are about three and five times larger, respectively as compared to those corresponding to Hamamatsu PMTs. (b) The ratio of Cherenkov to the total number of hits on Hamamatsu PMTs as a function of the N^{th} hit in the CNO ROI (in red) and ^{7}Be ROI (in blue). The very first hits (until $\sim 4^{th}$) are dominated by the dark noise, hence they exhibit a very small ratio (< 0.01). The contribution of the Cherenkov is maximal in the 9^{th} and 8^{th} hit: the ratios reach $\sim$0.029 and $\sim$0.017 in the CNO and ^{7}Be ROIs, respectively. After the peak, the ratio decreases as the scintillation light becomes increasingly dominant.

where the hit-time corresponds to the time when the photon hits the photocathode, TTS is the transit time spread of the hit PMT, and TOF is the time-of-flight of the photon, representing the time elapsed from its production to its interaction with the PMT. For each hit, the hit-time and the TTS are stored in the MC true information of the event, whereas the TOF is calculated analytically taking into account the JUNO detector geometry, dimensions, and the true interaction position of the event:

$$\mathrm{TOF} = \frac{(D - \mathrm{WL}) \cdot n_{\mathrm{LS}}}{c} + \frac{\mathrm{WL} \cdot n_{\mathrm{H2O}}}{c}, \tag{8.2}$$

where D is the distance between the true event position and the center of the hit PMT and WL is the distance traveled by the photon in water. The refractive indices of the liquid scintillator and of water are given by n_{LS} and n_{H2O}, respectively. From the recent measurements of these quantities at λ of $\sim$400 nm, their values were fixed at $n_{\mathrm{LS}} = 1.5$ and $n_{\mathrm{H2O}} = 1.355$. Through trigonometric considerations, it is possible to calculate WL:

$$\mathrm{WL} = R_{\mathrm{PMT}} \cdot \cos\theta_{\mathrm{WL}} - \sqrt{R^2_{\mathrm{PMT}} \cdot \cos^2\theta_{\mathrm{WL}} - R^2_{\mathrm{PMT}} + R^2_{\mathrm{LS}}}, \tag{8.3}$$

$$\theta_{\mathrm{WL}} = \frac{R^2_{\mathrm{PMT}} + D^2 - R^2_{\mathrm{evt}}}{2 \cdot D \cdot R_{\mathrm{PMT}}}, \tag{8.4}$$

where R_{PMT} is the distance between the center of the detector and the PMT glass, $R_{\mathrm{LS}} = 17.82$ m is the radius of the central detector plus the acrylic width, and R_{evt} is the distance between the center of the detector and the event position. Finally, θ_{WL} corresponds to the angle between the two vectors defined by the detector center to the hit PMT and event position to the hit PMT directions. The possible Rayleigh scatterings and the refraction of light at the LS-water interface are neglected in the calculation.

Figure 8.3b shows the distribution of t_{corr} of Cherenkov and Non-Cherenkov photon hits on Hamamatsu PMTs only for selected events in the CNO ROI. Since the Cherenkov photons are emitted earlier than scintillation photons, the corrected time

Hit type	^{7}Be ROI	CNO ROI
Cherenkov	0.14%	0.23%
Re-emitted Cherenkov	1.06%	1.71%
Scintillation	86.63%	90.34%
Physical	87.83%	92.28%
Dark noise	12.14%	7.69%
After pulse	0.03%	0.03%
Noise	12.17%	7.72%

Table 8.1: Relative occurrence of various hit types on Hamamatsu PMTs in both ^{7}Be and CNO ROIs. Note that all hits are considered here. The so-called physical hits, which account for ∼88-92% of the total hits, are composed of the hits caused by photons impacting on the PMTs photocathodes. They include hits from the primary Cherenkov photons (the only ones correlated to the Sun's position), re-emitted Cherenkov light, and the scintillation photons. The so-called noise hits, which account for ∼8-12% of the total hits, are mainly composed of dark noise hits and only a 0.03% of after pulses. In both the ROIs, the vast majority of the total hits derive from the dominant scintillation light.

of Cherenkov hits is, on average, smaller. In each event, the hits are sorted in ascending order of time using their t_{corr}. Figure 8.4a shows the ratio of Cherenkov to the total number of hits in the CNO ROI as a function of the sorted N$^{\text{th}}$ hits for Hamamatsu PMTs (red) and NNVT PMTs (blue). It can be seen that the maximum Cherenkov contribution is about 2.9% for the early hits detected by the Hamamatsu PMTs only, while for hits detected by NNVT PMTs only, the maximum Cherenkov contribution is ∼1%. This is due to the fact that the high dark noise rate of the NNVT PMTs (∼20% of all detected hits in the CNO ROI), which is approximately three times larger than the Hamamatsu PMTs' dark noise rate, would completely overshadow the Cherenkov hits crucial for the CID analysis. In addition, the large TTS of NNVT PMTs, which is about five times larger than the TTS of Hamamatsu PMTs (1.3 ns) [265], also highly smears the hit time distributions and leads to a smaller Cherenkov to total number of hits ratio in individual sorted hits. Therefore, the hits corresponding to Hamamatsu PMTs only are analyzed and used further.

Figure 8.4b shows the Cherenkov to total hits ratio as a function of the sorted N$^{\text{th}}$ hit on Hamamatsu PMTs only in the two ROIs. As expected, the Cherenkov contribution is higher at earlier hits: the maximum is reached at the 8$^{\text{th}}$ hit in the ^{7}Be ROI and at the 9$^{\text{th}}$ hit in the CNO ROI, respectively. The peak values in the two regions are ∼0.017 and ∼0.029, respectively. Again, since the simulated electrons are more energetic in the CNO ROI, the Cherenkov contribution in this region is more significant. Finally, it is important to note that the very first hits (1$^{\text{st}}$-4$^{\text{th}}$) contain very few Cherenkov hits since they are dominated by dark noise hits. For CID analysis, a range of N$^{\text{th}}$ hits, starting from 5$^{\text{th}}$ hit and comprising 26 hits in total, is chosen qualitatively based on the Cherenkov contribution in each time sorted hit.

8.1.3 Production of $\cos\alpha$ PDFs

In this section, the toy MC approach to construct the $\cos\alpha$ distributions for each N$^{\text{th}}$ hit for both the solar neutrino signal and the background is described. The approach includes the implementation of physical processes in JUNO, described below:

Sun's position and neutrino direction: The incoming direction of solar neutrino, one of the major ingredient for the $\cos\alpha$ calculation, is given by the Sun's position. The

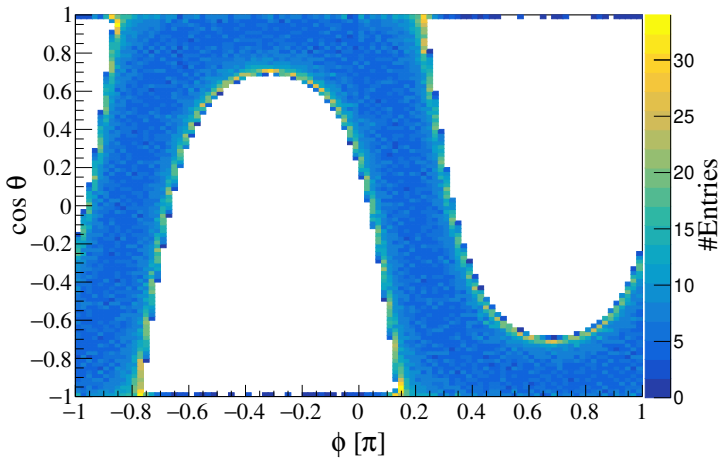

Figure 8.5: Distribution of the Sun's position over 1 calendar year (2024) in the JUNO-based coordinate system with ∼15 minutes time step.

Sun's position is calculated using JUNO detector's geographical coordinates (longitude and latitude): 112°31′05″ E and 22°07′05″ N and the absolute time of the simulated event. The obtained Sun's *altitude* and *azimuth* in the geographical coordinates are then transformed to the JUNO-based coordinate system, following the definition of JUNO's coordinate system:

$$\theta = \frac{\pi}{180^\circ} \cdot (90^\circ - altitude), \tag{8.5}$$

$$\phi = \frac{\pi}{180^\circ} \cdot (180^\circ - 56.7^\circ - azimuth). \tag{8.6}$$

The resulting distribution of the Sun's position over 1 calendar year starting from 2024 in the JUNO coordinate system is shown in Fig. 8.5 with a time bin of ∼15 minutes. All these positions have been considered in the creation of the $\cos\alpha$ PDFs for both signal and background. It has been tested that the $\cos\alpha$ PDFs are not affected by a different choice in the number of years. For signal events, the neutrino direction in Cartesian coordinates is calculated as follows:

$$X_{dir} = -\sin\theta \cdot \cos\phi, \tag{8.7}$$

$$Y_{dir} = -\sin\theta \cdot \sin\phi, \tag{8.8}$$

$$Z_{dir} = -\cos\theta. \tag{8.9}$$

Scattered electron energy: The recoiled electron energy needs to be taken into account for signal as the direction of recoiled energy is dependent on it. For signal events, the energy spectra of the recoiled e^- scattered off by ^{7}Be and *pep* solar neutrinos are calculated analytically using the cross-section and survival probability functions taken from [191, 266]. The oscillation parameters are taken from [36]. The event energy (T) is then sampled from the calculated energy spectrum, in the energy interval of the respective ROIs. The ^{7}Be or *pep* solar neutrinos are chosen for PDFs production because ^{7}Be-ν and *pep*-ν are dominant in the ^{7}Be ROI and CNO ROI, respectively. For background events, as the direction of electron is independent of its energy, its energy is not taken into account.

Electron recoil angle and direction: For signal events, the recoil angle θ_e between the initial solar-ν direction and the scattered electrons is calculated using eq. 2.18. Figure

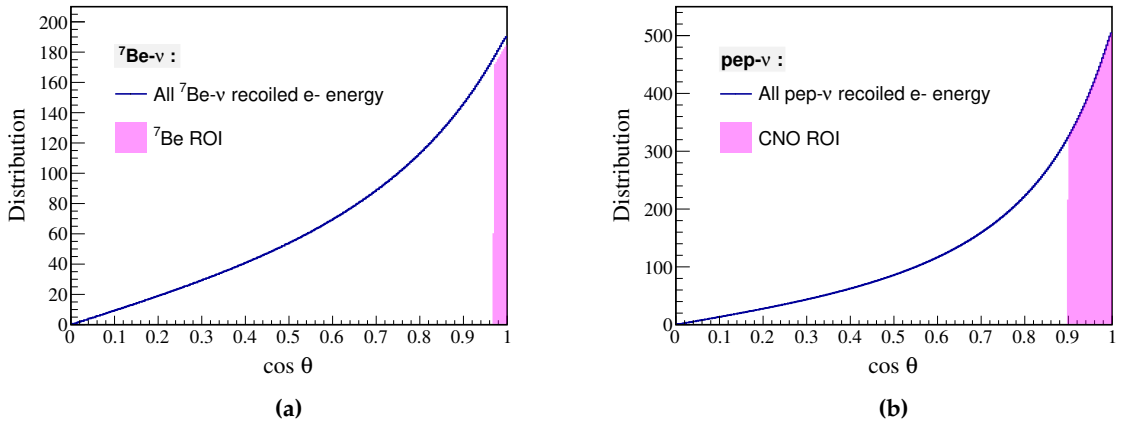

Figure 8.6: The cosine of scattering angle ($\cos\theta_e$) distributions of electrons scattered by ^{7}Be-ν (a) and *pep*-ν (b). The blue curves show the $\cos\theta_e$ distribution for all possible values of recoiled electron energy, while the pink distributions show the $\cos\theta_e$ for the energy regions of the CID analysis, as defined in Section 8.1.1. The width of the pink distributions are different in (a) and (b) due to the different ROIs. The blue distribution in (a) covers both mono-energetic ^{7}Be lines (0.384 MeV and 0.862 MeV) and all scattered electrons, while only recoiled electrons from the 0.862 MeV ^{7}Be line lie in the chosen ^{7}Be ROI. Therefore, the heights of blue and pink distributions in (a) are slightly different.

8.6 shows the $\cos\theta_e$ distributions of electrons scattered by ^{7}Be-ν and *pep*-ν. The blue curves represent the distributions for all possible values of energy of scattered electrons T_e in eq. 2.18, while the pink distributions correspond to $\cos\theta_e$ values of the electrons scattered by ^{7}Be and *pep* neutrinos whose energy lies in ^{7}Be ROI and CNO ROI, respectively. Using this angle, the direction vector of recoiled electron is calculated with respect to the solar neutrino. The direction of the recoiled electron is then transformed to JUNO's coordinate system using a rotation matrix. In this study, it is assumed that the neutrino-electron scattering and the energy deposition happens at the same location. In fact, the distance travelled by the scattered electron is negligible (∼few mm). The Coulomb scattering of electron is not simulated. For background events, the direction of the electron is random and independent from the Sun's position.

Position of PMTs: Only Hamamatsu PMTs and their position in JUNO are considered for the production of solar neutrino and background $\cos\alpha$ PDFs.

Fiducial volume: Both solar neutrino and background events' positions are generated uniformly within the same spherical fiducial volume with 14 m radius.

Angle of the Cherenkov cone: The angle of the Cherenkov cone (θ_{Cher}) is calculated using an effective refractive index of $n = 1.5$ for the liquid scintillator:

$$\cos(\theta_{\text{Cher}}) = \frac{1}{n\beta}, \qquad \beta = \sqrt{1 - \left(\frac{m_e}{m_e + T}\right)^2}, \qquad \beta = v/c. \tag{8.10}$$

The average expected values of $\cos(\theta_{\text{Cher}})$ are ∼0.75 and ∼0.71 in the ^{7}Be and CNO ROIs, respectively.

Generation of Cherenkov and Non-Cherenkov PMT hits: The following toy MC generates directly the PMT hits for each N$^{\text{th}}$ hit generation following the Cherenkov to Non-Cherenkov ratio from the JUNO MC (Fig. 8.4b) for the solar neutrinos. For

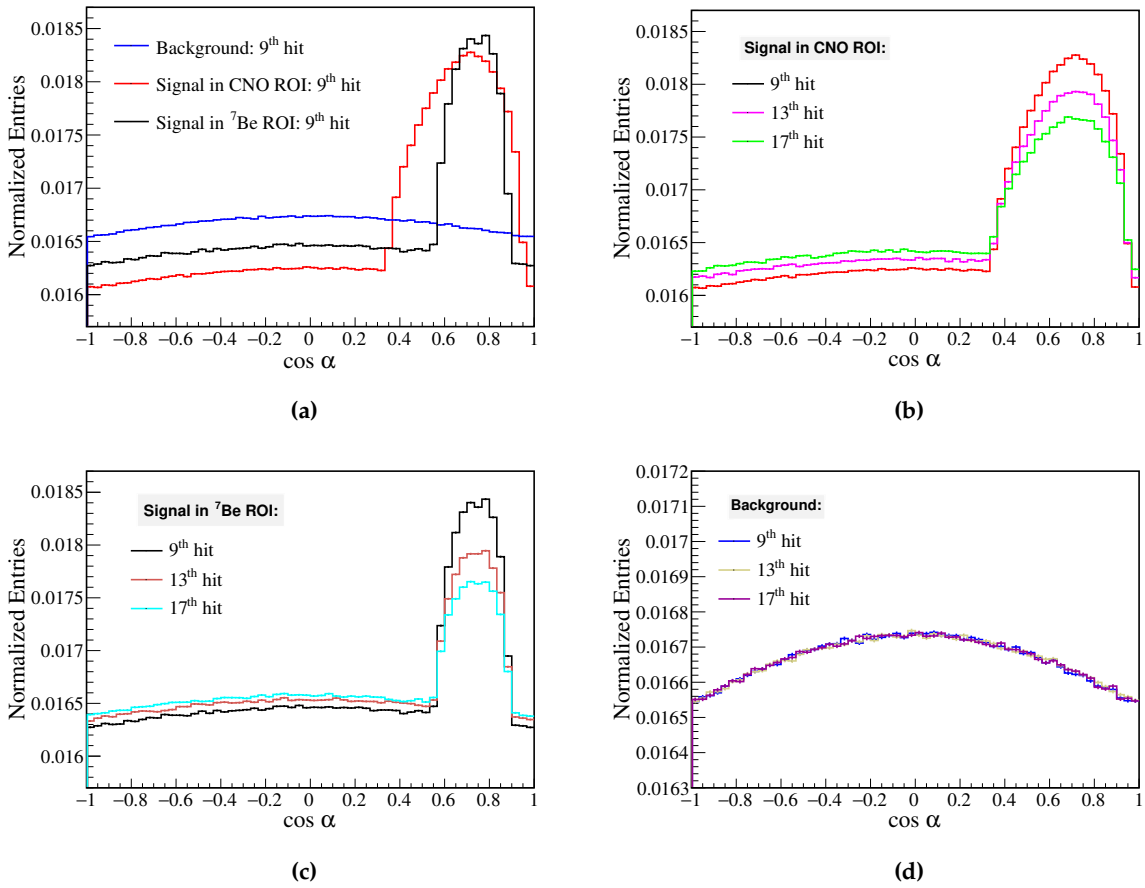

Figure 8.7: The $\cos\alpha$ PDFs of neutrino signal and backgrounds: Here, the *pep*-ν is signal in CNO ROI, and ^{7}Be-ν is signal in ^{7}Be ROI. The same background PDF is used in both ROIs, as discussed in the text. (a) The comparison of CID $\cos\alpha$ distribution of 9th hit from backgrounds' (blue), signal in CNO ROI (red), and signal in ^{7}Be ROI (black). (b) The comparison of CID $\cos\alpha$ distribution of various Nth hits from signal events in the CNO ROI. (c) The comparison of CID $\cos\alpha$ distribution of various Nth hits from signal events in the ^{7}Be ROI. (d) The comparison of CID $\cos\alpha$ distribution of various Nth hits from background events. All CID $\cos\alpha$ distributions are normalized to unit area.

backgrounds, both Cherenkov and Non-Cherenkov PMT hits are simulated randomly in direction, as all hits' directions are uncorrelated to the Sun's position.

Procedure of combined JUNO MC and toy MC

The toy MC, used to construct the $\cos\alpha$ PDFs, is based on the Cherenkov to Non-Cherenkov hits ratio as a function of the Nth sorted hit obtained from the JUNO MC simulations (refer to Sec. 8.1.2 and Fig. 8.4b). In this way, the JUNO MC is exploited to reproduce, as accurately as possible, all the physical phenomena of each event and of its sorted hits individually. Most importantly, the relative time behaviour of detected Cherenkov hits with respect to Non-Cherenkov hits using time-sorted hits is included automatically, also effectively taking into account the light propagation in JUNO LS and the electronic effects such as the dark noise and TTS of Hamamatsu PMTs.

For each signal event, the Sun's position, neutrino direction, scattered electron kinetic energy and direction are calculated as explained at the beginning of this section. Then, the several hits are simulated that represent the Nth sorted hits, starting from the 5th hit to 30th hit. Each generated hit is assigned to be Cherenkov or Non-Cherenkov in a probabilistic way according to the Cherenkov to total hits ratio from the JUNO MC. This probability is different for each Nth hit, following Fig. 8.4b, after taking into

account the time ordering of hits. If a hit is assigned to be Non-Cherenkov, a random Hamamatsu PMT is simulated to be hit as it is not correlated to the Sun's position. Each PMT has a probability to be hit that is inversely proportional to the squared distance between the event and PMT positions to take into account the non-uniformity of photon collection if an event happens off-center. Otherwise, if a hit is assigned to be Cherenkov, a random Hamamatsu PMT that lies in the Cherenkov cone is simulated to be hit. The vertex of the Cherenkov cone coincides to the event position, its axis corresponds to the electron direction, and its angle is evaluated through eq. 8.10.

For the background events, as the PMT hits are not correlated with the Sun's position, regardless of being Cherenkov or Non-Cherenkov, a random Hamamatsu PMT is simulated to be hit, including the probability of hit PMT to be inversely proportional to the squared distance between the background event and PMT positions. Here, the energy dependency of background events is not simulated, as the direction of background events are uncorrelated to the Sun's position, irrespective of their energy. So, the same background PDFs are used in both ROIs.

The $\cos\alpha$ values for each N^{th} hit and for both signal and background can be calculated using the Sun, the event, and the hit PMT positions. A large statistics of events ($\sim 10^8$) for each of the signal and backgrounds is generated to build PDFs in order to avoid statistical fluctuations. Figure 8.7a shows the comparison of $\cos\alpha$ distributions for 9^{th} hit of *pep* (in CNO ROI) and ^{7}Be (in ^{7}Be ROI) solar neutrinos as well as for the background events. Figure 8.7b, 8.7c, and 8.7d show the comparison of $\cos\alpha$ distributions for various hits of *pep*-ν in CNO ROI, ^{7}Be-ν in ^{7}Be ROI, and background events, respectively. One can see that the overall shapes of the $\cos\alpha$ distributions for different hits of solar neutrinos differ with each other due to different relative Cherenkov photon contribution, while the shapes of the $\cos\alpha$ distributions for different hits of backgrounds are equivalent, except for the statistical fluctuations. The shape of backgrounds' $\cos\alpha$ distribution is non-flat due to the geometric effect from the finite number of Hamamatsu PMTs and their non-uniform spatial distribution in combination with the non-uniform position of the Sun as seen by JUNO.

8.1.4 Systematic effects

In Chapter 5, it has been discussed that the position reconstruction bias is one of the major systematic effect for the CID analysis in Borexino. The effect of position reconstruction bias (Δr_{dir}) on $\cos\alpha$ PDFs has also been investigated in JUNO. The first step is to produce the distribution of Δr_{dir} calculated using eq. 5.6 for all selected events in fiducial volume of radius 14 m, which are simulated with JUNO MC as in Sec. 8.1.2. The Δr_{dir} distribution obtained is shown in Fig. 8.8a and the mean of the distribution is 1.25 ± 0.34 cm. In order to obtain this distribution, the MC simulation including the event reconstruction stage has been performed.

As discussed in Sec. 8.1.2, the true vertex of simulated event is used for TOF correction to produce the distribution of Cherenkov to total number of hits ratio as a function of N^{th} hits. The impact of using reconstructed event position for TOF correction is also studied to produce the distribution of Cherenkov to total hits ratio as function of N^{th} hits. Figure 8.8b shows the comparison of the ratio of Cherenkov to total number of hits as function of N^{th} hits with reconstructed vertices (blue) and with using true vertices (red) of events. It can be seen that using the reconstructed event position for TOF calculation does not significantly influence the Cherenkov hit contribution relative to the total number of hits as function of N^{th} hits, that is, the maximum ratio changes from 0.029 to 0.028 after using the reconstructed event position in TOF calculation in eq. 8.2.

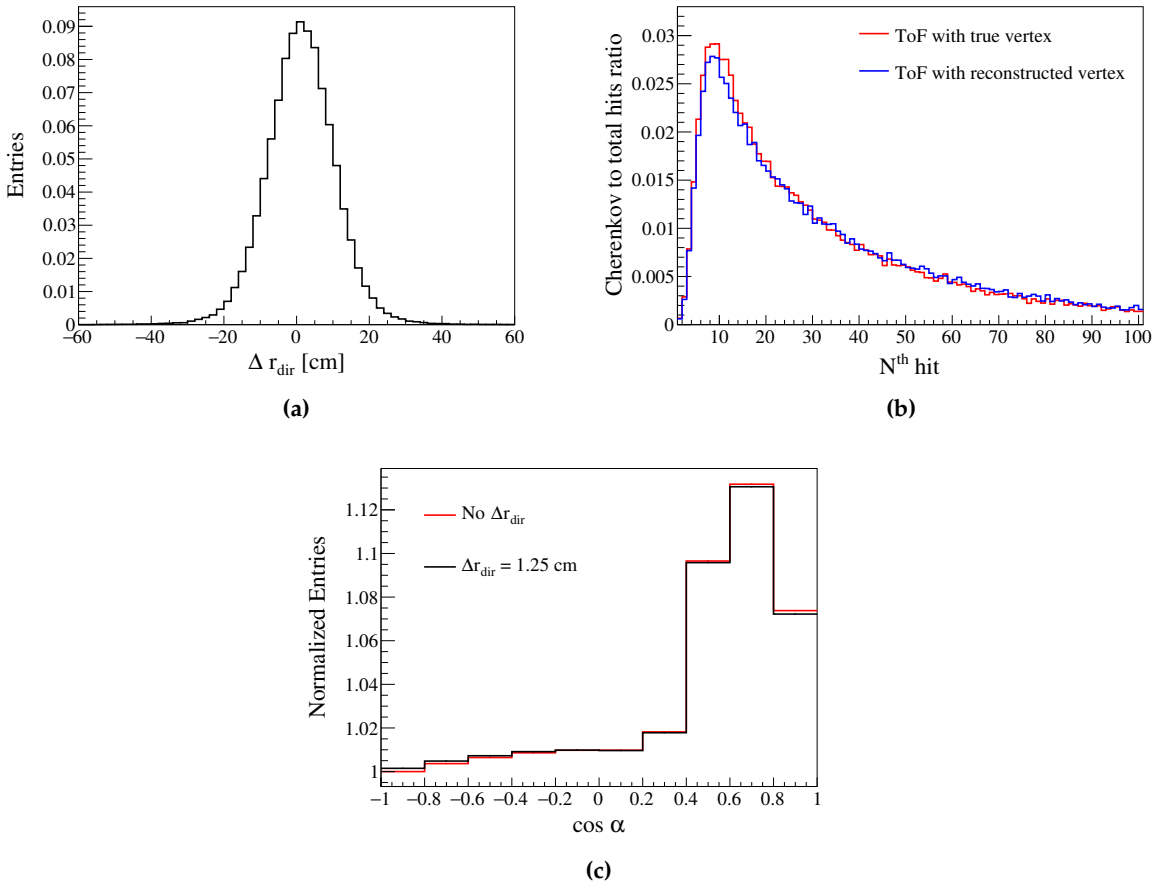

Figure 8.8: Position reconstruction bias in JUNO: (a) Distribution of Δr_{dir} parameter evaluated using eq. 5.6 for each simulated electron event using JUNO MC in true energy range of 0.8-1.4 MeV and fiducial volume of radius 14 m. The distribution has mean of 1.25 ± 0.34 cm. (b) The comparison of the ratio of Cherenkov to total number of hits as a function of N^{th} hits obtained using TOF correction for hits of each event with its reconstructed vertex (blue) and with using true vertex (red). (c) Comparison of the CID angular distributions for solar neutrinos, without (red) and with (black) Δr_{dir}, in order to show the effect of Δr_{dir} on the $\cos\alpha$ calculation.

The effect of Δr_{dir} parameter on the $\cos\alpha$ distribution of signal events in JUNO is shown in Fig. 8.8c, where in the $\cos\alpha$ calculation, the biased vertex ($\vec{r}_{biased}$) with respect to uniformly generated event position ($\vec{r}_{gen}$) in the direction of scattered e- ($\vec{d}_{true}$) is used in toy MC. The biased vertex is calculated as:

$$\vec{r}_{biased} = \vec{r}_{gen} + \Delta r_{dir} \cdot \vec{d}_{true}, \tag{8.11}$$

where Δr_{dir} is sampled from Fig. 8.8a. These studies have shown that the systematic effect of Δr_{dir} parameter on signal PDFs is negligible ($\sim$0.1%). The reason can be attributed to the large detector size of JUNO as compared to Borexino (Chapter 5), where a bias of 1-2 cm is negligible as compared to the long distance travelled by the photons in JUNO. The systematic uncertainty associated to the position reconstruction bias are not included in this proof of principle analysis for JUNO. More comprehensive studies on the influence of position reconstruction bias will be studied using JUNO MC studies, where the simultaneous impact of position reconstruction bias on both TOF correction on the hit-time and on the shape of $\cos\alpha$ distribution of early hits of the same event will be analyzed, which is a limitation of the toy MC approach.

Other major systematic uncertainty, the group velocity correction for Cherenkov photons relative to the scintillation photons, is planned to be studied using the PDFs

produced from JUNO MC simulated solar neutrino events, where the expected precision of this parameter can be estimated using the calibration γ sources or using the ^{7}Be solar neutrinos in ^{7}Be ROI by following the approach adopted in Chapter 5. Then, the effect of obtained precision of the group velocity parameter can be included for extracting the CNO solar neutrinos in CNO ROI. However, these approaches has their own limitations, that is, the γ sources are not optimal as the reconstruction of γ direction posed a large systematic error in Chapter 5 and the calibration in ^{7}Be ROI can not be performed if ^{7}Be solar neutrinos also need to be measured using CID. Therefore, a calibration strategy of a possible electron source is under study, in which the direction of emitted electron is known [267].

As the goal of this analysis is to provide the proof of principle of CID method for solar neutrinos in JUNO and the systematic errors in JUNO are not expected to be larger than the ones in Borexino, the systematic uncertainties are not included here.

8.2 Sensitivity estimation

This section is dedicated to summarize the potential of the CID analysis in JUNO by performing sensitivity studies using the neutrino and background $\cos\alpha$ PDFs produced in the previous section. To do so, 10^4 toy datasets are generated by randomly sampling $\cos\alpha$ PDFs [268]. Here, the contributions from both neutrino and background species are summed according to the expected statistics for the Medium Background scenario in the two ROIs for six years of data taking. The number of expected neutrino and background events used to create the toy dataset are reported in Table 8.2. Each toy dataset consists of 26 $\cos\alpha$ histograms for each N^{th} hit in the range of 5^{th}-30^{th} hit. The generated toy dataset is fitted with a model comprising of the signal and background PDF of each N^{th} hit simultaneously using a χ^2 function, as discussed in Chapter 5. In the fit, the total number of solar neutrinos N_ν is the only free parameter and to obtain resulting N_ν, a $\Delta\chi^2$ profile is produced for each fit in each ROI.

The fit results for only one dataset in both ^{7}Be and CNO ROIs are shown in Fig. 8.9 and Fig. 8.10, respectively. The plots show the $\cos\alpha$ distribution of 5^{th}, 7^{th}, 8^{th}, 9^{th}, 10^{th}, 15^{th}, 25^{th}, and 30^{th} hits of data (black) and the best fit distribution (red) under the assumption of the Medium Background scenario for 6 years of data taking. The background only hypothesis is shown in blue. The resulting distribution of relative uncertainty of N_ν, extracted from 10^4 fits in each ROI are shown in the left panel of Fig. 8.11, with median of about 9% and 3% in CNO and ^{7}Be ROIs, respectively. The $\Delta\chi^2$ profiles produced in each fit for both ROIs are also shown as orange lines in the right panel Fig. 8.11.

The sensitivity to CNO and ^{7}Be neutrinos has been studied by subtracting the contribution of solar neutrinos of non-interest in each ROI. For this, a median profile of all $\Delta\chi^2$ profiles produced in each fit in each ROI is obtained, shown as a black curve in the right panel Fig. 8.11, and is transformed into the probability distribution. Using the convolution method discussed in Sec. 5.6.5 and assuming both high and low metallicity SSM predictions on *pep* neutrino interaction rate, the resulting distribution of number of CNO neutrinos in JUNO is obtained and converted in interaction rate (cpd/kt) as shown in Fig. 8.12. The extracted CNO-ν rate is 50.1 ± 15.0 cpd/kt with a relative uncertainty of about 30%. The same procedure is performed in the ^{7}Be ROI to analyse the CID sensitivity to ^{7}Be neutrinos in JUNO. The contributions of *pep*, and CNO solar neutrinos are subtracted through the convolution. The probability distribution of *pep* neutrino interaction rate in JUNO is built using SSM predictions, as the one used in CNO ROI. The distribution of CNO is derived from the results obtained in CNO ROI, so that the amount of CNO-ν subtracted is not influenced by the SSM metallicity

	^{7}Be ROI	CNO ROI
N(^{7}Be)	6.38×10^{5}	-
N(pep)	0.55×10^{5}	1.34×10^{5}
N(CNO)	0.73×10^{5}	0.57×10^{5}
N_{ν}	7.66×10^{5}	1.91×10^{5}
N(^{210}Po)	5.2×10^{3}	-
N(^{85}Kr)	9.1×10^{4}	-
N(^{210}Bi)	2.38×10^{6}	1.24×10^{6}
N(^{40}K)	5.2×10^{5}	1.06×10^{6}
N(^{238}U)	2.16×10^{6}	2.46×10^{6}
N(^{232}Th)	9.4×10^{5}	9.2×10^{5}
N(^{11}C)	-	2.13×10^{6}
N_{bkg}	6.10×10^{6}	7.81×10^{6}
$\frac{N_{\nu}}{N_{bkg}}$	1.3×10^{-1}	2.5×10^{-2}

Table 8.2: Expected number of solar neutrinos (N_{ν}) and background (N_{bkg}) events, with the contribution of each species within the two ROIs of interest of CID analysis after six years of data taking and with a fiducial volume of $R_{FV} = 14$ m. For signal events, the number of expected events is calculated using high-metallicity SSM predictions (see Table 6.4). For the estimation of background event contribution, the Medium Background scenario is assumed [268].

scenarios which are significantly different to each other (∼28%). The resulting distribution of number of ^{7}Be neutrinos in JUNO is obtained and converted in interaction rate (cpd/kt) as shown in Fig. 8.12. The extracted ^{7}Be-ν rate is 489 ± 23 cpd/kt with a relative uncertainty of about 4.7%.

By including the CID analysis results into the spectral fit discussed in Chapter 7, the sensitivity results on ^{7}Be and CNO solar neutrinos is further improved. In order to achieve this, the extracted results on N_{ν} from CID fit only in the two ROIs are included as the Gaussian likelihood pull terms in the total likelihood discussed in Sec. 7.1.2. For this, 10^{4} energy spectral fits are performed on the toy datasets in the energy range of 0.45-1.7 MeV as described in Sec. 7.1.2 using the likelihood maximisation assuming the Medium Background scenario and 6 years of data taking.

The sensitivity to ^{7}Be and CNO neutrinos in JUNO are extracted in three configuration: spectral fit (SF) only, SF + 1-CID constraint, and SF + 2-CID constraints. In SF + 1-CID constraint case, the spectral fit for CNO (^{7}Be) analysis includes one CID constraint obtained in CNO (^{7}Be) ROI, while in SF + 2-CID constraints scenario, both CID constraints are added. Figure 8.13 shows the extracted relative uncertainty on CNO and ^{7}Be rate in all three configurations. Table 8.3 reports the median relative uncertainty on CNO and ^{7}Be rate in three fit configurations. Using SF only, the median relative uncertainty on CNO and ^{7}Be rate are $18.8\ ^{+4.0}_{-2.8}$ % and $0.4624^{+0.0028}_{-0.0023}$ %, respectively. The uncertainties are obtained by taking the distance between median and the 68% C.L band extremes. To follow the strategy adopted in Chapter 7, no constraint is set on *pep* neutrinos to obtain ^{7}Be rate, while to obtain CNO results, a Gaussian pull term on *pep* neutrinos rate is additionally applied. The impact of including CID constraints in the

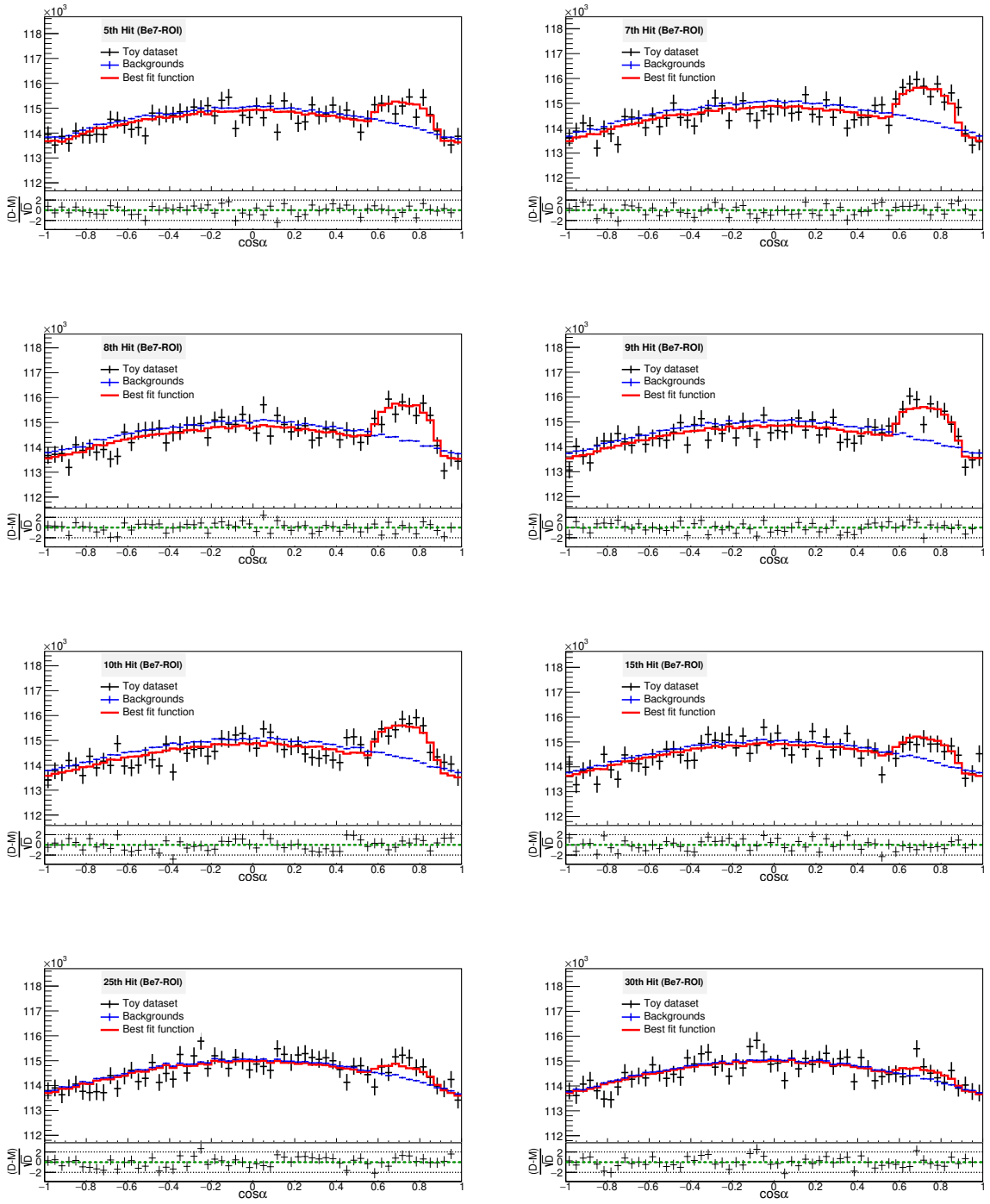

Figure 8.9: Fit example of the $\cos\alpha$ distributions in the ^{7}Be ROI for six years of data taking in the Medium Background scenario. The $\cos\alpha$ distributions of the 5^{th}, 7^{th}, 8^{th}, 9^{th}, 10^{th}, 15^{th}, 25^{th}, and 30^{th} hits are shown. The toy datasets are represented by black points and the best fit functions are shown in red lines. The background only hypothesis is shown in blue. From [268].

spectral fit is evident for the CNO relative uncertainty distribution, whose median sensitivity improves to $14.0^{+2.7}_{-1.9}$ % and $11.6^{+1.9}_{-1.5}$ % in case of one and two CID constraints, respectively. However, the precision on ^{7}Be neutrinos rate is governed by the spectral fit and only a tiny improvement is observed: $0.4420^{+0.0019}_{-0.0018}$ % and $0.4375^{+0.0018}_{-0.0018}$ % using one and two CID constraints, respectively.

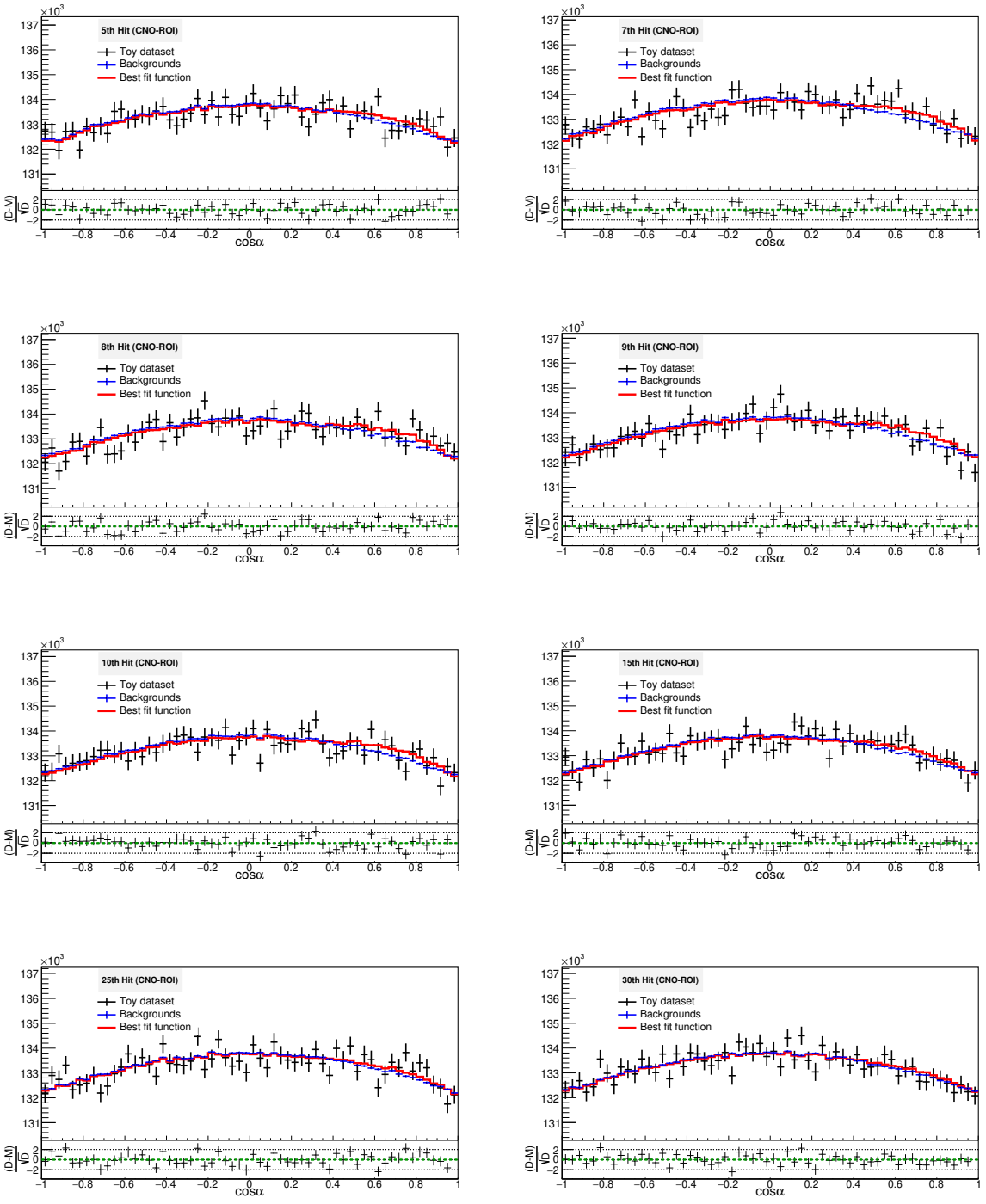

Figure 8.10: Fit example of the $\cos\alpha$ distributions in the CNO ROI for six years of data taking in the Medium Background scenario. The $\cos\alpha$ distributions of the 5^{th}, 7^{th}, 8^{th}, 9^{th}, 10^{th}, 15^{th}, 25^{th}, and 30^{th} hits are shown. The toy datasets are represented by the black points and the best fit functions are shown in red lines. The background only hypothesis is shown in blue. From [268].

8.3 Summary

In summary, this chapter has reported the analysis strategy used to evaluate the JUNO sensitivity to measure ^{7}Be and CNO neutrinos, exploiting the CID method described in Chapter 5. The CID analysis is performed in the two energy regions of interests,

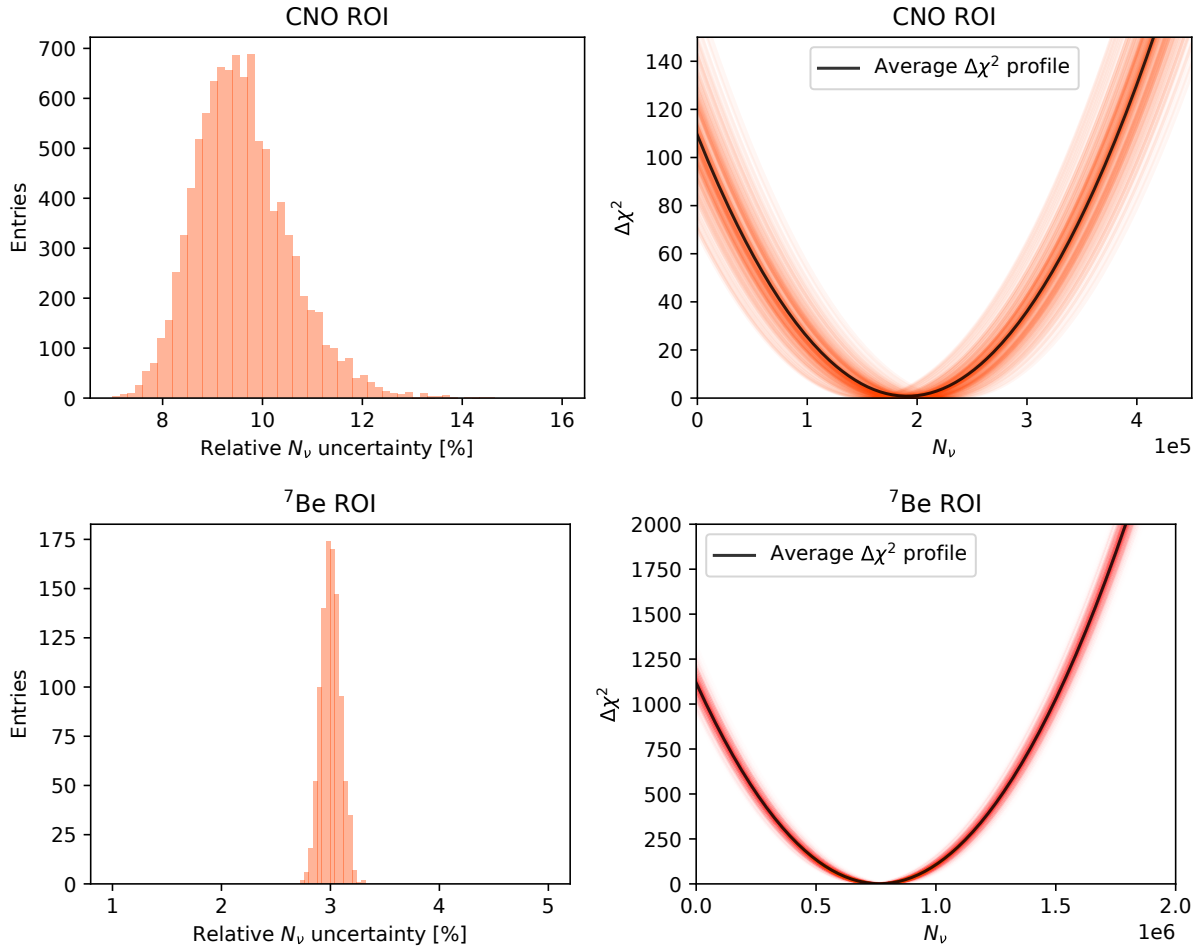

Figure 8.11: CID analysis results for 6 years of data-taking under Medium Background conditions: Left panel: the distribution of relative uncertainties of N_ν obtained with 10^4 independent toy datasets in CNO ROI (up) and in ^{7}Be ROI (bottom). Right panel: the example $\Delta\chi^2(N_\nu)$ profiles, shown as orange lines in CNO ROI (up) and in ^{7}Be ROI (bottom). The final profile is selected as the median of the profiles and is shown in black. From [268].

0.6 MeV - 0.75 MeV and 0.8 MeV - 1.4 MeV, where the contribution of ^{7}Be and CNO solar neutrino is maximal, respectively. As the CID method exploits the time sorted detected hits of each event, the cos α PDFs are produced for each N$^{\text{th}}$ hit using a combined JUNO MC and a toy MC approach. In this approach, the relative Cherenkov contribution, taking into account effectively the JUNO LS characteristics and including PMTs' timing properties, is extracted using JUNO MC simulation software. Using this as an input, the PDFs of CID angular distributions for the signal are produced for each selected N$^{\text{th}}$ hit of an simulated event using a toy MC framework, that also simulates the physical processes inside JUNO as realistic as possible. This approach includes the directional information of solar neutrino event, which is lacking in the current version of the JUNO MC and its implementation is under progress. In order to study and include the systematic effects in the CID analysis, a calibration strategy of a possible electron source is under study, in which the direction of emitted electron is known [267]. The PDFs of background events, whose hit direction is uncorrelated to the Sun's position, are also produced using the toy MC simulation. The investigation of Cherenkov photon properties, development of toy MC framework, and production chain of CID PDFs encompasses my work. I have also studied the systematic effect of position reconstruction bias on the CID PDFs in JUNO, which has been found to be negligible and more studies from JUNO MC with direction information of the event will be performed. Using these PDFs, the relative precision of ^{7}Be and CNO neutrino rate in JUNO has been

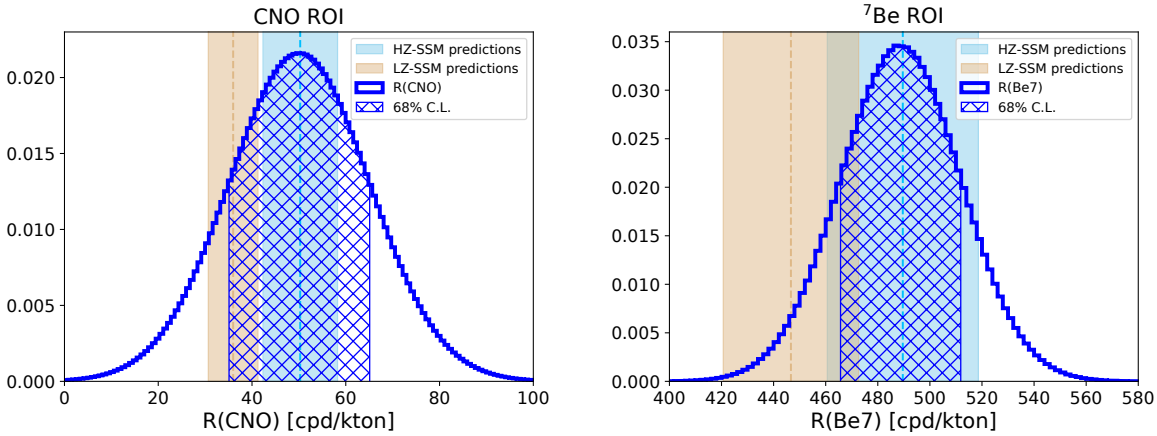

Figure 8.12: Results of the CID only analysis in the CNO ROI (left) and ^{7}Be ROI (right) assuming the Medium Background scenario and six years of data taking. Left: Reconstructed CNO interaction rate (blue line) is obtained by subtracting the *pep* neutrinos contribution. Right: Reconstructed ^{7}Be interaction rate (blue line) is obtained by subtracting the *pep* and CNO neutrinos contributions from the CID results. The blue and orange boxes correspond to the SSM predictions in the high and low metallicity scenarios, respectively for CNO and ^{7}Be neutrino rate. The patterned area under the histogram corresponds to the 68% confidence interval, around the median value, of the resulting distribution. From [268].

Configuration	R(^{7}Be) relative uncertainty [%]	R(CNO) relative uncertainty [%]
SF	$0.4624^{+0.0028}_{-0.0023}$	$18.8^{+4.0}_{-2.8}$
SF + 1-CID	$0.4420^{+0.0019}_{-0.0018}$	$14.0^{+2.7}_{-1.9}$
SF + 2-CID	$0.4375^{+0.0018}_{-0.0018}$	$11.6^{+1.9}_{-1.5}$

Table 8.3: JUNO sensitivity to ^{7}Be and CNO neutrinos in three different configurations: SF stands for the spectral fit analysis discussed in Chapter 7. The SF + 1-CID configuration represents the results obtained by adding an additional constraint based on the CID results obtained in CNO ROI (for CNO neutrinos) and ^{7}Be ROI (for ^{7}Be neutrinos), while SF + 2-CID represents the results with both CID constraints obtained in the CNO and ^{7}Be ROIs [268].

extracted using the CID analysis only as well as using the CID results as constraint in the spectral fit discussed in the previous chapter. These studies have been performed in the case of six years of exposure and the Medium Background scenario. Not only the results obtained using this approach show the improvement in the sensitivity results in JUNO, especially to CNO solar neutrinos, demonstrating the promising potential of CID method in JUNO, but also this approach has led to the understanding of Cherenkov light properties in JUNO and the development of whole analysis chain as well as it paved the way for the future analysis with JUNO MC framework.

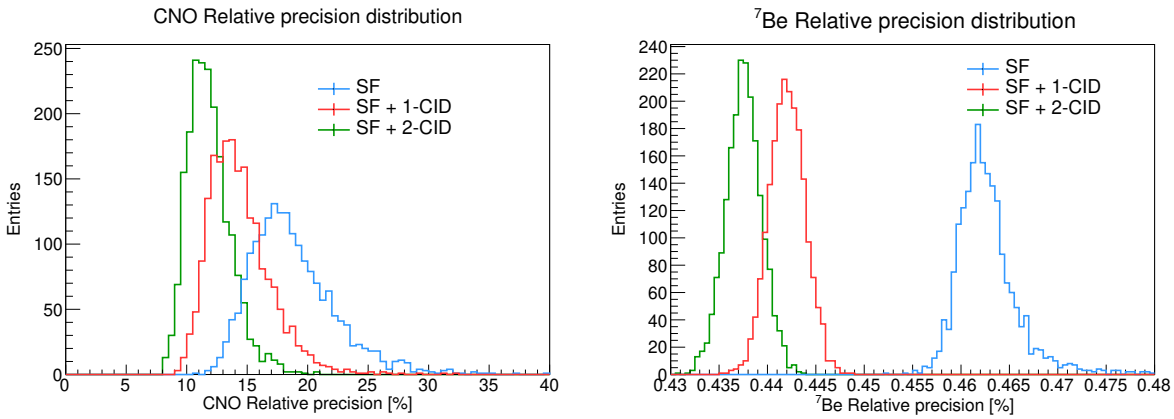

Figure 8.13: Relative error distributions of the CNO and ^{7}Be solar neutrinos in the left and right panels, respectively. The distributions obtained with the spectral fit only are shown in blue. The red distributions illustrate the results obtained by applying a constraint based on the CID results obtained in the CNO ROI (for CNO neutrinos) and ^{7}Be ROI (for ^{7}Be neutrinos). The green distributions report the results obtained when both CID constraints are applied. Note that all distributions correspond to the Medium Background scenario and six years of data taking. From [268].

Conclusion and outlook

This thesis has presented the analysis strategy and results of the recent solar neutrino measurements with the Borexino experiment and the future potential with the JUNO experiment.

The dominant process for nuclear fusion reactions in the Sun is the proton-proton (*pp*) cycle. The Carbon-Nitrogen-Oxygen (CNO) fusion cycle is a subdominant process in the Sun, where C,N, and O catalyzes its energy production mechanism of the hydrogen to helium conversion. The CNO cycle is hypothesized to be a primary nuclear fusion sequence in heavier stars. The motivation for the CNO solar neutrino flux measurement lies in deriving information on the metallicity of the Sun's core and provides a solution towards the "solar metallicity problem". Metallicity is a crucial input to the Standard Solar Model (SSM) and is generally classified to into two based on the Sun's photospheric measurements: low-metallicity (LZ) and high-metallicity (HZ). The Borexino experiment took data from May 2011 to October 2021, where the complete data-taking period is divided into three: Phase-I (May 2007 - May 2010), Phase-II (December 2011 - May 2016), and Phase-III (July 2016 - October 2021). In Chapter 4, an updated CNO solar neutrino measurement has been carried out with the Borexino experiment, using its recent data in Phase-III from January 2017 to October 2021. The measured CNO-ν rate corresponds to $6.7^{+2.0}_{-0.8}$ cpd/100 t and this translates to a CNO-ν flux of $(6.6^{+2.0}_{-0.9}) \times 10^8$ cm^{-2}s^{-1}, taking into account the neutrino oscillation and matter effects. The null hypothesis of no CNO-ν signal has been excluded with about 7σ C.L. This analysis uses a multivariate spectral fit of data with Monte Carlo (MC) probability density functions (PDFs), which exploits the energy and radial information of the signal and background events. I have co-produced the data and MC PDF inputs for the spectral fit undergoing a series of selection cuts and quality checks, and I also performed the final multivariate fit to obtain CNO-ν rate. The crucial backgrounds for the CNO-ν analysis are *pep*-ν and the β-decaying ^{210}Bi, because their spectral shapes are similar to the recoiled electron spectra by CNO-ν. A symmetric constraint on the *pep*-ν rate is used, which is estimated with 1.4% precision level from the global analysis of all independent solar-ν data, theoretical predictions, and the error on the neutrino oscillation parameters. The asymmetric constraint on ^{210}Bi rate has been obtained by estimating the minimum rate of its daughter ^{210}Po in an so-called Low Polonium Field (LPoF). Thanks to the thermal insulation campaign of Borexino, this region is almost free of ^{210}Po contribution, that was brought from the nylon vessel surface by convective currents, which were caused by seasonal and man-made temperature changes. An upper limit on ^{210}Bi rate has been obtained by fitting the ^{210}Po data, which is selected using a pulse shape discrimination (PSD) technique, with a model describing its spatial distribution in LPoF. I have contributed towards the determination of model parameter, representing the inefficiency of PSD, taking into account the selection of some β-like events as the ^{210}Po candidates. The final upper limit on the ^{210}Bi interaction rate is 10.8 ± 1.0 cpd/100 t, which has been used in the spectral fit to obtain CNO-ν rate. The updated CNO measurement has been used to evaluate C+N abundance relative to the hydrogen abundance, corresponding to $(5.78^{+1.86}_{-1.00}) \times 10^{-4}$, which has been compared with the independent measurements of the Sun's photosphere to provide insights on the solar metallicity problem. This result is in a good agreement with the

HZ compilations, while it features a $\sim 2\sigma$ tension with the LZ ones. This analysis used ^{8}B-ν flux from the global analysis of independent data from all solar neutrino experiments, breaking the ambiguity due to opacity and metallicity degeneracy. This is the first determination of C+N solar abundances using the solar neutrinos. The future experiments could provide a crucial element to access the longstanding solar metallicity problem, by providing more precise measurements on the CNO-ν flux.

A directional measurement of sub-MeV solar neutrinos has been provided with the Borexino experiment in Chapter 5. This marks the first analysis of solar neutrinos using directional Cherenkov light in a liquid scintillator detector. The method, that has been developed and exploited in this analysis, is referred to as the Correlated and Integrated Directionality (CID) technique. In this method, the direction of the early photons of an event is correlated to the well known position of the Sun, where the direction of photons is given by the reconstructed position of the event and the hit PMT position. This is integrated over a large number of events, which results in a CID angular distribution. The proof-of-principle analysis of CID was done in the ^{7}Be-ν shoulder energy region, based on a favorable signal to background ratio. The CID angular distributions of the first two hits of data events have been fitted with the MC PDFs of solar neutrino and background CID angular distributions, with optimised number of bins. I have performed the optimisation of number of bins using a sensitivity analysis. The first two hits, which are sorted in time, are optimised to maximise the sensitivity for fast and directional Cherenkov photons, whose contribution is subdominant ($\sim$0.4% of all hits) with respect to the isotropic and dominant scintillation light. From a χ^2 fit, the total number of solar neutrinos (^{7}Be+*pep*+CNO) in the selected energy region is extracted. The major sources of systematic uncertainties include the position reconstruction bias Δr_{dir} and the effective correction of the Cherenkov group velocity gvc_{ch}. The parameter gvc_{ch} has been estimated with $\sim$36% relative uncertainty using the γ calibration sources from the year 2009 used in Borexino. As the deterioration of the detector response at a level of sub-nanosecond precision with time can not be excluded, this correction has been considered valid only for Phase-I and therefore, the CID analysis is performed in Phase-I only. The parameter gvc_{ch} has been constrained using a Gaussian pull term in the fit. The Δr_{dir} parameter cannot be constrained due to the lack of a dedicated source, where the direction of the e^- is known and therefore, it is treated as a free nuisance parameter. Various other systematic effects have also been studied and included. In this regard, my contribution includes the study of various systematic effects on the shape of simulated background PDFs, including development of a toy MC framework. The null hypothesis of no solar neutrinos in the region of interest has been excluded with $>5\sigma$ significance, by solely using their directionality. The inferred total number of solar neutrino events using CID in Phase-I is $10{,}887^{+2{,}386}_{-2{,}103}(\text{stat.}) \pm 947(\text{syst.})$. The expected value using SSM predictions is $10{,}187^{+541}_{-1{,}127}$ events and thus, the CID measurement is well in agreement with the SSMs. The result on the ^{7}Be interaction rate, after fixing the sub-dominant contributions of the CNO and *pep* solar neutrinos from the SSM predictions and including the systematic uncertainties is $51.6^{+13.9}_{-12.5}$ (stat. + syst.) cpd/100t. In addition, the background-only hypothesis is found to be incompatible with the data of all the three Borexino phases with a significance of $>5\sigma$, and a detection of solar neutrinos is performed only using their directionality, without any Cherenkov calibration.

In Chapter 5, the CID method has also been exploited to perform CNO-ν measurement, where no constraint on ^{210}Bi background rate has been applied. For this, an energy region of about (0.85-1.3) MeV is selected, where the *pep*-ν and CNO-ν are the dominant signal including a small contribution ($\sim$1% of all events) from ^{8}B solar neutrinos. This energy region is independent from the ^{7}Be shoulder energy region, used before. The ^{7}Be shoulder energy region has been used to calibrate the gvc_{ch} parameter

by performing the CID analysis, where the number of solar neutrinos are now constrained to the SSM predictions and the gvc_{ch} parameter is free to vary. This analysis has been performed in Phase-I and Phase-II+III, separately, in order to compare the gvc_{ch} results with the one obtained using calibration sources and investigate the variation of detector response over time. With this new strategy, the gvc_{ch} parameter can now be obtained for all phases of Borexino and it can be used in the same data taking period for the CNO-ν measurement. I estimated the expected number of solar neutrinos used for the constraint and performed the fit to extract gvc_{ch} in the ^{7}Be shoulder energy region. Moreover, in contrast to the previous proof-of-principle analysis, the number of early hits chosen for this analysis corresponds to $\lesssim$15, which has been supported by the sensitivity studies and MC simulations. Thanks to the maximised early number of hits up to $\sim$15, not only the direct information from Cherenkov photons up to $\sim$4 hits can be used, but also the information from the position reconstruction bias influencing the shape of signal CID angular distribution up to $\sim$15 hits, can also be exploited. I have performed the optimisation of bins and the sensitivity analysis for the number of hits selection in the CID analysis. Using the gvc_{ch} results as a pull term constraint in the fit, the number of solar neutrino events is obtained in CNO energy region. By estimating the Bayesian posterior distribution and constraining non-CNO solar neutrinos, the exclusion of no-CNO hypothesis is provided at about 5.3σ credible interval for all combined phases using CID only. The final CID result for the CNO-ν rate, using the full dataset of Borexino is $7.2^{+2.8}_{-2.7}$ cpd/100 t. This method has provided an alternative approach with respect to the standard multivariate analysis. I have also contributed by performing the CID fits to extract the final results as well as evaluating the systematic uncertainties. Finally, the CID results has been combined with the standard multivariate fit performed on Phase-III data, to obtain the CNO interaction rate = $6.7^{+1.2}_{-0.8}$ cpd/100 t. The significance against the absence of a CNO signal is now increased to about 8σ.

The above results in Borexino have shown the proof of principle for the CID method. In addition, a combined solar neutrino analysis approach using CID and the multivariate spectral fit has also been demonstrated. The future liquid scintillator experiments can benefit from CID, without any need of specialised hardware or LS mixtures. The sensitivity of CID could be improved by performing a dedicated e^- Cherenkov calibration, in order to reduce the major uncertainties arising from the position reconstruction bias and the Cherenkov group velocity correction.

In Chapter 7, JUNO's sensitivity to ^{7}Be, *pep*, and CNO solar neutrinos has been explored in a visible energy region of (0.45-1.7) MeV. Here, the sensitivity study is performed using MC based pseudo-experiments, where toy datasets are created from the energy PDFs of each neutrino and background components, which are obtained from the MC simulations. The contribution of different types of solar neutrinos in the pseudo-data is fixed to the SSM predictions. The internal background contributions are fixed assuming different radiopurity scenarios of JUNO. I performed the fits of pseudo-data with MC PDFs as a function of the exposure in various radiopurity levels and extracted the relative precision of ^{7}Be, *pep*, and CNO solar neutrino rates in JUNO, which are quoted as the sensitivity results. Thanks to the large statistics of solar neutrinos that will be accumulated by JUNO, it can provide solar neutrino measurements with the best precision so far. In all radiopurity cases, JUNO can provide ^{7}Be-ν measurements with unprecedented statistical precision after a few years of data-taking. Even in the so-called High Background case, the ^{7}Be solar neutrinos can be measured with a relative error of $\approx$1% for long periods of data taking. The statistical precision for ^{7}Be-ν measurements has also been studied in the case of unforeseen levels of some backgrounds and the backgrounds that can be present out-of-equilibrium from their

parent decay chain, which has been observed in other solar neutrino experiments. After about 6 years, the *pep* neutrino measurement in JUNO will also be highly competitive in all background scenarios with respect to the current measurements. It has also been shown that the *pep* neutrino rate can be measured without constraining the rate of CNO solar neutrinos for the first time. For the CNO solar neutrinos, the results are highly influenced by considering different background levels. JUNO has a potential to reduce the CNO neutrino measurement uncertainty to 12%-19% level, after 6 years of data taking and depending upon the background scenario assumed. These results have been obtained using a constraint on *pep*-ν rate, but without applying a constraint on the ^{210}Bi rate in the spectral fit in JUNO. Furthermore, JUNO has the potential to measure individually for the first time the rate of the two main components of the CNO flux, ^{13}N and ^{15}O solar neutrinos, except in the case of worst radiopurity scenario. In this study, a perfect knowledge of detector response as well as of the spectral shape of neutrino and background energy distributions is assumed and the investigation of the corresponding possible systematic errors is beyond the scope of this dissertation.

Chapter 8 reported the CID analysis strategy to evaluate JUNO's sensitivity to measure the ^{7}Be and CNO neutrinos. The two energy regions of interests, (0.6 - 0.75) MeV and (0.8 - 1.4) MeV have been chosen, where the contribution of ^{7}Be and CNO solar neutrino is maximal, respectively. Using a combined JUNO MC and a toy MC approach, the CID angular PDFs are produced for each time sorted hit for the solar neutrino events. In this approach, the relative Cherenkov contribution, taking into account effectively the JUNO LS characteristics and including PMTs' timing properties, is extracted using JUNO MC simulation software. Using this as an input, the CID PDFs are produced using a toy MC framework, that also simulates the physical processes inside JUNO as realistic as possible. I performed the study of Cherenkov properties in JUNO MC and the development of toy MC framework to produce the CID PDFs. This approach includes the directional information of the solar neutrino events, which is lacking in the current version of JUNO MC and its implementation is under progress. I also produced the PDFs of background events using the toy MC simulation. I have also studied the systematic effect of position reconstruction bias on the CID PDFs in JUNO, which has been found to be negligible and more studies with the JUNO MC with directional information are foreseen. Finally, the expected precision of ^{7}Be and CNO neutrino rate in JUNO has been extracted using the CID analysis only, where the pseudo-experiments based on the toy MC developed PDFs are performed. Moreover, the CID results have also been used as a constraint in the spectral fit, assuming six years of exposure and the Medium Background scenario. The obtained preliminary results show the improvement in the sensitivity results in JUNO, especially for the CNO solar neutrinos, which demonstrates the promising potential of the CID method in JUNO. The presented analysis has also led to the understanding of Cherenkov light properties in JUNO. This combined MC analysis has been useful for the development of the whole analysis chain as well as it paved the way for the future analysis with the JUNO MC framework. In future, the Cherenkov calibration studies can also be done by adopting the methods developed in Borexino, in order to estimate the precision of gvc_{ch} that can be achieved in JUNO and to evaluate final sensitivity to the solar neutrinos using CID. In addition, a calibration strategy of a possible electron source is also under study.

Appendix A

Effective group velocity correction of Cherenkov photons for CNO solar neutrino analysis using CID with Borexino

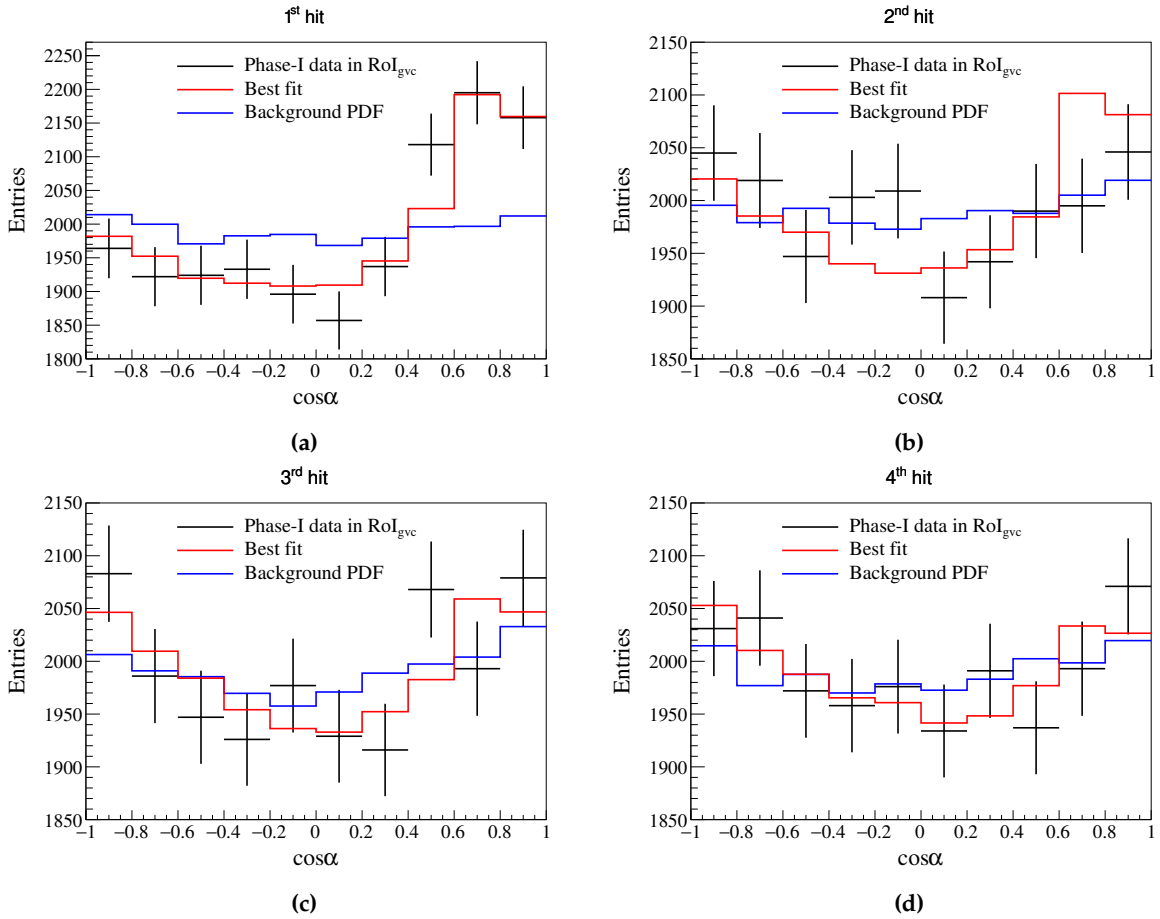

Figure A.1: Illustration of the best fit results in RoI_{gvc} for N^{th} hits ≤ 4, that contain direct Cherenkov information, of events in the Phase-I period. The CID data is shown in black points and the best fit distribution is shown in red. For comparison, the background PDF (blue), scaled to the total number of events, is also shown.

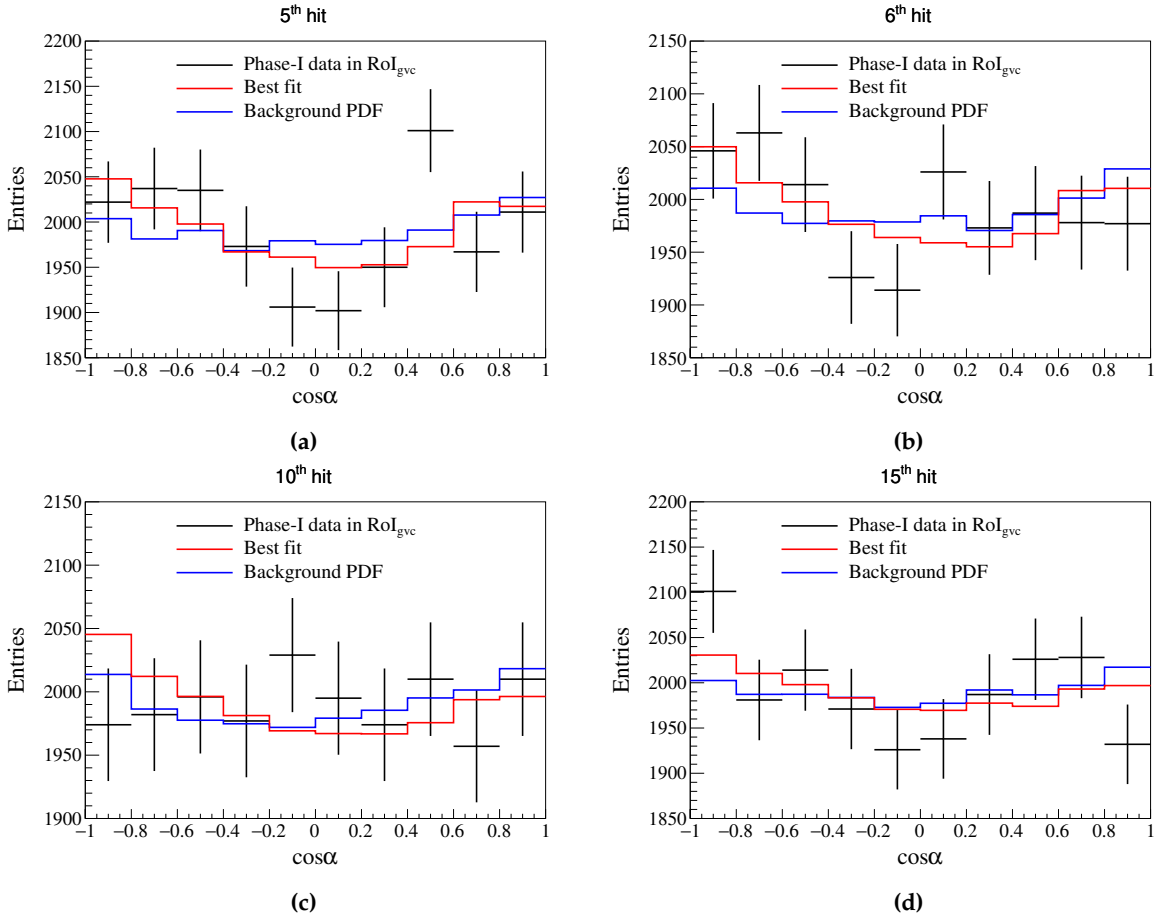

Figure A.2: Illustration of the best fit results in RoI_{gvc} for some individual N^{th} hits > 4, that contain indirect Cherenkov information, of events in the Phase-I period. The CID data is shown in black points and the best fit distribution is shown in red. For comparison, the background PDF (blue), scaled to the total number of events, is also shown. It can also be observed that the indirect Cherenkov effect reduces as a function of N^{th} hit, which has been discussed in Sec. 5.6.2.

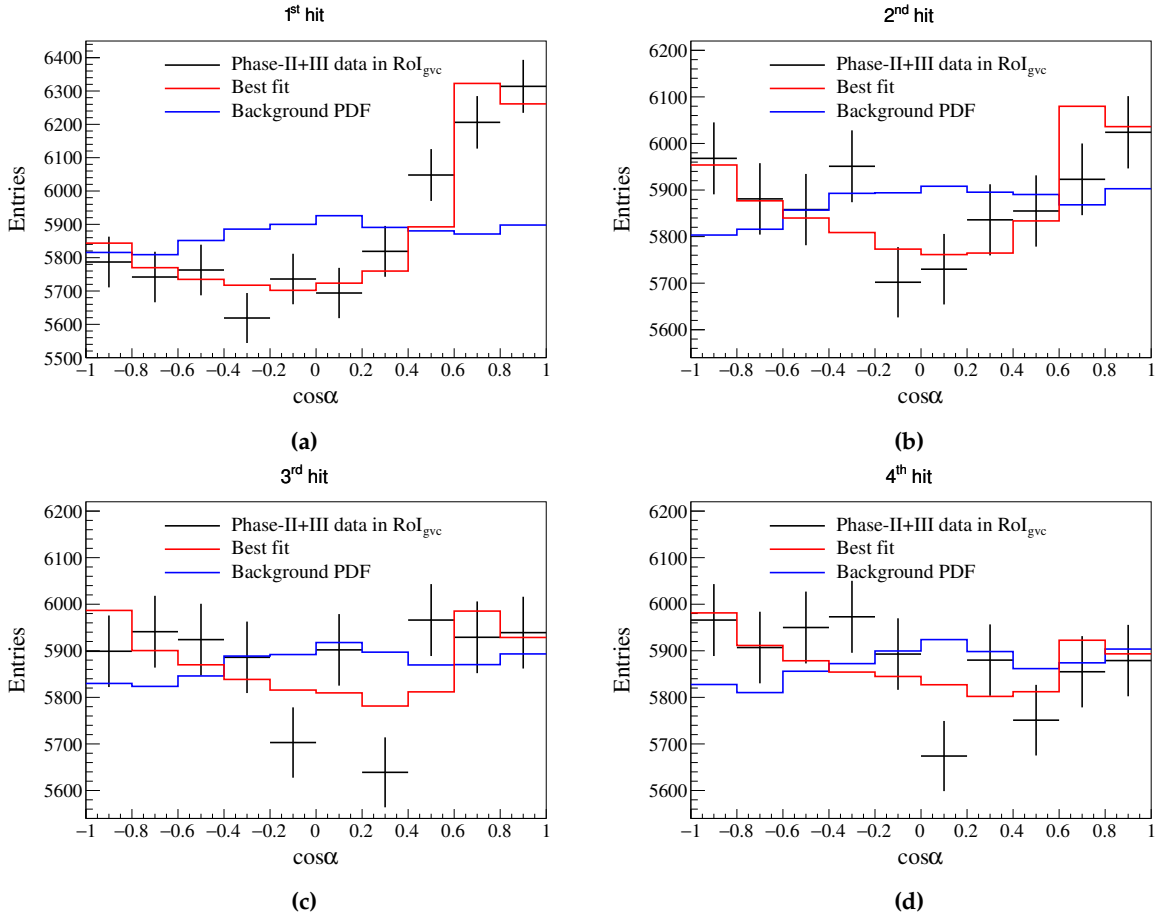

Figure A.3: Illustration of the best fit results in RoI_{gvc} for N^{th} hits ≤ 4, that contain direct Cherenkov information, of events in the Phase-II+III period. The CID data is shown in black points and the best fit distribution is shown in red. For comparison, the background PDF (blue), scaled to the total number of events, is also shown.

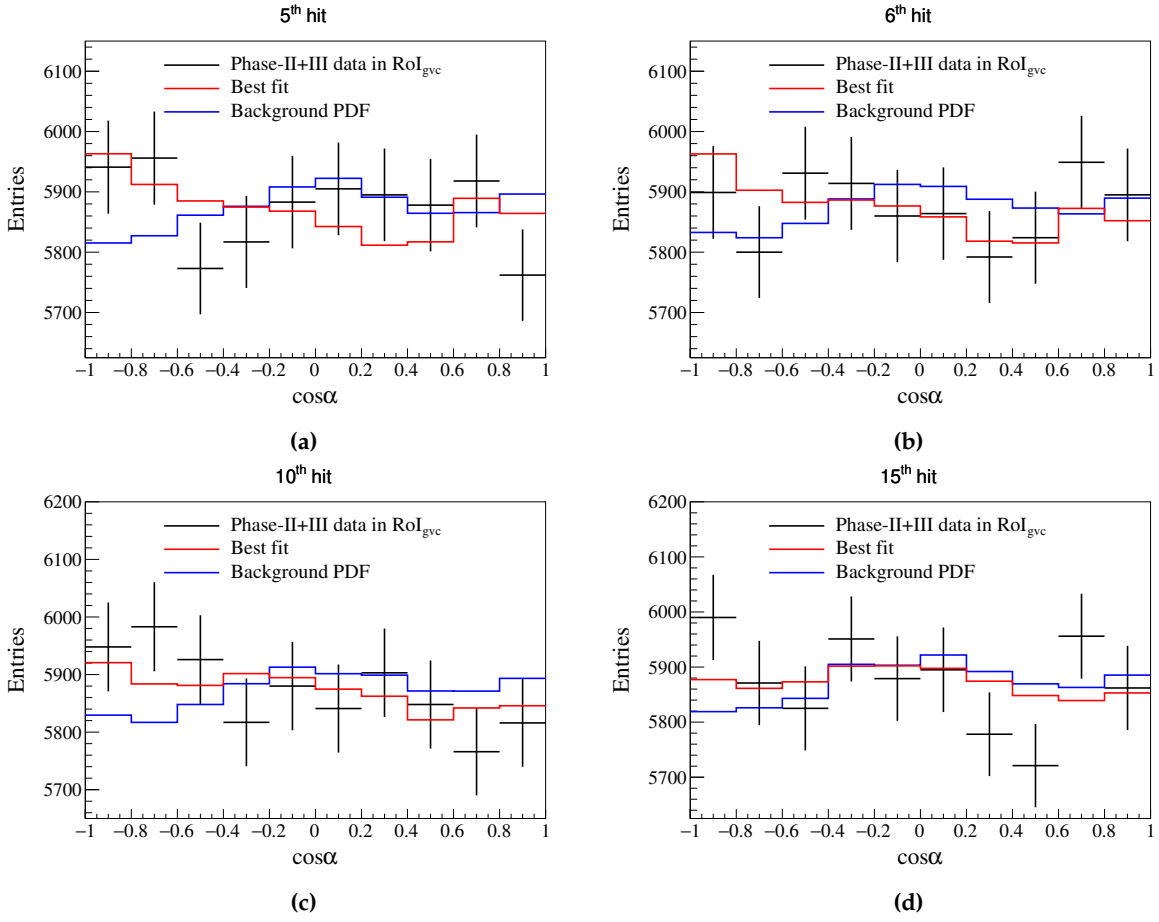

Figure A.4: Illustration of the best fit results in RoI_{gvc} for some individual N^{th} hits > 4, that contain indirect Cherenkov information, of events in the Phase-II+III period. The CID data is shown in black points and the best fit distribution is shown in red. For comparison, the background PDF (blue), scaled to the total number of events, is also shown. It can also be observed that the indirect Cherenkov effect reduces as a function of N^{th} hit, which has been discussed in Sec. 5.6.2.

Appendix B

CNO solar neutrino measurement using CID with Borexino

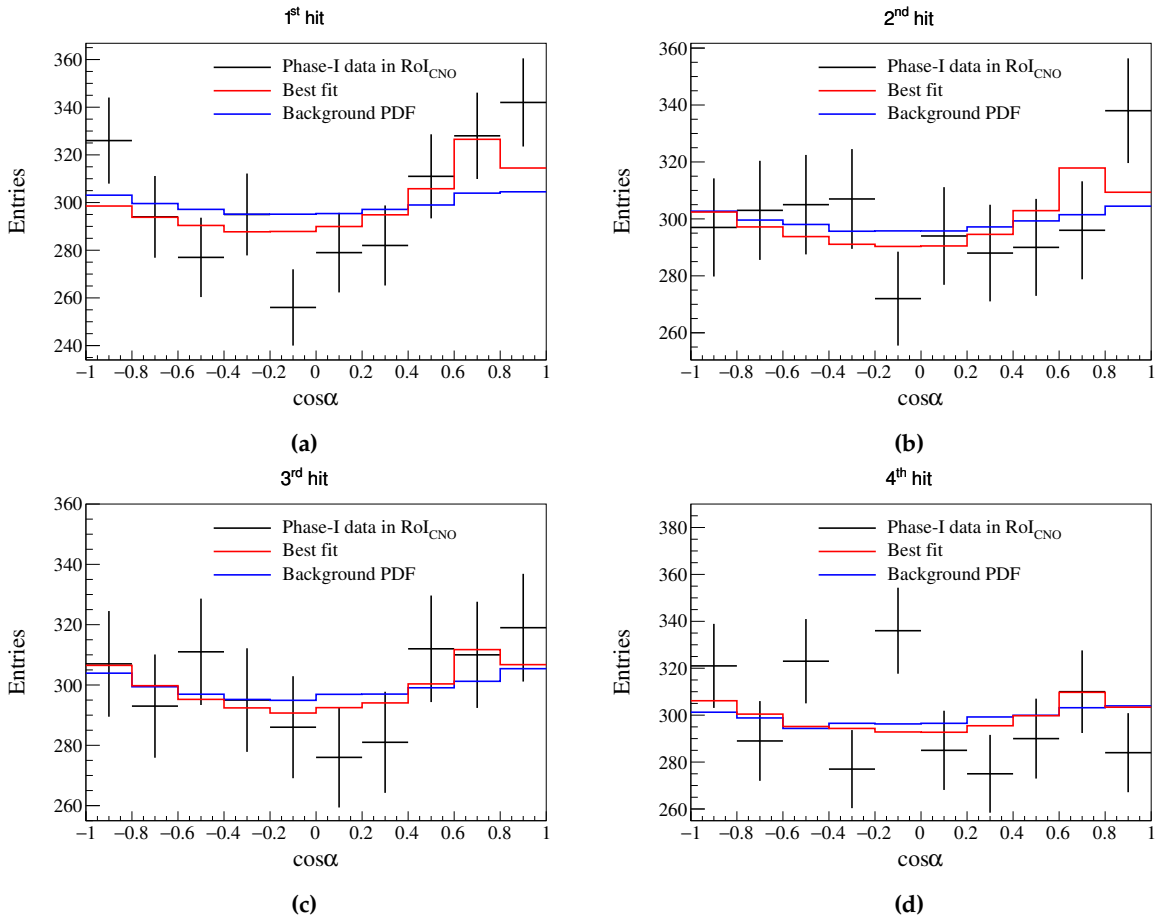

Figure B.1: Illustration of the best fit results in RoI$_{CNO}$ for Nth hits ≤ 4, that contain direct Cherenkov information, of events in the Phase-I period. The CID data is shown in black points and the best fit distribution is shown in red. For comparison, the background PDF (blue), scaled to the total number of events, is also shown.

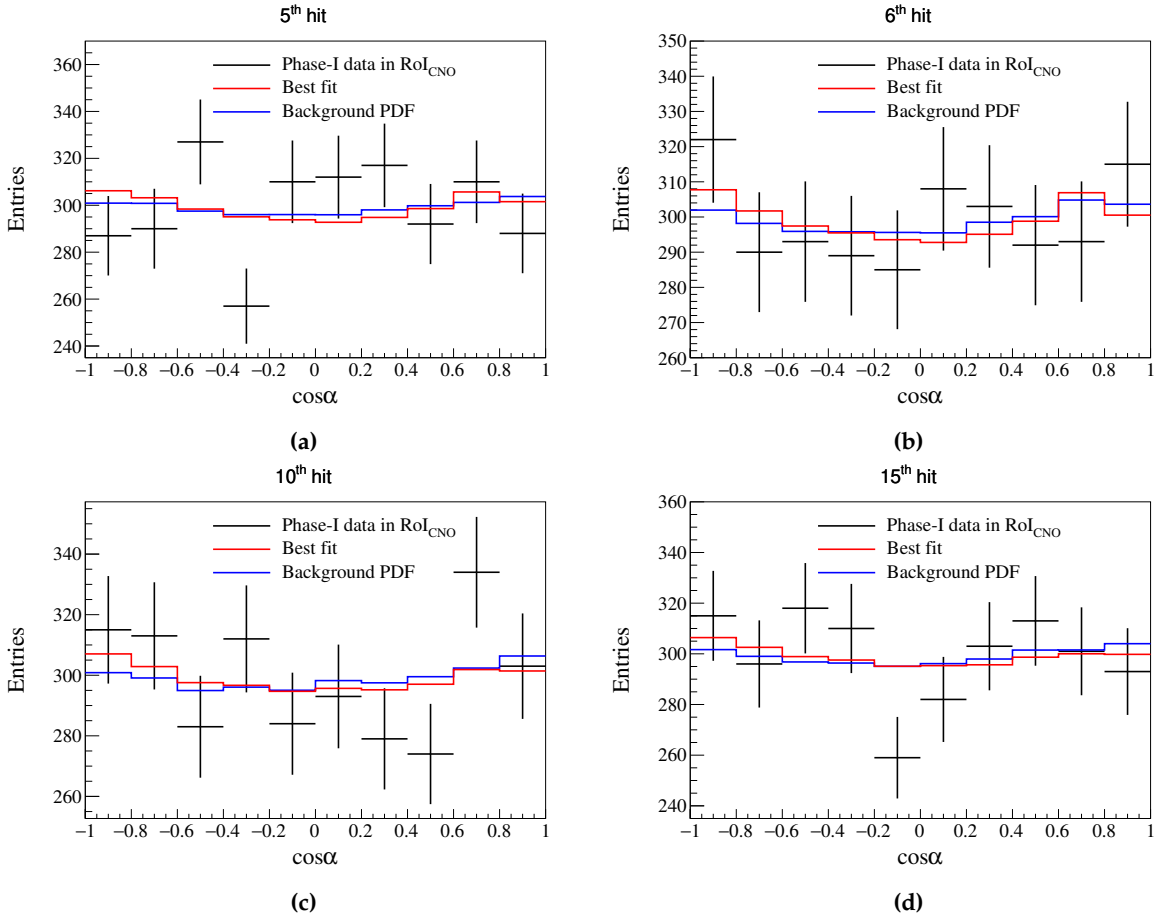

Figure B.2: Illustration of the best fit results in RoI_{CNO} for some individual N^{th} hits > 4, that contain indirect Cherenkov information, of events in the Phase-I period. The CID data is shown in black points and the best fit distribution is shown in red. For comparison, the background PDF (blue), scaled to the total number of events, is also shown. It can also be observed that the indirect Cherenkov effect reduces as a function of N^{th} hit, which has been discussed in Sec. 5.6.2.

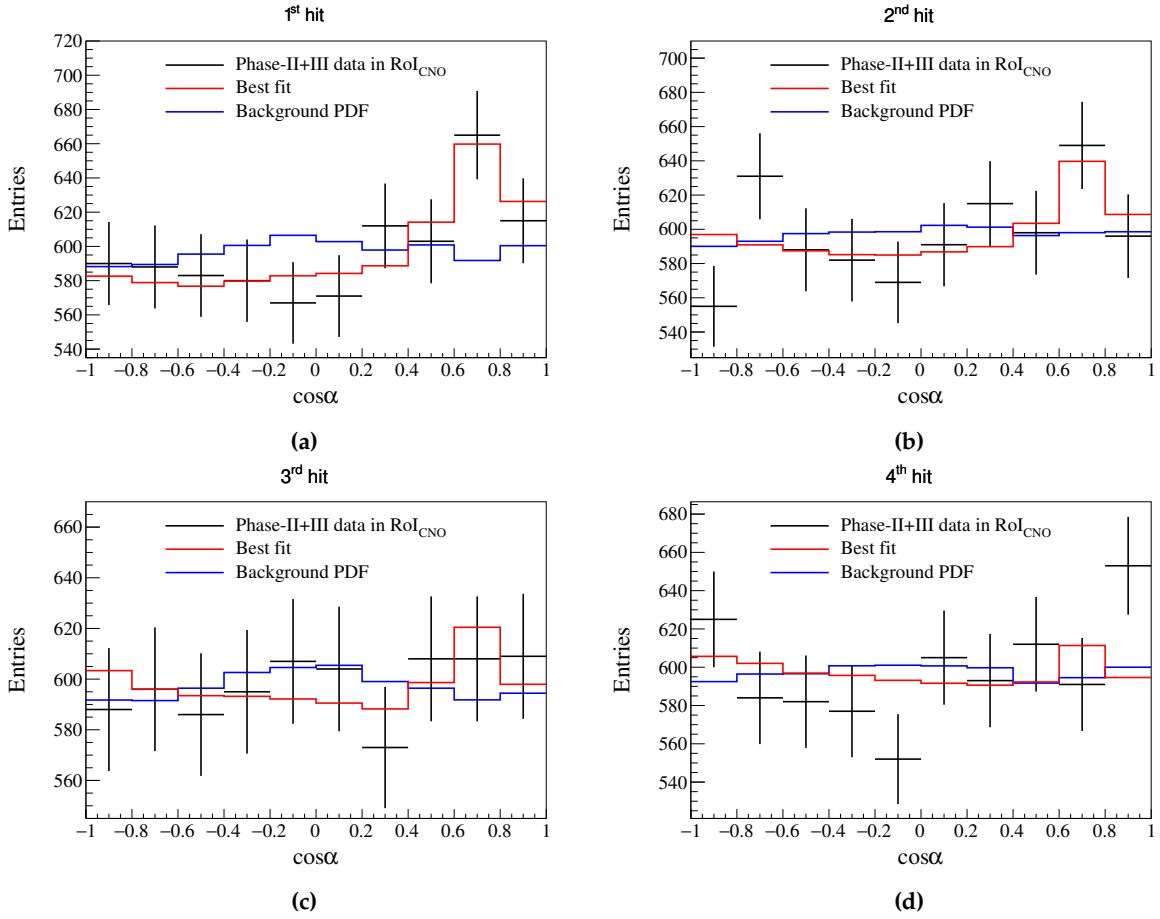

Figure B.3: Illustration of the best fit results in RoI_{CNO} for N^{th} hits ≤ 4, that contain direct Cherenkov information, of events in the Phase-II+III period. The CID data is shown in black points and the best fit distribution is shown in red. For comparison, the background PDF (blue), scaled to the total number of events, is also shown.

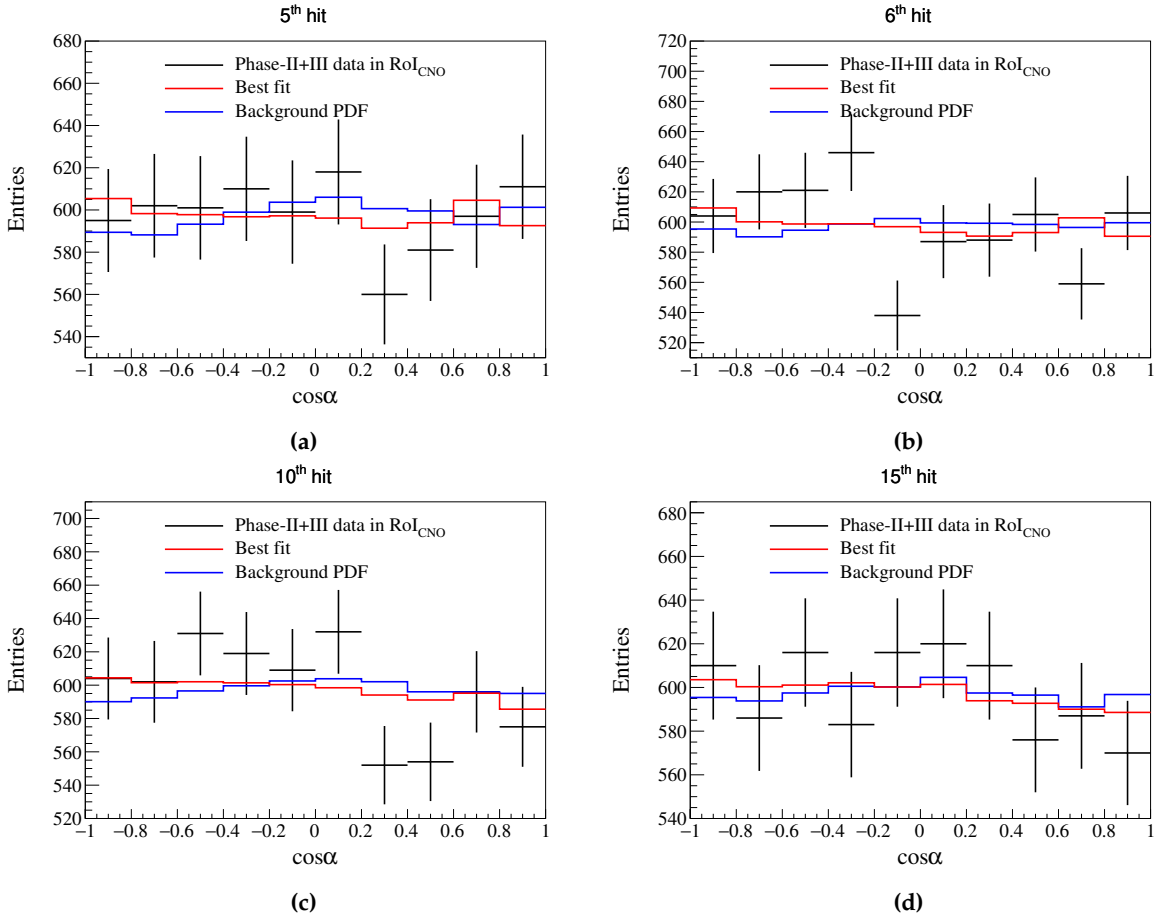

Figure B.4: Illustration of the best fit results in RoI_{CNO} for some individual N^{th} hits > 4, that contain indirect Cherenkov information, of events in the Phase-II+III period. The CID data is shown in black points and the best fit distribution is shown in red. For comparison, the background PDF (blue), scaled to the total number of events, is also shown. It can also be observed that the indirect Cherenkov effect reduces as a function of N^{th} hit, which has been discussed in Sec. 5.6.2.

Appendix C

PMT hit time correction for CNO solar neutrino measurement using CID in Borexino

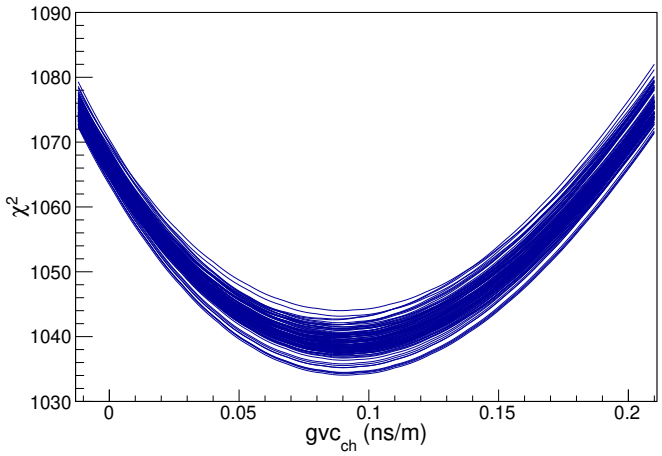

Figure C.1: The 100 χ^2 profiles as a function of gvc_{ch}, where each χ^2 profile is obtained by propagating the PMT hit correction uncertainty discussed in Sec.5.6.3 through Gaussian smearing.

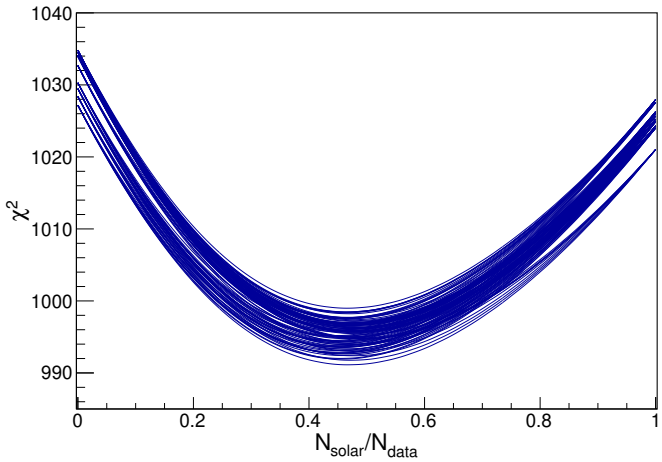

Figure C.2: The 100 χ^2 profiles as a function of N_{solar}/N_{data} ratio, where each χ^2 profile is obtained by propagating the PMT hit correction uncertainty discussed in Sec.5.6.4 through Gaussian smearing.

Declaration of Authorship / Eidesstattliche Erklärung

I, Apeksha Singhal, declare that this thesis and the work presented in it are my own and has been generated by me as the result of my own original research. /
Ich, Apeksha Singhal, erklärt hiermit, dass diese Dissertation und die darin dargelegten Inhalte die eigenen sind und selbstständig, als Ergebnis der eigenen originären Forschung, generiert wurden.

I do solemnely swear that/ *Hiermit erkläre ich an Eides statt:*

- This work was done wholly or mainly while in candidature for the doctoral degree at this faculty and university / *Diese Arbeit wurde vollständig oder größtenteils in der Phase als Doktorand dieser Fakultät und Universität angefertigt*;
- Where any part of this thesis has previously been submitted for a degree or any other qualification at this university or any other institution, this has been clearly stated / *Sofern irgendein Bestandteil dieser Dissertation zuvor für einen akademischen Abschluss oder eine andere Qualifikation an dieser oder einer anderen Institution verwendet wurde, wurde dies klar angezeigt*;
- Where I have consulted the published work of others or myself, this is always clearly attributed / *Wenn immer andere eigene- oder Veröffentlichungen Dritter herangezogen wurden, wurden diese klar benannt*;
- Where I have quoted from the work of others or myself, the source is always given. This thesis is entirely my own work, with the exception of such quotations / *Wenn aus anderen eigenen- oder Veröffentlichungen Dritter zitiert wurde, wurde stets die Quelle hierfür angegeben. Diese Dissertation ist vollständig meine eigene Arbeit, mit der Ausnahme solcher Zitate*;
- I have acknowledged all major sources of assistance / *Alle wesentlichen Quellen von Unterstützung wurden benannt*;
- Where the thesis is based on work done by myself jointly with others, I have made clear exactly what was done by others and what I have contributed myself / *Wenn immer ein Teil dieser Dissertation auf der Zusammenarbeit mit anderen basiert, wurde von mir klar gekennzeichnet, was von anderen und was von mir selbst erarbeitet wurde*;
- Parts of this work have been published before as *Ein Teil oder Teile dieser Arbeit wurden zuvor veröffentlicht und zwar in* [3], [4], [5], [269], [6], [270], [7], [271], and [272].

Date / *Datum*:
Signature / *Unterschrift*:

Acknowledgements

The journey until the last stage of my PhD, the thesis writing, has been challenging and rewarding. The work described in this thesis would not have been possible without the support, encouragement, and guidance from many people. I am indebted to everyone, who have contributed to my academic and personal growth during this journey.

First and foremost, I would like to thank my supervisor and mentor, Livia Ludhova, under whose guidance I have completed my master as well as doctoral thesis. She has been a source of inspiration, not only for the research and analysis skills, but also being a energetic personality with a love for travel. Her research excellence has allowed to contribute significantly in the two amazing experiments, Borexino and JUNO. Thanks to her support, I have been involved in various meetings of the collaboration as well as participating in conferences and summer school, some of which were offline in the last year of the PhD only due to COVID. These gave me the opportunity to travel around the world and have the possibility to acquire the subject knowledge and meet physicists online and offline from all over the world. Thanks to her mentorship and support to take extra courses, I have enhanced my skills in presentation and writing scientific articles. Also, thanks for reading this thesis carefully and providing comments.

Certainly, this acknowledgement is incomplete without expressing gratitude to the people with whom I have worked and collaborated with. I'd especially like to thank Johann, with whom I have worked on the Borexino Directionality analyses, acquiring a significant chunk of this thesis. From him, I have learnt not only the basics of CID method, but also two unforgettable Italian words (Molto bene!) and statistics through Wikipedia links and Skype discussions. I have also worked on directionality and Borexino CNO analysis with Sindhujha. I would like to thank her for her support and helping me with my first ever business trip as well as provided details about the visa administration in Aachen. Due to her, I have also got to try and know some good restaurants for vegetarians in Aachen. A special thanks to my colleague and friend, Luca, with whom I have worked on all the thesis topics together in both direct and indirect ways. I will always cherish the times of joint presentations, discussions including the ones while travelling to and from office, shared moments (also during stressful periods), providing constructive feedback and always maintaining positive vibes. I will never forget the good times that I have also had with the ex-Borexinoers in our group: Antonia, Ömer, Giulio, Mariia, and Zara.

I would also like to thank Anita and Marco, with whom I have worked on JUNO solars during a part of my PhD time in the group. Even though we didn't work together, I would like to acknowledge the time spent and shared our experiences with other JUNO colleagues, Mariam, Nikhil, Cornelius, Yury, Kaku, Cristobal, and Ricky, during the lunch times as well as sometimes outside the work. I would like to thank all my colleagues in the group, who were always ready to help me, whenever I needed. I feel very lucky to have worked in a such a big and international group.

My next thanks goes to Barbara for all the support during Borexino and JUNO analyses as well as the organisation of JUNO CID meetings in Milano. I feel grateful not only to have also worked with Davide in achieving Borexino and JUNO solar results as well as with Claudio for the crosscheck of JUNO CID analysis, but also to have helpful and fun collaboration with them. Thanks Alessandra as well as the CNAF people who provided me the resources to work on all the analyses in this thesis in a productive

manner. I would also like to thank Xuefeng for discussions that we had regarding the ^{210}Bi constraint model. Thanks to all Borexino and JUNO collaboration members, as the experiment and all the analyses are the result of the collaborative efforts over the years.

Thanks Ashish for the endless amount of love and support and for everything so far. I would like to thank all my friends, whom I know since my previous education period as well as the ones whom I met during my PhD, for providing support and a good social life outside the work. Finally, I would like to acknowledge the contribution from my family. I would like to thank my parents, Beenu and Rajesh Singhal, for always believing in me, for always making an effort that I got the best possible education as well as that I have fulfill my dreams and become a strong and independent person. Thanks to my siblings, Divyanshi and Aviral Singhal, for always providing me with the mental support and for being best siblings I could have wished for.

Bibliography

[1] M. Agostini *et al.*, "Comprehensive measurement of *pp*-chain solar neutrinos," *Nature*, vol. 562, pp. 505–510, 2018.

[2] M. Agostini *et al.*, "Experimental evidence of neutrinos produced in the CNO fusion cycle in the Sun," *Nature*, vol. 587, pp. 577–582, 2020.

[3] S. Appel *et al.*, "Improved Measurement of Solar Neutrinos from the Carbon-Nitrogen-Oxygen Cycle by Borexino and Its Implications for the Standard Solar Model," *Phys. Rev. Lett.*, vol. 129, p. 252701, 2022.

[4] M. Agostini *et al.*, "First Directional Measurement of Sub-MeV Solar Neutrinos with Borexino," *Phys. Rev. Lett.*, vol. 128, p. 091803, 2022.

[5] M. Agostini *et al.*, "Correlated and integrated directionality for sub-MeV solar neutrinos in Borexino," *Phys. Rev. D*, vol. 105, p. 052002, 2022.

[6] D. Basilico *et al.*, "Final results of Borexino on CNO solar neutrinos," *Phys. Rev. D*, vol. 108, p. 102005, 2023.

[7] A. Abusleme *et al.*, "JUNO sensitivity to ^{7}Be, pep, and CNO solar neutrinos," *Journal of Cosmology and Astroparticle Physics*, vol. 2023, no. 10, p. 022, 2023.

[8] J. Chadwick, "Intensitätsverteilung im magnetischen Spectrum der β-Strahlen von radium B + C," *Verhandl. Dtsc. Phys. Ges.*, vol. 16, p. 383, 1914.

[9] C. D. Ellis and W. A. Wooster, "The average energy of disintegration of radium E," *Proc. Roy. Soc. Lond. A*, vol. 117, no. 776, pp. 109–123, 1927.

[10] L. Meitner and W. Orthmann, "Über eine absolute Bestimmung der Energie der primären β-Strahlen von Radium E," *Zeitschrift für Physik*, vol. 60, pp. 143–155, 1930.

[11] W. Pauli, "On the Earlier and more recent history of the neutrino," *Camb. Monogr. Part. Phys. Nucl. Phys. Cosmol.*, vol. 14, pp. 1–22, 2000.

[12] J. Chadwick, "Possible Existence of a Neutron," *Nature*, vol. 129, p. 312, 1932.

[13] E. Fermi, "An attempt of a theory of beta radiation. 1.," *Zeitschrift für Physik*, vol. 88, pp. 161–177, 1934.

[14] H. Bethe and R. Peierls, "The 'neutrino'," *Nature*, vol. 133, p. 532, 1934.

[15] B. Pontecorvo, "Inverse beta process," *Camb. Monogr. Part. Phys. Nucl. Phys. Cosmol.*, vol. 1, pp. 25–31, 1991.

[16] J. C. Street and E. C. Stevenson, "New Evidence for the Existence of a Particle of Mass Intermediate Between the Proton and Electron," *Phys. Rev.*, vol. 52, pp. 1003–1004, 1937.

[17] S. H. Neddermeyer and C. D. Anderson, "Note on the Nature of Cosmic-Ray Particles," *Phys. Rev.*, vol. 51, pp. 884–886, 1937.

[18] B. Pontecorvo, "Nuclear Capture of Mesons and the Meson Decay," *Phys. Rev.*, vol. 72, pp. 246–247, 1947.

[19] G. W. Rodeback and J. S. Allen, "Neutrino Recoils Following the Capture of Orbital Electrons in A^{37}," *Phys. Rev.*, vol. 86, pp. 446–450, 1952.

[20] A. H. Snell and F. Pleasonton, "Spectrometry of Recoils from Neutrino Emission in Argon-37," *Phys. Rev.*, vol. 97, pp. 246–248, 1955.

[21] A. Abbott, "The singing neutrino Nobel laureate who nearly bombed Nevada," *Nature*, vol. 593, pp. 334–335, 2021.

[22] F. Reines and C. L. Cowan, "Detection of the Free Neutrino," *Phys. Rev.*, vol. 92, pp. 830–831, 1953.

[23] C. L. Cowan *et al.*, "Detection of the Free Neutrino: a Confirmation," *Science*, vol. 124, no. 3212, pp. 103–104, 1956.

[24] E. J. Konopinski and H. M. Mahmoud, "The Universal Fermi Interaction," *Phys. Rev.*, vol. 92, pp. 1045–1049, 1953.

[25] R. Davis, "Attempt to Detect the Antineutrinos from a Nuclear Reactor by the $Cl^{37}(\overline{\nu}, e^{-})A^{37}$ Reaction," *Phys. Rev.*, vol. 97, pp. 766–769, 1955.

[26] R. P. Feynman and M. Gell-Mann, "Theory of the Fermi Interaction," *Phys. Rev.*, vol. 109, pp. 193–198, 1958.

[27] E. C. G. Sudarshan and R. E. Marshak, "Chirality Invariance and the Universal Fermi Interaction," *Phys. Rev.*, vol. 109, pp. 1860–1862, 1958.

[28] M. Goldhaber, L. Grodzins, and A. W. Sunyar, "Helicity of Neutrinos," *Phys. Rev.*, vol. 109, pp. 1015–1017, 1958.

[29] G. Danby *et al.*, "Observation of High-Energy Neutrino Reactions and the Existence of Two Kinds of Neutrinos," *Phys. Rev. Lett.*, vol. 9, pp. 36–44, 1962.

[30] B. Pontecorvo, "Electron and Muon Neutrinos," *Zh. Eksp. Teor. Fiz.*, vol. 37, pp. 1751–1757, 1959.

[31] J. Bienlein *et al.*, "Spark chamber study of high-energy neutrino interactions," *Physics Letters*, vol. 13, no. 1, pp. 80–86, 1964.

[32] M. L. Perl and other, "Evidence for Anomalous Lepton Production in $e^{+} - e^{-}$ Annihilation," *Phys. Rev. Lett.*, vol. 35, pp. 1489–1492, 1975.

[33] S. M. Bilenky, "Neutrino," *Physics of Particles and Nuclei*, vol. 44, pp. 1–46, 2013.

[34] K. Kodama *et al.*, "Observation of tau neutrino interactions," *Physics Letters B*, vol. 504, no. 3, pp. 218–224, 2001.

[35] S. Schael *et al.*, "Precision electroweak measurements on the Z resonance," *Phys. Rept.*, vol. 427, pp. 257–454, 2006.

[36] P. Zyla *et al.*, "Review of Particle Physics," *PTEP*, vol. 2020, no. 8, p. 083C01, 2020.

[37] Y. Fukuda *et al.*, "Evidence for Oscillation of Atmospheric Neutrinos," *Phys. Rev. Lett.*, vol. 81, pp. 1562–1567, 1998.

[38] Q. R. Ahmad *et al.*, "Direct evidence for neutrino flavor transformation from neutral current interactions in the Sudbury Neutrino Observatory," *Phys. Rev. Lett.*, vol. 89, p. 011301, 2002.

[39] B. Pontecorvo, "Inverse beta processes and nonconservation of lepton charge," *Zh. Eksp. Teor. Fiz.*, vol. 34, p. 247, 1957.

[40] Z. Maki, M. Nakagawa, and S. Sakata, "Remarks on the unified model of elementary particles," *Prog. Theor. Phys.*, vol. 28, pp. 870–880, 1962.

[41] N. Foppiani, *Neutrinos Within the Standard Model*, pp. 7–22. Cham: Springer Nature Switzerland, 2023.

[42] S. Bilenky and B. Pontecorvo, "Lepton mixing and neutrino oscillations," *Physics Reports*, vol. 41, no. 4, pp. 225–261, 1978.

[43] I. Esteban *et al.*, "Nufit 5.3 (2024)." `http://www.nu-fit.org/?q=node/278`.

[44] L. Wolfenstein, "Neutrino oscillations in matter," *Phys. Rev. D*, vol. 17, pp. 2369–2374, 1978.

[45] S. P. Mikheyev and A. Y. Smirnov, "Resonance Amplification of Oscillations in Matter and Spectroscopy of Solar Neutrinos," *Sov. J. Nucl. Phys.*, vol. 42, pp. 913–917, 1985.

[46] J. N. Bahcall and C. Peña-Garay, "Solar models and solar neutrino oscillations," *New Journal of Physics*, vol. 6, no. 1, p. 63, 2004.

[47] G. L. Fogli, E. Lisi, A. Marrone, D. Montanino, and A. Palazzo, "Getting the most from the statistical analysis of solar neutrino oscillations," *Phys. Rev. D*, vol. 66, p. 053010, 2002.

[48] S. Kumaran *et al.*, "Borexino Results on Neutrinos from the Sun and Earth," *Universe*, vol. 7, no. 7, 2021.

[49] V. I. Kopeikin, "Flux and Spectrum of Reactor Antineutrinos," *Physics of Atomic Nuclei*, vol. 75, no. 2, p. 143–152, 2012.

[50] F. An *et al.*, "Neutrino physics with JUNO," *J. Phys. G: Nucl. Part. Phys.*, vol. 43, no. 3, p. 030401, 2016.

[51] K. Eguchi *et al.*, "First Results from KamLAND: Evidence for Reactor Antineutrino Disappearance," *Phys. Rev. Lett.*, vol. 90, p. 021802, 2003.

[52] A. Gando *et al.*, "Reactor on-off antineutrino measurement with KamLAND," *Phys. Rev. D*, vol. 88, p. 033001, 2013.

[53] F. P. An *et al.*, "Observation of Electron-Antineutrino Disappearance at Daya Bay," *Phys. Rev. Lett.*, vol. 108, p. 171803, 2012.

[54] J. K. Ahn *et al.*, "Observation of Reactor Electron Antineutrinos Disappearance in the RENO Experiment," *Phys. Rev. Lett.*, vol. 108, p. 191802, 2012.

[55] Y. Abe *et al.*, "Indication of Reactor $\overline{\nu}_e$ Disappearance in the Double Chooz Experiment," *Phys. Rev. Lett.*, vol. 108, p. 131801, 2012.

[56] T. A. Mueller *et al.*, "Improved predictions of reactor antineutrino spectra," *Phys. Rev. C*, vol. 83, p. 054615, 2011.

[57] G. Mention *et al.*, "Reactor antineutrino anomaly," *Phys. Rev. D*, vol. 83, p. 073006, 2011.

[58] D. Adey *et al.*, "Improved measurement of the reactor antineutrino flux at Daya Bay," *Phys. Rev. D*, vol. 100, p. 052004, 2019.

[59] S. G. Yoon *et al.*, "Measurement of reactor antineutrino flux and spectrum at RENO," *Phys. Rev. D*, vol. 104, p. L111301, 2021.

[60] H. de Kerret *et al.*, "Double Chooz θ_{13} measurement via total neutron capture detection," *Nature Phys.*, vol. 16, no. 5, pp. 558–564, 2020.

[61] F. P. An *et al.*, "Evolution of the Reactor Antineutrino Flux and Spectrum at Daya Bay," *Phys. Rev. Lett.*, vol. 118, p. 251801, 2017.

[62] F. P. An *et al.*, "Joint Determination of Reactor Antineutrino Spectra from ^{235}U and ^{239}Pu Fission by Daya Bay and PROSPECT," *Phys. Rev. Lett.*, vol. 128, p. 081801, 2022.

[63] J. H. Choi *et al.*, "Observation of Energy and Baseline Dependent Reactor Antineutrino Disappearance in the RENO Experiment," *Phys. Rev. Lett.*, vol. 116, p. 211801, 2016.

[64] C. Zhang, X. Qian, and M. Fallot, "Reactor antineutrino flux and anomaly," *Progress in Particle and Nuclear Physics*, vol. 136, p. 104106, 2024.

[65] F. P. An *et al.*, "Improved Measurement of the Evolution of the Reactor Antineutrino Flux and Spectrum at Daya Bay," *Phys. Rev. Lett.*, vol. 130, no. 21, p. 211801, 2023.

[66] A. Abusleme *et al.*, "TAO Conceptual Design Report: A Precision Measurement of the Reactor Antineutrino Spectrum with Sub-percent Energy Resolution," 2020. arxiv:2005.08745.

[67] C. Achar *et al.*, "Detection of muons produced by cosmic ray neutrinos deep underground," *Physics Letters*, vol. 18, no. 2, pp. 196–199, 1965.

[68] F. Reines *et al.*, "Evidence for high-energy cosmic-ray neutrino interactions," *Phys. Rev. Lett.*, vol. 15, no. 9, p. 429 – 433, 1965.

[69] Z. Li *et al.*, "Measurement of the tau neutrino cross section in atmospheric neutrino oscillations with Super-Kamiokande," *Phys. Rev. D*, vol. 98, p. 052006, 2018.

[70] M. G. Aartsen *et al.*, "Measurement of atmospheric tau neutrino appearance with icecube deepcore," *Phys. Rev. D*, vol. 99, p. 032007, 2019.

[71] A. Albert *et al.*, "Measuring the atmospheric neutrino oscillation parameters and constraining the 3+1 neutrino model with ten years of ANTARES data," *Journal of High Energy Physics*, vol. 06, p. 113, 2019.

[72] R. Abbasi and others., "Measurement of atmospheric neutrino mixing with improved IceCube DeepCore calibration and data processing," *Phys. Rev. D*, vol. 108, p. 012014, 2023.

[73] K. Abe *et al.*, "Measurements of neutrino oscillation parameters from the T2K experiment using 3.6×10^{21} protons on target," *Eur. Phys. J. C*, vol. 83, no. 9, p. 782, 2023.

[74] M. A. Acero *et al.*, "Improved measurement of neutrino oscillation parameters by the NOvA experiment," *Phys. Rev. D*, vol. 106, p. 032004, 2022.

[75] P. Adamson *et al.*, "Combined Analysis of $\nu_\mu \to \nu_e$ Appearance in MINOS Using Accelerator and Atmospheric Neutrinos," *Phys. Rev. Lett.*, vol. 112, p. 191801, 2014.

[76] B. Abi *et al.*, "Volume I. Introduction to DUNE," *Journal of Instrumentation*, vol. 15, no. 08, p. T08008, 2020.

[77] K. Abe *et al.*, "Letter of Intent: The Hyper-Kamiokande Experiment — Detector Design and Physics Potential —," 2011. arXiv:1109.3262.

[78] M. Agostini *et al.*, "Comprehensive geoneutrino analysis with Borexino," *Phys. Rev. D*, vol. 101, p. 012009, 2020.

[79] S. Abe *et al.*, "Abundances of Uranium and Thorium elements in Earth estimated by geoneutrino spectroscopy," *Geophysical Research Letters*, vol. 49, no. 16, 2022.

[80] V. Albanese *et al.*, "The SNO+ experiment," *Journal of Instrumentation*, vol. 16, no. 08, p. P08059, 2021.

[81] J. F. Beacom *et al.*, "Physics prospects of the Jinping neutrino experiment," *Chinese Physics C*, vol. 41, no. 2, p. 023002, 2017.

[82] A. Abusleme *et al.*, "Real-time monitoring for the next core-collapse supernova in JUNO," *Journal of Cosmology and Astroparticle Physics*, vol. 2024, no. 01, p. 057, 2024.

[83] A. Mirizzi *et al.*, "Supernova Neutrinos: Production, Oscillations and Detection," *Riv. Nuovo Cim.*, vol. 39, no. 1-2, pp. 1–112, 2016.

[84] K. Hirata *et al.*, "Observation of a Neutrino Burst from the Supernova SN 1987a," *Phys. Rev. Lett.*, vol. 58, pp. 1490–1493, 1987.

[85] R. M. Bionta *et al.*, "Observation of a neutrino burst in coincidence with supernova 1987A in the Large Magellanic Cloud," *Phys. Rev. Lett.*, vol. 58, pp. 1494–1496, 1987.

[86] E. N. Alekseev *et al.*, "Detection of the neutrino signal from sn1987a in the lmc using the inr baksan underground scintillation telescope," *Phys. Lett.*, vol. B205, pp. 209–214, 1988.

[87] D. N. Schramm and J. W. Truran, "New physics from supernova 1987A," *Physics Reports*, vol. 189, no. 2, pp. 89–126, 1990.

[88] S. A. Kharusi *et al.*, "SNEWS 2.0: a next-generation supernova early warning system for multi-messenger astronomy," *New Journal of Physics*, vol. 23, no. 3, p. 031201, 2021.

[89] K. Abe *et al.*, "Diffuse supernova neutrino background search at Super-Kamiokande," *Phys. Rev. D*, vol. 104, p. 122002, 2021.

[90] S. Abe *et al.*, "Limits on Astrophysical Antineutrinos with the KamLAND Experiment," *The Astrophysical Journal*, vol. 925, no. 1, p. 14, 2022.

[91] M. Agostini *et al.*, "Search for low-energy neutrinos from astrophysical sources with Borexino," *Astroparticle Physics*, vol. 125, p. 102509, 2021.

[92] M. Harada *et al.*, "Search for Astrophysical Electron Antineutrinos in Super-Kamiokande with 0.01% Gadolinium-loaded Water," *The Astrophysical Journal Letters*, vol. 951, no. 2, p. L27, 2023.

[93] A. Abusleme *et al.*, "Prospects for detecting the diffuse supernova neutrino background with JUNO," *Journal of Cosmology and Astroparticle Physics*, vol. 2022, no. 10, p. 033, 2022.

[94] W. C. Haxton, R. G. Hamish Robertson, and A. M. Serenelli, "Solar neutrinos: Status and prospects," *Annual Review of Astronomy and Astrophysics*, vol. 51, pp. 21–61, 2013.

[95] S. K. Agarwalla *et al.*, "Constraints on flavor-diagonal non-standard neutrino interactions from Borexino Phase-II," *Journal of High Energy Physics*, vol. 02, p. 038, 2020.

[96] J. A. Formaggio, A. L. C. de Gouvêa, and R. H. Robertson, "Direct measurements of neutrino mass," *Physics Reports*, vol. 914, pp. 1–54, 2021.

[97] A. Ghosh, T. Thakore, and S. Choubey, "Determining the Neutrino Mass Hierarchy with INO, T2K, NOvA and Reactor Experiments," *Journal of High Energy Physics*, vol. 04, p. 009, 2013.

[98] M. G. Aartsen *et al.*, "PINGU: a vision for neutrino and particle physics at the South Pole," *J. Phys. G: Nucl. Part. Phys.*, vol. 44, no. 5, p. 054006, 2017.

[99] S. Adrián-Martínez *et al.*, "Letter of intent for KM3NeT 2.0," *J. Phys. G: Nucl. Part. Phys.*, vol. 43, no. 8, p. 084001, 2016.

[100] A. Abusleme *et al.*, "JUNO physics and detector," *Progress in Particle and Nuclear Physics*, vol. 123, p. 103927, 2022.

[101] C. Kraus *et al.*, "Final results from phase II of the Mainz neutrino mass search in tritium beta decay," *Eur. Phys. J. C*, vol. 40, pp. 447–468, 2005.

[102] V. N. Aseev *et al.*, "Upper limit on the electron antineutrino mass from the Troitsk experiment," *Phys. Rev. D*, vol. 84, p. 112003, 2011.

[103] M. Aker *et al.*, "Direct neutrino-mass measurement with sub-electronvolt sensitivity," *Nature Phys.*, vol. 18, no. 2, pp. 160–166, 2022.

[104] A. A. Esfahani *et al.*, "Determining the neutrino mass with cyclotron radiation emission spectroscopy - Project 8," *J. Phys. G*, vol. 44, no. 5, p. 054004, 2017.

[105] L. Gastaldo *et al.*, "The Electron Capture ^{163}Ho Experiment ECHo: an overview," *J. Low Temp. Phys.*, vol. 176, no. 5-6, pp. 876–884, 2014.

[106] M. Faverzani *et al.*, "Status of the HOLMES Experiment," *J. Low Temp. Phys.*, vol. 199, no. 3-4, pp. 1098–1106, 2020.

[107] M. J. Dolinski, A. W. P. Poon, and W. Rodejohann, "Neutrinoless Double-Beta Decay: Status and Prospects," *Ann. Rev. Nucl. Part. Sci.*, vol. 69, pp. 219–251, 2019.

[108] M. Agostini *et al.*, "Final Results of GERDA on the Search for Neutrinoless Double-β Decay," *Phys. Rev. Lett.*, vol. 125, no. 25, p. 252502, 2020.

[109] S. Abe *et al.*, "Search for the Majorana Nature of Neutrinos in the Inverted Mass Ordering Region with KamLAND-Zen," *Phys. Rev. Lett.*, vol. 130, no. 5, p. 051801, 2023.

[110] D. Q. Adams *et al.*, "Search for Majorana neutrinos exploiting millikelvin cryogenics with CUORE," *Nature*, vol. 604, no. 7904, pp. 53–58, 2022.

[111] N. Aghanim *et al.*, "Planck 2018 results. VI. Cosmological parameters," *Astron. Astrophys.*, vol. 641, p. A6, 2020. [Erratum: Astron.Astrophys. 652, C4 (2021)].

[112] E. Di Valentino, S. Gariazzo, and O. Mena, "Most constraining cosmological neutrino mass bounds," *Phys. Rev. D*, vol. 104, no. 8, p. 083504, 2021.

[113] M. E. Levi *et al.*, "The Dark Energy Spectroscopic Instrument (DESI)," 2019. arXiv:1907.10688.

[114] M. Fukugita and T. Yanagida, "Baryogenesis Without Grand Unification," *Phys. Lett. B*, vol. 174, pp. 45–47, 1986.

[115] J. Lagoda, "Neutrino oscillations," in *Proceedings of The European Physical Society Conference on High Energy Physics — PoS(EPS-HEP2023)*, vol. 449, p. 020, 2023.

[116] B. Abi *et al.*, "Long-baseline neutrino oscillation physics potential of the DUNE experiment," *Eur. Phys. J. C*, vol. 80, no. 10, p. 978, 2020.

[117] K. Abe *et al.*, "Hyper-Kamiokande Design Report," 2018. arxiv:1805.04163.

[118] T. Wester *et al.*, "Atmospheric neutrino oscillation analysis with neutron tagging and an expanded fiducial volume in Super-Kamiokande I–V," *Phys. Rev. D*, vol. 109, p. 072014, 2024.

[119] M. S. Athar *et al.*, "Status and perspectives of neutrino physics," *Progress in Particle and Nuclear Physics*, vol. 124, p. 103947, 2022.

[120] A. Aguilar *et al.*, "Evidence for neutrino oscillations from the observation of ν_e appearance in a ν_μ beam," *Phys. Rev. D*, vol. 64, p. 112007, 2001.

[121] A. A. Aguilar-Arevalo *et al.*, "Significant Excess of Electronlike Events in the MiniBooNE Short-Baseline Neutrino Experiment," *Phys. Rev. Lett.*, vol. 121, p. 221801, 2018.

[122] C. Giunti and M. Laveder, "Statistical significance of the gallium anomaly," *Phys. Rev. C*, vol. 83, p. 065504, 2011.

[123] V. Barinov and D. Gorbunov, "BEST impact on sterile neutrino hypothesis," *Phys. Rev. D*, vol. 105, p. L051703, 2022.

[124] G. Cheng *et al.*, "Dual baseline search for muon antineutrino disappearance at $0.1\text{eV}^2 < \Delta m^2 < 100\text{eV}^2$," *Phys. Rev. D*, vol. 86, p. 052009, 2012.

[125] B. Armbruster *et al.*, "Upper limits for neutrino oscillations $\bar{\nu}_\mu \to \bar{\nu}_e$ from muon decay at rest," *Phys. Rev. D*, vol. 65, p. 112001, 2002.

[126] C. A. Argüelles *et al.*, "MicroBooNE and the ν_e Interpretation of the MiniBooNE Low-Energy Excess," *Phys. Rev. Lett.*, vol. 128, p. 241802, 2022.

[127] A. P. Serebrov *et al.*, "Search for sterile neutrinos with the Neutrino-4 experiment and measurement results," *Phys. Rev. D*, vol. 104, p. 032003, 2021.

[128] D. Lhuillier, "Sterile Neutrino Searches at Reactors," 2024.

[129] F. Aston, "The mass-spectra of chemical elements ," *The London, Edinburgh, and Dublin Philosophical Magazine and Journal of Science*, vol. 39, no. 233, pp. 611–625, 1920.

[130] A. Eddington, "The Internal Constitution of the Stars," *Nature*, vol. 106, no. 2653, pp. 14–20, 1920.

[131] H. A. Bethe and C. L. Critchfield, "The Formation of Deuterons by Proton Combination," *Phys. Rev.*, vol. 54, pp. 248–254, 1938.

[132] H. A. Bethe, "Energy Production in Stars," *Phys. Rev.*, vol. 55, pp. 434–456, 1939.

[133] C. F. von Weizsäcker, "Über Elementumwandlungen im Innern der Sterne," *Physikalische Zeitschrift*, vol. 38, pp. 176–191, 1937.

[134] W. Fowler, "Experimental and theoretical nuclear astrophysics; the quest for the origin of the elements," *Rev. Mod. Phys.*, vol. 56, no. 149, 1984.

[135] J. N. Bahcall and R. K. Ulrich, "Solar models, neutrino experiments, and helioseismology," *Rev. Mod. Phys.*, vol. 60, no. 2, pp. 297–372, 1988.

[136] N. Grevesse and A. Sauval, "Standard Solar Composition," *Space Science Reviews*, vol. 85, p. 161, 1998.

[137] N. Vinyoles *et al.*, "A New Generation of Standard Solar Models," *The Astrophysical Journal*, vol. 835, no. 2, p. 202, 2017.

[138] M. Asplund *et al.*, "The Chemical Composition of the Sun," *Annu. Rev. Astron. Astrophys.*, vol. 47, p. 481, 2009.

[139] E. Caffau *et al.*, "Solar Chemical Abundances Determined with a CO5BOLD 3D Model Atmosphere," *Solar Physics*, vol. 268, pp. 255–269, 2011.

[140] M. Asplund *et al.*, "The chemical make-up of the Sun: A 2020 vision," *Astron. Astrophys.*, vol. 653, no. A141, 2021.

[141] E. Magg *et al.*, "Observational constraints on the origin of the elements," *Astron. Astrophys.*, vol. 661, no. A140, 2022.

[142] J. N. Bahcall, "Neutrino-electron scattering and solar neutrino experiments," *Rev. Mod. Phys.*, vol. 59, pp. 505–521, 1987.

[143] B. T. Cleveland *et al.*, "Measurement of the Solar Electron Neutrino Flux with the Homestake Chlorine Detector," *The Astrophysical Journal*, vol. 496, no. 1, p. 505, 1998.

[144] R. Davis, "Nobel lecture: A half-century with solar neutrinos," *Rev. Mod. Phys.*, vol. 75, 2003.

[145] J. Abdurashitov *et al.*, "Results from SAGE (The Russian-American gallium solar neutrino experiment)," *Physics Letters B*, vol. 328, no. 1-2, pp. 234–248, 1994.

[146] P. Anselmann *et al.*, "Solar neutrinos observed by GALLEX at Gran Sasso," *Nuclear Physics B - Proceedings Supplements*, vol. 31, pp. 117–124, 1993.

[147] M. Altmann *et al.*, "Complete results for five years of GNO solar neutrino observations," *Physics Letters B*, vol. 616, no. 3, pp. 174–190, 2005.

[148] J. N. Abdurashitov *et al.*, "Measurement of the solar neutrino capture rate with gallium metal. III. Results for the 2002–2007 data-taking period," *Phys. Rev. C*, vol. 80, p. 015807, 2009.

[149] Y. Fukuda *et al.*, "Solar neutrino data covering solar cycle 22," *Phys. Rev. Lett.*, vol. 77, pp. 1683–1686, 1996.

[150] K. S. Hirata *et al.*, "Observation of ^{8}B solar neutrinos in the Kamiokande-II detector," *Phys. Rev. Lett.*, vol. 63, p. 16, 1989.

[151] S. Fukuda *et al.*, "The Super-Kamiokande detector," *Nucl. Instrum. Meth. A*, vol. 501, no. 2, pp. 418–462, 2003.

[152] K. Abe *et al.*, "Solar neutrino measurements using the full data period of Super-Kamiokande-IV," *Phys. Rev. D*, vol. 109, p. 092001, 2024.

[153] S. Fukuda *et al.*, "Solar ^{8}B and hep Neutrino Measurements from 1258 Days of Super-Kamiokande Data," *Phys. Rev. Lett.*, vol. 86, pp. 5651–5655, 2001.

[154] J. Boger *et al.*, "The Sudbury Neutrino Observatory," *Nucl. Instrum. Meth. A*, vol. 449, no. 1, pp. 172–207, 2000.

[155] Q. R. Ahmad *et al.*, "Measurement of the Rate of $\nu_e + d \rightarrow p + p + e^-$ Interactions Produced by ^{8}B Solar Neutrinos at the Sudbury Neutrino Observatory," *Phys. Rev. Lett.*, vol. 87, p. 071301, 2001.

[156] A. Renshaw *et al.*, "First Indication of Terrestrial Matter Effects on Solar Neutrino Oscillation," *Phys. Rev. Lett.*, vol. 112, p. 091805, 2014.

[157] B. Aharmim *et al.*, "Combined analysis of all three phases of solar neutrino data from the Sudbury Neutrino Observatory," *Phys. Rev. C*, vol. 88, p. 025501, 2013.

[158] B. Aharmim *et al.*, "A Search for Neutrinos from the Solar hep Reaction and the Diffuse Supernova Neutrino Background with the Sudbury Neutrino Observatory," *The Astrophysical Journal*, vol. 653, no. 2, p. 1545, 2006.

[159] G. Bellini *et al.*, "Final results of Borexino Phase-I on low-energy solar neutrino spectroscopy," *Phys. Rev. D*, vol. 89, p. 112007, 2014.

[160] G. Alimonti *et al.*, "The Borexino detector at the Laboratori Nazionali del Gran Sasso," *Nucl. Instrum. Meth. A*, vol. 600, no. 3, pp. 568–593, 2009.

[161] A. Gando *et al.*, "^{7}Be solar neutrino measurement with KamLAND," *Phys. Rev. C*, vol. 92, p. 055808, 2015.

[162] A. Gando *et al.*, "Measurement of the double-β decay half-life of ^{136}Xe with the KamLAND-Zen experiment," *Phys. Rev. C*, vol. 85, p. 045504, 2012.

[163] A. Allega *et al.*, "Event-by-event direction reconstruction of solar neutrinos in a high light-yield liquid scintillator," *Phys. Rev. D*, vol. 109, p. 072002, 2024.

[164] M. Yeh *et al.*, "A new water-based liquid scintillator and potential applications," *Nucl. Instrum. Meth. A*, vol. 660, no. 1, pp. 51–56, 2011.

[165] Z. Guo *et al.*, "Slow liquid scintillator candidates for MeV-scale neutrino experiments," *Astroparticle Physics*, vol. 109, pp. 33–40, 2019.

[166] E. Graham *et al.*, "Light yield of Perovskite nanocrystal-doped liquid scintillator," *Journal of Instrumentation*, vol. 14, no. 11, p. P11024, 2019.

[167] A. Lyashenko *et al.*, "Performance of Large Area Picosecond Photo-Detectors (LAPPDTM)," *Nucl. Instrum. Meth. A*, vol. 958, p. 162834, 2020. Proceedings of the Vienna Conference on Instrumentation 2019.

[168] T. Kaptanoglu *et al.*, "Spectral photon sorting for large-scale Cherenkov and scintillation detectors," *Phys. Rev. D*, vol. 101, p. 072002, 2020.

[169] M. Askins *et al.*, "Theia: an advanced optical neutrino detector," *Eur. Phys. J. C*, vol. 80, no. 416, 2020.

[170] M. Agostini *et al.*, "Identification of the cosmogenic ^{11}C background in large volumes of liquid scintillators with Borexino," *Eur. Phys. J. C*, vol. 81, no. 1075, 2021.

[171] B. R. and R. F., "ROOT — An object oriented data analysis framework," *Nucl. Instrum. Meth. A*, vol. 389, no. 1, pp. 81–86, 1997. New Computing Techniques in Physics Research V.

[172] H. Back *et al.*, "Borexino calibrations: hardware, methods, and results," *Journal of Instrumentation*, vol. 7, no. 10, p. P10018, 2012.

[173] M. Agostini *et al.*, "Simultaneous precision spectroscopy of *pp*, ^{7}Be, and *pep* solar neutrinos with Borexino Phase-II," *Phys. Rev. D*, vol. 100, p. 082004, 2019.

[174] S. Kumaran, "Geoneutrinos and solar neutrinos with the Borexino experiment," *Ph.D thesis*, 2022.

[175] M. Agostini *et al.*, "The Monte Carlo simulation of the Borexino detector," *Journal of Physics: Conference Series*, vol. 1342, no. 1, p. 012035, 2020.

[176] D. Basilico *et al.*, "Novel techniques for alpha/beta pulse shape discrimination in Borexino," 2023. arXiv:2310.11826.

[177] M. Agostini *et al.*, "Seasonal modulation of the ^{7}Be solar neutrino rate in Borexino," *Astroparticle Physics*, vol. 92, pp. 21–29, 2017.

[178] L. Pelicci *et al.*, "MLP cut updates," *Document Database, Internal Document*, 2021.

[179] A. Singhal, "Observation of CNO solar neutrinos with the Borexino Experiment," *Master thesis*, 2020.

[180] X. Ding, "High Precision Solar Neutrino Spectroscopy with Borexino and JUNO," *Ph.D thesis*, 2019.

[181] X. Ding and S. Kumaran, "LPoF Analysis and conclusions for GM," *Document Database, Internal Document*, 2021.

[182] F. Vissani, "Luminosity constraint and entangled solar neutrino signals," *Solar Neutrinos, Proc. 5th International Solar Neutrino Conference*, pp. 121–141, 2019.

[183] J. Bergström *et al.*, "Updated determination of the solar neutrino fluxes from solar neutrino data," *Journal of High Energy Physics*, vol. 2016, no. 132, 2016.

[184] F. Capozzi, E. Lisi, A. Marrone, and A. Palazzo, "Global analysis of oscillation parameters," *Journal of Physics: Conference Series*, vol. 1312, no. 1, p. 012005, 2019.

[185] M. Agostini *et al.*, "Sensitivity to neutrinos from the solar CNO cycle in Borexino," *Eur. Phys. J. C*, vol. 80, no. 1091, 2020.

[186] M. Gromov, "MLP efficiency update," *Document Database, Internal Document*, 2019.

[187] I. Drachnev and S. Marcocci, "MLP-subtracted fit approach," *Document Database, Internal Document*, 2019.

[188] X. Ding and A. Singhal, "Beta leakage and MLP efficiency summary," *Document Database, Internal Document*, 2022.

[189] D. Basilico and R. Biondi, "Towards CNO for Neutrino 2022 ^{210}Bi systematics, Phase-III final datasets," *Document Database, Internal Document*, 2022.

[190] P. de Holanda, W. Liao, and A. Smirnov, "Toward precision measurements in solar neutrinos," *Nuclear Physics B*, vol. 702, no. 1, pp. 307–332, 2004.

[191] J. N. Bahcall, M. Kamionkowski, and A. Sirlin, "Solar neutrinos: Radiative corrections in neutrino-electron scattering experiments," *Phys. Rev. D*, vol. 51, no. 11, pp. 6146–6158, 1995.

[192] M. Redchuk, "Looking inside the sun with the Borexino experiment : detection of solar neutrinos from the proton-proton chain and the CNO cycle," *Ph.D thesis*, 2020.

[193] D. Basilico *et al.*, "DataMCAgreement_GM," *Document Database, Internal Document*, 2020.

[194] L. Ludhova *et al.*, "NewQECalculation_C700," *Document Database, Internal Document*, 2021.

[195] O. Penek, "Measurement of pp and CNO cycle solar neutrinos with Borexino," *Ph.D thesis*, 2021.

[196] S. Marcocci, "Precision Measurement of Solar ν Fluxes with Borexino and Prospects for $0\nu\beta\beta$ Search with ^{136}Xe-loaded Liquid Scintillators," *Ph.D thesis*, 2016.

[197] N. Rossi *et al.*, "Chi2 smearing," *Document Database, Internal Document*, 2022.

[198] I. Esteban *et al.*, "The fate of hints: updated global analysis of three-flavor neutrino oscillations," *Journal of High Energy Physics*, vol. 2020, 2020.

[199] L. Pelicci *et al.*, "Systematics uncertainty budget for Phase-III Final," *Document Database, Internal Document*, 2022.

[200] F. Calaprice *et al.*, "Systematics to CNO evidence from the Bi-210 shape," *Document Database, Internal Document*, 2020.

[201] A. Re, "Inclusion of the Borexino (new) CNO result in the global analysis of neutrino data," *Document Database, Internal Document*, 2022.

[202] A. Gando *et al.*, "Constraints on θ_{13} from a three-flavor oscillation analysis of reactor antineutrinos at KamLAND," *Phys. Rev. D*, vol. 83, p. 052002, 2011.

[203] I. Esteban *et al.*, "The fate of hints: updated global analysis of three-flavor neutrino oscillations," *Journal of High Energy Physics*, vol. 2020, 2020.

[204] X. Ding *et al.*, "Solar Physics implications of Borexino CNO measurement," *Document Database, Internal Document*, 2022.

[205] X. Ding *et al.*, "CN abundance from solar neutrino data," *Document Database, Internal Document*, 2022.

[206] A. Serenelli, C. Peña Garay, and W. C. Haxton, "Using the standard solar model to constrain solar composition and nuclear reaction *S* factors," *Phys. Rev. D*, vol. 87, p. 043001, 2013.

[207] K. Abe *et al.*, "Solar neutrino measurements in Super-Kamiokande-IV," *Phys. Rev. D*, vol. 94, p. 052010, 2016.

[208] R. Bonventre and G. D. Orebi Gann, "Sensitivity of a low threshold directional detector to CNO-cycle solar neutrinos," *Eur. Phys. J. C*, vol. 78, no. 435, 2018.

[209] C. Aberle *et al.*, "Measuring directionality in double-beta decay and neutrino interactions with kiloton-scale scintillation detectors," *Journal of Instrumentation*, vol. 9, no. 06, p. P06012, 2014.

[210] B. Wonsak *et al.*, "Topological track reconstruction in unsegmented, large-volume liquid scintillator detectors," *Journal of Instrumentation*, vol. 13, no. 07, p. P07005, 2018.

[211] A. Elagin *et al.*, "Separating double-beta decay events from solar neutrino interactions in a kiloton-scale liquid scintillator detector by fast timing," *Nucl. Instrum. Meth. A*, vol. 849, pp. 102–111, 2017.

[212] J. Caravaca *et al.*, "Cherenkov and scintillation light separation in organic liquid scintillators," *Eur. Phys. J. C*, vol. 77, no. 811, 2017.

[213] J. Gruszko *et al.*, "Detecting Cherenkov light from 1–2 MeV electrons in linear alkylbenzene," *Journal of Instrumentation*, vol. 14, no. 02, p. P02005, 2019.

[214] A. R. Back *et al.*, "Accelerator Neutrino Neutron Interaction Experiment (ANNIE): Preliminary Results and Physics Phase Proposal," 2017. arXiv:1707.08222.

[215] J. Martyn, "Correlated and integrated directionality in Borexino : using Cherenkov directionality for the measurement of solar neutrinos in high light-yield liquid scintillator detectors," *Ph.D thesis*, 2023.

[216] A. Wessel, "Directionality-Selection Cuts," *Document Database, Internal Document*, 2021.

[217] J. Martyn, "Directionality Part 1: Summary of MC Production," *Document Database, Internal Document*, 2021.

[218] D. Basilico *et al.*, "CID combined with the spectral fit," *Document Database, Internal Document*, 2023.

[219] J. Martyn *et al.*, "CID for CNO Results," *Document Database, Internal Document*, 2022.

[220] J. Martyn, "CID last crosschecks," *Document Database, Internal Document*, 2023.

[221] A. C. Re, "Low energy solar-ν: expected values for survival probability and interaction rate in Borexino," *Document Database, Internal Document*, 2023.

[222] G. D'Agostini, "A multidimensional unfolding method based on Bayes' theorem," *Nucl. Instrum. Meth. A*, vol. 362, no. 2, pp. 487–498, 1995.

[223] G. Cowan, "Statistics for Searches at the LHC," in *69th Scottish Universities Summer School in Physics: LHC Physics*, pp. 321–355, 2013. arxiv:1307.2487.

[224] A. Abusleme *et al.*, "The Design and Technology Development of the JUNO Central Detector," 2023. arXiv:2311.17314.

[225] A. Abusleme *et al.*, "Optimization of the JUNO liquid scintillator composition using a Daya Bay antineutrino detector," *Nucl. Instrum. Meth. A*, vol. 988, p. 164823, 2021.

[226] G. Cao *et al.*, "JUNO Energy Resolution Technical Note," *Document Database, Internal Document*, 2023.

[227] A. Abusleme *et al.*, "The JUNO experiment Top Tracker," *Nucl. Instrum. Meth. A*, vol. 1057, p. 168680, 2023.

[228] A. Abusleme *et al.*, "The design and sensitivity of JUNO's scintillator radiopurity pre-detector OSIRIS," *Eur. Phys. J. C*, vol. 81, no. 973, 2021.

[229] R. Wirth, "Status Osiris Calibration (charge, engergy)," *Document Database, Internal Document*, 2024.

[230] A. Abusleme *et al.*, "Prospects for Identifying the Neutrino Mass Ordering with Reactor Antineutrinos in JUNO," *Document Database, Internal Document*, 2024.

[231] A. Abusleme *et al.*, "Calibration Strategy of the JUNO Experiment," *J. High Energ. Phys.*, vol. 03, p. 004, 2021.

[232] D. Basilico, "AFG Calibration summary," *Document Database, Internal Document*, 2023.

[233] A. Takenaka, "Low-energy calibration with ^{241}Am Source," *Document Database, Internal Document*, 2023.

[234] A. Abusleme *et al.*, "Radioactivity control strategy for the JUNO detector," *Journal of High Energy Physics*, vol. 11, p. 102, 2021.

[235] D. Basilico, A. Göttel, and L. Pelicci, "Backgrounds estimation for JUNO low and intermediate energy solar neutrino analysis," *Document Database, Internal Document*, 2021.

[236] G. Alimonti *et al.*, "Measurement of the ^{14}C abundance in a low-background liquid scintillator," *Phys.Lett.B*, vol. 422, no. 1-4, pp. 349–358, 1998.

[237] G. Keefer, "Laboratory Studies of Lead Removal from Liquid Scintillator in Preparation for KamLAND's Low Background Phase," *AIP Conference Proceedings*, vol. 1338, 2011.

[238] S. Abe *et al.*, "Production of radioactive isotopes through cosmic muon spallation in KamLAND," *Phys. Rev. C*, vol. 81, p. 025807, 2010.

[239] M. Ambrosio *et al.*, "Measurement of the residual energy of muons in the Gran Sasso underground laboratories," *Astropart. Phys.*, vol. 19, no. 3, pp. 313–328, 2003.

[240] G. Bellini *et al.*, "Cosmogenic Backgrounds in Borexino at 3800 m water-equivalent depth," *Journal of Cosmology and Astroparticle Physics*, vol. 2013, no. 08, pp. 049–049, 2013.

[241] X. B. Ma, W. L. Zhong, L. Z. Wang, Y. X. Chen, and J. Cao, "Improved calculation of the energy release in neutron-induced fission," *Phys. Rev. C*, vol. 88, no. 1, 2012.

[242] S. Agostinelli *et al.*, "Geant4—a simulation toolkit," *Nucl. Instrum. Meth. A*, vol. 506, no. 3, pp. 250–303, 2003.

[243] T. Lin *et al.*, "Simulation software of the JUNO experiment," *Eur. Phys. J. C*, vol. 83, no. 382, 2023.

[244] G. Huang *et al.*, "Data-driven simultaneous vertex and energy reconstruction for large liquid scintillator detectors," *Nuclear Science and Techniques*, vol. 34, no. 83, 2023.

[245] A. Abusleme *et al.*, "Sub-percent precision measurement of neutrino oscillation parameters with JUNO," *Chinese Physics C*, vol. 46, no. 12, p. 123001, 2022.

[246] A. Abusleme *et al.*, "Feasibility and physics potential of detecting ^{8}B solar neutrinos at JUNO," *Chinese Physics C*, vol. 45, no. 2, p. 023004, 2021.

[247] Y. Nakajima, "Recent results and future prospects from Super-Kamiokande," *Neutrino 2020, Zenodo, 10.5281/zenodo.3959640*, 2020.

[248] I. Esteban *et al.*, "Global analysis of three-flavour neutrino oscillations: synergies and tensions in the determination of θ_{23}, δ_{CP}, and the mass ordering," *Journal of High Energy Physics*, vol. 2019, no. 106, 2019.

[249] J. Zhao *et al.*, "Model independent approach of the JUNO ^{8}B solar neutrino program," 2024. arXiv:2210.08437v2.

[250] G. Bellini *et al.*, "Absence of a day–night asymmetry in the ^{7}Be solar neutrino rate in Borexino," *Physics Letters B*, vol. 707, no. 1, pp. 22–26, 2012.

[251] B. Aharmim *et al.*, "Searches for high-frequency variations in the ^{8}B solar neutrino flux at the Sudbury Neutrino Observatory," *The Astrophysical Journal*, vol. 710, no. 1, p. 540, 2010.

[252] G. Chen and Y. Huang, "pp solar neutrino analysis status," *Document Database, Internal Document*, 2024.

[253] X. Zhao, "Prospect for the Detection of the Geo-neutrino Signal with JUNO," *XX International Workshop on Neutrino Telescopes (Neutel 23), Zenodo, 10.5281/zenodo.10571926*, 2023.

[254] L. Ludhova *et al.*, "Geoneutrino Sensitivity: Status from Jülich," *Document Database, Internal Document*, 2024.

[255] G. Li, "Atmospheric neutrino oscillations at JUNO," *XX International Workshop on Neutrino Telescopes (Neutel 23), Zenodo, 10.5281/zenodo.10571194*, 2023.

[256] A. Khatun *et al.*, "NMO sensitivity with Atmopsheric neutrino," *Document Database, Internal Document*, 2024.

[257] A. Abusleme *et al.*, "JUNO sensitivity on proton decay $p \to \bar{\nu}K^+$ searches," *Chinese Physics C*, vol. 47, no. 11, p. 113002, 2023.

[258] K. Abe *et al.*, "Search for proton decay via $p \to \nu K^+$ using 260 kiloton $\cdot$ year data of Super-Kamiokande," *Phys. Rev. D*, vol. 90, p. 072005, 2014.

[259] A. Abusleme *et al.*, "JUNO sensitivity to the annihilation of MeV dark matter in the galactic halo," *Journal of Cosmology and Astroparticle Physics*, vol. 2023, no. 09, p. 001, 2023.

[260] D. Basilico *et al.*, "JUNO sensitivity to intermediate energy solar neutrinos, ^{7}Be, pep, and CNO: results of the two independent analysis performed by Milano and Jülich," *Document Database, Internal Document*, 2022.

[261] A. Savitzky and M. J. E. Golay, "Smoothing and Differentiation of Data by Simplified Least Squares Procedures.," *Analytical Chemistry*, vol. 36, no. 8, pp. 1627–1639, 1964.

[262] A. S. Göttel, "Solar neutrino detection: CNO discovery with Borexino and preparations for success in JUNO and OSIRIS," *Ph.D thesis*, 2022.

[263] D. Basilico *et al.*, "Updated JUNO sensitivity to intermediate energy solar neutrinos, ^{7}Be, pep, and CNO: results of the two independent analysis performed by Milano and Jülich," *Document Database, Internal Document*, 2022.

[264] G. Bellini *et al.*, "Neutrinos from the primary proton–proton fusion process in the Sun," *Nature*, vol. 512, pp. 383–386, 2014.

[265] A. Abusleme *et al.*, "Mass testing and characterization of 20-inch PMTs for JUNO," *Eur. Phys. J. C*, vol. 82, no. 1434-6052, 2022.

[266] M. Maltoni and A. Y. Smirnov, "Solar neutrinos and neutrino physics," *Eur. Phys. J. A*, vol. 52, no. 4, 2016.

[267] J. Martyn and M. Wurm, "Preliminary Ideas for a Cherenkov Calibration Source," *Document Database, Internal Document*, 2023.

[268] D. Basilico *et al.*, "Technote on the analysis strategy to measure ^{7}Be and CNO solar neutrinos with the Correlated Directional Analysis exploiting Cherenkov light," *Document Database, Internal Document*, 2024.

[269] A. Singhal *et al.*, "Understanding the systematic effects for the directional detection of sub-MeV solar neutrinos with Borexino," *Journal of Physics: Conference Series*, vol. 2156, no. 1, p. 012202, 2021.

[270] A. Singhal *et al.*, "Combined directional and spectral analysis of solar neutrinos from Carbon-Nitrogen-Oxygen fusion cycle with Borexino Experiment," in *Proceedings of The European Physical Society Conference on High Energy Physics - PoS(EPS-HEP2023)*, vol. 449, p. 163, 2023.

[271] A. Singhal, "JUNO's sensitivity to ^{7}Be, *pep*, and CNO solar neutrinos," *XX International Workshop on Neutrino Telescopes (Neutel 23), Zenodo, 10.5281/zenodo.10568598*, 2024.

[272] A. Singhal *et al.*, "JUNO's sensitivity to ^{7}Be, *pep*, and CNO solar neutrinos," in *Proceedings of The European Physical Society Conference on High Energy Physics - PoS(EPS-HEP2023)*, vol. 449, p. 193, 2023.